Geofluids

Advances in Enhancing Coalbed Methane and Shale Gas Recovery

Lead Guest Editor: Yong Li
Guest Editors: Zhejun Pan, Jian Shen, Songqi Pan, Yanjun Meng, and Haijiao Fu

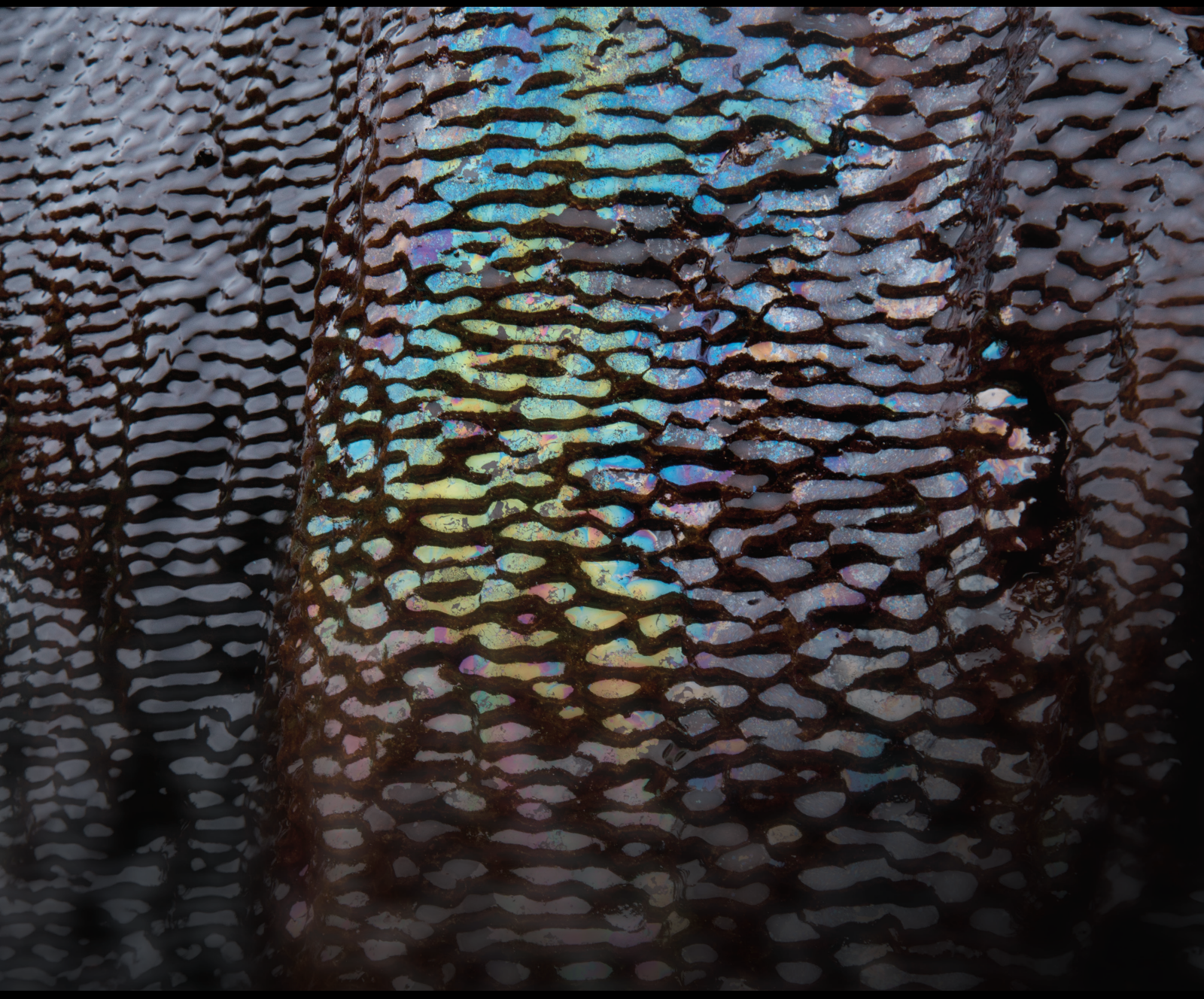

Advances in Enhancing Coalbed Methane and Shale Gas Recovery

Geofluids

Advances in Enhancing Coalbed Methane and Shale Gas Recovery

Lead Guest Editor: Yong Li
Guest Editors: Zhejun Pan, Jian Shen, Songqi Pan, Yanjun Meng, and Haijiao Fu

Contents

Fluidity Influencing Factors Analysis and Ratio Optimization of New Sealing Materials Based on Response Surface Method

Xin Guo, Sheng Xue, Yaobin Li, Chunshan Zheng, and Gege Yang

Research Article (15 pages), Article ID 5538302, Volume 2021 (2021)

Hindawi
Geofluids
Volume 2021, Article ID 8298579, 14 pages
https://doi.org/10.1155/2021/8298579

Review Article

Review of the Hydrogeological Controls on Coalbed Methane (CBM) and Development Trends

Bo Wang,[1,2] Dangliang Wang,[3] Wenjie Cao,[4] Guofu Li,[1] Wei Hou,[5,6] Xinrui Cui,[7] Tao Hou,[7] and Mingjian Shi[2]

[1]*State Key Laboratory of Coal and Coalbed Methane Co-mining, Shanxi Jincheng Anthracite Mining Group Co., Ltd., Jincheng 048000, China*
[2]*Information Institute of the Ministry of Emergency Management of PRC, Beijing 100029, China*
[3]*School of Geoscience & Surveying Engineering, China University of Mining & Technology (Xuzhou), Xuzhou 221116, China*
[4]*School of Geoscience & Surveying Engineering, China University of Mining & Technology (Beijing), Beijing 100083, China*
[5]*PetroChina Coalbed Methane Company Limited, Beijing 100083, China*
[6]*Zhonglian CBM State Engineering Research Center Co., Ltd., Beijing 100095, China*
[7]*PetroChina Huabei Oilfield Company, Renqiu 062550, China*

Correspondence should be addressed to Dangliang Wang; wangdangliang@cumt.edu.cn

Received 8 April 2021; Revised 10 September 2021; Accepted 8 October 2021; Published 22 November 2021

Academic Editor: Chris Harris

Hydrogeological conditions can control the generation, preservation, enrichment, and production of coalbed methane (CBM) in the field; however, research on these impacts is insufficient, resulting in the limitation of the development of coalbed methane. This paper summarizes the current research status and development trends of the effect of hydrogeology on CBM using methods such as mathematical statistics, literature analysis, well logging, and hydrochemical analysis. The results indicate that it is beneficial for the generation of secondary biogenic gases in low-rank coal seams under the situations like active hydrodynamic conditions with a salinity less than 1000 mg/L, a pH range from 5.9 to 8.8, or a range of oxidation-reduction potential from -540 mV to -590 mV. The abnormally high temperature due to the magmatic-hydrothermal fluids accelerates the metamorphism of coal rocks, leading to the promotion of the generation of thermogenic gases. When the coalbed structural conditions of one area are similar to the depositional conditions in that area, the CBM is accumulated if the conditions of that area meet the following criteria: the water type is $NaHCO_3$, the salinity is greater than 1500 mg/L, the desulfurization coefficient is less than 1, and the sodium-chloride coefficient is less than 10. The stable isotope analysis of CBM well-produced water shows that the δD values in the groundwater shift to the left of the global meteoric water line, indicating that the produced water comes from atmospheric precipitation. In the CBM enrichment zone, the area with a relatively high salinity and a low sodium-chloride coefficient is the high-production area. Based on our study, three high CBM-production patterns are summarized: coalbed structure-hydraulic trapping, fold limb-fracture development, and syncline core-water stagnation. Additionally, four development trends of the control of hydrogeology on CBM are proposed: transformation from qualitative evaluation to quantitative evaluation, from a singular evaluation standard to multiple evaluation standards, from static evaluation to dynamic evaluation, and from pure theoretical research to theoretical guidance on production practices.

1. Introduction

Hydrogeological conditions have impacts on the processes of the formation, enrichment, accumulation, and production of CBM in coalbed. Groundwater is not only the medium for the generation of CBM [1, 2] but also the driving force for the migration of CBM and the carrier of the production of CBM [3–5]. After nearly 20 years of explorations and studies on CBM, abundant theoretical findings about the role of hydrogeological conditions in gas controlling are achieved,

which effectively guides the selection of CBM enrichment areas. However, few studies on the quantitative evaluation about the hydrogeology in the enrichment areas and its effect on high CBM production are conducted. Therefore, on the basis of reviewing the current research on the gas controlling effect of hydrogeology around the world, this paper analyzes the existing scientific problems and explores the development trends of gas control research with the expectation to guide the efficient extraction of CBM in China.

2. Role of Water in CBM Formation

Coalbed methane forms as either biogenic gas or thermogenic gas [6–9]. The effect of water on the formation of biogenic gas is realized by hydrodynamic conditions, water salinity, and hydrological environments. For the formation of thermogenic gas, the effect of water can be reflected by the heating effect that enhances the coalification process, which further increases the potential of methane generation. The preceding results explain the mechanism of water effect on CBM formation, which is important for selecting the method to extract CBM of different coal ranks.

2.1. Influence of Water on Biogenic Gases. To compare with the secondary biogenic gases, primary biogenic gases are hard to be preserved and accumulated to form reservoirs. Studies around the world indicate that active hydrodynamic conditions with proper salinity, a proper pH value, and oxidation-reduction reactions are beneficial for the formation of secondary biogenic gases in low-rank coals. The hydrodynamic and hydrochemical conditions which are required for producing secondary biogenic gases are as follows: the range of the pH value from 5.9 to 8.8 is suitable for methanogens to survive and grow as well as the most beneficial range for producing methane [10, 11]. Xianbo et al. conducted an experiment in the laboratory and found that, under the same conditions, the low-rank coal has the maximum methane production capability in the water environment with a pH of 8 [12]. In a water environment where the oxidation-reduction reactions are lower than -330 mV, the capability of generating secondary biogenic gases is normal; however, when the oxidation-reduction reactions range is from -540 mV to -590 mV, the methanogens have the highest activity rate and the gas generation capability in low-rank coals reaches the maximum [13]. A temperature range from 36°C to 42°C is most beneficial for the growth of methanogens [14]. When the salinity does not exceed 4000 mg/L, a large amount of secondary biogenic gases is generated. When the salinity is greater than 10000 mg/L, the gas generation capacity of low-rank coals decreases sharply [15–17]. Taking Powder River Basin in the United States as an example, groundwater is quite active in the slope area on the eastern edge. The salinity in that area is less than 1000 mg/L; thereby, the methanogens are very active, which speeds up the generation of secondary biogenic gases [18]. All these theoretical results provide evidence for selecting the best place for extracting CBM in low-rank coals.

2.2. Influence of Water on Thermogenic Gases. Thermogenic gases are generated mostly during the stage where coal undergoes metamorphism. The heat is the main factor that speeds up the metamorphism process while the groundwater plays an additional role during the formation of thermogenic gases. As fluids carrying the heat, the groundwater directly exchanges heat with coal seams, driving the metamorphism of coal seams. There are two ways for hydrothermal fluids to speed up the metamorphism process: one is the direct contact between coal seams and magma. Magma contains volatiles, which emits high-temperature steams. When the temperature reaches a critical point, high-temperature steams become hydrothermal fluids. This process is also called the pneumatolytic hydrothermal process [19]. The other method is that the water in the coal seam and in the neighboring aquifer becomes high-temperature hydrothermal fluids [20] because the water temperature is increased due to influences from the heat source in the depth of the ground.

3. Hydrogeological Controls on CBM Enrichment

3.1. Relationship between Hydrodynamic Zones and CBM Enrichment. Hydrodynamic conditions affect the distribution of methane in coal seams by controlling groundwater movements and changing fluid pressure. To provide evidence for exploring the mechanisms of groundwater movement and finding CBM enrichment zones, this paper carefully divides Qinshui Basin into several hydrodynamic zones.

3.1.1. Classification of Hydrodynamic Fields. At present, representative views on the controlling effect of hydrodynamic zones on the enrichment of CBM in China are as follows: the sealing or plugging of hydraulic flows creates a favorable environment for CBM enrichment. The hydraulic forces cause the methane to migrate and dissipate, resulting in the destruction of CBM reservoirs [21]. Taking the southern Qinshui Basin as an example, domestic scholars divide the basin into three zones based on the geological structure, salinity, and runoff intensity: strong runoff zone, medium runoff zone, and weak runoff zone. The strong runoff zone is located within the belt of 3 km–5 km of the basin margin. Within the zone, the salinity generally ranges from 357 mg/L to 542 mg/L, and the average gas content in main coal seams ranges from 6 to 8 m^3/t. The medium runoff zone is located at the slope zone around the basin with a width range from 3 km to 8 km. In the zone, the runoff condition is relatively strong, and the salinity is generally between 466 mg/L and 1399 mg/L. What is more, the gas content in the coal seam varies greatly, ranging from 3 to 16 m^3/t. The weak runoff zone is located at the internal of the basin, which is abundant in groundwater. The salinity in the zone reaches 1824 mg/L. Due to weak groundwater runoff, the content of CBM in this zone is generally high, reaching 26 m^3/t [22, 23].

On the basis of hydrodynamic zoning at the basin level, domestic scholars worked out a block-level method for identifying hydrodynamic zones according to exploration and

practice data. Based on the ground pressure data collected in the field testing, they calculated the converted water table and drew the converted water table map to analyze the groundwater flowing state [14]. Then, they divided the groundwater hydrodynamic fields into three zones according to the following conditions such as the structure, hydrochemical characteristics, and runoff intensity in the basin (see Table 1): strong runoff zone, medium runoff zone, and stagnant zone [22–25].

3.1.2. CBM Reservoir Formation Pattern Based on Hydrodynamic Zones. A hydrodynamic condition is one of the main factors controlling the formation of CBM reservoirs. In general, scholars associate hydrodynamic conditions with structural conditions to figure out the formation pattern of CBM reservoirs. Then, they locate the area which is most favorable for CBM enrichment [26]. Fu et al. were the first to propose a conceptual model that combined hydrodynamic conditions with structural conditions. They divided the seal-capping capability of hydraulic runoffs in Qinshui Basin into three types: stagnant runoffs on the pothole-shaped equipotential surface, slow runoffs on the half-graben equipotential surface, and slow runoffs on the fan-shaped equipotential surface [27]. Qin et al. proposed a CBM reservoir formation pattern in which the CBM reservoir was formed because of the seal-capping of hydraulic flows and the imbricate thrust faults in the Zhuozishan mining area, giving a new way of thinking about how to explain the controlling effect of hydrodynamic conditions under complex compositions [28]. Zhu et al. summarized two CBM reservoir formation patterns according to the hydrochemistry, hydrodynamics, and composition characteristics of the Gujiao mining area in the Xi'shan coalfield: monocline structure with hydraulic sealing and horst with hydraulic sealing [29]. Zeng et al. further put forward three CBM enrichment patterns [30]: monocline hydrodynamics, syncline hydrodynamics, and fault hydrodynamics. All the preceding results are of great significance to be referenced when selecting an area with highly enriched CBM.

In the preceding studies, the reservoir formation patterns are classified based on the relationships between geological structures and hydrodynamic zones, which takes fewer considerations on the capping combination condition under the subsidence control, and the scale of CBM reservoirs formed through these patterns is relatively small.

Based on the coupling between geological structures, hydrodynamics, and sedimentary substances, the author dissected the Qinnan-Xiadian area and set up a configured block-level CBM reservoir formation pattern based on main control elements (see Figure 1). The Qinnan-Xiadian area is mainly a syncline structure. One limb of the syncline is cut off by two faults. Combining the geological structure, hydrodynamics, and sedimentary forces, the author divided the limb into three basic systems: open type, semiopen type, and close type. These three basic systems correspond to the recharge zone, weak runoff zone, and pressure-bearing and stagnant zone, respectively, in the figure. The Qinnan-Xiadian block is a delta sedimentary area with the upper roof made by mudstone which has good sealing and capping performance. The mudstone roof is distributed stably in the whole zone. The lower floor is made of mudstone or silty mudstone which has a relatively good sealing and capping performance. Therefore, the coupling between geological structures and hydrodynamics is the main factor controlling CBM enrichment in this block. The recharge zone is located at the eastern limb of the syncline. The boundaries of the recharge zone are mainly divided into three types: the water-conducting boundary, jacking overflow boundary, and infiltration recharge boundary. The boundaries are closely related to surface hydraulics. Therefore, the hydraulic activity in the recharge zone is strong, thereby dissolving the methane easily and creating a poor CBM preservation condition. The gas content in the coal seam is less than $8\,m^3/t$. The gas saturation is less than 48%. The weak runoff zone is located on both sides of the eastern fault. The boundaries are mainly divided into three types: the boundary for gas dissipation, the boundary for sealing water and trapping gases, and the boundary for water discharge and gas leakage. This zone is partly supplemented by atmospheric precipitation. The CBM preservation conditions are relatively good. The gas output from CBM wells is stable. Gas content is greater than $16\,m^3/t$, and gas is evenly distributed. The pressure-bearing and stagnant zone is located at the low-potential area of the syncline. The hydrodynamic runoff conditions in that zone are poor. The boundaries are mainly divided into two types: the boundary for sealing water and trapping gases and the boundary for storing stagnant water. This zone is basically not recharged by atmospheric precipitation. Therefore, it is enriched with CBM. The gas content is greater than $14\,m^3/t$. The gas saturation is greater than 82%.

3.2. Response Mechanism of Hydrogeochemistry to CBM Enrichment. Hydrogeochemistry features are closely related to CBM. Different groundwater salinity values have varying impacts on CBM enrichment [31]. The isotopic distribution indicates the cause for water produced in coal seams, which further affects the CBM enrichment. Both can indicate the supply source for groundwater, the movement paths of groundwater, and the runoff intensity of groundwater. The groundwater salinity and isotopic distribution can be used to find the CBM enrichment rules under different geological conditions, to figure out the best solution for selecting highly productive and enriched areas of CBM, and to improve the efficiency of extracting and exploring CBM.

3.2.1. Hydrogeochemical Parameter Characterization and Its Relationship with CBM Enrichment. Parameters that mainly characterize hydrogeochemistry features include the water type, salinity, and content of main ions. Currently, the common diagrams for determining the water type mainly include a six-axis diagram (Tickel diagram), three-line diagram, Stiff diagram, and Kurlov diagram [31].

This paper employs the Stiff diagram to visually display the differences in the chemical composition of water which is produced from CBM wells in several typical blocks of Qinshui Basin and Ordos Basin. Figure 2 shows the main findings of the study. From the figure, we can see the specific content of main cations and anions in water which is

Table 1: Conditions for identifying different hydrodynamic zones.

Identification condition	Strong runoff zone	Medium runoff zone	Stagnant zone
Fault development characteristics	Strongly fractured fault with a high hydraulic conductivity	Fractures and faults distributed within the zone with a relatively low hydraulic conductivity	No fractures or fewer fractures within the zone
Connection with surface water	Close relationship between the surface water in the zone and the aquifer	Hydraulic relationships between part of the surface water in the zone and the aquifer	No hydraulic relationship between the surface water and the aquifer
Water type	$SO_4 \cdot Cl^- - Na \cdot K$	$HCO_3 \cdot Cl - Na \cdot K$	$Cl - Na \cdot K$
Converted hydraulic gradient	>0.3 m/m	0.1~0.3 m/m	Less than 0.1 m/m
Salinity	Low	Medium	High

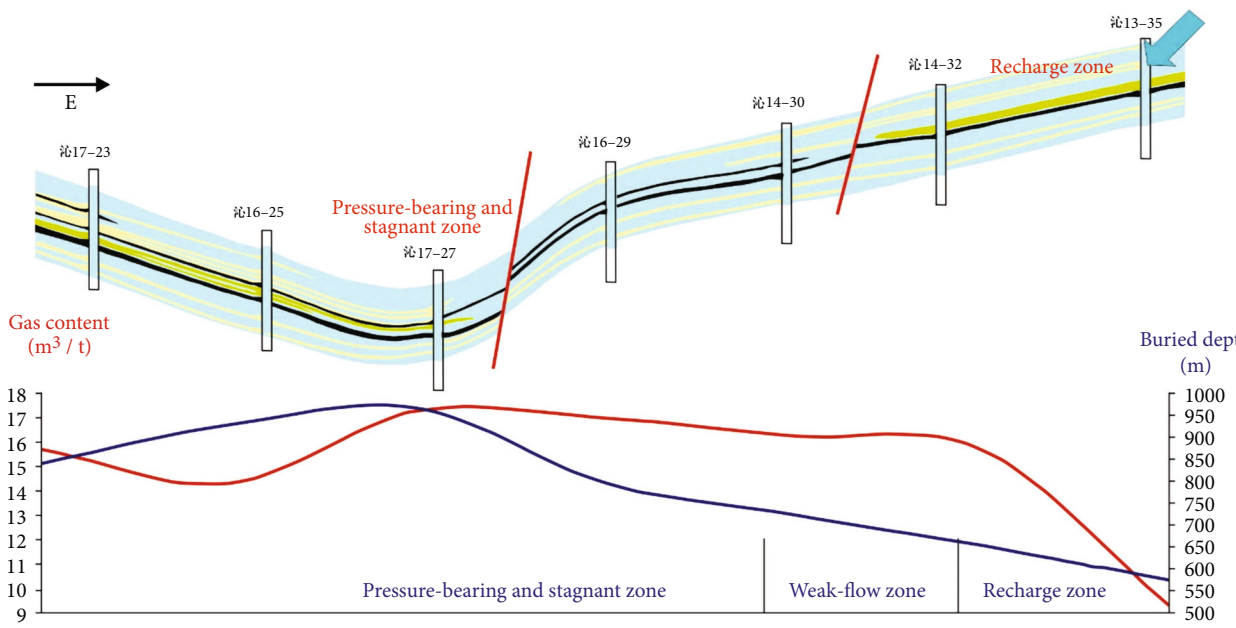

Figure 1: Analysis map of the accumulation model of the Qinnan-Xiadian area.

produced from different blocks and the corresponding Stiff diagrams. It can be concluded from Figure 2 that blocks that were highly developed have similar hydrogeochemical characteristics. Water in the CBM enrichment areas is mainly classified into two types: Na-HCO_3 and Na-Cl-HCO_3. For both water types, the cation characteristics are as follows: Na^+ and K^+ are the dominating cations, accounting for more than 90% of the total amount of cations. The content of Mg^{2+} and Ca^{2+} is very low, which accounts for less than 10% of the total amount of cations. The anion characteristics are as follows: HCO_3^- is the dominating anion, or Cl^- and HCO_3^- are the dominating anions.

Salinity can be used as an important reference to determine the sealing conditions and hydrodynamic conditions of coal reservoirs. Generally speaking, the areas with stagnant groundwater have high salinity; thus, CBM is more likely to be enriched. However, in the areas close to the recharge zone or the areas with intense groundwater runoffs, CBM can be easily dissipated along with groundwater movements. CBM is not easy to be preserved. Domestic scholars have reached similar conclusions through sampling and analyzing the water which is produced from CBM wells in places with relatively simple geological structural conditions such as Fanzhuang, Shijiazhuang, Panzhuang, and Shizhuangnan [32–36] in Qinshui Basin: CBM is more enriched in the areas which have the following conditions: the salinity is greater than 1500 mg/L, the desulfurization coefficient is less than 1, and the coefficient of sodium and chloride is less than 10 (see Table 2).

3.2.2. Response Mechanism of Isotope Geochemistry. The stable isotope compositions of hydrogen and oxygen can provide evidence for the mixture of CBM well-produced water and atmospheric precipitation or groundwater in the surrounding rock aquifers, thus indicating changes in the permeability and water flow rate. In addition, the stable

Block Name	main cation ($mg \cdot L^{-1}$)	main anion ($mg \cdot L^{-1}$)	stiff diagram	water type
Fanzhuang block	$Na^{+}+K^{+}$ 262.1～1141 Mg^{2-} 0. 5～38. 2 Ca^{2-} 0. 8～30. 2	SO_4^{2-} 0. 9～763 Cl^{-} 37. 3～1096 HCO_3^{-} 200. 8～1689	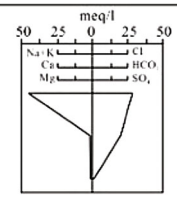	$Na\text{-}Cl\text{-}HCO_3$
Zhengzhuang block	$Na^{+}+K^{+}$ 434.3～861 Mg^{2-} 1. 5～28. 7 Ca^{2-} 3. 1～32. 6	SO_4^{2-} 4. 2～239. 7 Cl^{-} 42. 7～127. 5 HCO_3^{-} 740. 3～1507	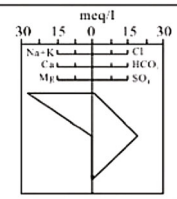	$Na\text{-}HCO_3$
Hancheng block	$Na^{+}+K^{+}$ 388. 5～1343. 5 Mg^{2-} 1. 1～38. 6 Ca^{2-} 5. 25～44. 4	SO_4^{2-} 0. 5～570 Cl^{-} 97. 2～1612 HCO_3^{-} 318～1504	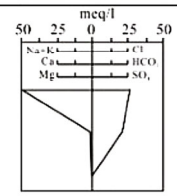	$Na\text{-}Cl\text{-}HCO_3$
Baode block	$Na^{+}+K^{+}$ 105～604 Mg^{2-} 24～92.8 Ca^{2-} 22～144	SO_4^{2-} 1～189 Cl^{-} 114～930 HCO_3^{-} 180～1073	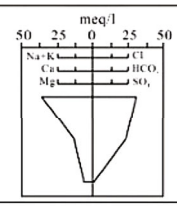	$Na\text{-}Cl\text{-}HCO_3$

Figure 2: Geochemical characteristics of groundwater in typical blocks of North China.

isotope compositions of hydrogen and oxygen are also effective indicators for determining the changes of runoff conditions of CBM well-produced water [36–38]. The stable isotope analysis of CBM well-produced water shows that positive deviations of $\delta^{18}O$ and δD values in the groundwater are related to high water yield and low gas yield in CBM wells, while negative deviations of $\delta^{18}O$ and δD values in the groundwater are related to low water yield and high gas yield in CBM wells [39]. These conclusions are based on the measured data and theoretical analysis. Some scholars find that shallow strata and areas with more active groundwater are greatly affected by surface water. The hydrogen and oxygen isotope ratios in produced water are high, showing positive deviations of $\delta^{18}O$ and δD from the global meteoric water line. However, in the deep strata which have a weak hydraulic connection with surface water, hydrogen and oxygen isotope ratios of produced water are low. It shows negative deviations of $\delta^{18}O$ and δD on the global precipitation curve. It means that the measured values of $\delta^{18}O$ and δD are lower than the reference values on GMWL. Considering the relationship between hydrodynamics and coalbed methane enrichment and high production, hydrogen and oxygen isotopes are proposed indicators showing coalbed methane enrichment and high production.

Figure 3 shows the H and O isotopes in coal seam-produced water from CBM wells in Qinshui Basin which is located at the central Guizhou uplift area and Bowen Basin in Australia. From Figure 3, we can see that $\delta^{18}O$ and δD values in Qinshui Basin are lower, with δD ranging from -80‰ to -75‰ and $\delta^{18}O$ ranging from -12‰ to -8‰. CBM wells are distributed on both sides of the global atmospheric precipitation line. Most of the CBM wells are at the right of the curve, indicating that the reason for forming coalbed water is complex. Most of the water is produced by sedimentation; however, the water in some wells is produced by infiltration. For the central Guizhou uplift area, there is a relatively large variation in hydrogen and oxygen isotopes, with δD ranging from -90‰ to -30‰ and $\delta^{18}O$ ranging from -11‰ to -4‰. The wells are mainly distributed at the left of the global meteoric water line. The δD has obvious *D* drifting characteristics, indicating that the coalbed water is mainly recharged by atmospheric precipitation as well as a strong interaction between water and rock [40]. The $\delta^{18}O$ and δD values in Bowen Basin CBM water are relatively higher, with δD ranging from -50‰ to -30‰ and $\delta^{18}O$ ranging from -8‰ to -4‰. The wells are mainly distributed near the global meteoric water line. The δD tends to shift to the right, indicating that the coalbed water is recharged by surface water, and most of the water is produced in sedimentary processes. The hydrogen and oxygen isotopes in atmospheric precipitation are relatively light, while the hydrogen and oxygen isotopes in sedimentary water are relatively heavy due to the influence of fractionation. Therefore, the source of coalbed water can be judged

Table 2: Geochemical characteristics of water produced from CBM wells in Qinshui Basin [4, 32–35].

Block	Well sequence number	Major ion concentration ($mg \cdot L^{-1}$)						Salinity ($mg \cdot L^{-1}$)	Coefficient for sodium-chloride	Desulfurization coefficient
		Na^++K^+	Mg^{2+}	Ca^{2+}	Cl^-	HCO_3^-	SO_4^{2-}			
Fanzhuang	FZ-1	537.7	4.6	8.65	129	1130.3	1.12	1811.37	6.43	0.32
	FZ-2	703.9	4.65	11.9	308	1341	0.94	2370.39	3.35	0.11
	FZ-3	551.1	1.47	4.13	119	1185.1	0.82	1861.62	7.15	0.25
	FZ-4	640	2.20	4.01	248	1115.9	7.46	2071.57	3.98	1.11
	FZ-5	1061.5	6.55	10.3	981	1019.1	1.62	3080.07	1.67	0.06
	FZ-6	598.07	2.45	4.66	75.5	1366.2	4.47	2051.35	12.23	2.19
North of Shijiazhuang	SJZ-1	476.26	2.36	7.7	37.7	1143	4.95	1718	19.5	4.86
	SJZ-2	391.79	2.50	7.88	42.3	938	0.86	1418	14.3	0.76
	SJZ-3	478.18	3.19	7.38	43.9	1081	1.69	1683	16.81	1.42
	SJZ-4	430.04	2.75	7.06	42.9	978	2.73	1516	15.47	2.35
	SJZ-5	410.09	1.96	6.17	52.3	959	1.68	1469	12.10	1.19
	SJZ-6	402.63	1.87	6.17	5.02	932	4.62	1437	123.79	34.03
	SJZ-7	419.22	2.94	8.12	36.7	953	0.7	1482	17.63	0.71
South of Shijiazhuang	SJZ-8	483.71	2.83	9.08	38.6	1145	2.5	1738	19.34	2.4
	SJZ-9	405.08	2.05	5.81	33.7	968	8.82	1452	18.55	9.68
	SJZ-10	424	1.80	5.60	39.9	1009	2.07	1520	16.40	1.92
	SJZ-11	394.67	2.08	7.44	35.2	906	0.68	1395	17.31	0.71
	SJZ-12	380.05	2.02	7.89	36.2	885	1.57	1358	16.20	1.60
	SJZ-13	401.18	2.50	6.4	36	904	0.33	1409	17.20	0.34
Panzhuang	PZ-1	821.3	7.70	11.3	322.2	1313.7	189.3	2742	3.93	21.73
	PZ-2	610.2	1.05	5.14	60.50	1384	0.59	2130	15.57	0.36
	PZ-3	635.92	4.21	8.09	136	1443	20.9	2258	7.22	5.68
	PZ-4	614.41	5.14	5.02	138	1225	44.9	2112	6.87	12.03
	PZ-5	589.84	7.53	5.89	72.3	1244	57.3	2067	12.59	29.31
	PZ-6	716.63	29.2	41.4	110	997	796	2697	10.06	267.59
South of Sizhuang	SZ-1	419.29	0.43	2.59	93.52	599.86	0.68	4208	6.92	0.27
	SZ-2	278.61	0.17	2.14	86.7	555.04	0.52	5553	4.96	0.22
	SZ-3	318.3	0.3	2.29	81.03	561.94	3.6	2425	6.06	1.64
	SZ-4	747.95	4.24	2.87	336.55	1082.5	0.62	2294	3.43	0.07
	SZ-5	443.03	0.35	2.65	70.35	810.15	0.26	1059	9.72	0.14

Data source from the literature [32–35].

based on the relationship between the hydrogen and oxygen isotopes and the atmospheric precipitation curve.

4. Hydrogeological Effects of High CBM Production

4.1. Water Production Features of High CBM-Production Areas. The average water production in the stage of drainage and pressure reduction is used as the basis for dividing CBM wells into three types: high-yield wells, medium-yield wells, and low-yield wells. The low-yield wells are CBM wells with an average daily discharge of less than 2 m^3/d of water during the drainage stage. The medium-yield wells are CBM wells with an average daily discharge of 2~5 m^3/d of water during the drainage stage. The high-yield wells are CBM wells with an average daily discharge of more than 5 m^3/d of water during the drainage stage. Taking the Fanzhuang block as an example, thirty-one high-yield CBM wells (the average daily water production before the entrance of CBM wells into the production decline stage was greater than 1000 m^3/d) are statistically analyzed (see Tables 1–3), and the water production curve is drawn. Among these wells, five wells are wells with a high gas production and high water yield, which are mainly located at the lower part of the local structure. The average daily water production of a single well is between 7.54 m^3/d and 9.74 m^3/d during the stage of drainage and pressure reduction. Ten wells are wells with a high gas production and medium water yield, which are located near the middle and higher parts of the local structure. The average daily water production of a single well is between 2.09 m^3/d and 4.83 m^3/d during the stage of drainage and pressure reduction. Eighteen wells are wells with a high gas production and low water yield, which are mainly located in the higher part of the local structure above the

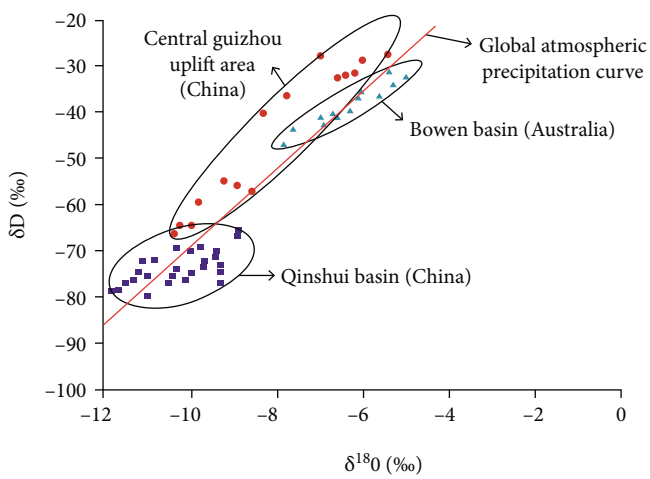

Figure 3: Diagrams of H and O isotopes in coal seam-produced water in different coal basins in China and Australia [38–40].

groundwater level. The average daily water production of a single well is between 0.09 m^3/d and 1.93 m^3/d during the stage of drainage and pressure reduction.

After analyzing the extraction characteristics of selected wells and well structures, the author summarized the following high CBM-production patterns: (1) coalbed structure-hydraulic trapping (see Figure 4(a)), (2) fold limb-fracture development (see Figure 4(b)), and (3) syncline core-water stagnation (see Figure 4(c)).

The area with the first CBM production pattern is located at the higher part of an asymmetric syncline or monocline where the fractures are not developed or water-resistant faults are developed. In Figure 4(a), CBM wells are placed in the higher part of the monocline and far away from the water-resistant fault and recharge source. According to the CBM and the mechanism of water movement, the coalbed water moves from the high-potential zone to the low-potential zone while CBM moves in the opposite direction [41]. However, due to the blocking function of the fault, the hydraulic connection between the hanging wall of the fault and the footwall of the fault is weak. The coalbed water is in a stagnant state in the hanging wall of the fault, which is beneficial for enriching the CBM, resulting in a high CBM content. At the same time, atmospheric precipitation forms hydraulic trapping forces for CBM that moves upwards along the monoclinal structure, preventing CBM in the lower-potential zone from dissipating during the extraction process, which is beneficial for high CBM production in the higher-potential zone. In addition, the coal seam in the higher part of the structure has a better permeability due to the lower pressure and the movements of water and gas. In this pattern, the rules for forming CBM in CBM wells are reflected as follows: a short gas breakthrough time, a low water yield, and a high gas yield. Affected by free gases, the coal seam may have a 100% of gas production.

The area with the second CBM production pattern is located at the limb of a syncline or anticline affected by tensile stress. In Figure 4(b), CBM wells are arranged in the limb of the syncline. Affected by tensile stress, fractures are developed in the coalbed layer and the buried depth of coals is shallow, which is generally about 300 m-800 m. The limb of the syncline is less affected by coalbed water. However, affected by free gases in the core of the syncline, there are more and more CBM formation sources. The fractures generated by the forces of tensile stress are developed on a large scale, leading to the fracturing of reservoirs and further resulting in the desorption of a large amount of CBM [41–43]. In this pattern, the rules for forming CBM in CBM wells are reflected as follows: a short gas breakthrough time in the preliminary stage, an increasing daily yield of gas, and a high peak of gas production.

The area with the third CBM production pattern is located near the core of a synclinore and secondary syncline in a large sedimentary basin. In Figure 4(c), CBM wells are arranged in the core of a broad and gentle syncline where stagnant water stays. No fault is developed, the sealing and capping capability of the roof is good, and the salinity is high. In a situation where the roof has a good water-resistant condition, CBM wells are less affected by external water and the exploitation of CBM wells is not affected. The high effective thickness of the upper layer, the buried depth of the coal seam, and the forces of tensile stress are all beneficial for enriching CBM. In this pattern, the rules for forming CBM in CBM wells are reflected as follows: a high water yield with a long time to enter the stable production phase, a low CBM yield and a high water yield at the beginning, and a long stable production phase with a high peak of gas production and stable gas yield.

4.2. Hydrochemical Features of Areas with a High CBM Yield. The hydrochemical coefficients can better reflect the sealing conditions of groundwater. For example, the coefficient of sodium and chloride can reflect the enrichment degree of sodium salt in groundwater, the metamorphic grade of groundwater, and the hydrogeochemical environment of the reservoir. The desulfurization coefficient is an important index to reflect the openness of groundwater. In general, a better formation closure has the following characteristics: a more thorough desulfurization, a lower SO_4^{2-} content, a smaller desulfurization coefficient, and a more intense reducing action [14].

A comprehensive analysis of hydrochemical characteristics and gas content in the southern part of the Fanzhuang block reveals that the salinity in the southern part of the block gradually increases from north to south, and the sodium-chloride coefficient gradually decreases from northwest to southeast. Two CBM enrichment centers are formed in the area with a high salinity (shown in Figure 5). The area with salinity greater than 2000 mg/L is the CBM stagnation area, and the coalbed gas content is above 26 m^3/t. The above information shows that the area with high salinity and the area with high CBM are positively correlated. However, CBM wells in the area with the highest salinity are not highly productive. The areas with high CBM production in the south of the Fanzhuang block are the intersecting areas with a medium salinity of 2000-3500 mg/L and rNa/rCl less than 6.

Taking the Fanzhuang block in Qinshui Basin as an example, we discussed the controlling effects of the

Table 3: CBM well gas and water productivity in the Fanzhuang block.

No.	Gas production		Total water production (m^3)	Gas-water ratio	Drainage and pressure reduction stage		
	Average (m^3/d)	Total (m^3)			Number of days (d)	Total discharged water (m^3)	Average daily discharged water (m^3/d)
FZ-1	1238	1770555	967.4	1830.2	210	468.00	2.23
FZ-2	1627	2241711	496.8	4512.3	240	440.30	1.83
FZ-3	1233	1541258	556.1	2771.5	193	403.70	2.09
FZ-4	2238	2715371	899.1	3020.1	233	595.90	2.56
FZ-5	1942	2832225	600.3	4718	258	499.20	1.93
FZ-6	1107	1877232	563.3	3332.6	279	446.30	1.60
FZ-7	1236	1436079	817.2	1757.3	393	549.30	1.40
FZ-8	1029	1099688	648.0	1697.1	366	320.70	0.88
FZ-9	2116	1410890	62.6	22538.1	48	14.60	0.30
FZ-10	2799	964503	57.1	16891.5	83	15.80	0.19
FZ-11	1141	4330482	3897.9	1111	1451	3276.40	2.26
FZ-12	1344	5896287	2404.1	2452.6	1144	1707.00	1.49
FZ-13	1008	3627541	5223.2	694.5	936	2971.20	3.17
FZ-14	1544	6624604	6084.1	1088.8	991	4634.20	4.68
FZ-15	1858	7349913	3661.6	2007.3	1935	3288.00	1.70
FZ-16	1064	3740135	10178	367.5	1896	9162.50	4.83
FZ-17	1346	2349283	2982.9	787.6	456	1174.70	2.58
FZ-18	5399	583072	138.3	4216.0	176	107.90	0.61
FZ-19	4938	2114079	349.9	6042.0	151	13.70	0.09
FZ-20	8249	3089116	30.0	102970.5	55	11.20	0.20
FZ-21	1025	7871921	348.6	22581.5	421	233.50	0.55
FZ-22	1250	9834482	2261.8	4348.1	1087	1825.60	1.68
FZ-23	1020	6859558	793.4	8645.8	356	478.70	1.34
FZ-24	1224	9335585	876.3	10653.4	540	427.80	0.79
FZ-25	8284	4076042	101.4	40197.7	124	29.80	0.24
FZ-26	3855	2070627	437.5	4732.9	183	253.30	1.38

Table 3: Continued.

No.	Gas production		Total water production (m^3)	Gas-water ratio	Drainage and pressure reduction stage		
	Average (m^3/d)	Total (m^3)			Number of days (d)	Total discharged water (m^3)	Average daily discharged water (m^3/d)
FZ-27	10362	3348692	938.1	3569.7	251	610.80	2.43
FZ-28	8365	2751742	2394.3	1149.3	217	2034.90	9.38
FZ-29	10682	1131285	2073.9	545.5	259	1953.10	7.54
FZ-30	8063	807480	3473.9	232.4	356	3467.00	9.74
FZ-31	6519	81626883	3621.8	22537.7	410	1754.31	4.28

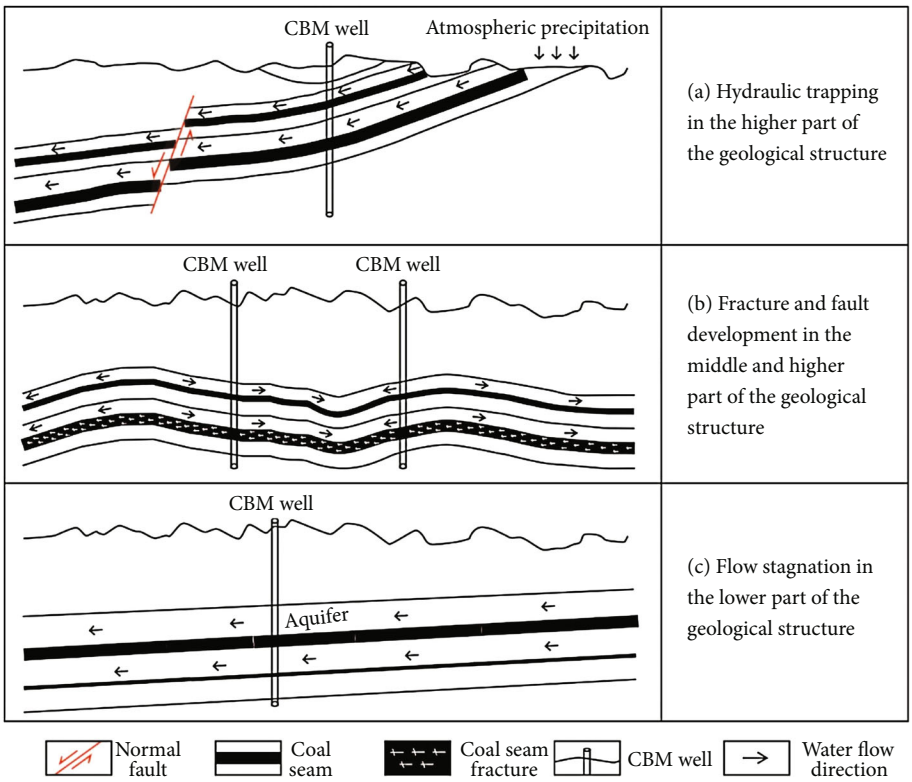

Figure 4: Schematic diagram of high-yield patterns of CBM wells.

coefficient of sodium and chloride, the desulfurization coefficient, and the H and O isotopes on the high CBM production in the CBM enrichment area in the southern part of the block. By studying the distribution of these coefficients in the Fanzhuang block, it is found that CBM wells with a high daily gas production are mainly distributed in the area with the coefficient of sodium and chloride ranging from 3.5 to 8. Besides, the distribution of CBM wells with a high daily gas production has a negative correlation with the sodium-chloride coefficient within a certain range. The lower the sodium-chloride coefficient, the more frequent the high-production wells appear in the area. The desulfurization coefficient can reflect how enclosed the groundwater environment is. The Fanzhuang block is located at the area with a desulfurization coefficient between 4 and 10 and a high distribution of high-yield wells. The desulfurization coefficient is also positively related to the daily gas production of a single well. The distribution of hydrogen and oxygen isotopes can reflect the cause for coalbed water generation and its permeability. In general, the densities of hydrogen and oxygen isotopes in coalbed water from different origins are different. The order of the densities should be as follows: the density of water from atmospheric precipitation>the density of surface water>the density of sedimentary water. Among the water from different origins, the permeability of water from atmospheric precipitation is preferred. The

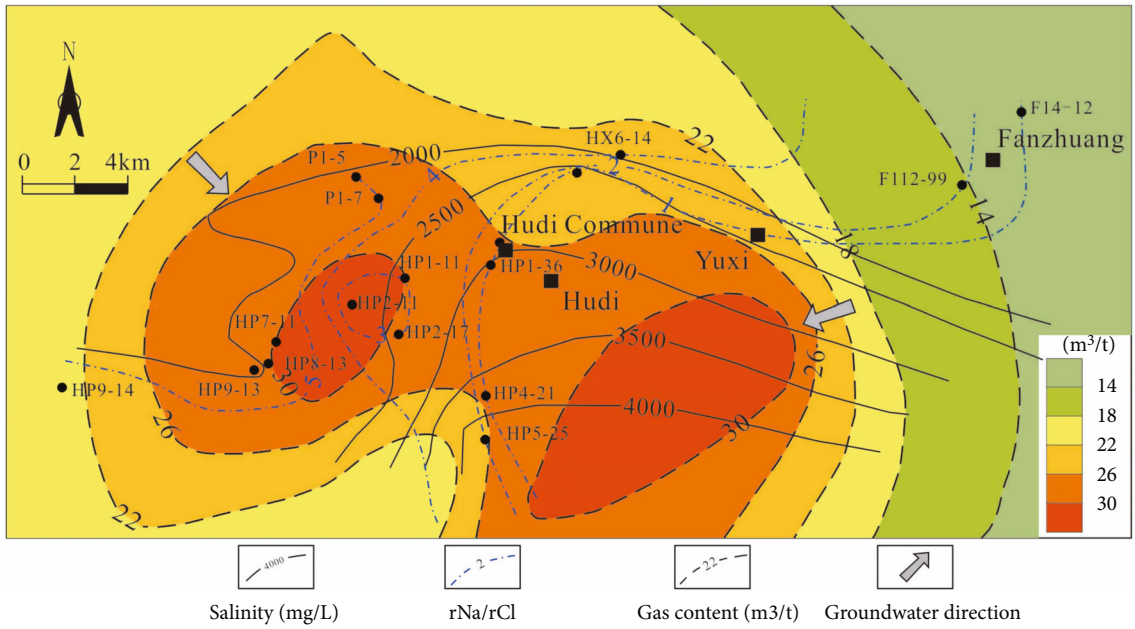

Figure 5: Relationship between the salinity of produced water (constant ratio) and the CBM in the south of the Fanzhuang block.

reason is that water from atmospheric precipitation is most conducive to the high production of CBM wells. The higher the permeability in areas with a lighter hydrogen isotope, the higher the CBM production is. The δD value of the Fanzhuang block ranges from -75‰ to -77‰, which is beneficial for CBM production [14].

In summary, in CBM enrichment areas, it is prone to produce high yields of CBM for the CBM wells with a relatively low sodium-chlorine coefficient, a relatively high desulfurization coefficient, and a good permeability due to water from atmospheric precipitation.

5. Typical Case Analysis

5.1. Fanzhuang Block in Qinshui Basin. In the Fanzhuang block of Qinshui Basin, fifty-eight CBM wells with a relatively rich concentration of CBM and permeability greater than 0.1 mD are selected for statistical analysis. Data in the initial stage of the two-phase flow of CBM wells is used for comparison. According to the daily gas production, the wells are divided into three types: high-yield wells (17 wells with daily gas production > 2000 m^3), medium-yield wells (16 wells with daily gas production between 1000 and 2000 m^3), and low-yield wells (25 wells with daily gas production < 1000 m^3).

The gas-water ratio of high-yield wells in the Fanzhuang block is between 212 and 6113 with an average value of 1988. These wells are mainly located at slopes and the higher part of the geological structure. The gas-water ratio of medium-yield wells is between 91 and 1944, with an average of 625. These wells are mainly located at slopes and the higher part of the geological structure. The gas-water ratio of low-yield wells is between 40 and 2035, with an average value of 373. These wells are distributed at slopes and higher parts and lower parts of the geological structure (see Table 4).

By analyzing the statistical results, it is found that the high-yield wells are mainly located at the slope zone and the higher part of the geological structure with a gas-water ratio higher than 500. Low-yield wells are mainly distributed at the lower part of the geological structure with a gas-water ratio of less than 500. One of the main reasons that cause the difference in gas production of medium-yield and high-yield wells is the dynamic effect of groundwater. The higher part of the geological structure and the slope zone are both conducive to draining away water and lowering the pressure of CBM wells. However, at the higher part of the geological structure, the good hydrodynamic conditions may cause the CBM to disperse along with water flows. In the slope zone, the poor hydrodynamic conditions are beneficial for CBM preservation and high production of wells.

5.2. Hancheng Mining Area in Ordos Basin. According to the research by Li et al. [25], the gas content and gas production of the No. 11 coal seam in the Hancheng mining area on the southeastern margin of Ordos Basin are highly correlated with the chemical composition of its coal seam water. Table 5 describes the relationships between hydrochemical zones and gas content (data from 25 samples). In their study, 249 samples that were used for the statistical study revealed the relationships among hydrochemical characteristics, gas content, and water content (see Table 6) [44].

In the Hancheng mining area, the CBM wells are mainly distributed in the HCO_3^-–Cl^-–Na^+ zone. The wells with the highest gas production are in the Cl^-–Na^+ zone, and the wells with the second-highest gas production are in the SO_4^{2-}–Cl^-–Ca^{2+}–Na^+ zone. On the contrary, the wells with the highest water production are in the HCO_3^-–Na^+ zone, and the wells with the second-highest water production are in the HCO_3^-–Cl^-–Na^+ zone. An obvious negative correlation exists between CBM production and water production

Table 4: The produced gas-water volume ratio of typical CBM wells and distribution of structural parts in the Fanzhuang block.

Gas production scale		High-yield wells	Medium-yield wells	Low-yield wells
Structural parts	Higher part	3	6	9
	Slope	14	9	10
	Lower part	0	1	6
Gas-water ratio		212~6113	91~1944	42~2035
Average value		1988	625	373

Table 5: Distribution of gas content in different hydrochemical zones of the No. 11 coal seam in the Hancheng mining area [44].

Hydrochemical zone	HCO_3^-–Na^+ zone	HCO_3^-–Cl^-–Na^+ zone	SO_4^{2-}–Cl^-–Ca^{2+}–Na^+ zone	Cl^-–Na^+ zone
Number of samples	5	10	5	5
Current gas content (m^3/t)	4~6	6~9	8~13	12~15
Current average gas content (m^3/t)	5.5	8.3	11.6	14.1
Original gas content (m^3/t)	11~15	10~15	9~16	10~16
Original average gas content (m^3/t)	13.9	14	14.1	14.3

Table 6: Water production and gas production of CBM wells in different hydrochemical zones of the No. 11 coal seam in the Hancheng mining area [44].

Hydrochemical zone	HCO_3^-–Na^+ zone	HCO_3^-–Cl^-–Na^+ zone	SO_4^{2-}–Cl^-–Ca^{2+}–Na^+ zone	Cl^-–Na^+ zone
Number of samples	10	212	10	17
Average water production (m^3/d)	9.92	5.64	3.62	1.61
Average gas production (m^3/d)	235	598	1056	1983

in the coalfield: the lower the water production, the higher the CBM production is.

By comparing the current gas content of coal seams in different hydrochemical zones, it is found that the Cl^-–Na^+ zone has the highest gas content, then followed by the SO_4^{2-}–Cl^-–Ca^{2+}–Na^+ zone and HCO_3^-–Cl^-–Na^+ zone, and the HCO_3^-–Na^+ zone has the least gas content. According to the calculation of the Lanchester equation, the gas content of original coal seams in different zones has no significant difference. Therefore, it can be deduced that Cl^-–Na^+ and HCO_3^-–Cl^-–Na^+ zones are more favorable for CBM preservation.

6. Existing Problems and Development Trends

6.1. Existing Problems. By reviewing the literature in China and other counties, we can find that predecessors have already made significant progress in studying the mechanisms for controlling the enrichment and high yield of CBM from the aspects of coalbed hydrodynamics, coalbed hydrogeochemistry, and hydrogeological conditions. All the research achievements provide solid theoretical bases and practices for selecting the CBM enrichment area and effectively extracting CBM. However, there are still some existing problems that need to be discussed and further studied:

(1) The distribution and migration of coalbed water determine the enrichment and dissipation of CBM. Due to the complexity of geological structures, the difference in reservoir permeability, and the interaction between water and rock, more finely and three-dimensional hydrogeological units are needed to make the CBM exploitation more economically beneficial. However, the current distribution rule of coalbed water is only at the stage of qualitative description, and it is urgent to establish a quantitative method to evaluate the heterogeneous distribution of coalbed water in both the longitudinal and lateral directions

(2) If the selection of favorable CBM zones and sweet spots involves hydrogeological conditions, hydrodynamic conditions are considered to a large extent. However, hydrogeochemistry, especially the isotope characteristics of coalbed water, is less considered. In addition, most of the previous studies mainly focus on the enrichment of CBM. Therefore, it is urgent to establish a comprehensive system to evaluate CBM enrichment and high production based on hydrogeological indicators

(3) The studies on the relationships among hydrodynamic conditions, hydrogeochemical characteristics, and the extraction efficiency of CBM wells are not enough. Various hydrodynamic models based on different hydrodynamic fields and dynamic changes of hydrochemistry are needed to guide highly efficient CBM extraction from CBM wells

6.2. Development Trends

6.2.1. Transform from Qualitative Evaluation to Quantitative Evaluation. Due to the differences in the hydrogeological conditions of groundwater, most of the predecessors defined boundaries of coalbed water distribution and divided the hydrogeological zones based on conditions such as the geomorphology, geological structure, and surface water system. However, the gas production of CBM wells in the same hydrogeological zone varies greatly. The reason is that the coalbed water has a strong vertical and horizontal heterogeneity in hydrogeological units. Therefore, it is necessary to establish a quantitative method to evaluate the heterogeneous distribution of coalbed water vertically and horizontally to accurately describe the heterogeneous distribution characteristics of hydrogeological units.

6.2.2. Transform from a Single Evaluation Standard to Multiple Evaluation Standards. The relationship between CBM enrichment and high yields shows that the area with high-yield CBM must be located at the CBM enrichment area. The coal seam water content, hydrodynamic zoning, and different hydrochemical conditions that are summarized by the predecessors obviously have controlling effects on CBM enrichment, especially on the coalbed gas content. However, the standard for evaluating the enrichment is more of a singular indicator. It is urgent to transform the singular way to evaluate CBM enrichment (gas content) to multiple ways to evaluate CBM enrichment (gas content and water content) and high production (gas production and water production) and establish an evaluation system with multiple evaluation indicators including the dynamic zones, flow intensity, water ion characterization, and water isotope.

6.2.3. Transform from Static Evaluation to Dynamic Evaluation. The hydrogeological conditions underground are accompanied by the production of CBM wells, and they are in a process of dynamic change. The content of coalbed water, hydrodynamic conditions, and hydrochemical characteristics will change with the production process of CBM. Therefore, analyzing static data to find the CBM controlling mechanism cannot meet the requirements of efficient development of CBM. On the basis of quantitatively characterizing the CBM controlling parameters of coalbed water, it is urgent to analyze the changing rules of hydrogeological parameters in the CBM production process and transform the static evaluation on the gas controlling mechanism of hydrogeological conditions to dynamic evaluation.

6.2.4. Transform Theoretical Studies to Practices Guided by Theoretical Results. The theoretical research of CBM in China starts in the 1970s and 1980s. Many theoretical breakthroughs and innovations have been made around the gas controlling effects of hydrogeological conditions. However, the hydrogeological conditions of coal seams in the CBM basin in China are of great variety. The aquifers are heterogeneously distributed. The relationships between hydrogeology and geological structures are complex. The research results are not closely related to the actual CBM extraction and production. Therefore, it is urgent to combine theoretical research studies with field practices to deepen the research studies on the gas controlling mechanism of hydrogeology, to construct a comprehensive hydrogeological evaluation system and a customized and efficient drainage system that serve the exploration and development of CBM and guide the selection and efficient development of CBM enrichment areas and high-yield zones.

7. Conclusion

(1) From the perspective of hydrogeology, this paper summarizes the fruitful research results achieved by domestic and foreign researchers on the gas controlling effect of hydrogeology under similar structural and deposition conditions in recent years. Among them, the water conditions suitable for biogenic gas formation are identified; the division of hydrodynamic zones and its index are summarized; the response mechanism of water geochemical characteristics to CBM is analyzed; and the high production model of CBM based on different water production characteristics is established

(2) According to the research progress and existing problems, this paper proposes the following trends about research on the controlling mechanism of hydrogeological conditions: transform from qualitative evaluation to quantitative evaluation, from a singular evaluation standard to multiple evaluation standards, from static evaluation to dynamic evaluation, and from pure theoretical research to practices under theoretical guidance

Data Availability

The data that support the findings and conclusions of this study are available on request from the corresponding author, Wang Dangliang (wangdangliang@cumt.edu.cn). The data are not publicly available due to the restrictions from the Natural Science Foundation of China (No. 41872179).

Conflicts of Interest

The authors declare that they have no conflicts of interest.

Acknowledgments

Funding support from the National Natural Science Foundation of China (41872179) and the open research fund program of State Key Laboratory of Coal and CBM Co-ming (2019KF05) are acknowledged.

References

[1] Y. Bao, D. Li, and Y. Ju, "Constraints of biomethane generation yield and carbon isotope fractionation effect in the pathway of acetotrophic with different coal-rank coals," *Fuel*, vol. 305, article 121493, 2021.

[2] Y. Bao, W. Wang, D. Ma et al., "Gas origin and constraint of $\delta^{13}C(CH_4)$ distribution in the Dafosi mine field in the southern margin of the Ordos Basin, China," *Energy and Fuels*, vol. 34, no. 11, pp. 14065–14073, 2020.

[3] S. Yan, L. Shaobo, Z. Mengjun et al., "Boundary types of coalbed methane reservoirs, main controlling factors for accumulation and prediction of enriched areas," *Natural Gas Industry*, vol. 29, no. 10, pp. 5–9, 2009.

[4] B. Wang, F. Sun, D. Tang, Y. Zhao, Z. Song, and Y. Tao, "Hydrological control rule on coalbed methane enrichment and high yield in FZ Block of Qinshui Basin," *Fuel*, vol. 140, pp. 568–577, 2015.

[5] Y. Bao, C. An, C. Wang, C. Guo, and W. Wang, "Hydrogeochemical characteristics and water–rock interactions of coalbed- produced water derived from the Dafosi biogenic gas field in the southern margin of Ordos basin, China," *Geofluids*, vol. 2021, Article ID 5972497, 13 pages, 2021.

[6] C. T. Rightmire, G. E. Eddy, and J. N. Kirr, *Coalbed Methane Resources of the United States: AAPG Studies in Geology Series 17*, The American Association of Petroleum Geologists, Tulsa, Oklahoma, 1984.

[7] B. E. Law and D. D. Rice, *Hydrocarbons from Coal: AAPG Studies in Geology Series 38*, The American Association of Petroleum Geologists, Tulsa, Oklahoma, 1993.

[8] A. R. Scott, W. R. Kaiser, and W. B. Ayers, "Thermogenic and secondary biogenic gases, San Juan basin, Colorado and New Mexico—implications for coalbed gas producibility," *AAPG Bulletin*, vol. 78, no. 8, pp. 1186–1209, 1994.

[9] D. Jinxing and P. Xigu, *China Natural Gas Geology, Volume 1*, Petroleum Industry Press, 1992.

[10] G. Deshi, "Living conditions of methanogens and biogas," *Natural Gas Industry*, vol. 10, no. 5, pp. 13–19, 1990.

[11] W. Bo, C. Haiyan, Z. Guiqiang et al., "Study on geological characteristics and gas control differences of high and low coal rank CBM reservoirs," *Acta Geologica Sinica*, vol. 10, pp. 1396–1401, 2008.

[12] S. Xianbo, X. Ying, W. Yu, and D.-P. Xia, "Effects of salinity and pH on biomethane production in low rank coal seams," *Journal of China Coal Society*, vol. 36, no. 8, pp. 1302–1306, 2011.

[13] M. P. Bryant, "Microbial methane production-theoretical aspects2," *Journal of Animal Science*, vol. 48, no. 1, pp. 193–201, 1979.

[14] W. Bo, "Coalbed methane enrichment and high-production rule & prospective area prediction in Qinshui Basin," China University of Mining and Technology, 2013.

[15] L. Benliang, W. Mingming, W. Guoqi et al., "Study on biogas migration and accumulation in Sanhu area of Qaidam Basin," *Geological Review*, vol. 1, pp. 93–100, 2003.

[16] L. Zhijun, L. Xinning, L. Hui et al., "Effect of hydrogeological conditions on low-rank coalbed methane in Tuha and Santanghu basins," *Xinjiang Petroleum Geology*, vol. 34, no. 2, pp. 158–161, 2013.

[17] Y. C. Wei, Q. Zhang, A. M. Wang, H. K. Ren, Y. Yuan, and D. Y. Cao, "The influence of the salinity of groundwater in coal measures on low rank coalbed methane in the south margin of Junggar basin," *Coal Geology & Exploration*, vol. 44, no. 1, pp. 31–37, 2016.

[18] W. Tao, D. Ze, H. Haiyan et al., "Study on characteristics comparison of low rank coal coalbed methane reservoirs at home and abroad," *Coal Science and Technology*, vol. 47, no. 9, pp. 41–50, 2019.

[19] L. Zhijian, "Analysis on the mechanism and characteristics of coal gas hydrothermal metamorphism," *Coal Geology & Exploration*, vol. 5, pp. 34–36, 1988.

[20] Z. Ningning and R. Deyi, "Changes of the carboniferous coal-bearing rock series in Henan under the coal thermal metamorphism–a preliminary discussion on the influence of groundwater hydrothermal on coal metamorphism," *Geological Review*, vol. 2, pp. 130–139, 1990.

[21] Y. Jianping, W. Qiang, and W. Zihe, "Controlled characteristics of hydrogeological conditions on the coalbed methane migration and accumulation," *Journal of China Coal Society*, vol. 5, pp. 459–462, 2001.

[22] W. Bo, "Study on contrast of reservoir character and physical simulation experiment of high and low rank coalbed methane," China University of Mining and Technology, 2006.

[23] S. Yan, M. Xingzhi, L. Shaobo, J. Lin, H. Feng, and Q. Yi, "Gas accumulation conditions and key exploration & development technologies in Qinshui coalbed methane field," *Acta Petrolei Sinica*, vol. 40, no. 5, pp. 621–634, 2019.

[24] T. Chong, T. Dazhen, Z. Zhijun, T. Shu, C. Xiaozhi, and S. Conglei, "Hydrogeological characteristics and their control on coalbed methane in Binchang mining area," *Coal Geology & Exploration*, vol. 40, no. 1, pp. 43–46, 2012.

[25] J. Li, B. Wang, L. Shao et al., "Hydrogeological zoning and its gas-controlling mechanism: a case study of Baode block, eastern Ordos gas field," *Journal of China University of Mining and Technology*, vol. 46, no. 4, pp. 869–876, 2017.

[26] S. Yan, L. Shao-Bo, Z. Meng-Jun et al., "Coalbed gas reservoirs: boundary types, main controll ing factors of gas pooling, and forecast of gas-rich areas," *Natural Gas Industry*, vol. 29, no. 10, pp. 5–9, 2009.

[27] X. H. Fu, Y. Qin, W. F. Wang, and S. H. Jiao, "Hydrogeological controlled properties of coal bed gas in central–southern Qinshui Basin," *Coal Geology of China*, vol. 1, pp. 31–34, 2001.

[28] Q. Rongfang, C. Daiyong, W. Anmin et al., "CBM reservoir-forming model of Zhuozishan mining area in western margin of Ordos basin," *Coal Geology & Exploration*, vol. 46, no. 3, pp. 54–58, 2018.

[29] Z. Yaru, S. Beilei, Z. Fangui et al., "Hydrogeological characteristics of CBM reservoirs and their controlling effects in Gujiao Mining Area, Xishan Coalfield," *Journal of China Coal Society*, vol. 43, no. 3, pp. 759–769, 2018.

[30] L. Zeng, X. G. Sun, S. H. Cui, and J. Y. Sui, "Controlling effects of structural-hydrogeological conditions on coalbed methane accumulation in Xishan Coalfield," *Coal Science and Technology*, vol. 47, no. 9, pp. 80–88, 2019.

[31] Y. C. Wei, X. X. Xiang, A. M. Wang, Q. Zhang, and D. Y. Cao, "Influence of water with different salinity on the adsorption performance of coal reservoir," *Journal of China Coal Society*, vol. 44, no. 9, pp. 2833–2839, 2019.

[32] S. Zhang, S. Tang, Z. Li, L. Qiao, and C. Men, "The hydrochemical characteristics and ion changes of the coproduced water: taking Shizhuangnan block, south of the Qinshui basin as an example," *Journal of China University of Mining and Technology*, vol. 44, no. 2, pp. 292–299, 2015.

[33] X. Zhanjie, "Study on isotopic geochemistry and origins of coalbed methane in the northern Qinshui Basin," China University of Mining and Technology Beijing, 2017.

[34] L. Chao, F. Guorui, and Z. Fangui, "Origin and geochemical characteristics of coalbed methane in abandonedcoal mines,

Panzhuang block, southern Qinshui basin," *Coal Geology & Exploration*, vol. 47, no. 6, pp. 67–72, 2019.

[35] L. Guangjing, "Analysis of geochemistry characteristics of water from coalbed methane wells in Shizhuang south block," *Coal Technology*, vol. 38, no. 1, pp. 60–62, 2019.

[36] J. C. McIntosh, L. M. Walter, and A. M. Martini, "Pleistocene recharge to mid-continent basins: effects on salinity structure andmicrobial gas generation," *Geochimica et Cosmochimica Acta*, vol. 66, pp. 1681–1700, 2002.

[37] S. D. Golding, C. J. Borehamb, and J. S. Esterle, "Stable isotope geochemistry of coal bed and shale gas and related production waters: a review," *International Journal of Coal Geology*, vol. 120, pp. 24–40, 2013.

[38] S. B. Wang, S. H. Tang, Y. Mo, Z. C. Li, and S. H. Zhang, "The hydrogen and oxygen isotope characteristics of drainage water from Taiyuan coal reservoir," *Journal of China Coal Society*, vol. 38, no. 3, pp. 448–454, 2013.

[39] E. C. Kinnon, S. D. Golding, C. J. Boreham, K. A. Baublys, and J. S. Esterle, "Stable isotope and water quality analysis of coal bed methane production waters and gases from the Bowen Basin, Australia," *International Journal of Coal Geology*, vol. 82, no. 3–4, pp. 219–231, 2010.

[40] C. Wu, Z. Yang, Y. Qin, J. Chen, Z. Zhang, and K. Luo, "Geochemical comparison and its geological significance of CBM produced water in the Songhe and Zhijin blocks," *Journal of China Coal Society*, vol. 43, no. 4, pp. 1058–1064, 2018.

[41] M. Fuyuan, "Theories and practice of CBM gas-water moving," *China Coalbed Methane*, vol. 13, no. 5, pp. 15–17, 2016.

[42] S. Fenjin, B. Wang, L. Mengxi et al., "Major geological factors controlling the enrichment and high yield of coalbed methane in the southern Qinshui Basin," *Acta Petrologica Sinica*, vol. 35, no. 6, pp. 1070–1079, 2014.

[43] B. Wang, Y. Hongxing, H. Wang et al., "Favorable and major geological controlling factors for coalbed methane accumulation and high production in the Chengzhuang Block, Qinshui Baisn," *Oil & Gas Geology*, vol. 39, no. 2, pp. 366–372, 2018.

[44] L. Jian, C. Yanqian, X. Xianyue et al., "Hydrochemistry field characteristic of 11# coal seam in Hancheng CBM field and its controlling effect on CBM," *Journal of China Coal Society*, vol. 23, no. 3, pp. 74–80, 2018.

Hindawi
Geofluids
Volume 2021, Article ID 1163413, 9 pages
https://doi.org/10.1155/2021/1163413

Research Article

Investigation on the CBM Extraction Techniques in the Broken-Soft and Low-Permeability Coal Seams in Zhaozhuang Coalmine

Zhaoying Chen,[1,2,3] Xuehai Fu,[1] Guofu Li,[2,3] Jian Shen,[2] Qingling Tian,[2,3] Ming Cheng,[1] and Yue Wang[2,3]

[1]*China University of Mining and Technology, Xuzhou 221116, China*
[2]*State Key Laboratory of Coal and CBM Co-mining, Jincheng 048012, China*
[3]*Yi'an Lanyan Coal and Coal-Bed Methane Simultaneous Extraction Technology Co., Ltd., Jincheng 048012, China*

Correspondence should be addressed to Xuehai Fu; fuxuehai@cumt.edu.cn

Received 6 May 2021; Accepted 20 August 2021; Published 1 October 2021

Academic Editor: Martina Zucchi

To enhance the coalbed methane (CBM) extraction in broken-soft coal seams, a method of drilling a horizontal well along the roof to hydraulically fracture the coal seam is studied (i.e., HWR-HFC method). We first tested the physical and mechanical properties of the broken-soft and low-permeability (BSLP) coal resourced from Zhaozhuang coalmine. Afterward, the in situ hydraulic fracturing test was conducted in the No. 3 coal seam of Zhaozhuang coalmine. The results show that (1) the top part of the coal seam is fractured coal, and the bottom is fragmented-mylonitic coal with a firmness coefficient value of less than 1.0. (2) In the hydraulic fracturing test of the layered rock-coal specimens in laboratory, the through-type vertical fractures are usually formed if the applied vertical stress is the maximum principal stress and is greater than 4 MPa compared with the maximum horizontal stress. However, horizontal fractures always developed when horizontal stress is the maximum or it is less than 4 MPa compared with vertical stress. (3) The in situ HWR-HFC hydraulic fracturing tests show that the detected maximum daily gas production is 11,000 m^3, and the average gas production is about 7000 m^3 per day. This implies that the CBM extraction using this method is increased by 50%~100% compared with traditional hydraulic fracturing in BSLP coal seams. The research result could give an indication of CBM developing in the broken-soft and low-permeability coal seams.

1. Introduction

Coalbed methane (CBM) resource is abundant in China. After decades of development, commercial CBM extraction has been achieved in Qinshui and Ordos Basin [1–3], especially in coal seams with excellent storage conditions, large gas content, and undamaged primary structure coal seams [4, 5]. However, the broken-soft and low-permeability (BSLP) coal seams are widely distributed in China, such as Jiaozuo, Huainan, and Lu'an coal fields, resulting in a relatively low CBM production [6–8].

The BSLP coal is always broken into pieces, grains, fragments, or powders, in which the original natural fracture network is destroyed or disappeared. Therefore, the BSLP coal has low mechanical strength and low permeability. When conducting drilling and hydraulic fracturing in the BSLP coal seam, problems such as difficulty in hole formation, poor cementing quality, and borehole blockage could occur.

To date, previous studies found that the pores, specific surface area, and roughness of coal increased with the broken degree of coal structures. Therefore, BSLP coal may have a high gas storage capacity [9, 10]. In primary structural coal, exogenous and endogenous discontinuities are well developed and the connected fracture/pore structures provide an effective channel for gas flow. In BSLP coal, semiclosed holes or fractures with poor permeability are often developed, which may result in short and narrow fracture networks [11, 12]. Specifically, for the mylonite coal with a large degree of fragmentation, only some microcracks exist in coal, which would further reduce the coal permeability. Therefore, it is difficult to form effective fracture networks when using hydraulic fracturing techniques in BSLP coal seams [13].

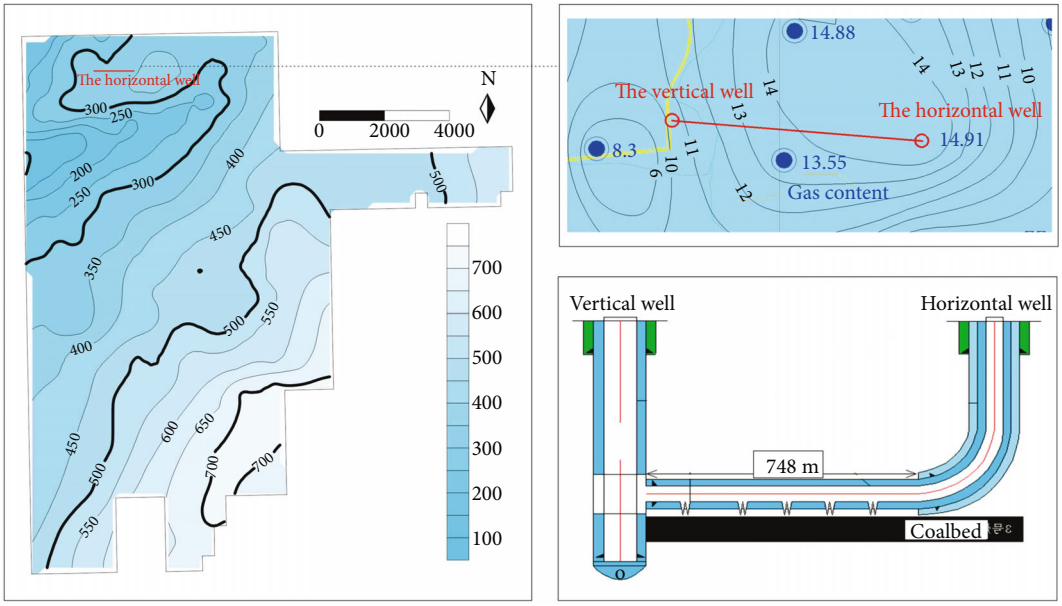

Figure 1: Buried depth isogram of No. 3 coal seam in Zhaozhuang coalmine and well structures.

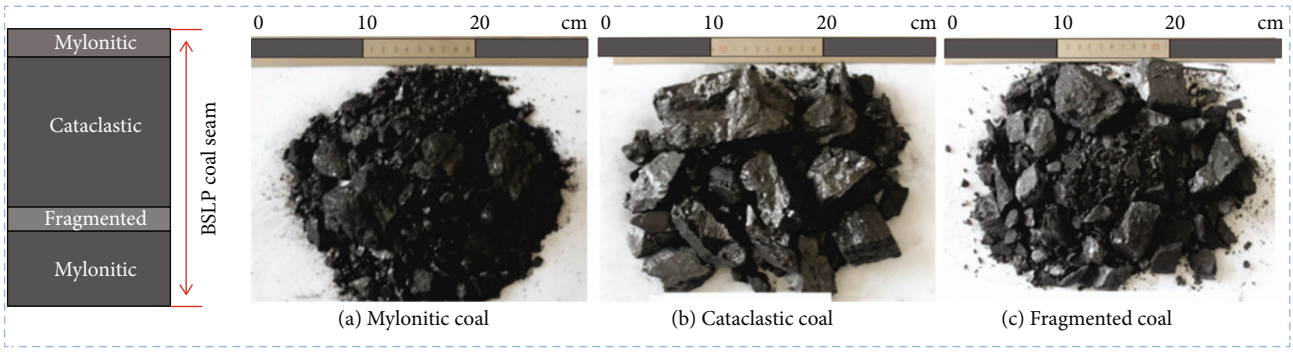

Figure 2: Coal sample of Zhaozhuang coalmine.

Table 1: Coal structure characteristics and description of Zhaozhuang coalmine.

Stratum	Thickness/m	Macrolithotype	Structure	Description
1	0.40~0.50	Semidark	Mylonitic	Mylonite, semidark coal, mainly in the form of scales, hand twist into powder, local visible
2	2.60-3.80	Semibright	Cataclastic	Mainly cataclastic coal, with thin layer of crushed coal, horizontal bedding, dip angle of 2°~3°, fissure development, fissure cut through bedding oblique crossing, a few centimeters to dozens of centimeters in length, fissure dip angle of 40° and 120°, obviously wrinkled mirror face
3	0.20~0.40	Semidark	Fragmented	Mainly fragmented coal, hand twist into granules
4	0.30~1.20	Semidark	Mylonitic	Mylonite coal, mainly in the form of scales, hand twisted into powder. At the top of the layer, there is a thin layer of carbonaceous mudstone gangue, which can be seen locally.

The virtual reservoir is a new concept considering drilling the horizontal well in the roof or floor strata but not in the coal seam [14, 15]. This technique has been successfully verified in many in situ projects [16, 17]. However, the hydraulic fracturing mechanism and fracture propagation along the coal/rock interface are not clear yet, which need to be further investigated. Therefore, in this study, we first studied the mechanical and hydraulic properties of the BSLP coal samples resourced from Zhaozhuang coalmine. Afterward, the numerical simulation was conducted to understand the HWR-HFC effect. Finally, the in situ test was done followed by some conclusions.

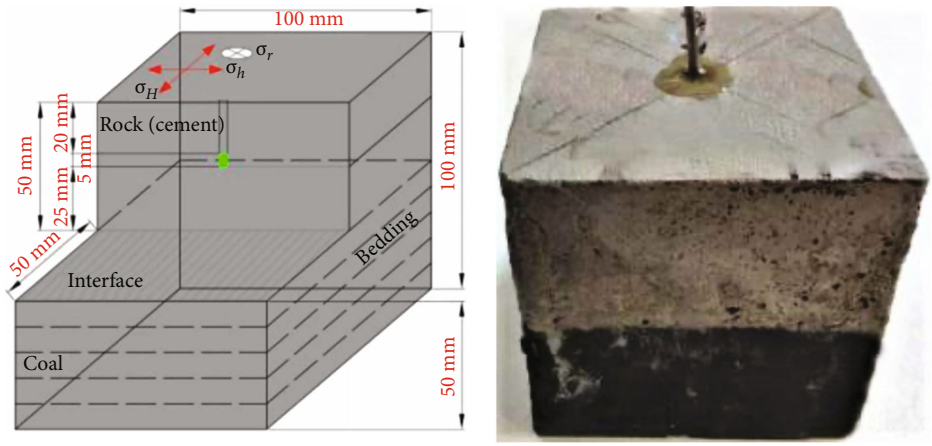

(a) Schematic diagram of specimen structure (b) Real specimen

Figure 3: Schematic diagram of coal-rock assemblage.

Table 2: Hydraulic fracturing test parameters and results.

Number	Stress state/MPa			Injection rate ml/min	Fracturing fluid	Fracture shape
	σ_h	σ_H	σ_V			
01#	3	5	6	20	Water	Coal seam unpenetrated
02#	3	5	7	20	Water	Coal seam unpenetrated
03#	3	5	7	20	Water	Coal seam unpenetrated
04#	3	5	8	20	Water	Coal seam unpenetrated
05#	3	5	8	20	Water	Coal seam unpenetrated
06#	3	5	9	20	Water	Coal seam penetrated
07#	3	5	9	20	Water	Coal seam penetrated
08#	3	5	9	20	Water	Coal seam penetrated
09#	3	5	15	20	Water	Coal seam penetrated

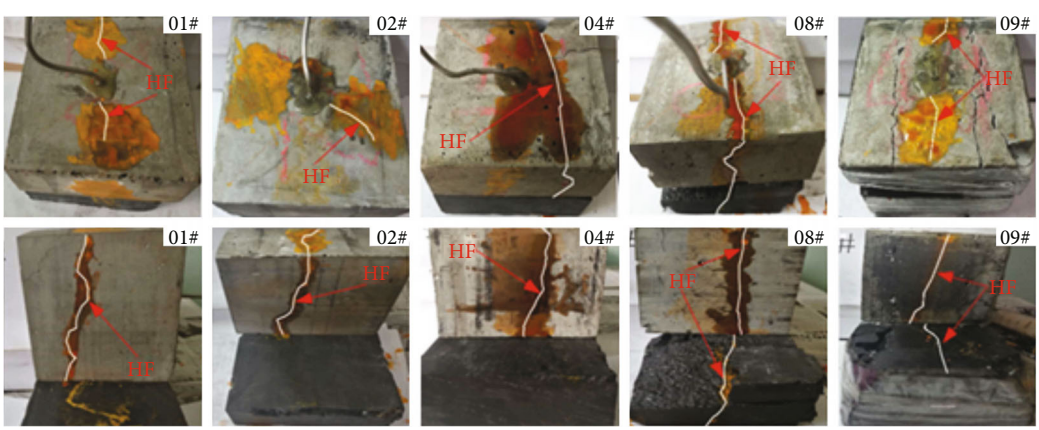

Figure 4: Fracture morphology distribution diagram of hydraulic fracturing in Zhaozhuang coal sample.

2. Geological Conditions of the BSLP Coal Seam

Zhaozhuang coal field is located in the Southern Qinshui Basin. Controlled by regional tectonic movement, it is a NNE regional monocline with a tendency to NE, at an angle of 5~10°. It contains faults and collapse columns, on the basis of which develop series of wide and gentle folds in the direction of NNE, formed the formation of wave ups and downs. The main faults and folds are in the direction of NNE, and the associated secondary faults are NE and NEE trending. The coal-bearing strata in the area are mainly the Taiyuan Formation (C_3t) of the Upper Carboniferous

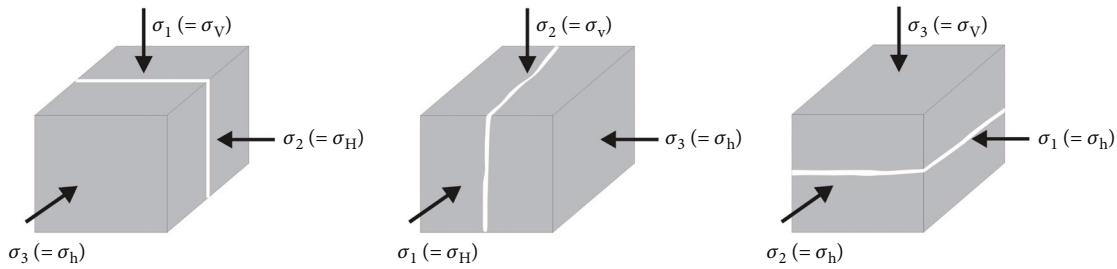

Figure 5: Relationship between fracture morphology and in situ stress state.

Table 3: Hydraulic fracturing monitoring results.

Well	Coal seam depth	Fracture shape	Area
CZ-X1	304.54-310.74	Horizontal	Adjacent area
CZ-X2	469.54-475.64	Horizontal	Adjacent area
HD-X1	490.50~496.40	Vertical	Adjacent area
ZZ-X1	594.11~598.53	Vertical	Research area
ZZ-X2	681.10~687.18	Vertical	Research area
ZZ-X03	684.78~689.4	Vertical	Research area

Series and the Shanxi Formation (P_1s) of the Lower Permian Series, with coal lines occasionally developed in the Lower Shihezi Formation and Benxi Formation. There are 15 layers of coal in Shanxi and Taiyuan Formation. Shanxi Formation contains 3 layers of coal, named No. 1, No. 2, and No. 3 from top to bottom. Taiyuan Formation contains 12 layers, named Nos. 5, 6, 7, 8_{-1}, 8_{-2}, 9, 11, 12, 13, 14, 15, and 16. The accumulated total thickness of Shanxi Formation and Taiyuan Formation is 118.19-206.86 m, generally 153.18 m. The total thickness of coal seam is 3.38-18.21 m, 12.80 m on average, and the coal coefficient is 8.33%.

The No. 3 coal seam in Zhaozhuang coalmine is a typical BSLP coal seam with a thickness of 0.50~6.60 m and a buried depth of 150~990 m. The floor elevation of the coal seam is between 120 m and 780 m (Figure 1). The ranks of coal are mainly lean and anthracite coal with a vitrinite maximum reflectivity (R_{omex}) of 2.23%-2.83%. The average Langmuir volume, pressure average, and gas saturation degree of the No. 3 coal are 32.21 cm^3/g, 2.04 MPa, and 59.6%, respectively. The in situ stress of this coal seam is 8.43~10.89 MPa with an underground stress gradient of 1.12~1.53 MPa/100 m. The reservoir gas pressure is 3.53~6.25 MPa with a gas pressure gradient of 0.46~0.86 MPa/100 m, which implies that this BSLP reservoir lacks gas pressure.

The layered characteristics of the coal seams are as follows: a layer of mylonitic coal at the top and bottom of No. 3 coal seam (Figure 2(a)), in which a thickness of about 0.45 m at the top and 0.3-1.20 m at the bottom (Table 1). Macroscopic coal is a kind of semidark coal, and the value of its hardness coefficient is less than 0.30. The upper part is mainly cataclastic coal (Figure 2(b)) with a thickness of 2.60~3.80 m, and the average hardness coefficient is about 0.60. Most of the lower part is fragmented coal (Figure 2(c)).

3. Material and Method

In the experimental test, combined rock and coal samples were employed. The sample consists of two parts: the upper part is a cement mortar sample, and the lower part is coal (Figure 3). The sizes of cement and coal samples are all 100 × 100 × 50 mm. During sample preparation, the cement mortar was placed on top of the coal sample to form a whole. Therefore, the dimension of the whole sample is 100 × 100 × 100 mm.

A borehole is drilled in the center of the sample with a size of Φ6 mm × 25 mm. Then, a steel pipe (Φ4 × 150 mm) is placed into the borehole. The sealing depth of the borehole is at the top 20 mm. The bottom 5 mm would be an open-hole section used for hydraulic fracturing. The structure diagram is shown in Figure 3 in detail. The uniaxial compressive strength, tensile strength, elastic modulus, and Poisson's ratio of the coal are 8.1 MPa, 1.26 MPa, 1.37 GPa, and 0.233, respectively. The sample was compressed by a triaxial compression test. The maximum horizontal stress and minimum horizontal stresses are 5 MPa and 3 MPa, respectively. The vertical stress varies from 6 to 15 MPa.

4. Experimental Test Results

Table 2 shows the failure modes of hydraulic fractured samples. Correspondingly, Figure 4 presents the pictures of samples after the hydraulic fracturing test. It can be seen that hydraulic fractures were only vertically developed in the cement when the vertical stress is less than 8 MPa. The fractures were extended along the interface between cement body and coal, such as samples 01#, 02#, and 04#. However, hydraulic fractures were propagated to the coal body at axial loading between 9 MPa and 15 MPa. Therefore, the hydraulic fracture shape would be changed with stress conditions. Specifically, when the difference between the vertical stress and the maximum horizontal stress increases over 4 MPa, the hydraulic fracture could punch into the coal body.

Previous studies concluded that hydraulic fractures would be developed in three forms when encounter the rock-coal interface, i.e., penetration type, crack arrest type, and deflection type [18]. When vertical stress is the maximum stress and the difference with maximum horizontal stress is over 5-6 MPa, vertical fractures would be formed. However, when the maximum stress is horizontal or it is not much different from the vertical stress, horizontal

Table 4: Physical mechanics test results of CBM well test.

Name	Elastic modulus/GPa	Poisson's ratio	Minimum horizontal principal stress/MPa	Maximum horizontal principal stress/MPa	Vertical stress/MPa
Coal seam roof (mudstone)	2.36	0.32	9.84	10.95	13.22
3# (upper hard layer)	0.98	0.35	7.67	8.92	13.31
3# (lower soft layer)	0.85	0.38	7.67	8.92	13.31

Table 5: Segmentation parameters of horizontal well.

No.	Bridge plug location (m)	Segment length (m)	Perforation interval/length (m)	Proppant (m^3)			Fracturing fluid volume (m^3)
				Fine sand	Medium sand	Rough sand	
1st	1549	92	1525-1528/3	3.08	38.53	12.94	702
2nd	1457	77	1433-1436/3	2.04	24.42	/	523
3rd	1380	119	1357-1360/3 1317-1320/3	/	75.98	/	1452
4th	1261	115	1237-1240/3 1194-1197/3	/	43.90	/	1584
5th	1146	79	1121-1124/3	/	62.03	/	2023
6th	1067	96	1044-1047/3	/	62.54	/	770
7th	971	91	947-950/3	/	56.43	10.39	814
8th	880	94	856-859/3	/	55.87	9.73	853

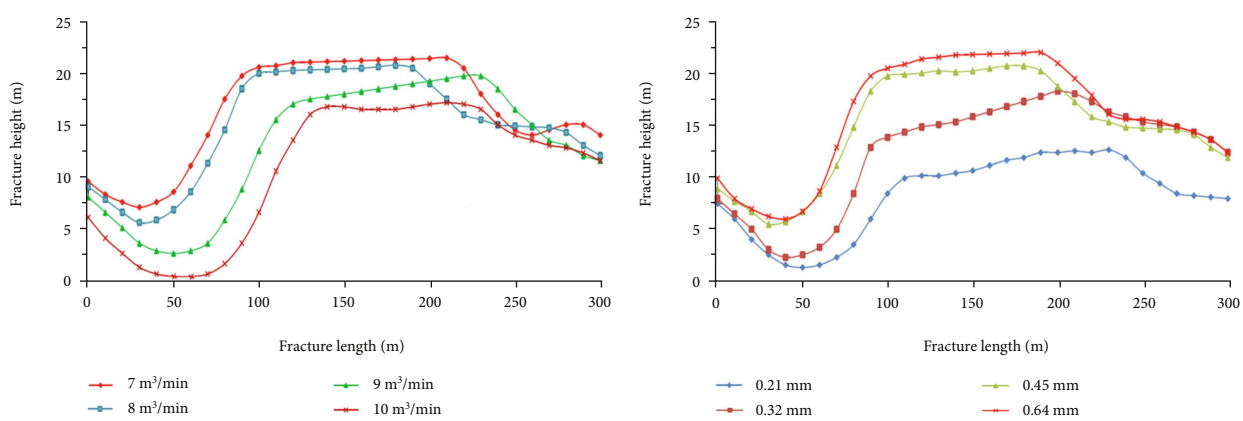

Figure 6: Influence of different fracturing fluid displacement and proppant particle size on the sand formation.

fractures or penetration type will be achieved [19–25]. These conclusions are consistent with our results.

5. In Situ HWR-HFC Technique Application

5.1. Well Locations. The in situ stress of coal includes vertical stress (σ_V) and horizontal stress (σ_H and σ_h). The vertical stress is mainly affected by the gravity of the overburden and can be estimated by the weight of the overburden. The characteristics of stress field are not only the key factors affecting the stability of coalmine roof, but also of great significance in the permeability prediction of coalbed methane reservoir and the morphology of fracture expansion. In general, when $\sigma_V > \sigma_H > \sigma_h$, it is normal fault stress mechanism, and hydraulic fracturing is more likely to produce vertical fractures (Figure 5). When $\sigma_H > \sigma_h > \sigma_V$ is the mechanism of reverse fault stress, hydraulic fracturing is more likely to produce horizontal fractures [26, 27].

The critical depth of in situ stress transfer in North China is about 400~1000 m. Above this critical depth, the horizontal stress would be the maximum stress. In this study, the average buried depth of the No. 3 coal seam is 667 m. Furthermore, fracturing monitoring results (Table 3) also show that the critical depth of in situ stress of No. 3 coal seam is about 500 m. Therefore, to produce vertical fracture from the roof towards coal seam, the well location should be prioritized at a buried depth deeper than 500 m.

Microseismic monitoring and fracture disclosure test results in coalmines show that hydraulic fractures extend in an elliptical shape. Furthermore, the hydraulic fracture

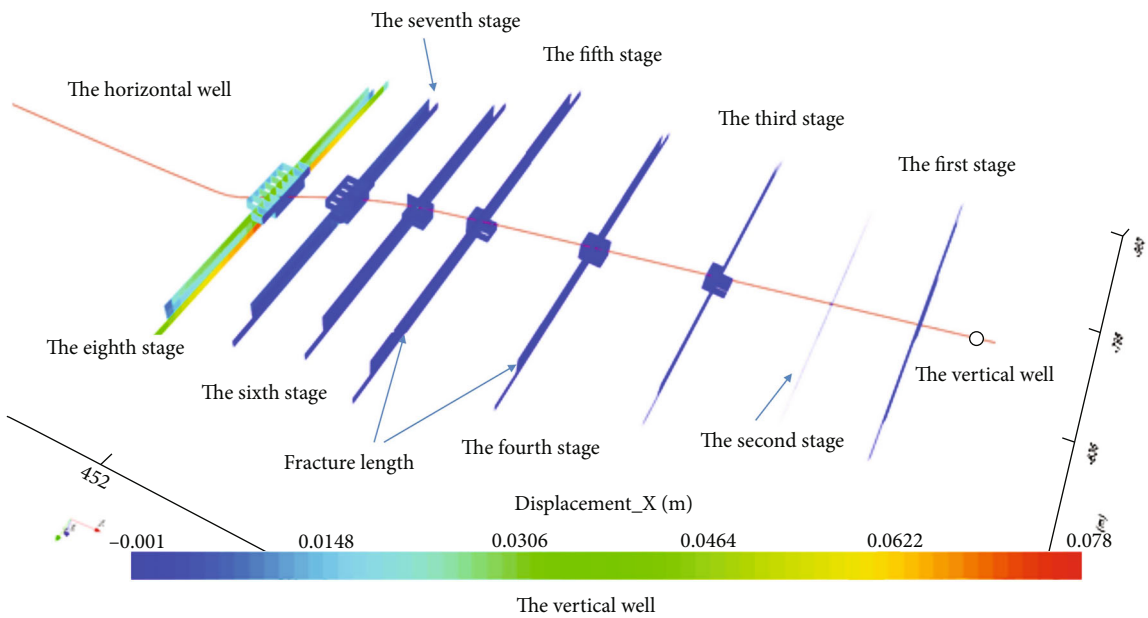

Figure 7: Numerical simulation results of horizontal good fracturing fractures

Table 6: Fracture monitoring results of horizontal well.

Fracture data		The 3rd stage (m) 1357-1360	The 3rd stage (m) 1317-1320	The 7th stage (m) 947-950
Length (m)	Left wing	43	46	100
	Right wing	0	68	74
	The whole wing	43	114	174
Height (m)		11	16	12
Direction (°)		SW70°	NE49°	NE45°
Attitude		Vertical		Vertical

would extend along the maximum horizontal stress direction and perpendicular to the minimum horizontal stress [28, 29]. In the target area, the maximum horizontal stress direction is generally NE30-45° and the main fracture extension direction of the adjacent wells is NE42°. To ensure effective communication between the wellbore and coal seam, the horizontal wellbore trajectory should be approximately vertical or oblique to the direction of the main fracture. Ideally, the horizontal well track should be approximately perpendicular to the direction of the main fracture with an orientation of about 138°. However, considering the geological conditions, the stability of the strata, and the distance between wells, the orientation of the horizontal well is finally determined as 96°.

The final depth of the vertical well is 703 m, while the coal seam is at a depth of 643.05 m. According to the mechanical test results of the BSLP coal and well test results (Table 4), the vertical stress is greater than the horizontal stress. Therefore, vertical fractures will be formed during hydraulic fracturing. Furthermore, the maximum principal stress of the No. 3 coal seam is vertical stress, which is greater than the maximum horizontal stress (over 4 MPa). Therefore, the hydraulic fractures will be punched from rock into the coal seam.

If the horizontal well is located along the floor, the coal particles are easy to flow into the horizontal well during drainage, which would weaken the efficiency of CBM extraction. Therefore, it is more reasonable to locate the horizontal well along the floor. Considering the roof lithology and perforation penetration ability, 0~2.0 m between the horizontal well and coal seam would be better.

5.2. Directional Perforation and Staged Fracturing Technology

(1) Horizontal well segmentation

The length of the horizontal well is about 800 m. During the segmentation designing, firstly, the horizontal segment was equally divided into several parts. Afterward, adjust the section length according to the geological conditions. The horizontal well segmentation should be the priority considering these conditions, i.e., close to the roof, easy cemented, and far away from the casing collar. Furthermore, the

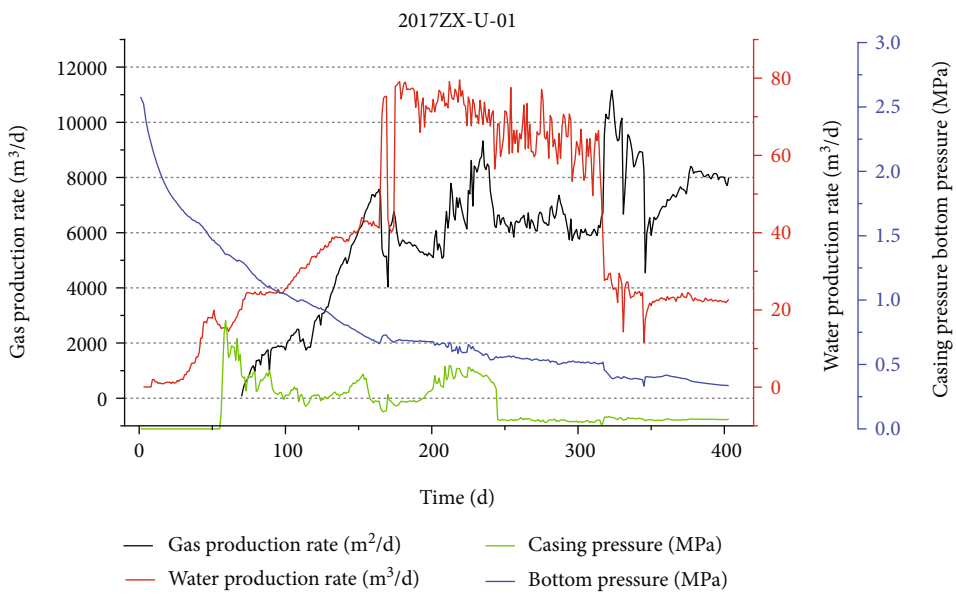

Figure 8: Drainage and production curve of ZX-U-01.

spacing between fractures should be controlled at about 80 m-120 m. The segmentation parameters are listed in Table 5 in detail.

(2) Deep penetration directional perforation technology

Composite deep penetration directional perforation technology was adopted to penetrate through the steel casing, cement ring, and the rock strata at the top of the coal seam, which could ensure the fracture extends to the No. 3 coal seam. This technology could create effective communication between the coal seam and wellbore and make a secondary impact on the formation by using gunpowder. This would produce multiple fracture networks in the near well zone.

The depth of deep penetration perforation channels can reach 1.2-1.5 m. The longest can reach 5 m, which greatly improves the perforating effect. According to the production casing size (φ139.7 mm), 95 mm perforating gun and 102 type perforating charges were selected. The perforating sections were divided into 8 sections and 10 clusters, each cluster was 3 m in length, and the hole density was 10 holes/m (Table 5).

(3) Fracturing technology

To solve the problems of difficulty in fracture initiation, extension, and support failure in the BSPLP coal seam, the fracturing technology of "large injection flux and high sand ratio" was employed. The comparative analysis of sand bar morphology under different fracturing fluid displacement rates (7-10 m^3/min) shows (Figure 6) that the displacement rate is proportionate to the equilibrium height of the proppant bar. The proppant settlement near the fracture inlet is unconspicuous due to the high displacement rate nearby. The overall shape of the proppant bar is laid deep into the fracture. According to the comparative analysis of sand bar morphology under different proppant particle sizes (0.21 mm-0.64 mm), the sand bar morphology of proppant moves to the depth of the fracture with the decrease of proppant particle size and tends to be laid to the fracture entrance position when the particle size is larger. Combined with the closing pressure and the length of the horizontal section, the fracturing flow rate was determined as 8-10 m^3/min and the maximum sand ratio was 20%. Proppant mainly consists of medium sand and rough sand, with a small amount of fine sand.

5.3. Numerical Modeling

(1) Numerical models

A 3D numerical software named USTIM was used to conduct hydraulic fracturing numerical simulation. In the numerical modeling, clear water was used as fracturing fluid and the fluid flow was set as 10 m^3/min. The amount of fracturing fluid and proppant in each section are shown in Table 5 in detail. Parameters in the numerical modeling are as follows: The bursting pressure of coal is 8.82 MPa, and the fracture gradient is 1.41 MPa/100 m. The closing pressure of fractures is 7.67 MPa. The reservoir gas pressure and pressure gradients are 1.97 MPa and 0.308 MPa/100 m, respectively. The average elastic modulus, Poisson's ratio, and the tensile strength of rock are 31.03 GPa, 0.28, and 6.98 MPa, respectively. The average elastic modulus, Poisson's ratio, and the tensile strength of coal are 39.04 GPa, 0.25, and 1.26 MPa, respectively.

(2) Fracture propagation monitoring and analysis

The lengths of induced fractures in the different sections are variable (Figure 7), which may be caused by the difference in fluid flux. For example, in the second hydraulic fracturing section, the fracture length is only 142 m under the

injection volume of 533 m^3. In the fifth section, hydraulic fracturing was conducted three times and the injection volume is about 2000 m^3. The fracture length in the fifth section was up to 252 m. Therefore, a smaller distance between the hydraulic fracturing site and well implies a better stimulating effect.

The surface microseismic monitoring device was employed to monitor the fracture propagation in the third and seventh sections. The results show that (Table 6) the fracture extends to NE. The seventh section adopts a single cluster perforation, and the total fracture length is 174 m, including 100 m on the left wing and 74 m on the right. Two clusters of perforations were used in the third stage. The first shot created 43 m fractures in the left, and the second shot created 114 m in length, in which the left fracture was 46 m and the right was 68 m.

6. In Situ CBM Extraction Results

The CBM extraction well named ZX-U-01 is the first horizontal well drilled in the roof of the Zhaozhuang coalmine. The horizontal well was divided into 8 sections, and each section was perforated by 10 clusters. Specifically, in the third and fourth sections, the single section with two cluster perforations was used to test the hydraulic fracturing efficiency. However, due to this method needed a higher injection pressure, secondary hydraulic fracturing was used. Similarly, the fifth section is far from the coal seam (over 2 m), and a third hydraulic fracturing was implemented. This well adopts the pumping method of a vertical good pumping, horizontal well, and vertical well combined producing gas.

At the initial stage of drainage (Figure 8), the bottom hole pressure was 2.408 MPa and the initial liquid level was 257 m above the roof of the No. 3 coal seam. The daily water volume gradually increased to 80 m^3/d. The maximum daily gas production reached 11,000 m^3/d. And the average gas production is about 7000 m^3/d. The cumulative water production and the cumulative gas production are 17,215.92 m^3 and 2350000 m^3, respectively. Compared with the traditional CBM extraction, gas production is increased by 50%-100%.

7. Conclusions

(1) The coal seam of the Zhaozhuang coalmine mainly consists of two layers: The top part of the coal seam is fractured coal, and the bottom is fragmented-mylonitic coal with a firmness coefficient value of less than 1.0. Specifically, a thin fragmented-mylonite layer is developed in the upper cataclastic coal layer in some areas

(2) The propagation law of hydraulic fracture in combined coal and rock samples was revealed. If the applied vertical stress is the maximum stress and greater than the maximum horizontal stress, the vertical hydraulic fractures are mostly developed, while if horizontal stress is the maximum or it is not much different from vertical stress, the horizontal fractures are easily formed or propagated along the interface between rock and coal

(3) By using the HWR-HFC technique, a maximum daily CBM gas production of 11,000 m^3/d was achieved and the average is about 7,000 m^3/d. This gas production is increased by 50%-100% compared with other types of horizontal wells in the study area

Data Availability

The data used in this paper are obtained from the experiment of the research and its partners.

Conflicts of Interest

The authors declare that they have no conflicts of interest.

Acknowledgments

This research was supported by the National Science and Technology Major Project (Grant No. 2016ZX05067), the Shanxi Province Major Science and Technology Projects (Grant Nos. 20191102001 and 20201102002), and the Key Research and Development (R&D) Projects of Shanxi Province (201901D111005(ZD)).

References

[1] Z. Xinmin, Z. Jun, and Z. Sui'an, *Coalbed Methane Resource Assessment in China*, Science Press, Beijing, 2002.

[2] Y. Jianping and L. Xiaoxia, "Development status and technical progress of China coalbed methane industry," *Coal Science and Technology*, vol. 44, no. 1, pp. 24–28, 2016.

[3] S. Baohong, L. Jianzhong, and L. Yi, "Present status and prospects of coal bed methane development and utilization technology of coal mine area in China," *Coal Science and Technology*, vol. 43, no. 2, pp. 1–4, 2015.

[4] C. Zhaoying, W. Baoyu, H. Haijin, and H. Chunsheng, "Analysis on drainage of features and drainage effect of coalbed methane well in Sihe Block," *Coal Science and Technology*, vol. 43, no. 2, pp. 100–105, 2015.

[5] S. Fenjin, W. Bo, and L. Mengxi, "Major geological factors controlling the enrichment and high yield of coalbed methane in the southern Qinshui Basin," *Acta Petrolei Sinica*, vol. 35, no. 6, pp. 1070–1079, 2014.

[6] W. Baoyu, B. Jianping, H. Chunsheng, and C. Zhaoying, "Effect analysis on fracturing of coalbed methane surface well and long distance boreholegas drainage technology in underground mine," *Coal Science and Technology*, vol. 43, no. 2, pp. 100–103, 2015.

[7] Y. Qingkui and J. Zhonghua, "Analysis of reasons for low yield of certain CBM well in Jiaozuo," *China Coalbed Methane*, vol. 9, no. 3, pp. 16–19, 2012.

[8] Y. Xu, Y. Zhu, and P. Zhang, "Application of CBM horizontal well development technology in the roof strata close to broken-soft coal seams," *Natural Gas Industry B*, vol. 6, no. 2, pp. 168–174, 2019.

[9] G. W. Lu, J. L. Wang, C. T. Wei et al., "Pore fractal model applicability and fractal characteristics of seepage and

adsorption pores in middle rank tectonic deformed coals from the Huaibei coal field," *Journal of Petroleum Science and Engineering*, vol. 171, pp. 808–817, 2018.

[10] Z. D. Cao, B. Q. Lin, and T. Liu, "The impact of depositional environment and tectonic evolution on coalbed methane occurrence in West Henan, China," *International Journal of Mining Science and Technology*, vol. 29, no. 2, pp. 297–305, 2019.

[11] S. L. Tang, D. Z. Tang, S. Li et al., "Fracture system identification of coal reservoir and the productivity differences of CBM wells with different coal structures: a case in the Yanchuannan Block, Ordos Basin," *Journal of Petroleum Science and Engineering*, vol. 161, pp. 175–189, 2018.

[12] F. L. Li, B. Jiang, G. X. Cheng, Y. Song, and Z. Tang, "Structural and evolutionary characteristics of pores-microfractures and their influence on coalbed methane exploitation in high-rank brittle tectonically deformed coals of the Yangquan mining area, northeastern Qinshui basin, China," *Journal of Petroleum Science and Engineering*, vol. 174, pp. 1290–1302, 2019.

[13] X. B. Su, Q. Wang, H. X. Lin, J. X. Song, and H. Y. Guo, "A combined stimulation technology for coalbed methane wells: part 1. Theory and technology," *Theory and Technology. Fuel*, vol. 233, pp. 592–603, 2018.

[14] M. Geng and G. Chunsheng, "Probing into gas drainage technology by virtual reservoir," *Safely in Coal Mines*, vol. 40, no. 5, pp. 94-95, 2009.

[15] Q. Zhang, C. G. Ge, W. Li et al., "A new model and application of coalbed methane high efficiency production from broken soft and low permeable coal seam by roof strata-in horizontal well staged hydraulic fracture," *Journal of China Society*, vol. 43, no. 1, pp. 150–159, 2018.

[16] X. Yaobo, Z. Shuangyu, and Z. Peihe, "Application of CBM horizontal well development technology in the roof strata close to broken-soft coal seams," *Natural Gas Industry*, vol. 38, no. 9, pp. 70–75, 2018.

[17] J. Jiancheng, C. Chen, D. Kui, W. Yan, and W. Minjie, "Research on the technology of high efficient to drainage CBM by multistage fracturing in horizontal well along the roof broken soft and low permeability coal seam," *Natural Gas Geoscience*, vol. 28, no. 12, pp. 1873–1881, 2017.

[18] P. Wu, W. Liang, H. Lian, Y. Jiang, Y. Geng, and M. Cao, "Mechanism and experimental investigation of the formation of hydro-fracture system by fracturing through the interface of large-size coal-rock," *Journal of China Coal Society*, vol. 43, no. 5, pp. 1381–1389, 2018.

[19] D. Q. Li, S. C. Zhang, and S. A. Zhang, "Experimental and numerical simulation study on fracturing through interlayer to coal seam," *Journal of Natural Gas Science and Engineering*, vol. 21, pp. 386–396, 2014.

[20] J. Yulong, L. Weiguo, L. Zhigang et al., "Expermental study on fracturing across coal-rock interfaces and the acoustic emission response characteristics," *Chinese Journal of Rock Mechanics and Engineering*, vol. 38, no. 5, pp. 875–887, 2019.

[21] Y. Jiang, H. Lian, V. P. Nguyen, and W. Liang, "Propagation behavior of hydraulic fracture across the coal-rock interface under different interfacial friction coefficients and a new prediction model," *Journal of Natural Gas Science and Engineering*, vol. 68, article 102894, 2019.

[22] N. D. Parab and W. W. Chen, "Crack propagation through interfaces in a borosilicate glass and a glass ceramic," *International Journal of Applied Glass Science*, vol. 5, no. 4, pp. 353–362, 2014.

[23] W. Fu, B. C. Ames, A. P. Bunger, and A. A. Savitski, "Impact of partially cemented and non-persistent natural fractures on hydraulic fracture propagation," *Rock Mechanics and Rock Engineering*, vol. 49, no. 11, pp. 4519–4526, 2016.

[24] M. Shangzhi, H. Bing, Z. Jian, T. Peng, and X. Zhenyu, "Experimental research on hydraulic fracture propagation through mixed layers of shale, tight sand and coal seam," *Journal of China Coal Society*, vol. 41, no. 1, pp. 221–227, 2016.

[25] M. Zhaoping, T. Yongdong, and L. Guofu, *Geological Theory and Method of Coalbed Methane Development*, Science Press, Beijing, 2010.

[26] M. Zhaoping, W. Yuheng, Z. Kun, L. Yixin, C. Jun, and Y. Meng, "Analysis of hydraulic fracturing cracks for coal reservoirs and in-situ stress direction in Southern Qinshui Basin," *Coal Science and Techology*, vol. 47, no. 10, pp. 216–222, 2019.

[27] K. Xinghui, *Research on Hydraulic Fracturing Propagation Rules in Coal Seam and Gas Extraction Drilling Optimization*, Chongqing University, Chongqing, 2014.

[28] L. Lindi, Z. Shicheng, and G. Meng, "A study of the propagation law of hydraulic fractures in coalbed gas reservoirs," *Natural Gas Industry*, vol. 30, no. 2, pp. 72–74, 2010.

[29] Z. Xuewen, F. Hongwen, Q. Yinan, and Z. Changshan, "A study on factors affecting the performance of hydraulically fractured horizontal well in low permeability reservoirs," *Acta Petrolei Sinica*, vol. 20, no. 4, pp. 51–55, 1999.

Hindawi
Geofluids
Volume 2021, Article ID 9015041, 17 pages
https://doi.org/10.1155/2021/9015041

Research Article

Pore Structure Differentiation between Deltaic and Epicontinental Tight Sandstones of the Upper Paleozoic in the Eastern Linxing Area, Ordos Basin, China

Jimei Deng,[1] **Huan Zeng**,[2] **Peng Wu**,[3] **Jia Du**,[3] **Jixian Gao**,[3] **Fei Zhao**,[3] **and Zhixun Jiang**[3]

[1]*School of Energy Resources, China University of Geosciences (Beijing), Beijing 100083, China*
[2]*College of Geoscience and Surveying Engineering, China University of Mining and Technology (Beijing), Beijing 100083, China*
[3]*China United Coalbed Methane Corporation Limited, Beijing 100016, China*

Correspondence should be addressed to Huan Zeng; 1710290328@student.cumtb.edu.cn

Received 8 May 2021; Revised 22 July 2021; Accepted 11 August 2021; Published 31 August 2021

Academic Editor: Afshin Davarpanah

Research on tight gas reservoirs in the eastern margin of the Ordos Basin, China, has recently become a hot spot. This paper mainly studies the reservoir characteristics of tight sandstone in the north-central area close to the provenance in eastern Linxing. Cast thin section, scanning electron microscopy, high-pressure mercury injection, and X-ray diffraction (XRD) were applied to discriminate the tight sandstone reservoir differences between the Permian Taiyuan and Shanxi formations in the study area. The results show that the deltaic tight sandstones in the Shanxi Formation are dominated by lithic quartz sandstone and lithic sandstone with an average porosity of 2.3% and permeability of 0.083 mD. The epicontinental tight sandstones in the Taiyuan Formation are mainly lithic sandstone and lithic quartz sandstone, with average porosities and permeabilities of 6.9% and 0.12 mD, respectively. The pore type is dominated by secondary dissolution pores, containing a small number of primary pores, and fractures are not developed. The capillary pressure curves of the Taiyuan Formation sandstone are mainly of low displacement pressure, high mercury saturation, and mercury withdrawal efficiency, while the Shanxi Formation sandstone is mainly of high displacement pressure, low mercury saturation, and withdrawal efficiency. The diagenetic evolution of sandstone in the Shanxi Formation is in meso-diagenesis stage A, and the Taiyuan Formation has entered meso-diagenesis stage B. The siliceous cement in the Taiyuan Formation sandstone enhanced the sandstone resistance to compaction and retained some residual intergranular pores. The pore types in the Shanxi Formation sandstone are all secondary pores, while secondary pores in the Taiyuan Formation sandstone account for approximately 90%. The results can be beneficial for tight gas production in the study area and similar basins.

1. Introduction

Tight sandstones have great development potential within coal measures on the eastern margin of the Ordos Basin [1, 2]. Even though all coal-bearing formations show potential tight gas production layers, their sedimentary environments are different [3]. The sandstones in the Taiyuan Formation were deposited in an epicontinental environment, while the Shanxi Formation was deposited in a deltaic environment [4, 5]. The sandstones have different pore structures influenced by both the sedimentary environment and complex diagenetic processes [6]. Tight gas is now being produced from all Upper Paleozoic sandstones, and clarifying the sandstone properties of different formations is crucial for favorable spot selection and well design.

Diagenesis refers to a series of physicochemical processes that are experienced after sediment deposition until metamorphism or repositioning due to tectonic movement [7–9]. Diagenesis is tightly correlated with clastic particle compaction in sandstone, the transformation of primary pores,

and the formation of secondary pores, which greatly affect its porosity and permeability [10–12]. The diagenetic evolution process is mainly influenced by the original clastic particle composition, sedimentary environment, geological fluid, stratum temperature, pressure, basin tectonic setting, and sedimentary burial process, which reflects the long geological process of interaction between inorganic minerals and organic matter [13, 14]. Diagenesis mainly includes compaction (mechanical compaction and chemical compaction), cementation, dissolution, metasomatism, recrystallization, and mineral polymorphism, in which compaction, cementation, and dissolution are of great significance in the process of reservoir physical transformation [15–17].

This study examined samples from 6 tight gas wells in the eastern Linxing area on the eastern margin of the Ordos Basin for a comprehensive study. There are differences in the composition, pore structure, and diagenesis of tight reservoirs in the Upper Paleozoic delta-continental margin sedimentary facies. This information is designed to predict the dominant reservoirs in the study area and lay a solid foundation for subsequent exploration and development of similar blocks.

2. Geological Setting

The Linxing area on the eastern margin of the Ordos Basin, which belongs to the Lvliang area, spans two tectonic units, the Yishan slope and the Jinxi flexural fold belt [1]. The structure of the area is relatively simple, the strata are gentle (the dip angle is generally less than 1°), and nose-like structures with a small range are mainly developed (Figure 1) [18]. The Carboniferous-Permian coal-bearing rock series in the eastern margin of the Ordos Basin is formed in a marine-continental transitional facies sedimentary environment. The Early Permian Taiyuan Formation strata are formed in an epicontinental sedimentary environment, and the study area is dominated by barrier coastal sedimentary systems, with river deltas, tidal flats, barrier sand bars, and other sedimentary environments developed in sequence from north to south. In the late early Permian, the sea in the study area retreated on a large scale and gradually transitioned to a continental sedimentary environment. The Shanxi Formation was dominated by river delta deposits [19–21].

3. Methods

In this paper, samples of the Shanxi Formation and Taiyuan Formation were tested by experimental analysis methods, such as casting thin section, scanning electron microscopy, high-pressure mercury intrusion, and X-ray diffraction (XRD), mainly to identify and classify rock types, pore types, diagenesis types and stages, and mineral compositions. After that, the porosity and permeability of tight sandstone were quantitatively analyzed by an E-HYFZ-00062 Autopore IV 9500 (maximum pressure: 228 MPa, pore diameter:$5*10^{-3}\,\mu$m~$103\,\mu$m) high-pressure mercury injection experiment, and the pore structure characteristics of tight sandstone were inferred by testing the displacement pressure (P_d), maximum pore throat radius ($r_{\max}$), withdrawal efficiency, porosity, and permeability, and other data [22].

Then, the reservoir differences between the Taiyuan Formation and Shanxi Formation can be determined. Moreover, D/max-2600 X-ray diffraction (XRD) was adopted to analyze the total detrital content and the relative clay mineral content of the samples. To study diagenesis and pore structure accurately, Leica DM4P thin sections were impregnated for observation. An FEI Quanta FEG 450 (FCG-004) scanning electron microscope (SEM) was adopted to observe the mineral composition and to understand the evolution of the mineral process. Then, the influence of the sedimentary environment and diagenesis on reservoir differences can be clarified [23, 24].

4. Results

4.1. Sandstone Petrology

4.1.1. Sandstone Composition. According to thin section identification, the debris content of the Taiyuan Formation sandstone samples in the study area was 58.0% ~85.0%, with an average of 74.5%, and the interstitial content was 8.0% ~34.0%, with an average of 22.0%. Among the crumb particles, the relative content of quartz particles is 26.0% ~41.0%, the average content is 35.4%, and the relative content of feldspar particles (potassium feldspar and plagioclase) is low, ranging from 5% to 27%, with an average of 14.1%; the lithic content is 35.0% ~66.0%, and the average content is 50.5%. According to the Folk (1974) sandstone triangle classification, the Taiyuan Formation sandstone samples are dominated by litharenite and feldspathic litharenite, followed by litharenite. The sandstone samples of the Shanxi Formation are dominated by litharenite and feldspathic litharenite (Figure 2).

The lithotripsy content of the coal-bearing sandstone in the study area is relatively high. The Taiyuan Formation sandstone is dominated by metamorphic rock cuttings, followed by volcanic rock cuttings and sedimentary rock cuttings and mica fragments, and is dominated by igneous rock cuttings and volcanic clastic rock cuttings in the Linxian area. The sandstone debris content of the Shanxi Formation is significantly higher than that of the Taiyuan Formation, mainly dominated by metamorphic rock cuttings, followed by igneous rock cuttings, mica fragments, and sedimentary rock cuttings (Figure 3).

The coal-bearing sandstones in the study area also have high interstitials, mainly including matrix and cement, and the matrix is mainly muddy. The average mud content of the Taiyuan Formation was 14.8%, and the mud content increased from 3% to 36% from bottom to top, reflecting the gradual transition of the sedimentary environment to the continental phase. The average mud content in the Shanxi Formation is 46.3%, which is much higher than the mud content of the Taiyuan Formation. The types of cement mainly include siliceous, clay minerals, calcite, and siderite. The cements of the Taiyuan Formation are mainly siderite and clay minerals, with contents of 4.0% to 16.0% and an average value of 8.5%. The cements in the Shanxi Formation are 3.0% ~19.0%, with an average of 9.5%, and are mainly composed of siderite and ferrocalcite.

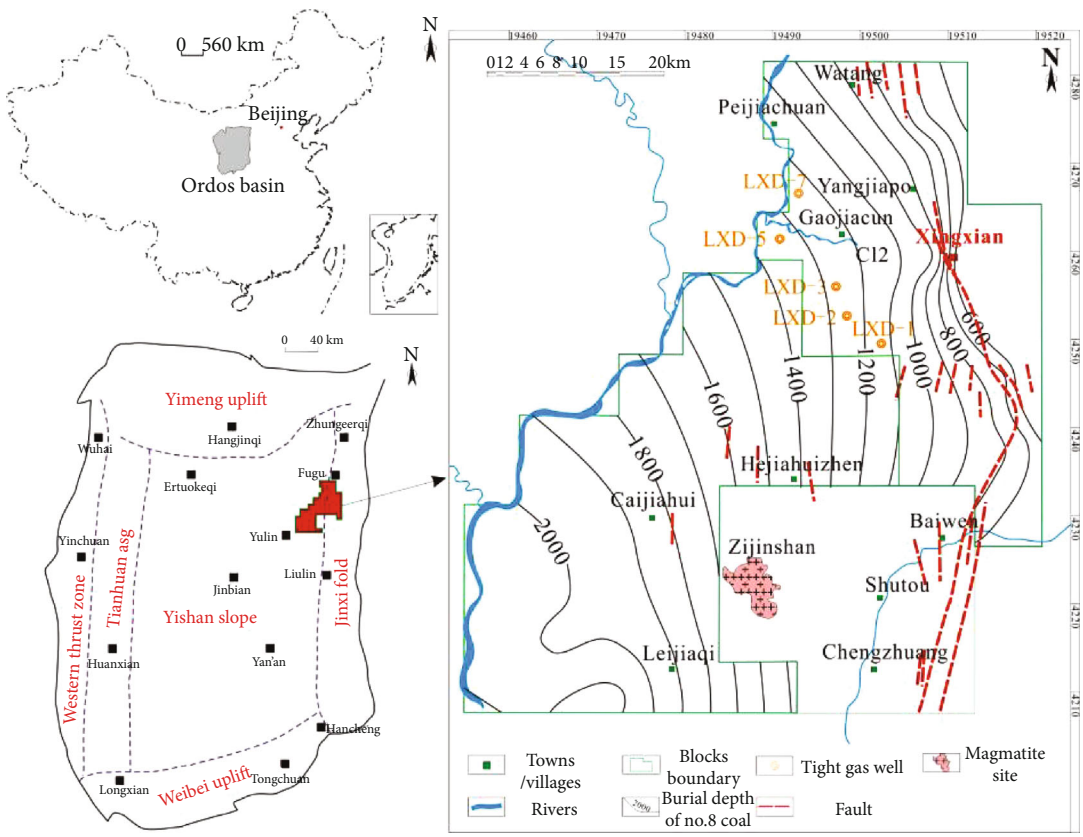

Figure 1: Location of the Linxing area, northeastern Ordos basin, modified after [4].

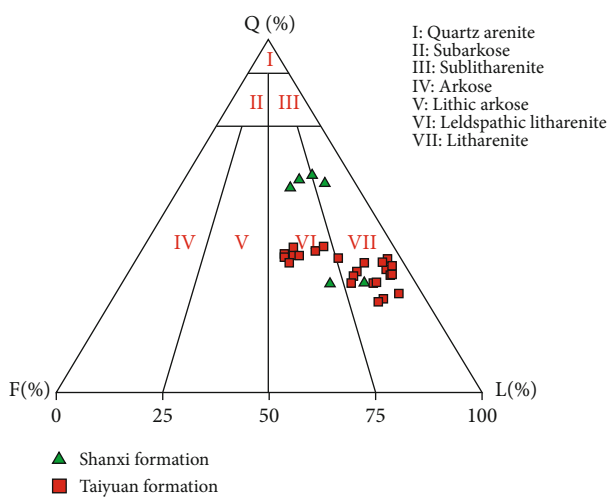

Figure 2: Ternary diagram of coal-measure tight sandstone types in the study area.

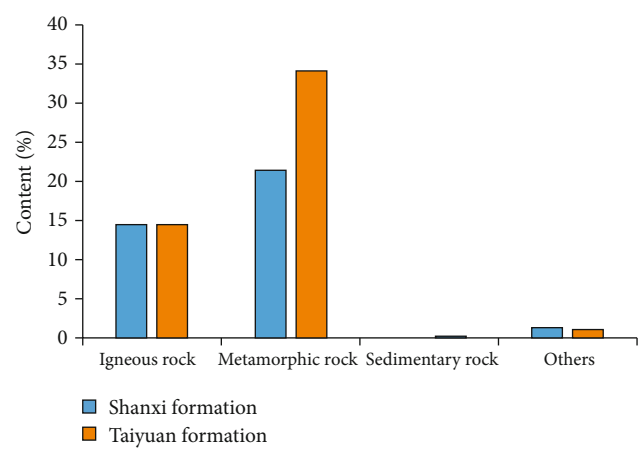

Figure 3: The types of rock fragments in coal-measure sandstones.

Overall, the Taiyuan Formation sandstone has a high content of litharenite and fewer quartz particles, and their composition is moderately mature. The sandstone quartz particles and feldspars in the Shanxi Formation are relatively high in content, and their component maturity is high. Among them, the high content of litharenite and miscellaneous in sandstone provides a material basis for the dissolution of secondary pores.

4.1.2. Texture of Detrital Grain. The sandstone structure of the Taiyuan Formation is dominated by medium-thick sand size, and the northern and southern margins are coarser in grain size and gradually decrease toward the middle and are dominated by medium-coarse sandstones in the study area. The sorting property is also gradually improved from both sides to the inside. Among them, feldspar lithic sandstone has good sorting properties, lithic sandstone has moderate sorting, and the clastic particles are mostly subcircular and subangular, with pore-type cementation as the main

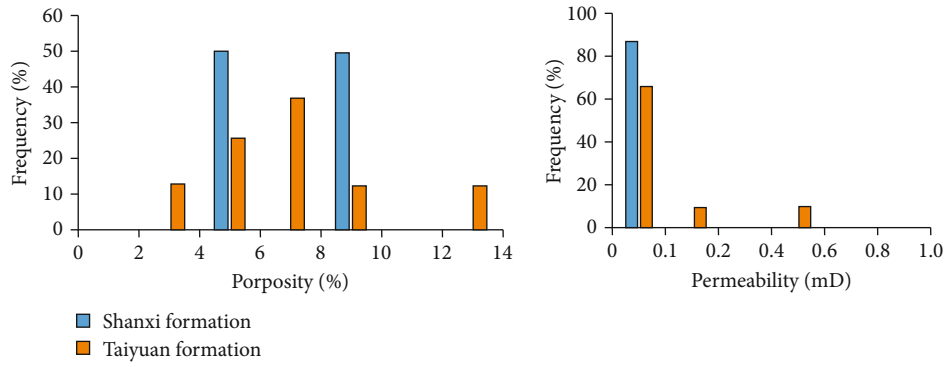

Figure 4: The porosity and permeability distribution of coal-measure sandstone in the study area.

component, line contact, and point-line contact between the particles. The sandstone structure of the Shanxi Formation is dominated by fine-grained and medium-grained structures, with moderate sorting, and the particles are mainly subcircular and subangular, with pore cementation as the main cementing types. The particles are mainly in line contact. The maturity of the sandstone structure of the Taiyuan Formation is lower than that of the Shanxi Formation sandstone. However, overall, from top to bottom, the structural maturity of the coal-bearing sandstone gradually increases.

4.2. Porosity and Permeability. Overall, the coal-bearing sandstones on the eastern margin of the basin are generally poor in physical properties. According to the results of gas measurement porosity, the porosity of the Taiyuan Formation sandstone is 2.3% ~12.2%, the average value is 6.9%, the permeability is 0.018~0.514 mD, and the average value is 0.12 mD; the sandstone porosity of the Shanxi Formation is 2.0% ~2.5%, the average value is 2.3%, the permeability is 0.071~0.95 mD, and the average value is 0.083 mD. The porosity and permeability of sandstone samples show a single polarization distribution (Figure 4). Among them, the porosity of the Taiyuan Formation sandstone is less than 10%, accounting for more than 90% of the total samples, while the porosity of the Shanxi Formation sandstone samples is less than 10%. The permeability of the Taiyuan Formation sandstone sample is less than 0.1 mD, accounting for more than 70%, and the Shanxi group is less than 0.1 mD, accounting for 100%. The physical properties of the Taiyuan Formation and the Shanxi Formation sandstone in the study area are poor, both of which belong to dense to ultratight sandstone, but the percolation conditions of the Taiyuan Formation are significantly better than those of the Shanxi Formation.

4.3. Pore Structures. The pore structure is the size, shape, distribution, and connectivity of the pores and throats within the reservoir [25]. In general, the size and distribution of pores determine the porosity of the reservoir, and the size and distribution of the throat control the permeability of the reservoir. For conventional reservoirs, it is feasible to evaluate the reservoir only by porosity and permeability. For low-permeability reservoirs, pore structure characteristics are the key factors determining reservoir performance [26]. In this paper, the pore type, size, shape, and distribution characteristics of sandstone samples in the study area were observed and counted in detail by casting thin sections and scanning electron microscopy. Typical sandstone samples were selected for high-pressure mercury intrusion experiments to study the pore structure characteristics of coal-bearing sandstones.

4.3.1. Microscopic Observation Results. Through the microscopic observation of the sandstone samples in the study area, it is found that the pore type of the coal-bearing sandstone reservoir in the study area is dominated by secondary pores and contains a small number of primary pores (Figure 5). Secondary pores include interparticle dissolution pores, intragranular dissolution pores, and intercrystalline pores of clay mineral aggregates, which are mainly formed by dissolution and metasomatism, in which interparticle dissolution pores are formed by an intergranular matrix or cement is dissolved. Intragranular dissolution pores are mainly composed of feldspar, lithic, and quartz particles, which are formed by the erosion of sandstone skeleton particles. The intercrystalline pores of clay minerals are mainly found in clay mineral aggregates, which are mainly composed of kaolinite intercrystalline pores. Primary pores are mainly residual intergranular pores after compaction and cementation damage, some residual intergranular pores are further enlarged under late dissolution, and it is difficult to distinguish the difference in the dissolved pores, which is unified into the category of dissolution pores. In addition, some samples can be seen as microfracture development.

According to the statistical results of the cast thin sections, samples of the Taiyuan Formation are mainly composed of secondary pores and contain a small amount of residual intergranular pores. The secondary pores accounted for 95.6% of the total surface porosity, and the residual intergranular pores accounted for 4.4%. The secondary pores are mainly composed of the dissolution pores of cuttings, quartz, and feldspar particles, followed by the intercrystalline pores. The interparticle dissolution pores account for 48% of the secondary pores, the intragranular dissolved pores account for 49%, and the intercrystalline pores of clay minerals account for 3%. Microcracks were visible in individual samples, and the number was small and not counted (Table 1).

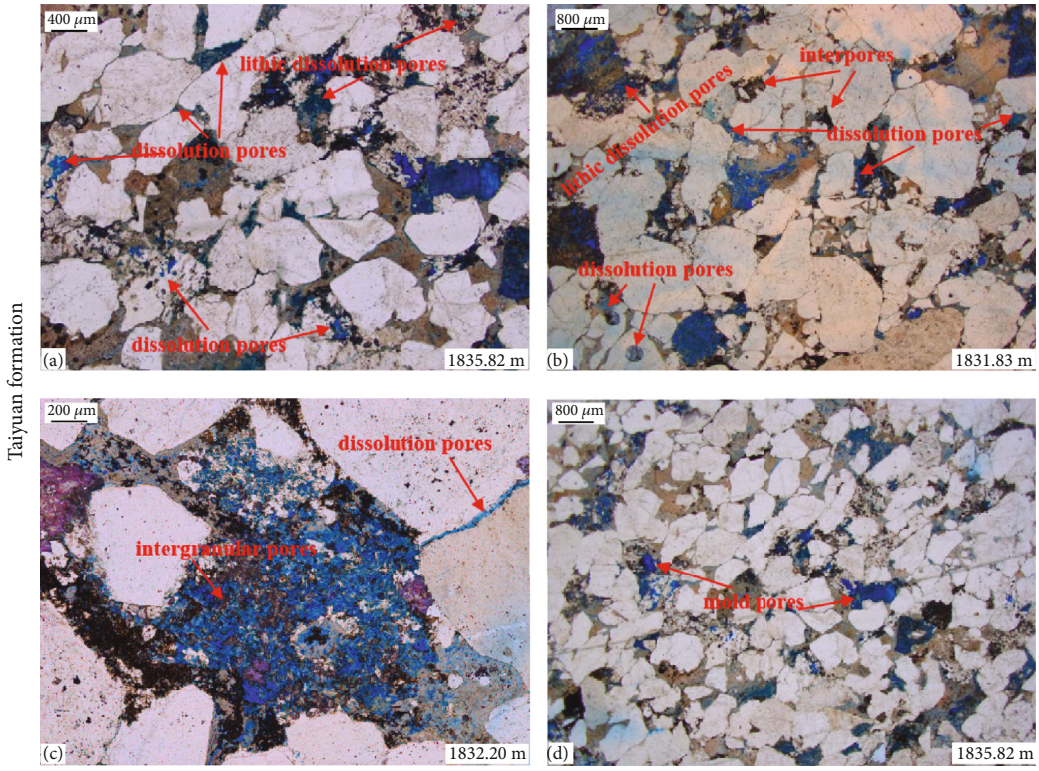

Figure 5: Pore type of coal-measure sandstone. All the sections were selected from well LXD-2, which is located in the central part of the study area, and the depths are marked. (a) Lithic dissolution pores and dissolution pores; (b) lithic dissolution pores, dissolution pores, and interparticle pores; (c) dissolution pores and intergranular pores; (d) mold pores.

Table 1: Proportion of pore types in coal-measure sandstone.

Layer	Residual intergranular pores (%)	Interparticle dissolution pores (%)	Intragranular dissolution pores (%)	Intercrystalline pores (%)	Rate (%)
Shanxi Formation	0	0.50	1.25	0.25	2.00
Taiyuan Formation	0.46	4.77	4.92	0.31	10.46

All of the Shanxi Formation sandstone samples were secondary pores, and no preserved primary pores were observed under the microscope. The secondary pores are mainly intragranular dissolved pores formed by the dissolution of feldspar and cuttings, followed by the interparticle dissolution pores formed by the dissolution of the intercrystalline pores and interstitials of the kaolinite aggregate, in which the intragranular dissolved pores accounted for 62.5%, the interparticle dissolution pores accounted for 25%, and the kaolinite intercrystalline pores accounted for 12.5% (Table 1).

4.3.2. Mercury Intrusion Porosimetry Results. The pore structure is the shape, size distribution, and connectivity of the pores and throats between the debris particles, reflecting the reservoir's reservoir and seepage capacity. High-pressure mercury intrusion experiments are one of the most effective methods for studying the pore structure of tight sandstone. Compared with the conventional mercury intrusion experiment, the maximum pressure of mercury in the high-pressure mercury intrusion experiment is larger (up to 200 MPa), and the range of test pores is larger, up to the nanometer scale. Structural parameters such as pore throat size and distribution of sandstone samples can be calculated from the relationship between capillary pressure and mercury influx.

The capillary pressure curves of the Taiyuan Formation samples can be divided into three categories (Figure 6(a)): class I curve (sample T1), the displacement pressure (Pd) is lower than 1.0 MPa, the curve of the middle curve of the mercury inlet curve is near level, and after the mercury saturation exceeds 70%, the curve rises sharply, the maximum mercury saturation is greater than 90%, the residual mercury saturation is 55.44%, and the withdrawal efficiency is 34.78%. The curve shows that the effective throat distribution of the reservoir is wide and unevenly distributed, the pore throat is larger, and the pore structure is better; class II curve (sample T2), the displacement pressure is approximately 3 MPa, the mercury inflow curve is near the horizontal step, with a sharp shift to the upper right, and the maximum mercury saturation is 73.0%. The residual mercury saturation is 71.4%, and the withdrawal efficiency is

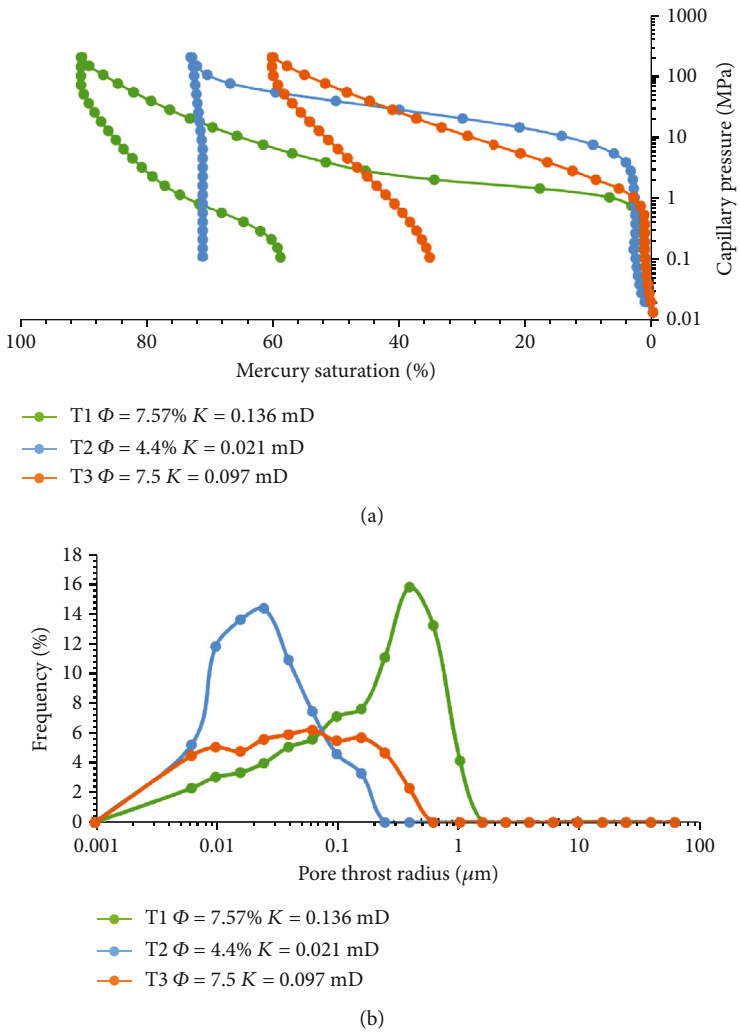

Figure 6: Capillary pressure curve and pore throat distribution of sandstone in the Taiyuan Formation.

low at 2.6%. The curve shows that the effective throat distribution of the reservoir is narrow, the pore throat is small, and the pore structure is poor. The class III curve (sample T3) has a displacement pressure of approximately 1 MPa, the mercury intrusion curve is nearly horizontal, the inclination to the upper right is not obvious, the maximum mercury saturation is approximately 60%, the residual mercury saturation is approximately 20%, and the withdrawal efficiency is approximately 40%. The curve shows that the effective throat distribution of the reservoir is narrow, the pore throat is larger, and the pore structure is better.

According to the capillary pressure curve, the pore throat distribution characteristics of the Taiyuan sandstone samples can be obtained (Figure 6(b)), and class I curve pore throat distribution range is wide, the radius is divided into 0.006 μm~1.048 μm, which is monomodal, with the peak to the right, and the maximum peak corresponding to the throat is 0.4 μm; the radius of the throat of the class II curve is mostly between 0.006 μm and 0.16 μm, the distribution range is narrow, and the radius of the throat of the main peak is 0.025 μm; the class III curve has a narrow range of pore throat distribution, which is concentrated between 0025 μm and 0.04 μm. There is little difference between the maximum and minimum values, and the pore throat radius distribution is relatively uniform.

The capillary pressure curve of the Shanxi Formation sandstone samples is similar to that of Taiyuan Formation III (Figure 7(a)), and the discharge pressure is approximately 0.76 MPa. The mercury intrusion curve rises steadily with a small slope and shifts to the upper right. The maximum mercury saturation is slightly higher than 80%, with an average of 81.05%. The remaining mercury saturation is 45.2% ~53.3%, with an average of 49.25%. The mercury removal efficiency is 26.0% ~36.2%, with an average of 31.1%. The curve shows that the effective throat distribution of the reservoir is narrow, the pore throat is small, and the pore structure is poor.

According to the capillary pressure curve, the pore throat distribution characteristics of the Shanxi Formation sandstone samples can be obtained (Figure 7(b)). The pore throat radius of the tight reservoir in the study area is mainly distributed between 0.006 μm and 0.63 μm, and the distribution range

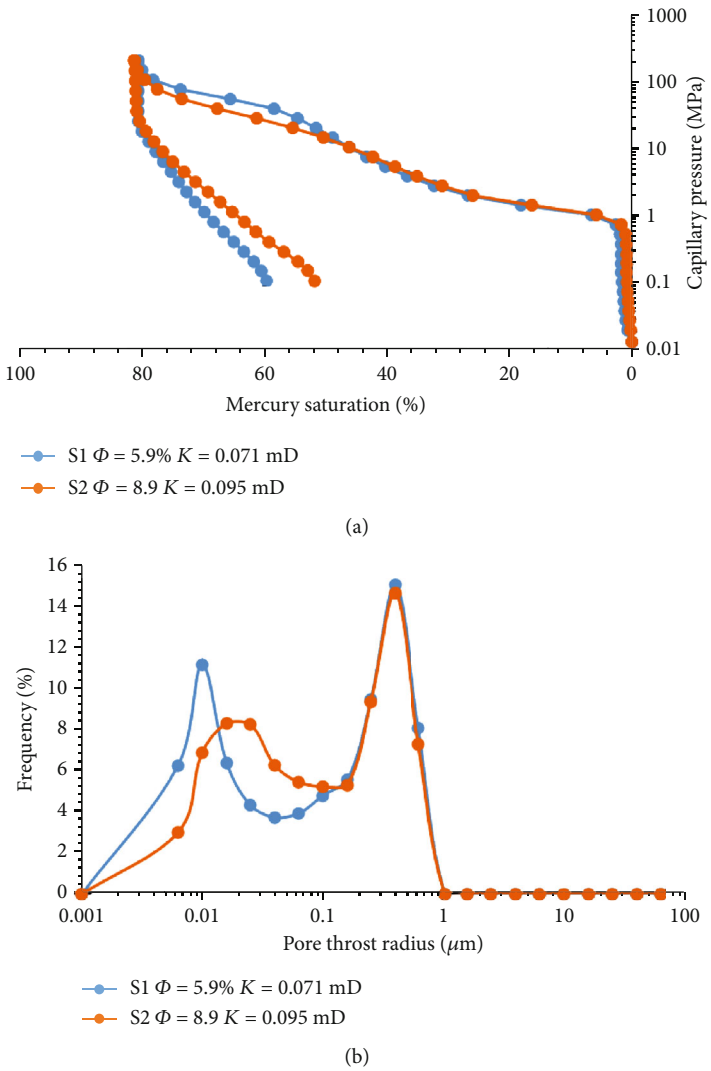

Figure 7: Capillary pressure curve and pore throat distribution of sandstone in the Shanxi Formation.

is narrow, showing a double-peak distribution. The main peak corresponds to a pore throat radius of 0.4 μm.

The capillary pressure curve of the Taiyuan Formation in the study area is dominated by class I, and there are fewer class II and class III curves. The Shanxi Formation sandstone is mainly curve III, and the pore structure of the Taiyuan Formation sandstone is better than that of the Shanxi Formation.

4.4. Diagenetic Sequences. The coal-bearing tight sandstones in the eastern margin of the basin have undergone various diagenesis transformations, and the diagenesis is strong, which is of great significance for the formation of current sandstone reservoir characteristics. In this paper, through microscopic observation, scanning electron microscopy, and XRD analysis of rock flakes, the diagenesis types and characteristics of coal-bearing sandstones in the study area are systematically studied. The diagenesis experienced by the coal-bearing tight sandstones in the study area mainly includes compaction, cementation, dissolution, and metasomatism.

4.4.1. Compaction. The coal-bearing sandstones in the eastern margin of the basin experienced intense compaction (Figure 8), and the primary pores were severely damaged. The specific performance is that the sandstone debris particles are closely arranged, and the contact mode is mainly line contact and bump contact. Plastic cuttings and mica fragments are severely deformed by extrusion, and cracks appear on the surface of rigid particles. Due to the difference in tectonic evolution, compaction is becoming more intense from north to south.

The sandstones of the Shanxi Formation are formed in an epicontinental sedimentary environment, with high contents of heterogeneous and plastic cuttings. The intergranular pores are most severely modified by compaction, and the particles are closely arranged and contain no primary intergranular pores. The Taiyuan Formation sandstone quartz has a high content of rigid particles and less heterogeneous and plastic cuttings, and the overall compaction resistance of the sandstone is stronger than that of the Shanxi Formation. The compaction transformation causes slightly less

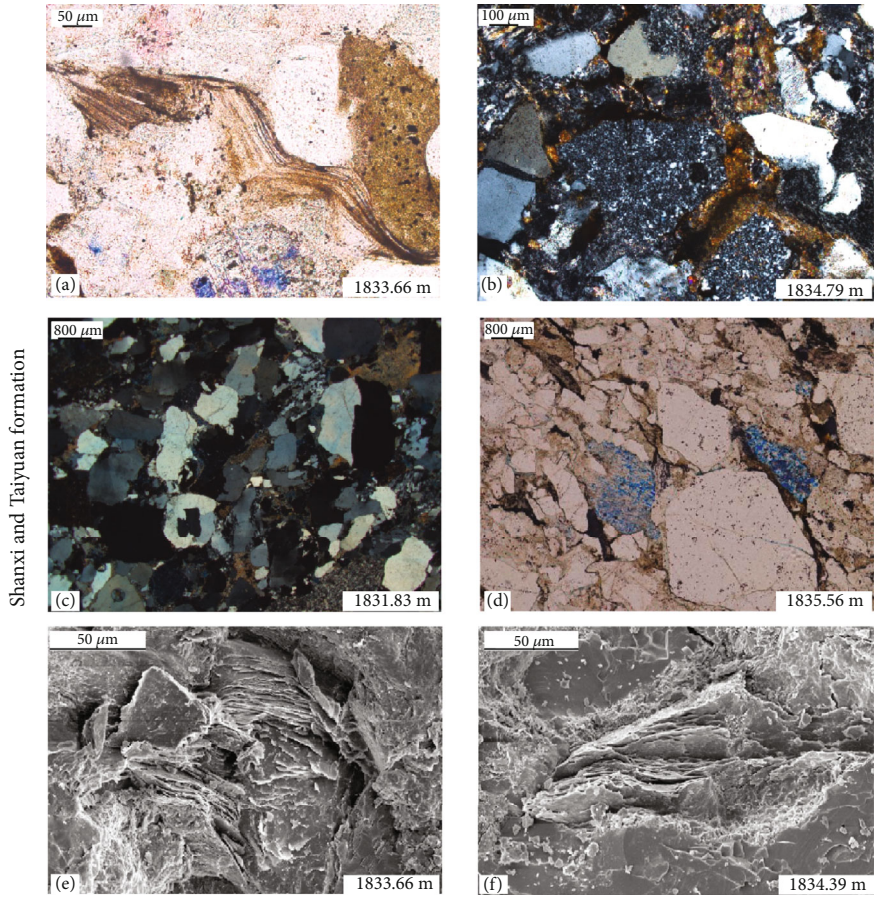

Figure 8: The compaction characteristics of coal-measure sandstone. All the sections were selected from the Taiyuan Formation of well LXD-2, which is located in the central part of the study area, and the depths are marked. (a) Mica extrusion deformation; (b) lithic extrusion deformation; (c) closely arranged quartz particles are in linear contact; (d) closely packed quartz particle bump contact; (e) and (f) Mica pieces under scanning electron microscopy (SEM) bending deformation.

physical damage to the reservoir than the Shanxi Formation, and some of the original intergranular pores are retained.

4.4.2. Cementation. Cementation mainly refers to the minerals precipitated from the pore solution cementing the crumb particles together so that the loose sediments are consolidated into rocks. It can occur in various periods of diagenesis and is one of the main factors leading to the decrease of reservoir porosity and permeability. In addition to filling the pores and blocking the throat and reducing the porosity and permeability of the sandstone, some cementation has the ability to enhance the compaction resistance of the sandstone skeleton particles and to some extent reduce the damage of the physical properties of the reservoir by compaction. This type of cementation is called retentive diagenesis [27]. For example, the early chlorite film wrapped the edge of quartz particles, hindering the secondary increase of quartz, enhancing the strength of early sediments, and slowing the damage of reservoir properties by compaction. Silica cementation is the most common cementation of coal-bearing sandstones in the eastern margin of the basin, followed by clay mineral cementation and carbonate cementation.

(1) Siliceous cementation

There are three main forms of siliceous cementation in the study area. The first is the secondary enlargement around the quartz crumb particles. Under the polarizing microscope and the scanning electron microscope, the contour of the original debris can be easily discerned by the clay film at the edge of the original crumb particles, and the optical orientation of the secondary enlarged side is consistent with the original quartz particles (Figures 9(a)–9(c)). This phenomenon of secondary quartz enlargement is very common in flakes, and the second-stage secondary side can be seen at most. The second type is quartz cement filled in the pores, which is generally cryptocrystalline or small granular. Under a scanning electron microscope, crystal-like self-generated quartz particles can be clearly seen and filled in the intergranular pores (Figure 9(d)). The third type is vermiculite cement, which can be epitaxially grown on the edge of quartz particles. Vermiculite cement is similar to secondary enlargement, but its extinction angle is inconsistent with quartz particles. This type is composed of many tiny plaque crystals, alternating between light and dark under orthogonal mirrors; it can also appear as a tiny crystal aggregate in the matrix. This type is as clean and smooth as a quartz

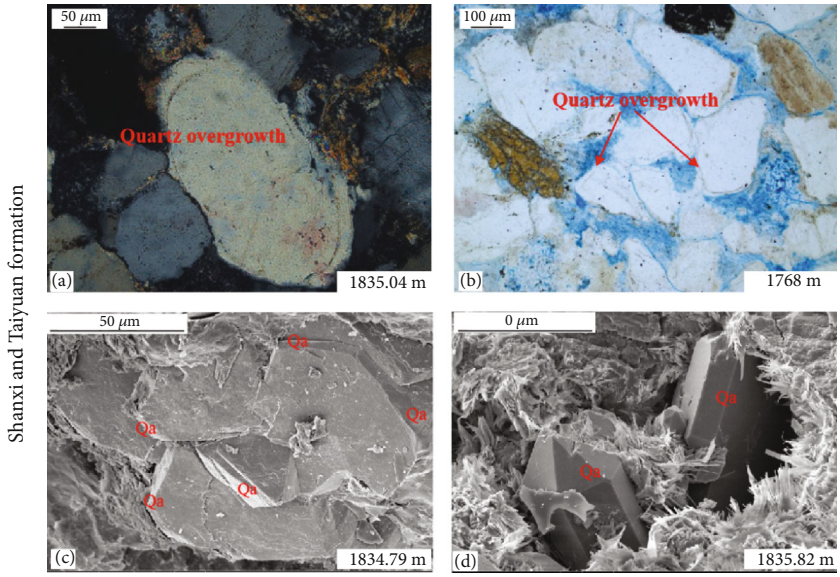

Figure 9: The quartz cement characteristics of coal-measure sandstone. All sections were selected from wells LXD-2 and LXD-5, which are located in the central part of the study area, and the depths are marked. (a) Quartz overgrowth (Taiyuan Formation); (b) quartz overgrowth (Shanxi Formation); (c) quartz secondary enlargement, crystal shape is better (Taiyuan Formation); (d) pore-filling authigenic quartz that is euhedrally crystallized (Taiyuan Formation).

particle under a single polarizer, and the tiny crystals are alternately arranged in light and dark under an orthogonal mirror. Vermiculite cement is often found under the microscope that siliceous cements often appear together with authigenic clay minerals, with authigenic quartz associated with illite and kaolinite, which indicates that the siliceous cement is derived from the conversion between kaolinite and clay minerals of feldspar. In the distribution, the Taiyuan Formation silicic cementation is more developed than the Shanxi Formation. In the Taiyuan Formation quartz sandstone flakes, pore cementation between the quartz particles was observed, and quartz secondary growth was particularly developed and mosaic (Figure 9(b)). The presence of siliceous cement in either form will reduce the radius of the primary intergranular pores and pore throats, which will greatly reduce the porosity and permeability of the coal-bearing sandstone in the study area. However, siliceous cementation also increases the grain strength of sandstone while reducing the porosity of sandstone, which makes some of the original intergranular pores in the Taiyuan Formation sandstone, which reduces the damage to reservoir physical properties to some extent.

(2) Clay cements

XRD analysis showed that (Table 2) the clay mineral content in the coal-bearing sandstone in the study area is high, and the clay mineral content of the Taiyuan Formation sandstone is 6% ~96%, with an average of 32.74%, in which illite has the highest relative content, followed by kaolinite and chlorite content, and I/S mixed clay is the lowest. The content of clay minerals in the sandstones of the Shanxi Formation is 51% ~73%, with an average of 60.25%. The relative content of illite is the highest, followed by kaolinite, and the chlorite content and I/S mixed clay content are the lowest. On the whole, the coal-bearing sandstones in the eastern margin of the basin have higher clay mineral contents, mainly kaolinite, followed by illite and chlorite contents, and the I/S mixed clay content is lower.

The clay minerals in the sandstone are both biosynthesized and self-generated. The microscopic and scanning electron microscopic observations are all self-generated clay minerals, and the mineral morphology can be clearly observed. These clays are cements; the deposited clay minerals are weathered from the parent rock, and the mineral species and morphology cannot be distinguished under the microscope. They are called argillaceous interstitials. The kaolinite in the sandstone of the eastern margin of the basin is mostly altered by feldspar or volcanic rock, and the crystal self-formation is higher. The single crystal is in the shape of a pseudohexagonal plate. The aggregates are mostly book-like, worm-like, filled in the intergranular pores, dissolution pores, or mold pores, the kaolinite aggregates are loosely arranged, and the intercrystalline pores are developed (Figures 10(a) and 10(b)).

The chlorite in the sandstone is generally produced as a film wrapped around the edge of the particle or in the form of a pore lining. In the sandstone samples of the study area, chlorite film or lining chlorite is rarely seen, and residual chlorite film is visible only at the edge of the grain or on the secondary side of the quartz, which is mainly due to the high content of organic matter in the coal system. The large number of organic acids formed during the diagenesis process erodes the early formation of chlorite film.

The illite fills the intergranular pores or wraps around the edges of the particles in the form of hair, honeycombs, and bridging under the microscope (Figures 10(d)–10(f)). There are two sources of illite in the study area: The first is

Table 2: Relative content of clay minerals in sandstones in coal measure.

Formation		Clay (%)	K (%)	I (%)	Ch (%)	I/S (%)	*S*/(I/S) (%)
Shanxi	Content	51-73	25-44	15-26	22-36	8-25	20-20
	Average	60.25	31.33	22.33	27.34	19	20
Taiyuan	Content	6-96	1-86	3-99	0-29	0-20	0-24
	Average	32.74	42.11	47.26	7.47	3.16	1.47

Clay: clay minerals; K: kaolinite; I: illite; Ch: chlorite; I/S: I/S mixed clay; *S*% (I/S): I/S mixed-layer rate.

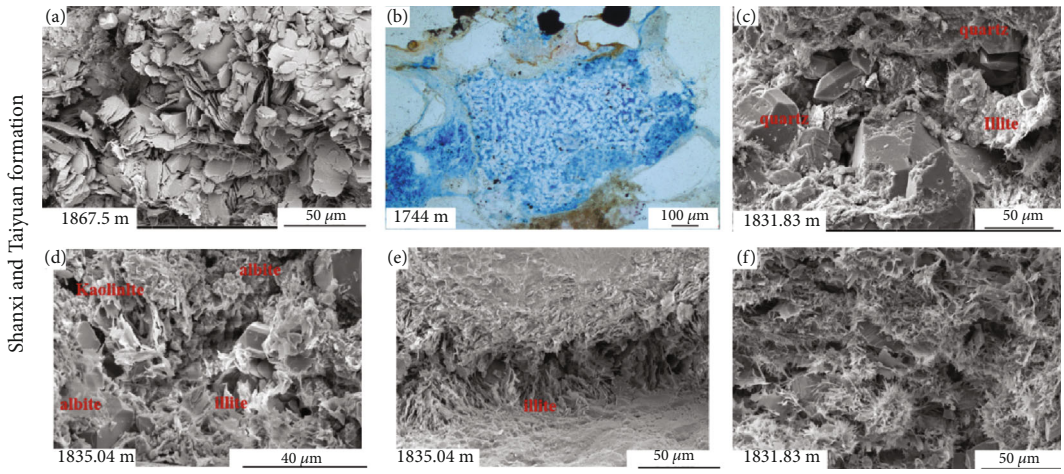

Figure 10: Shape characteristics of clay minerals in coal-measure sandstone. All sections were selected from wells LXD-2 and LXD-5, which are located in the central part of the study area, and the depths are marked. (a) Arranging loose flake kaolinite, intergranular pore development (Taiyuan Formation); (b) dissolution pores and worm-like kaolinite (Shanxi Formation); (c) authigenic quartz occurring with illite (Taiyuan Formation); (d) autogenous albite occurring together with filamentous illite and kaolinite (Taiyuan Formation); (e) bridging illite (Taiyuan Formation); (f) fibrous illite (Taiyuan Formation).

the transformation of smectite, in which the I/S mixed layer clay is the transition product of smectite to illite conversion, the honeycomb illite is transformed from the I/S mixed layer mineral, second, kaolinite and potassium feldspar in acidic conditions can occur in kaolinite Yili petrochemical (formula 1). The reaction can promote the dissolution of K-feldspar to form secondary pores and improve the physical properties of the reservoir, but the excess silica in the conversion process can provide a material source for siliceous cementation and has a certain negative impact on the reservoir properties. Scanning electron microscopy often shows fine authigenic quartz particles near illite. Illite does provide a source of siliceous cement when formed (Figures 10(c) and 10(d)). Luo et al. [27] studied the genetic origin of authigenic illite in the coal-bearing sandstone of the Xujiahe Formation in Sichuan. It is believed that the illite envelope can prevent the secondary increase in quartz during diagenesis, which has a positive impact on the protection of sandstone reservoir properties [27].

$$KAl_2Si_3O_8 + Al_2Si_2O_5(OH)_4 = KAl_3Si_3O_{10}(OH)_2 + 2SiO_2 + H_2O. \quad (1)$$

The I/S clay is a product of the conversion of smectite to illite, which is generally filled in the pores in the form of a honeycomb or attached to the edges of the granules. In the early days of diagenesis, smectites were altered by volcanic tuff or volcanic rock. As the diagenesis deepens, the smectite gradually transforms into illite, and the smectite content in the mixed minerals gradually decreases until the smectite is completely converted into illite.

(3) Carbonate cements

The carbonate mineral test results show that the carbonate cement content is 1.0% ~18.0%, and the average value is 5.5%. The content is higher in the vicinity of the limestone or the contact surface with the mudstone, the content of the sand body is lower, and no carbonate rock debris is found in the flake, indicating that the carbonate cement is mainly exogenous. Sandstone thin section identification results show that the carbonate cement in the study area mainly includes calcite (mainly iron calcite), iron dolomite, and siderite. Under the microscope, iron calcite cement filled the dwarf dissolved pores, and feldspar dissolved pores to enclose the quartz secondary enlarged edges (Figures 11(a) and 11(b)), and no signs of calcite dissolution were observed. This finding indicates that calcite cementation occurs in the later stage of diagenesis after the dissolution of lithic and feldspar and the secondary increase in quartz. Iron dolomite is dyed by ruthenium, which is light blue

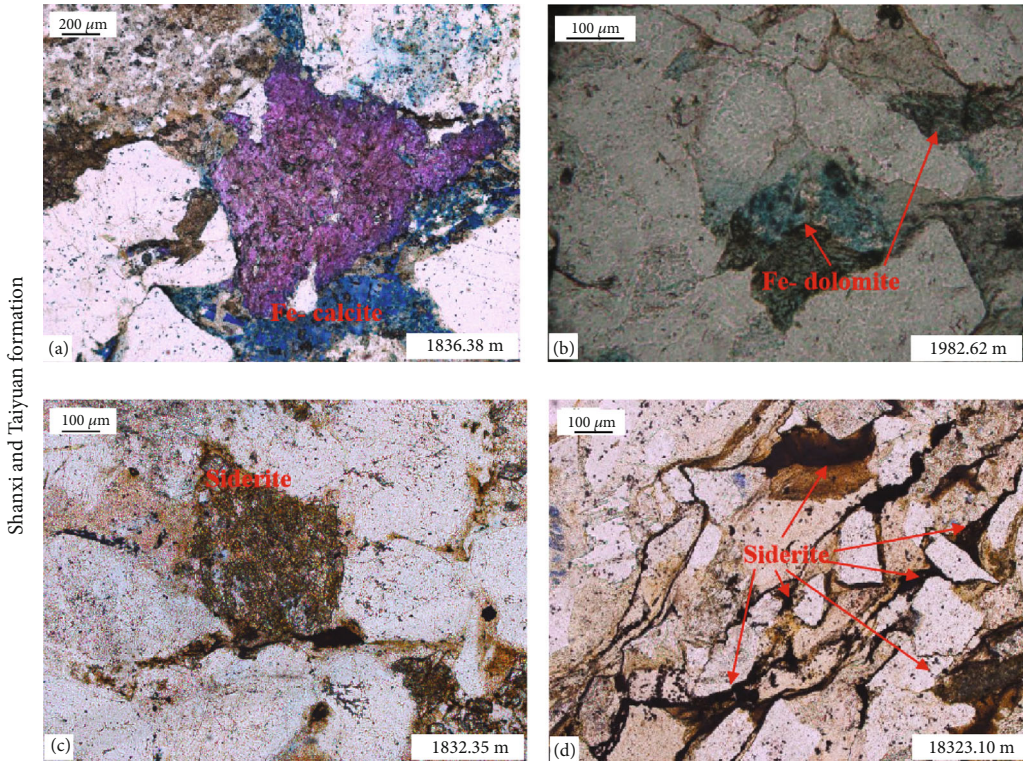

Figure 11: Characteristics of carbonate cements in coal-measure sandstone. All the sections were selected from the Taiyuan Formation of well LXD-2, which is located in the central part of the study area, and the depths are marked. (a) Fe-calcite fills the dissolution pores; (b) Fe-dolomite cementation; (c) clustered siderite; (d) siderite with a zonal distribution.

under the microscope, the shape is mostly rhomboid, and the surface is cleaved and fills the pores (Figure 11(b)). The siderite is generally a collection of mud crystals, which are in the form of a mass and spread in layers (Figures 11(c) and 11(d)). In the black mudstones of the Shanxi Formation and the Taiyuan Formation, which are close to the sandstone in the field profile, many of the siderites are also distributed along the bedding, and the genesis should be related; the content of dolomite cement is small, and it is mostly filled with fine crystals.

4.4.3. Dissolution. Dissolution is an important constructive diagenesis. Any debris, miscellaneous, or authigenic minerals in sandstone reservoirs can undergo different degrees of dissolution in certain diagenetic environments. The formation of secondary pores improves the porosity and permeability of sandstone, making it a good reservoir. According to the nature of the fluid causing dissolution, it can be divided into the dissolution of atmospheric leaching water and the dissolution of organic acids. The former is mainly for the dissolution of carbonic acid, the dissolution ability is small, and the organic acid has a strong ability to dissolve, which is the main reason for the formation of secondary pores [28, 29].

The dissolution of the study area is very developed and is a key factor for the development of tight sandstones in coal-bearing strata. Under the microscope, there are mainly feldspar, cuttings, and interstitial dissolution. In the Taiyuan Formation samples, quartz particles or secondary enlarged edges are observed (Figure 12).

(1) *Feldspar Corrosion.* The dissolution of feldspar is mostly carried out along the cleavage plane to form intragranular dissolved pores, and further, the entire feldspar particles are eroded away to form larger mold pores. In the mirror, almost no intact feldspar particles are seen, most of the kaolinite aggregates retain the shape of the feldspar particles, or the feldspar particles that have been dissolved along the cleavage surface are preserved by later calcite cementation. Therefore, dissolution is one of the reasons for the low content of sandstone in the area. After the feldspar is dissolved, only the dissolved material is transported out to maximize the reservoir physical properties. However, after feldspar is dissolved, clay minerals are formed in situ, which has many effects on the reservoir physical properties

(2) *Corrosion of the Interstitium.* The interstitium between the skeleton particles forms intergranular dissolved pores under the dissolution of the organic acid or enlarges the residual intergranular pores, or the interstitial alterations form a loosely arranged kaolinite aggregate. All of the above factors can increase the porosity of the reservoir and improve the permeability of the reservoir

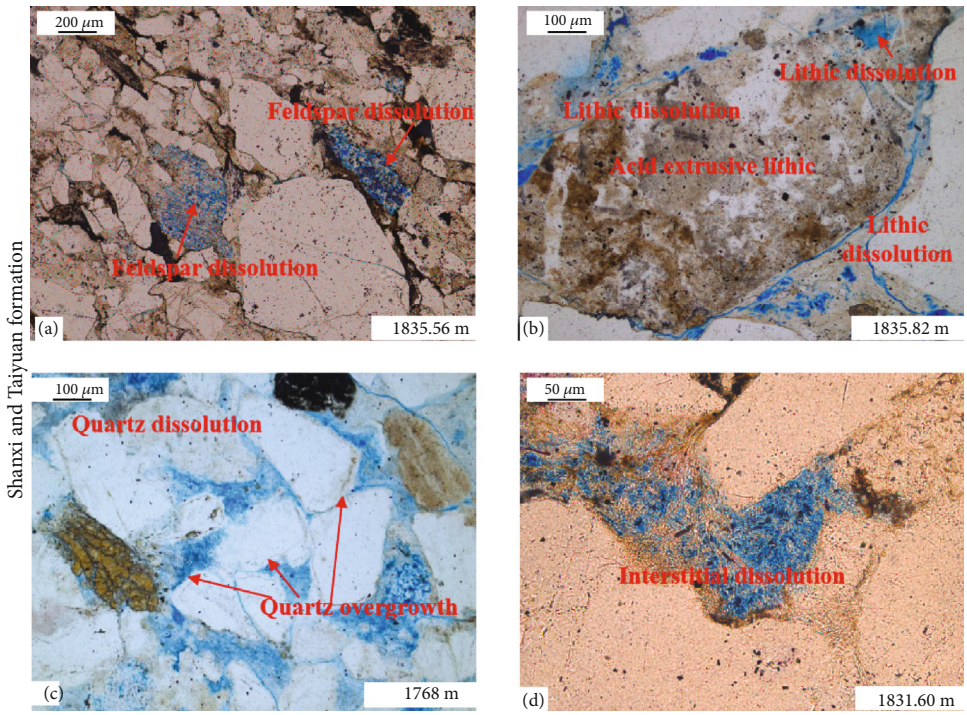

Figure 12: Characteristics of dissolution in coal-measure sandstone. All the sections were selected from the Taiyuan Formation of well LXD-2 and Shanxi Formation of well LXD-5, which is located in the central part of the study area, and the depths are marked. (a) Feldspar dissolution (Taiyuan Formation); (b) acid extrusive lithic dissolution (Taiyuan Formation); (c) quartz particle dissolution (Shanxi Formation); (d) interstitial dissolution (Taiyuan Formation).

(3) *Deposition of Cuttings*. Under the microscope, it can be seen that the cuttings are dissolved to form intergranular dissolved pores and mold pores

(4) *Corrosion of Quartz*. The dissolution of quartz particles in the sandstone of the Taiyuan Formation in the study area formed intragranular dissolved pores, and the secondary enlarged edges of quartz were eroded into a harbor shape, which increased the residual intergranular pores and improved the reservoir properties

4.5. Diagenetic Stages. The diagenetic evolution process of clastic rocks undergoes a series of complex diagenetic events, and different types of diagenesis occur in different diagenetic stages, which are arranged in chronological order to form the diagenetic sequence of a regional clastic rock. The division of the diagenetic stage and the establishment of diagenetic sequences are an important part of reservoir evaluation, which is of great significance for understanding the physical properties of clastic reservoirs, the evolution of pore structures, and the prediction of favorable reservoir space.

The classification marks of diagenetic stages are different in different diagenetic environments, "Code for the Division of Diagenetic Stages of Clastic Rocks" (SY/T 5477–2003) can be divided into freshwater–brackish water, diagenetic stage classification under acidic, and alkaline environments according to the acidity and alkalinity of pore water in clastic rocks [30]. During the diagenetic evolution of coal-bearing strata, the formation of organic acids makes the pore water of the clastic rocks acidic, and the diagenetic evolution of clastic rocks in the coal-bearing rock series is an acidic medium environment. According to the paleotemperature, illite content in the I/S mixed layer, authigenic mineral combination characteristics, skeleton particle contact type, and pore type, the diagenesis stage is divided into five stages: syngenetic rock stage, early diagenetic stage, medium diagenetic stage, late diagenetic stage, and surface-generated rock stage.

(1) Rock structure and pore type

The coal-bearing sandstone structure in the study area is dense, and the skeleton particles are closely arranged. The contact relationship is mainly line contact and concave-convex contact, and cracks are visible on the surface of the particles. The pore type is dominated by secondary pores, and the intergranular pores are less preserved.

(2) Clay mineral combination

The clay minerals in the coal-bearing sandstones in the study area are mainly kaolinite and illite. The proportion of smectite in the clay minerals of the I/S layer is approximately 20%. In the I/S clay, the proportion of smectite increases from Taiyuan to Shanxi, showing an increasing trend; the Taiyuan Formation is approximately 1.47%, and the Shanxi Formation is approximately 20%.

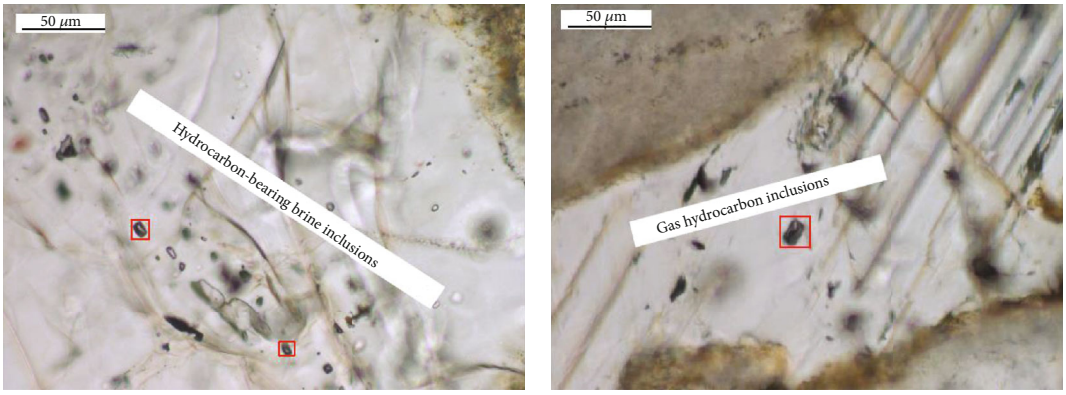

(a) (b)

Figure 13: Shape of fluid inclusions in coal-measure sandstones. (a) Hydrocarbon-bearing brine inclusions in quartz grain cracks; (b) carbon dioxide gaseous hydrocarbon inclusions in calcite fractures.

(3) Spontaneous mineral distribution

In the sandstone sample sheets of the whole study area, the secondary increase in quartz is very developed, and the secondary growth of the two phases is common. The secondary quartz of the local sample is especially developed, so the quartz particles are mosaic. Compared with the stone box formation, there are more carbonate cements, mainly iron calcite, iron dolomite is visible, and siderite is developed in different layers.

(4) Fluid inclusion uniform temperature

The formation of fluid inclusions in sandstone is closely related to the diagenesis process. Information on the composition and temperature of geological fluids in the original diagenesis process is an important means to study the evolution process of diagenesis. In the coal-sedimentary sandstones of the study area, a large number of fluid inclusions are developed in the secondary marginal, healing, and carbonate cements of quartz, mainly in brine inclusions and hydrocarbon inclusions, which are distributed in a beaded or strip shape (Figure 13).

The uniform temperature of fluid inclusions in coal-bearing sandstones in the study area is mainly distributed between 20°C and 130°C, showing two concentrated distribution intervals: 28°C ~38°C and 104°C ~130°C, indicating that there are two stages of geological fluids in the diagenetic evolution process. Among them, in the interval of 28°C ~38°C, it is mainly the fluid inclusions in the fracture zone of calcite, which is dominated by brine inclusions, indicating that the secondary increase of quartz in this stage is formed in the stage A of the diagenetic stage; in the interval of 104°C ~130°C, it is mainly the liquid hydrocarbon inclusions and a small amount of accompanying brine inclusions in the second-stage secondary and healing joints of quartz, indicating that the secondary quartz enlargement in this period is also formed in the stage A of the diagenetic stage.

According to the comprehensive evaluation and analysis of sandstone sample structure, pore development, authigenic mineral distribution, mixed layer ratio of I/S clay, and uniform temperature of fluid inclusions, the coal-bearing sandstone in the study area has entered the meso-rock stage.

4.6. Diagenesis Sequence. During the evolution process of litharenite and feldspathic litharenite in the study area, the destructive effects of compaction, cementation, and constructive effects of dissolution are mainly experienced. Suppose the diagenesis sequence is consolidation diagenesis—compaction—cementation—dissolution (Figure 14). Conversely, when consolidating in diagenesis, the primary porosity of the litharenite is 31.3%; after that, the compaction lost 23.8%, the cementation loss is 7.4%, the dissolution increased by 6.7%, and the final porosity is 6.8%.

The primary porosity of feldspathic litharenite, consolidating diagenesis, is 27.8%, compaction and cementation lose all pores, dissolution increases the porosity by 2.3%, and the final porosity is 2.3% (Table 3).

5. Discussions

The sedimentary environment affects the composition of sandstone, controls the quality of the primary reservoir, and then affects the diagenetic evolution and later transformation of the reservoir. The effects of diagenesis on the physical properties of sandstone reservoirs can be divided into three categories. The first type is destructive, changing the pore structure of sandstone and reducing the porosity and permeability of sandstone, making it more compact, mainly including compaction and cementation. The second type is constructive. During the diagenesis process, new pores are generated, and the porosity and permeability of the reservoir are improved, mainly with dissolution. The third type is protective, which can increase the strength of the sandstone reservoir skeleton particles during diagenesis, thereby reducing or slowing the damage of the sandstone reservoir porosity and permeability by destructive diagenesis. To a certain extent, this type is a kind of protection for reservoir porosity and permeability, mainly for cementation around sandstone particles, such as early ring-shaped chlorite cement.

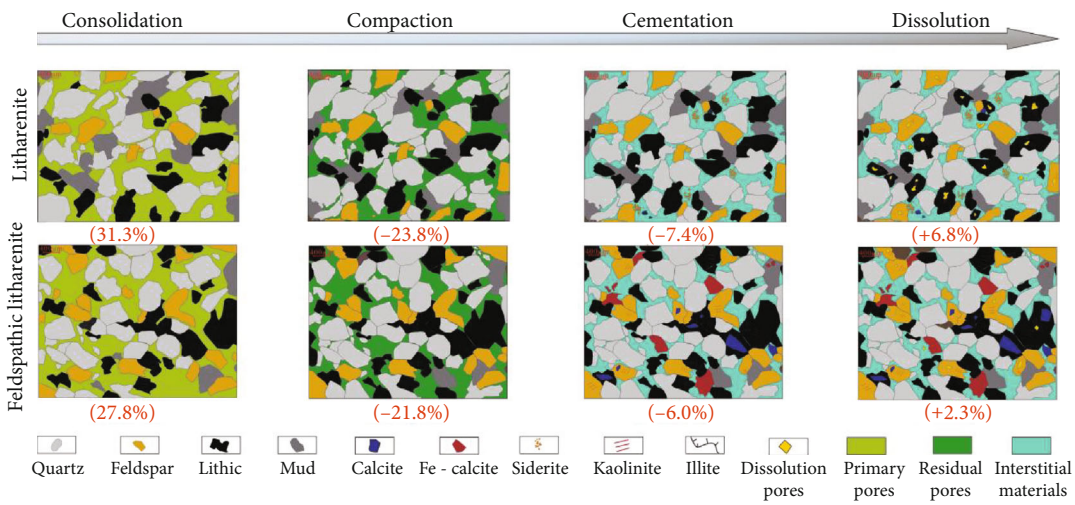

Figure 14: Diagenetic sequence of lithic arenite and feldspathic lithic arenite.

Table 3: Pore evolution process of lithic arenite and feldspathic lithic arenite.

Sandstone type	Primary porosity (%)	Compaction porosity loss (%)	Cementation porosity loss (%)	Dissolution increased porosity (%)
Lithic arenite	31.3	23.8	7.4	6.8
Feldspathic lithic arenite	27.8	21.8	6.0	2.3

The Taiyuan Formation and the Shanxi Formation sandstones in the study area are developed in coal-bearing strata and are affected by coal-bearing organic acid fluids during diagenesis. The presence of organic acids does not simply enhance the strength of the dissolution and improve the porosity and permeability of the reservoir. At different stages of diagenetic evolution, the effects of organic acids on diagenesis and reservoir properties are different.

5.1. Sedimentary Environment Effect on Primary Reservoir Quality. Tight sandstones of the Taiyuan Formation in the study area are mainly developed in barrier islands and tidal phases and are affected by tides (Figure 15). These sandstones are mainly medium-coarse-grained mud-bearing lithic arenite and coarse-grained and feldspathic lithic arenite, rock sorts medium, and the roundness is low; the delta phase of the Shanxi Formation has relatively weak hydrodynamic force, and the main deposits are extremely fine: fine-grained feldspathic lithic arenite, rock sorting is medium, and the roundness is low (Figure 15). In the Taiyuan Formation, sandstone has low maturity, relatively good pore structure, and large porosity, and its primary reservoir quality is better, but lower quartz fragments result in a weak resistance to compaction, and high feldspar and lithic contents lay the foundation for dissolution. In contrast, the Shanxi Formation has poor primary reservoir quality, strong compaction resistance, and weak dissolution.

5.2. Compaction and Cementation Effect on Reservoir Physical Properties. Compaction is a typical destructive diagenesis. Under the pressure of the overlying strata, the sandstone skeleton particles are rearranged and become increasingly compact, resulting in a decrease in reservoir porosity and permeability. Compaction, including mechanical compaction and chemical compaction, is an irreversible effect that increases with depth. The coal-bearing sandstone in the study area experienced a maximum burial depth of 1900 m. The particles were in contact with the bumps, indicating that the compaction experienced was strong. The primary pores of the Shanxi Formation sandstone were destroyed. The Taiyuan Formation sandstone retained only some residual intergranular pores.

Cementation is mainly wrapped at the edge of the particles or filled in the pores. The influence on the physical properties of the reservoir is complicated. The stage or occurrence state of the reservoir is different, and the impact on the reservoir is completely different. Most of the cementation blocks the pores, reduces the porosity and permeability of the reservoir, and causes damage to the reservoir. The secondary sandstone quartz in the Taiyuan Formation has a large number of secondary cementations, which reduces the intergranular pore volume, makes the pore throat smaller, and reduces the porosity and permeability of the sandstone reservoir. There is also a favorable side for the general secondary increase in quartz particles, which makes the sandstone particles mosaic, enhances the anticompacting ability between the particles, and retains some residual intergranular pores. To a certain extent, it has a protective effect on reservoir properties.

5.3. Dissolution Effect on Reservoir Property. Dissolution is a typical constructive diagenesis, producing secondary pores during diagenesis, which greatly improves reservoir physical

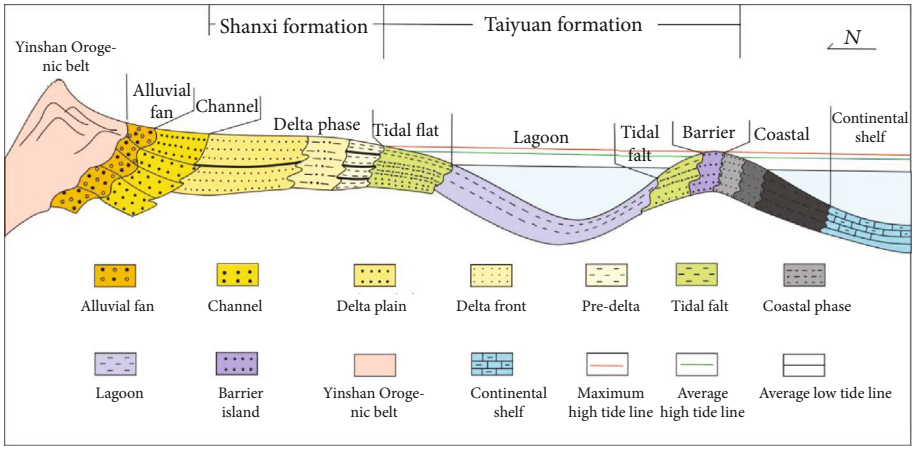

Figure 15: Sedimentary pattern of Linxing area.

properties. The coal-bearing strata have high organic matter content. The organic matter of the Shanxi Formation matures in middle diagenetic phase A and releases a large amount of organic acids, which causes the sandstone in this area to strongly dissolve and produce a large number of secondary pores, which improves the physical properties of the reservoir in the study area. The dissolution of quartz particles in the Taiyuan Formation sandstone in the B-stage alkaline water medium in the middle diagenetic stage also has a positive impact on reservoir physical properties. The statistical results of the cast thin slices show that the existing pores in the Shanxi Formation sandstone are all secondary pores, and there are no residual intergranular pores. The secondary pores in the Taiyuan Formation sandstone account for approximately 95.6% of the total pores, and the residual intergranular pores only account for 4.4%. Therefore, dissolution is a key factor in the development of coal-bearing sandstones in the region.

5.4. Sedimentary Environment and Diagenesis Comprehensively Affect Reservoir Characteristics. The sedimentary environment and diagenesis have an important influence on tight reservoirs. The sedimentary environment mainly controls the primary reservoir conditions, which in turn affects the evolution of diagenesis and the transformation of reservoirs. The sedimentary environment has an important influence on the composition of clastic rocks. Generally, with a strong hydrodynamic force, the clastic materials deposited in areas have a large grain size, low maturity, moderate deviation in sorting, and low quartz content, and the roundness is mainly angular or subangular-subcircular, so the original quality of the reservoir is relatively good. However, under weak hydrodynamic conditions, after long-term transportation, the debris components have good maturity, fine particle size, and preference for sorting. The particles are mainly subcircular or subangular-subcircular, the primary pores are poor, and the primary quality of the reservoir is poor. The tight sandstones formed in the barrier islands and tidal flats have large and many primary pores, but under the combined influence of burial depth and rigid minerals, there are almost no residual pores in the study area. However, due to the relatively high contents of feldspar and rock fragments in barrier islands and tidal flats with turbulent water environments, dissolution is relatively developed, secondary pores are developed, and the porosity and permeability conditions are improved. Therefore, the quality of the reservoir of the Taiyuan Formation is better.

6. Conclusions

The tight sandstones of the coal-bearing in the study area are mainly feldspathic lithic sandstone and lithic sandstone. The Taiyuan Formation is dominated by lithic sandstone and feldspathic lithic sandstone, followed by feldspathic lithic sandstone. The average porosity is 6.9%, and the average permeability is 0.12 mD. The Shanxi Formation is dominated by lithic quartz sandstone and feldspathic lithic sandstone with an average porosity of 2.3% and an average permeability of 0.083 mD, all of which are tight sandstone reservoirs.

The pore type is dominated by secondary dissolution pores, containing a small number of primary pores, and fractures are not developed. The pore structure is poor, and the pore throat radius distribution is narrow, mainly between 0.0025 μm and 1.048 μm. The capillary pressure curves of the Taiyuan Formation sandstone are mainly of low displacement pressure, high mercury saturation, and mercury withdrawal efficiency, while the Shanxi Formation sandstone is mainly of high displacement pressure, low mercury saturation, and withdrawal efficiency.

The diagenetic evolution of sandstone in the Shanxi Formation is in stage A of meso-diagenesis, and the Taiyuan Formation has entered stage B of meso-diagenesis. The development of siliceous cement in the Taiyuan Formation sandstone enhanced the sandstone's resistance to compaction and retained some residual intergranular pores. The pore types in the Shanxi Formation sandstone are all secondary pores. The secondary pores in the Taiyuan Formation sandstone account for approximately 90% of the total pores.

The structural maturity of the lithic sandstone in the tidal flat and barrier phases is relatively low, the original reservoir quality is better, and dissolution is relatively developed. The feldspar lithic sandstone in the delta front deposition phase has a high structural maturity, the original reservoir quality is poor, and the dissolution development is weak.

Data Availability

Data has been included in the manuscript.

Conflicts of Interest

None of the authors have any conflicts of interest.

Acknowledgments

This study was supported by the National Science Foundation of China (Grant no. 42072194) and the Major National Science and Technology Project of China (nos. 2016ZX 05066001-002 and 2017ZX05064-003-001), and we thank the Research Institute of Petroleum Exploration and Development and Tarim Oil Co. of CNPC for providing testing samples and our colleagues for beneficial suggestions.

References

[1] Y. Li, J. H. Yang, Z. J. Pan, S. Meng, K. Wang, and X. Niu, "Unconventional natural gas accumulations in stacked deposits: a discussion of Upper Paleozoic coal-bearing strata in the east margin of the Ordos Basin, China," *Acta Geologica Sinica (English Edition)*, vol. 93, no. 1, pp. 111–129, 2019.

[2] J. Li, X. Zhang, J. Tian, Q. Liang, and T. Cao, "Effects of deposition and diagenesis on sandstone reservoir quality: a case study of Permian sandstones formed in a braided river sedimentary system, northern Ordos Basin, northern China," *Journal of Asian Earth Sciences*, vol. 213, p. 104745, 2021.

[3] Y. Li, Z. Wang, Q. Gan, X. Niu, and W. Xu, "Paleoenvironmental conditions and organic matter accumulation in Upper Paleozoic organic-rich rocks in the east margin of the Ordos Basin, China," *Fuel*, vol. 252, pp. 172–187, 2019.

[4] Y. Li, D. Tang, P. Wu et al., "Continuous unconventional natural gas accumulations of Carboniferous-Permian coal-bearing strata in the Linxing area, northeastern Ordos basin, China," *Journal of Natural Gas Science and Engineering*, vol. 36, pp. 314–327, 2016.

[5] Y. Li, A. Fan, R. Yang, Y. Sun, and N. Lenhardt, "Sedimentary facies control on sandstone reservoir properties: a case study from the Permian Shanxi Formation in the southern Ordos basin, Central China," *Marine and Petroleum Geology*, vol. 129, p. 105083, 2021.

[6] X. Zhang, H. Zhu, B. Lei, J. Zhang, D. Wang, and J. Yong, *Sedimentary and Diagenetic Facies of Tidal Flat in Epeiric Sea and Its Related Descriptive Method-a Case of Ma51-4 Submember in Jingbian Gas Field of Ordos Basin, China*, Petroleum, 2020.

[7] S. M. Z. Aid, "Provenance, diagenesis, tectonic setting and geochemistry of Rudies sandstone (Lower Miocene), Warda Field, Gulf of Suez, Egypt," *Journal of African Earth Sciences*, vol. 66, pp. 56–71, 2012.

[8] M. Liu and X. Chen, "Diagenesis and reservoir quality of deep-lacustrine sandy-debris-flow tight sandstones in Upper Triassic Yanchang Formation, Ordos Basin, China: implications for reservoir heterogeneity and hydrocarbon accumulation," *Journal of Petroleum Science and Engineering*, vol. 202, p. 108548, 2021.

[9] H. Rong, Y. Jiao, L. Wu, X. Zhao, M. Cao, and W. Liu, "Effects of igneous intrusions on diagenesis and reservoir quality of sandstone in the Songliao Basin, China," *Marine and Petroleum Geology*, vol. 127, article 104980, 2021.

[10] G. Wang and W. Um, "Mineral dissolution and secondary precipitation on quartz sand in simulated Hanford tank solutions affecting subsurface porosity," *Journal of Hydrology*, vol. 472–473, pp. 159–168, 2012.

[11] W. Wei, X. Zhu, K. Azmy, S. Zhu, M. He, and S. Sun, "Depositional and compositional controls on diagenesis of the mixed siliciclastic-volcaniclastic sandstones: a case study of the Lower Cretaceous in Erennaoer Sag, Erlian Basin, NE China," *Journal of Petroleum Science and Engineering*, vol. 188, p. 106855, 2020.

[12] J. Qiao, J. Zeng, S. Jiang, and Y. Wang, "Impacts of sedimentology and diagenesis on pore structure and reservoir quality in tight oil sandstone reservoirs: implications for macroscopic and microscopic heterogeneities," *Marine and Petroleum Geology*, vol. 111, pp. 279–300, 2020.

[13] X. Gao, S. Meng, P. Wu, X. Niu, P. Qiao, and D. Elsworth, "Diagenetic sequences of continuously deposited tight sandstones in various environments: a case study from upper Paleozoic sandstones in the Linxing area, eastern Ordos basin, China," *AAPG Bulletin*, vol. 103, p. 2757, 2019.

[14] X. Guo and W. Mao, "Division of diagenesis and pore evolution of a Permian Shanxi shale in the Ordos Basin, China," *Journal of Petroleum Science and Engineering*, vol. 182, article 106351, 2019.

[15] H. Li, Q. Wang, X. Du, X. Yang, and H. Zhu, "Residual carboxylic acids (nonpyrolytic) in mudstones and their implications and constraints on sandstone diagenesis, Bozhong Depression, offshore Bohai Bay Basin, East China," *Organic Geochemistry*, vol. 151, article 104149, 2021.

[16] D. Wu, H. Li, L. Jiang et al., "Diagenesis and reservoir quality in tight gas bearing sandstones of a tidally influenced fan delta deposit: the Oligocene Zhuhai Formation, western Pearl River Mouth Basin, South China Sea," *Marine and Petroleum Geology*, vol. 107, pp. 278–300, 2019.

[17] L. Zhu, K. Wu, and Y. Yang, "Study on controlling factors and depositional model of sedimentary facies in the fifth member of the Ordovician Majiagou formation, Linxing-Shenfu area in the Ordos Basin," *The Journal of Geology*, vol. 42, 2018.

[18] J. Wang, S. Wu, Q. Li, and S. Xiao, "Controls of diagenetic alteration on the reservoir quality of tight sandstone reservoirs in the Triassic Yanchang formation of the Ordos Basin, China," *Journal of Asian Earth Sciences*, vol. 200, article 104472, 2020.

[19] Y. Xing, *Sedimentary Characteristics of Carboniferous Permian and Its Control on Reservoir in Linxing Area*, Shandong University of Science and Technology, 2018.

[20] Y. Xing, Y. Lin, X. Li, X. Ma, and Y. Shu, *Sedimentary Microfacies and Its Control on Sand Bodies in the Second Member of Taihe Formation in Linxing Area*, Energy and Environmental Protection, 2017.

[21] C. Xue, J. Wu, J. Zhong et al., "Characteristics of reservoir variability of transitional and continental shale, Shanxi

Formation, Linxing and Shenfu area, Northeastern Ordos Basin," *Journal of Central South University (Science and Technology)*, vol. 51, 2020.

[22] F. Zhang, Z. Jiang, W. Sun et al., "A multiscale comprehensive study on pore structure of tight sandstone reservoir realized by nuclear magnetic resonance, high pressure mercury injection and constant-rate mercury injection penetration test," *Marine and Petroleum Geology*, vol. 109, pp. 208–222, 2019.

[23] J. Chen, J. Yao, Z. Mao et al., "Sedimentary and diagenetic controls on reservoir quality of low-porosity and low-permeability sandstone reservoirs in Chang101, upper triassic Yanchang Formation in the Shanbei area, Ordos Basin, China," *Marine and Petroleum Geology*, vol. 105, pp. 204–221, 2019.

[24] C. Su, F. Song, L. Qiu, and W. Zhang, "Diagenetic evolution and densification mechanism of the Upper Paleozoic tight sandstones in the Ordos Basin, Northern China," *Journal of Asian Earth Sciences*, vol. 205, article 104613, 2021.

[25] N. Vaisblat, N. B. Harris, K. Ayranci et al., "Compositional and diagenetic evolution of a siltstone, with implications for reservoir quality; an example from the Lower Triassic Montney Formation in western Canada," *Marine and Petroleum Geology*, vol. 129, article 105066, 2021.

[26] B. Q. Ma, S. M. Chen, W. L. Yan et al., "Pore structure evaluation of low permeability clastic reservoirs based on sedimentation diagenesis: A case study of the Chang 8 reservoirs in the Zhenbei region, Ordos Basin," *Journal of Petroleum Science and Engineering*, vol. 196, pp. 920–4105, 2021.

[27] L. Luo, W. B. Meng, J. Gluyas et al., "Diagenetic characteristics, evolution, controlling factors of diagenetic system and their impacts on reservoir quality in tight deltaic sandstones: Typical example from the Xujiahe Formation in Western Sichuan Foreland Basin, SW China," *Marine and Petroleum Geology*, vol. 103, pp. 231–254, 2019.

[28] Y. Abe, A. Iizuka, H. Nagasawa, A. Yamasaki, and Y. Yanagisawa, "Dissolution rates of alkaline rocks by carbonic acid: influence of solid/liquid ratio, temperature, and CO_2 pressure," *Chemical Engineering Research and Design*, vol. 91, no. 5, pp. 933–941, 2013.

[29] C. Liu, H. Rong, S. Chen, J. Jia, Y. Tang, and Y. Deng, "Occurrence, mineralogy and geochemistry of fracture fillings in tight sandstone and their constraints on multiple-stage diagenetic fluids and reservoir quality: an example from the Kuqa foreland thrust belt, Tarim Basin, China," *Journal of Petroleum Science and Engineering*, vol. 201, p. 108409, 2021.

[30] F. X. Ying, D. B. He, and Y. M. Long, *Code for the Division of Diagenetic Stages of Clastic Rocks (SY/T 5477–2003)*, Petroleum Industry Press, 2003.

Hindawi
Geofluids
Volume 2021, Article ID 4023704, 15 pages
https://doi.org/10.1155/2021/4023704

Research Article

A New Quantitative Approach for Element-Mineral Determination Based on "EDS (Energy Dispersive Spectroscopy) Method"

Peigang Liu,[1,2] **Zhelin Wang**,[2,3] **and Zhiqiang Zhang**[2]

[1]*College of Computer Science and Technology in China University of Petroleum (East China), Qingdao 266580, China*
[2]*School of Earth and Space Sciences in Peking University, Beijing 100871, China*
[3]*SINOPEC Petroleum Exploration and Production Research Institute, Beijing 100083, China*

Correspondence should be addressed to Peigang Liu; dongfangwy@126.com

Received 7 May 2021; Revised 24 July 2021; Accepted 29 July 2021; Published 29 August 2021

Academic Editor: Yanjun Meng

With the continuous development of hydrocarbon exploration, how to efficiently, economically, accurately, and comprehensively obtain mineral species, composition, and structure and diagenesis information has become one of the hot topics in both the academia and industry. By scanning electron microscopy (SEM) and energy dispersive spectroscopy (EDS), a new method of qualitative mineral identification and quantitative measurement is established. Typical tight sandstone reservoir rock samples in the Ordos Basin are selected; through the element surface scanning image of "mineral element composition" and "pixel element combination", mineral types are distinguished, and mineral parameters such as types, characteristics, and content are rapidly and accurately determined. Meanwhile, such results achieved via the new method are compared with conventional XRD and TIMA methods. The results show that the new method exhibits several advantages: cost advantages compared to XRD experiment analysis technology and TIMA system and ability to analyze low content minerals which XRD techniques are hard to identify; it allows quantitative characterization on the phenomenon of mineral miscibility, which is of great significance to explore the mineral diagenetic evolution.

1. Introduction

The rapid development of oil and gas exploration requires more detailed study of the tight reservoirs. Qualitative analyses and quantitative measurements of mineral compositions within the tight reservoir are of great significance to practical application. The identification of rocks and minerals can provide accurate and comprehensive information including mineral composition and structural characteristics and diagenesis and allows revealing the reservoir heterogeneity and pore structure [1–4].

At present, the methods of qualitative observation of minerals include the optical microscope method, scanning electron microscopy, and infrared spectroscopy [5–7]. The optical microscopy method provides comprehensive analysis of mineral characteristics and mutual relationships. However, because of the limitation of resolution, it can do little in terms of determining the qualitative analysis of small particles, especially micro-nanoscale mineral morphology and structural characteristics [8–10]. The scanning electron microscopy method focuses on the surface morphology of nanometer/micron scale minerals via secondary electronic imaging [11]. The scanning electron microscope and the X-ray methods are often combined to realize the comprehensive analysis of the mineral components and microstructure [12, 13]. The infrared spectrum method is to obtain the structure information of the mineral molecules and obtain composite database by establishing the infrared spectrum diagram. This method has been used to qualitatively characterize the minerals, to study the composition of oil and gas inclusion, and the temperature

of the abundance of the oil and gas [14–18]. The laser Raman spectroscopy provides accurate and rapid measurement of the fluid components in the rock by using the laser Raman spectrometer [19–23]. It is, however, difficult to accurately determine the mineral type and calculate the mineral content, yet it can only analyze the mineral composition elements. Therefore, to make quantitative characterization of minerals/elements, to combine the Raman spectrometer and other methods and instruments has become one of the key development trends of Raman spectroscopy [24–27].

X-ray diffraction (XRD) is the main method for quantitative mineral analysis. According to the positive correlation between diffraction intensity and content of minerals, mineral content in rocks can be rapidly and accurately analyzed [28]. For instance, X-ray diffraction can be used to rapidly analyze the content of calcite and dolomite in carbonate rocks [29], study the order degree of dolomite [30], and identify the minerals in phyllite and kimberlite, so as to evaluate the deposit [31, 32]. However, close symbiosis and associated phenomena of different minerals in rocks exist, and it is susceptible to the influence of diffraction peaks of other minerals when the content of measured minerals is low [33]. In addition, the mineral morphology cannot be directly observed by using the X-ray diffraction method, and the change of some mineral compositional structure could lead to errors in the analysis results [9].

Mineral identification methods that combine qualitative observation with quantitative analysis include mineral dissociation analysis (MLA) [7, 34], quantitative evaluation of minerals by scanning electron microscopy (QEMSCAN), and automatic mineral characterization quantitative analysis system (AMICS) ([6, 35–37]). This method establishes a set of mineral quantitative analysis system through scanning electron microscopy and energy spectrometer and uses the backscattered electron (BSE) image which can reflect the difference of mineral phase composition and X-ray energy spectrum rapid analysis technology to accurately identify minerals [7, 38]. Some scholars used INCA software on OXFORD spectrometer to establish a synthetic energy spectrum database and retrieval system for minerals and used it to identify minerals [39]. Such methods have already realized quantitative identification of rare earth minerals which conventional identification methods are difficult to accomplish, yet problems such as high measurement cost and difficulty in application and promotion still exist [40–48].

Aiming at the existing disadvantages regarding the qualitative identification and quantitative measurements of minerals, the objectives of this paper are to introduce a new method of mineral identification and measurement based on SEM and EDS, and it is named "EDS method." This method allows identification of minerals in the microsurface area using the element surface scanning image of "mineral element composition" and "pixel element combination" and can determine accurately and quickly the mineral types, mineral characteristics, and mineral content. This method also enables qualitative identification and quantitative characterization of minerals that affect pore throat system, and it has been applied to the Triassic Yanchang Formation, Ordos Basin, to analyze the mineral composition and content.

2. Methodology

Existing literature suggests that the rock mineral identification has evolved to a trend that requires both qualitative morphological determination and quantitative structural and principle analyses (e.g., Liao 2018). Accordingly, with the rapid development of equipment, the Fourier infrared spectrometer, X-ray diffractometer, Raman spectrometer, and scanning electron microscope have been applied to mineral identification [6, 9, 34].

The EDS method proposed in this paper is based on surface micro area identification via SEM-EDS image "mineral element composition" and "pixel element association" (Table 1): mineral element association: based on chemical formula discrimination of basic minerals; pixel element association: based on scanning every single pixel "one and only" element association.

The procedures are as follows (Figure 1):

(1) Draw element content distribution map. Samples and local positions are selected, holographic surface scan is run using the OXFORD INCA X-MAX50 250+, and distribution map of basic element composition and element content are generated

(2) Determine pixel element distribution. The distribution map is divided into pixel points, according to the relative mineral element content distribution, and the mineral type of each point is determined

(3) Run new algorithm of mineral identification. Based on the skeleton and element associations of clay minerals, the mineral identification is realized based on "pixel element association" method

(4) Run denoise and correction process. After the mineral type is identified, the skeleton mineral is denoised using the marginal examination method and compared to the original image so that they are in line with the actual situation

On the basis of "mineral element association," "impurity element and substitute element," and "statistics of energy spectrum point," considering all the possible element associations (Table 2), the mineral identification is realized.

In order to achieve a better recognition effect, it is necessary to take full consideration of the "one and only" element combinations at pixel points when using the new method, including (1) the alternative elements that may exist in some mineral element combinations, such as the alternative elements Mg and Fe in kaolinite ($Al_4[Si_4O_{10}](OH)_8$); (2) when the sample is not oil-washed, the influence of element C should be considered due to the existence of residual oil in clay minerals and some skeleton minerals; (3) the analysis should be carried out according to the actual situation of the energy spectrum points of each mineral. In the process of miscibility of different minerals, impurity elements may exist, such as potassium feldspar ($K[AlSi_3O_8]$) and albite ($Na[AlSi_3O_8]$) in the perthite, yet mixing of Ca element may exist.

Table 1: Rock mineral major and associated and impurity element.

Type	Mineral	Chemical formula	Major element	Associated/impurity element
Oxide	Quartz	SiO_2	Si, O	C
Silicates carbonate	Potash feldspar	$K[AlSi_3O_8]$	K, Al, Si, O	Na, C
Silicate	Plagioclase	$Na[AlSi_3O_8]$ $Ca[Al_2Si_2O_8]$	Na/Ca, Al, Si, O	C
	Calcite	$Ca[CO_3]$	Ca, C, O	Si, Fe
Carbonate	Dolomite	$CaMg[CO3]_2$	Ca, Mg, C, O	Si, Fe
	Siderite	$Fe[CO_3]$	Fe, C, O	/
Sulfide	Pyrite	$Fe[S_2]$	Fe, S	C
Silicate	Illite	$K_{0.75}(Al_{1.75}MgFe)[Al_{0.5}Si_{3.5}O_{10}](OH)_2$	K, Mg, Fe, Al, Si, O	Na, C
Silicate	Chlorite	$(Mg_3/Al_3/Fe_3)[Si_4O_{10}](OH)_2$	Mg, Fe, Al, Si, O	C
Silicate	Smectite	$E_x(B2O)_4\{(Al_{2-x},Mg_x)_2[(Si,Al)_4O_{10}](OH)_2\}$	Mg, Al, Si, O	Na, Ca, K, C
Silicate	Kaolinite	$Al_4[Si_4O_{10}](OH)_8$	Al, Si, O	Mg, Fe, C
Pore	Residual oil	C	O	

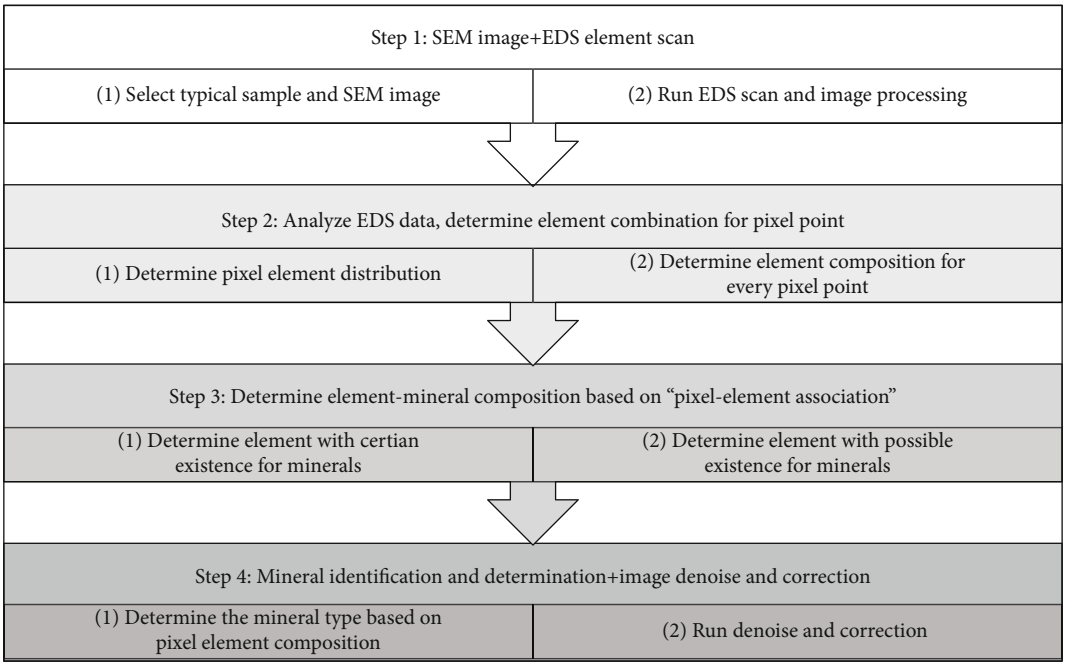

Figure 1: Technical process of EDS element-mineral identification.

3. Results

3.1. SEM-EDS Element Scan Results. Planar scanning is run through the scanning electron beam on the specimen surface observation area, and different element displays on the screen in different colors, respectively, showing the distribution of the image. It can also correspond to acquisition of secondary electron image, which is intuitive and clear—the more points, the higher brightness and thus the higher indicator element content. Although the accuracy of quantitative analysis of light elements by this method is not ideal at present, it is still of practical significance to take the quantitative analysis result as the data of relative comparison. The back and bottom noise of surface scanning will also produce a small amount of bright spots, which cannot be distinguished from low-content elements. The sample surface is required to be smooth, and the thin slice sample after cutting should be selected and treated with soot blowing and cadmium spraying. As shown in Figure 2, the SEM scanning electron microscope image and local mineral characteristics of sample 284-3-9-Z were selected, and EDS holographic scanning was performed.

According to the distribution of holographic scanning results of common elements, the relative contents and areal distribution of K, Na, Ca, Mg, Al, Si, Fe, C, and O were obtained (Figure 3). Then, according to the new SEM-EDS element-mineral determination method, the common skeleton minerals and clay minerals are identified and displayed.

Table 2: Element associations for new mineral identification method.

No.	Minerals	Element with certain existence	Elements with possible existence
1	Quartz	Si, O	C
2	Potash feldspar	K, Al, Si, O	Na, C
3	Albite	Na, Al, Si, O	Ca, C
4	Anorthite	Ca, Al, Si, O	C
5	Calcite	Ca, C, O	Si, Fe
6	Dolomite	Ca, Mg, C, O	Si, Fe
7	Siderite	Fe, C, O	/
8	Pyrite	Fe, S	C
9	1 Illite 1	K, Mg, Fe, Al, Si, O	Na, C
10	2 Illite 2	Na, Mg, Fe, Al, Si, O	K, C
11	Chlorite	Mg, Fe, Al, Si, O	C
12	Smectite	Mg, Al, Si, O	Na, Ca, K, C
13	Kaolinite	Al, Si, O	Fe, C
14	Pore	C	O

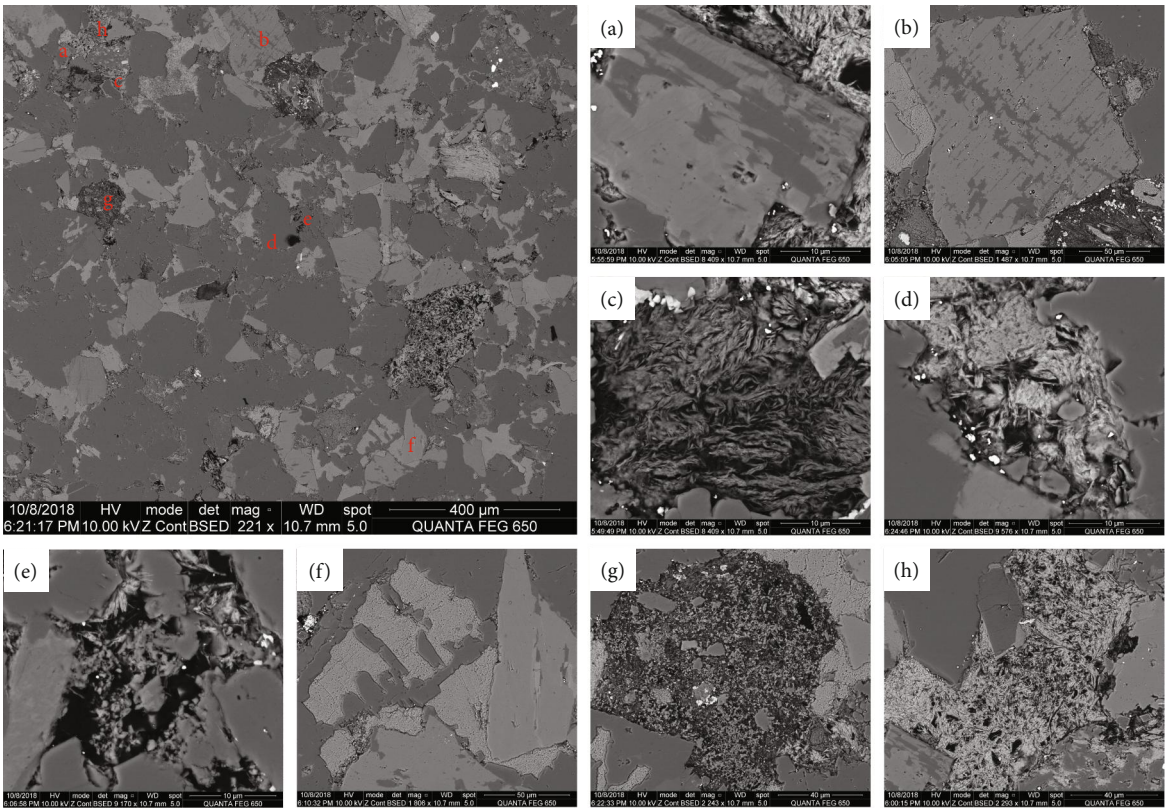

Figure 2: Sample 284-3-9-Z SEM-EDS holographic scanning and local mineral features. (a, b) Miscible potassium and sodium feldspar; (c, d) clay minerals; (e) minerals and pores; (f) dissolved potassium feldspar which is filled with calcite; (g, h) mixed mineral debris in pores.

3.2. Mineral Identification Results and Verification. Based on the element associations and content relationship discussed above, mineral type identification and mineral content determination are realized using the new planar scanning method (Figure 4). First, the major mineral of the selected sample is determined, including the skeleton mineral (quartz, potash feldspar, albite, and carbonate minerals) and clay minerals (illite, chlorite, smectite, kalinite, etc.). In addition, the mineral content planar distribution is analyzed, while the rest represents pores.

The rock skeleton mineral is characterized by smooth and complete surface, such as quartz, potash feldspar, albite,

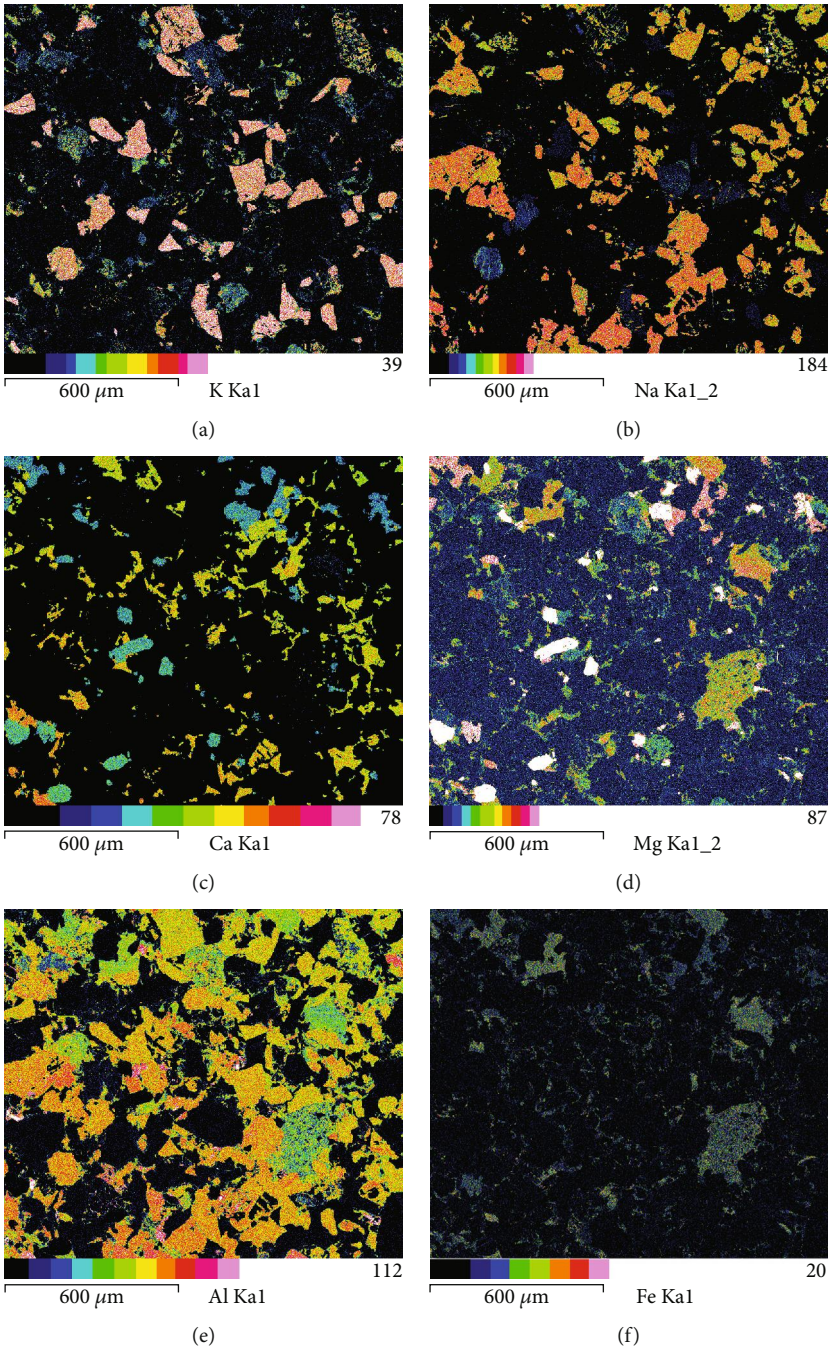

Figure 3: Continued.

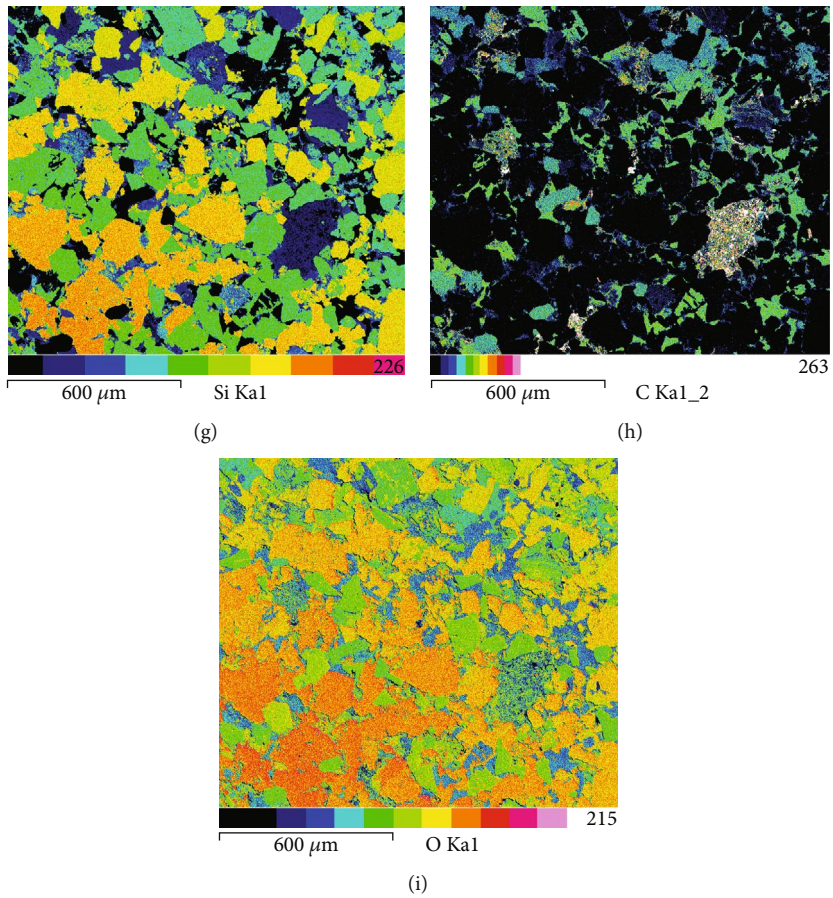

Figure 3: Sample 284-3-9-Z SEM-EDS major element distribution map: (a) K; (b) Na; (c) Ca; (d) Mg; (e) Al; (f) Fe; (g) Si; (h) C; (i) O.

and carbonate minerals. The denoise process for the skeleton mineral surface is required using marginal examination method (Figure 5). Clay minerals are relatively plastic and mainly distributed within primary pores; their morphological characteristics are closely related to the pore morphologies. Clay minerals are distributed within different types of micro-nanoscale pores, the mineral surfaces are relatively rough, and denoise is thus not required.

The SEM-EDS planar scanning element-mineral identification results are as follows (Figure 6): (1) the skeleton minerals have smooth surfaces and are widely distributed, while clay minerals are distributed within pores formed between skeleton grains; (2) the selected sample is mainly composed of skeleton minerals (quartz, albite, and potash feldspar) with proportion of 66.01%, carbonate minerals (calcite and dolomite) with 19.5%, and clay minerals (mainly chlorite and smectite and secondly kalinite and illite) with 10.59%. The proportion of pores in the selected slice is 3.78%.

Through the analysis of the minerals in the local area of the selected sample, the occurrence mode for various kinds of minerals could be clearly displayed (Figure 7). Quartz grains are developed with high content and good roundness (Figures 7(a) and 7(b)). Feldspar is mainly composed of potash feldspar and albite, and these two minerals display mutual mineral metasomatic phenomenon in many areas (Figure 7(d)), which is mainly caused by the uneven distribution of the K and Na elements in minerals. In addition, in the process of fluid filling, the albite will be dissolved into pores and filled with clay minerals and later formed carbonate minerals (Figures 7(e) and 7(f)). The clay minerals mainly attach to the surface of skeleton mineral particle and fill into large pore throats (Figures 7(c) and 7(e)).

4. Discussion

4.1. Comparison of EDS Identification and XRD Analysis. The identification results via the EDS new method are compared with the XRD mineral quantitative analyses and suggest that difference exists regarding the skeleton minerals including quartz, feldspar, carbonate, and clay minerals content, and they include the following.

(1) Quartz content: XRD analysis indicates the quartz content ranges from 25.5% to 36%, with average 30.4%, while EDS analysis indicates the quartz content ranges from 23.8% to 33.1%, with average 29.0%; the difference lies 0.3-4.8%

(2) Feldspar content: for potash feldspar, XRD analysis indicates the content ranges from 6.1% to 14.0%,

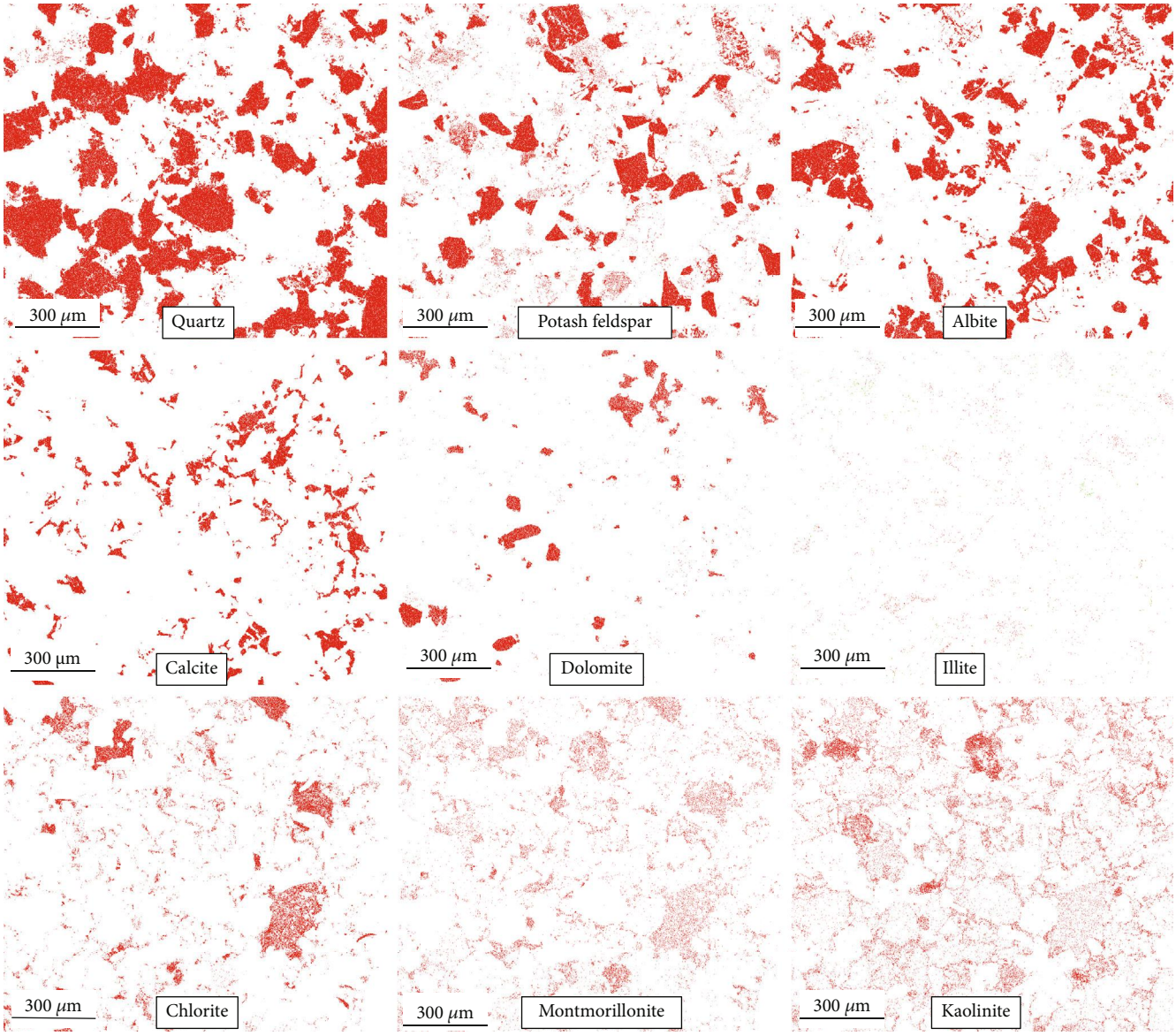

Figure 4: Sample 284-3-9-Z SEM-EDS planar scanning mineral content distribution map (before denoise).

with average 10.2%, while EDS analysis indicates the content ranges from 6.1% to 18.5%, with average 12.0%; the difference lies 0-4.5%. For albite/plagioclase: XRD analysis indicates the content ranges from 18% to 40.7%, with average 30.3%, while EDS analysis indicates the content ranges from 22% to 35%, with average 28.7%; the difference lies 1.1-5.9%

(3) Carbonate content: for calcite, XRD analysis indicates the content ranges from 0.5% to 14.2%, with average 2.4%, while EDS analysis indicates the content ranges from 0.5% to 12.1%, with average 2.9%; the difference lies 0-2.1%. For dolomite, XRD analysis indicates the content ranges from 0.8% to 13.1%, with average 7.0%, while EDS analysis indicates the content ranges from 1.8% to 11.9%, with average 7.7%; the difference lies 0-0.6-3.8%

(4) Clay minerals: XRD analysis indicates the content ranges from 11% to 36.1%, with average 19.7%, while EDS analysis indicates the content ranges from 10.7% to 33.7%, with average 19.8%; the difference lies 0-5%

In general, the content of skeleton minerals identified and calculated by the new EDS method is higher than that obtained by the XRD results (Figure 8). The reasons may include the following: (1) the new method is based on scanning electron microscopy, and skeleton minerals need to be firstly cut for sample preparation, which leads to a larger plane distribution area of skeleton minerals; (2) miscible minerals will appear identification bias, and XRD identification is based on a certain industry standard classification, which will also cause deviation; (3) the new mineral identification method can denoise the skeleton minerals and increase the surface area of the skeleton minerals.

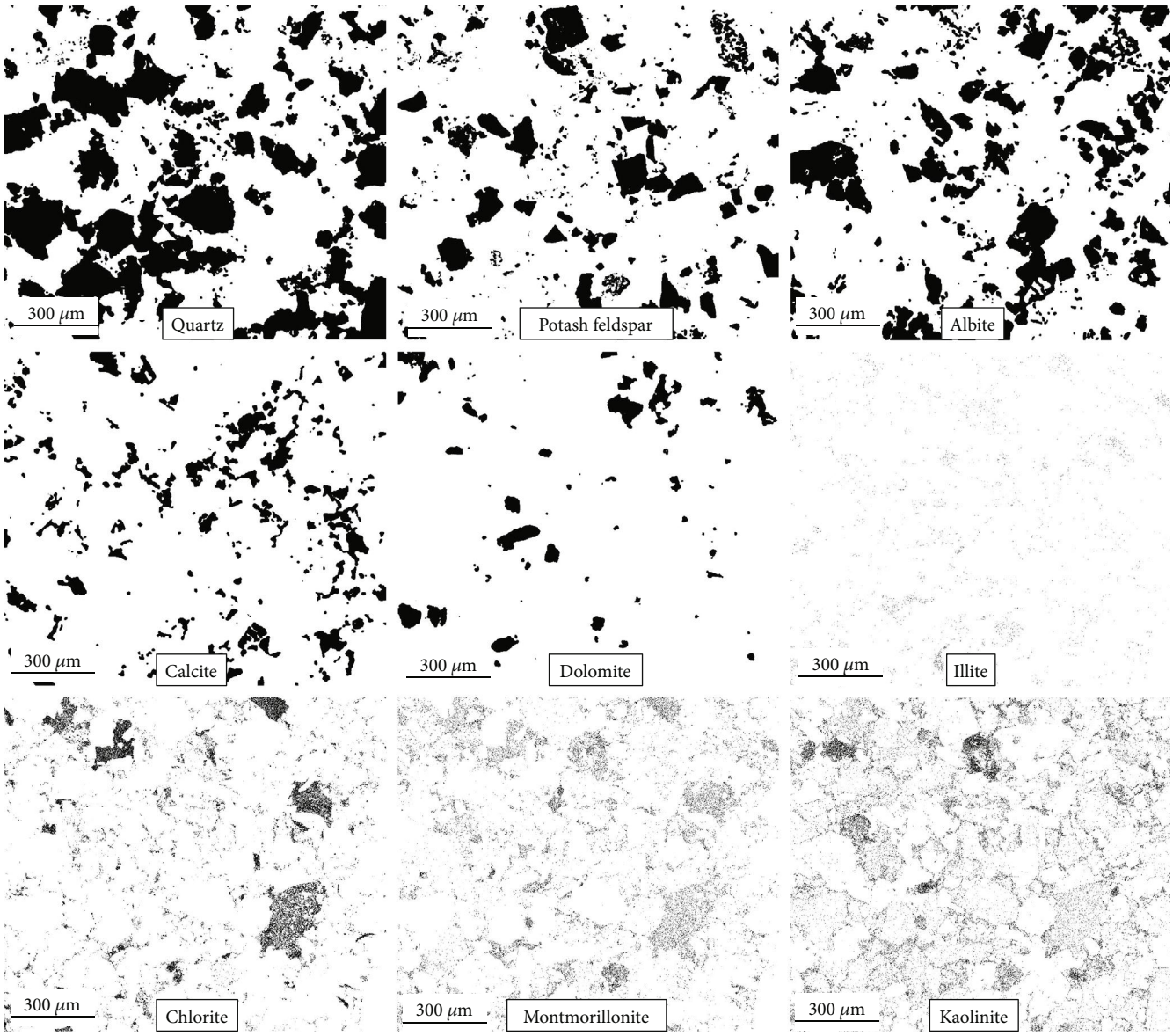

Figure 5: Sample 284-3-9-Z SEM-EDS planar scanning mineral content distribution map (after denoise).

The relative contents of clay minerals (illite, smectite, chlorite, and kaolinite) had little difference: (1) illite content: XRD content ranged from 0.9% to 10.1%, with an average of 4.5%, and EDS content ranges from 1.6% to 11%, with an average of 4.8%, with a difference of 0-2.1%; (2) smectite content: XRD content was distributed in the range of 1.9%-16.5%, with an average of 7.8%; EDS content was distributed in the range of 2%-17%, with an average of 7.4%, with a difference of 0.1-6.3%; (3) chlorite content: XRD content was 3.8%-10.2%, with an average of 7.4%, and EDS content was 3.9%-10.8%, with an average of 7.0%, with a difference of 0.1-2.4%; (4) kaolinite content: the kaolinite content in the sample area is relatively low (generally less than 1%), and XRD fails to effectively identify it. The mineral content identified by EDS is generally less than 1%, with an average content of 0.6%, and the performance of EDS identification is obviously better than that of XRD analysis.

In general, the content of clay minerals identified and calculated by the new method is higher than that analyzed by XRD (Figure 9). The reasons are perhaps as follows. (1) The new method is based on scanning electron microscopy, skeleton minerals are cut after rock slice processing, and the polishing fluid could pollute the surface characteristics of clay minerals in the reservoir, which increases the difficulty of identification. (2) After the completion of mineral identification, the new method does not denoise clay minerals, and the relative content of clay minerals may be small. (3) The minerals in the illite/smectite mixed layer cannot be effectively distinguished via the current new method.

Based on the results discussed above, the "EDS method" is able to qualitatively identify minerals, although differences exist compared to the XRD method. Advancing sampling techniques and higher resolution microscopes will reduce such differences. Meanwhile, the EDS method possess obvious

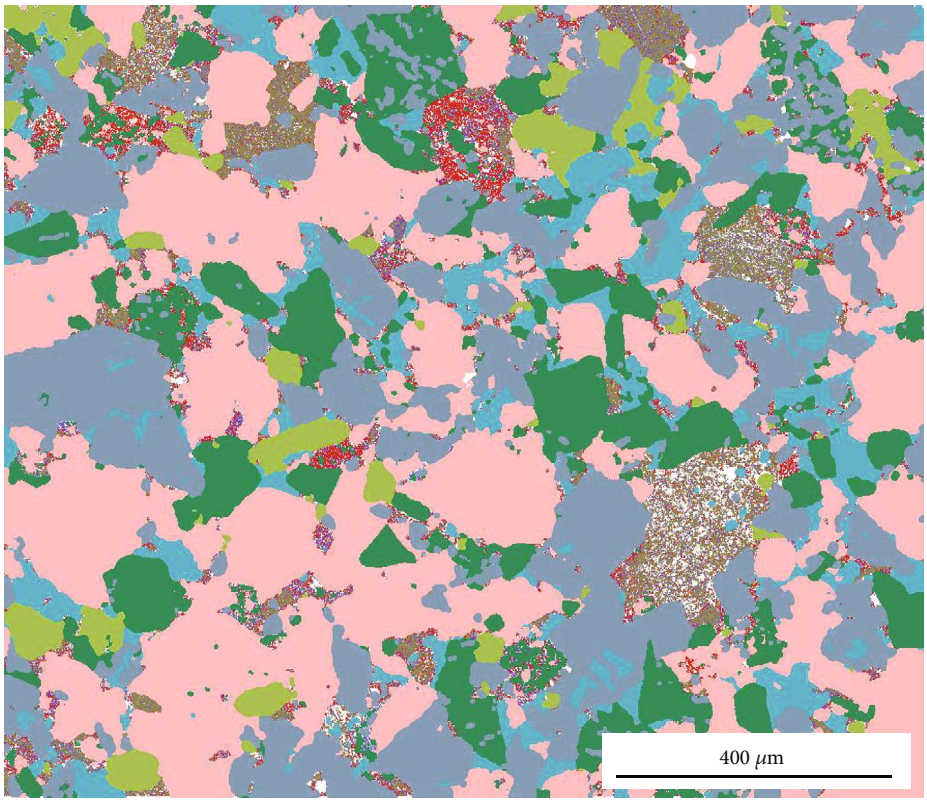

Mineral composition	Percentage content (%)
Quartz	30.86%
Potash Feldspar	10.03%
Albite	25.12%
Calcite	11.67%
Dolomite	7.60%
Siderite	0.12%
Illite	0.97%
Chlorite	4.79%
Montmorillo nite	3.11%
Kaolinite	1.84%
Pore	3.89%

Figure 6: Sample 284-3-9-Z SEM-EDS planar scanning element-mineral identification result.

advantages including (1) qualitative identification and quantitative calculation are both realized through element scanning at mineral surfaces and calculating mineral content; (2) able to identify low-content minerals through element associations determination, for instance, the pyrite and siderite in this study, whereas XRD method finds it hard to identify; (3) able to identify the characteristics of miscibility minerals and calculate their content, which is of great significance to mineral characteristics and diagenesis.

4.2. EDS Identification and TIMA Analysis. The SEM-TIMA composite mineral analysis system in the School of Earth and Space Sciences, Peking University, allows analysis of microstructure and granular structure containing mineral dissociation and assemblage. This system is composed of TESCAN field emission scanning electron microscopy, TESCAN composite mineral analyzer, YAG scintillator backscattering detector BSE, and cathode fluorescence detector CL synchronous detection system [49, 50]. This system allows identification and measurement of more than 5,000 types of mineral content, through analyzing the overlap degree of mineral element spectrum, representing the cutting-edge technology [51]. The sample is also submitted to this system for analysis, and the results show that 9.68% of the area fails to recognize any minerals (Figure 10).

The sample GJ141-7-25 is analyzed via the EDS method, XRD, and TIMA method to compare the practicability. Mineral identification results obtained via the EDS method and the XRD method are similar, whereas they both display considerable differences compared to the TIMA method (Figure 11). The TIMA results rely on the standard spectrum database; to require more accurate results, it requires modification of the samples compared to the standard database. Meanwhile, although the TIMA method can identify thousands of types of minerals, it cannot identify clay minerals as accurate as the XRD and EDS methods.

4.3. "EDS Method" Advantages. The EDS method is developed on the basis of scanning electron microscopy and energy spectrum analysis in field emission environment. It is a quantitative characterization method, based on mineral element composition and pixel element combination to distinguish mineral types in microsurface areas. As a visual mineral analysis method, it has significant advantages over the XRD method. In addition to obtaining the characteristics and relative content of mineral components, this method can also display the characteristics of pore structure, which expands the characterization content of pore structure based on scanning electron microscopy and enables the micropores of oil flow with mineral properties.

The TIMA method is oriented to various rocks and multiple mineral facies of one certain mineral. In contrast, the "EDS method" is a mineral analysis method specially designed for reservoir rocks in the field of petroleum geology. By referring to XRD analysis and testing standards and other relevant industry standards in the petroleum field,

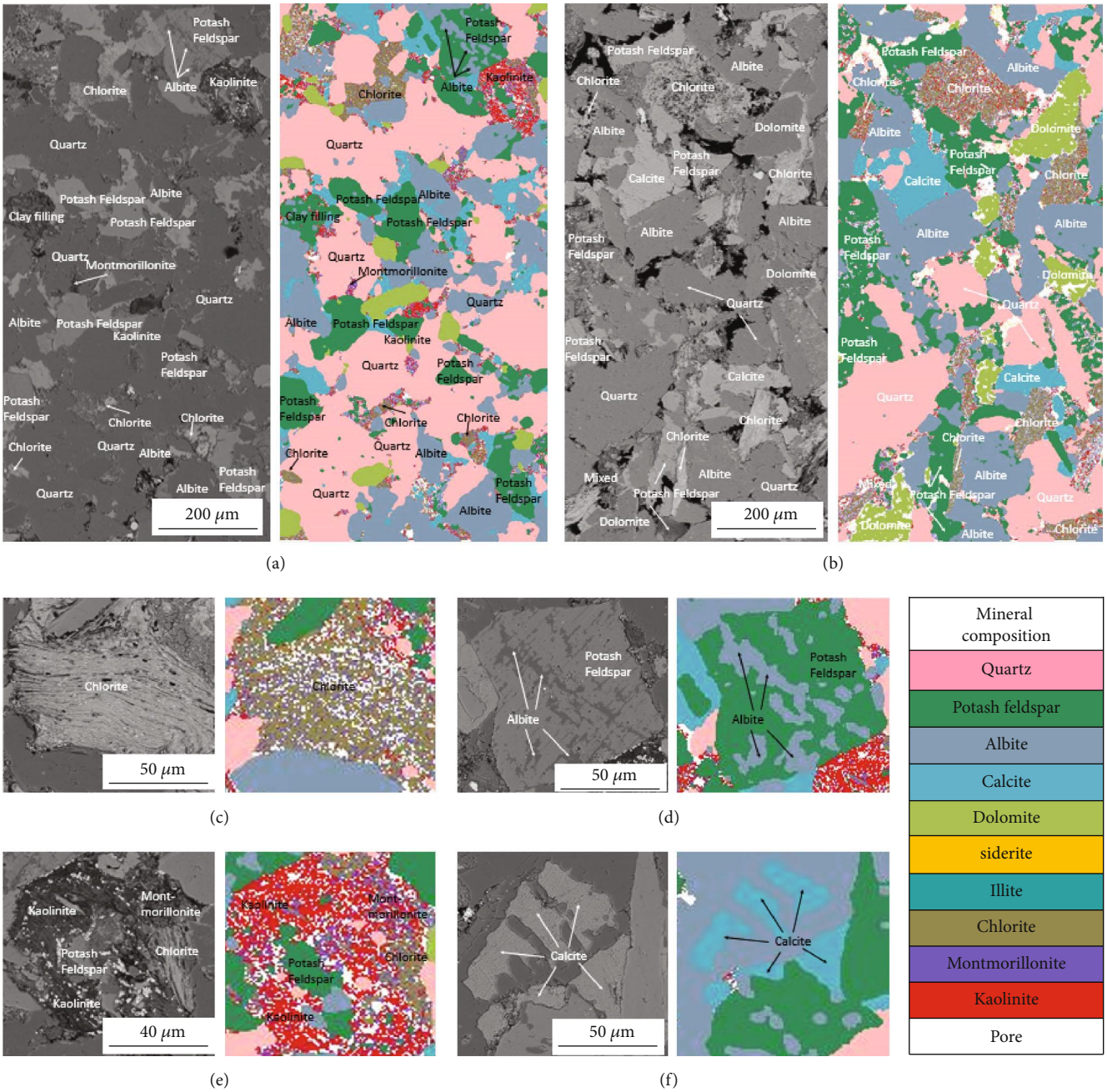

Figure 7: Sample 284-3-9-Z EDS element-mineral local characteristics. (a, b) Sample 284-2-45 and 284-3-9 backscatter and EDS element-mineral identification map; (c) two images of chlorite; (d) two images of potash feldspar and albite; (e) two images of major clay minerals; (f) two images of calcite.

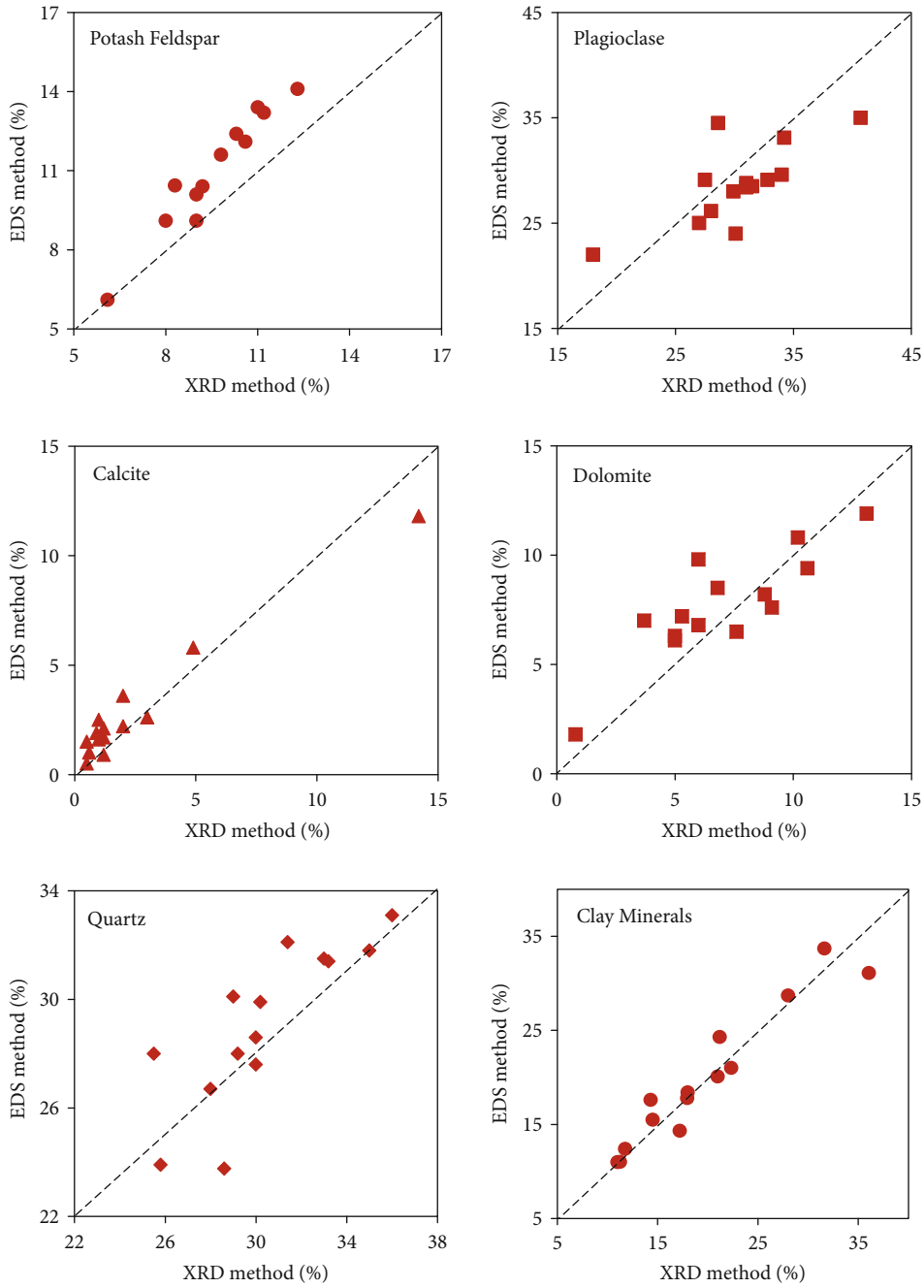

Figure 8: Skeleton mineral content results obtained via the EDS method vs. the XRD method.

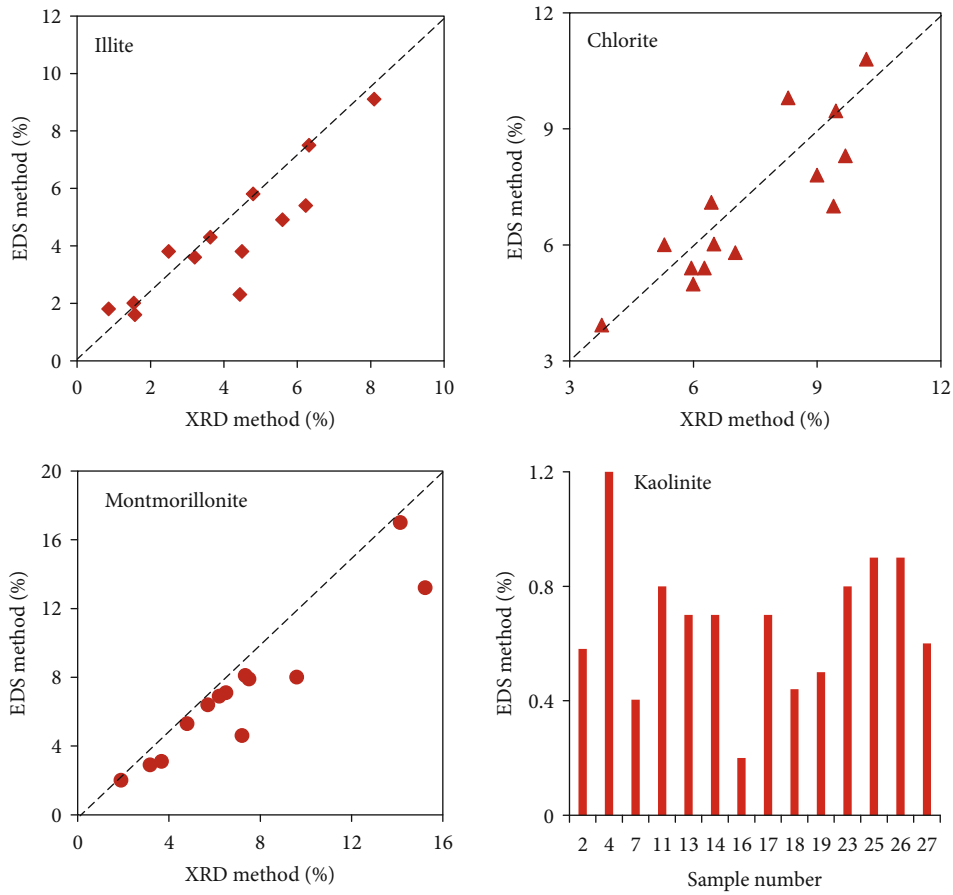

Figure 9: Clay mineral content results obtained via EDS method vs. XRD method.

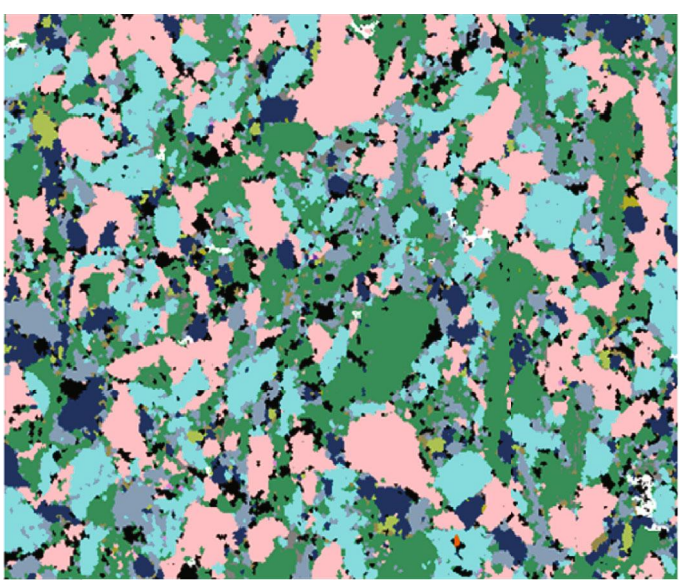

Mineral composition	Percentage content (%)
Quartz	23.86%
Orthoclase	23.29%
Plagioclase	30.01%
Calcite	8.62%
Dolomite	2.01%
Illite	1.10%
Chlorite	1.43%
Unrecognized	9.68%

Figure 10: Results obtained via SEM-TIMA method, sample Y416-3-53.

the element composition library of common minerals in various reservoirs is established to realize and strengthen the parallel comparison between various reservoir physical analysis techniques. Figure 11 shows that the EDS method analysis results are more consistent with the XRD whole-rock mineral analysis results obtained by testing under the oil

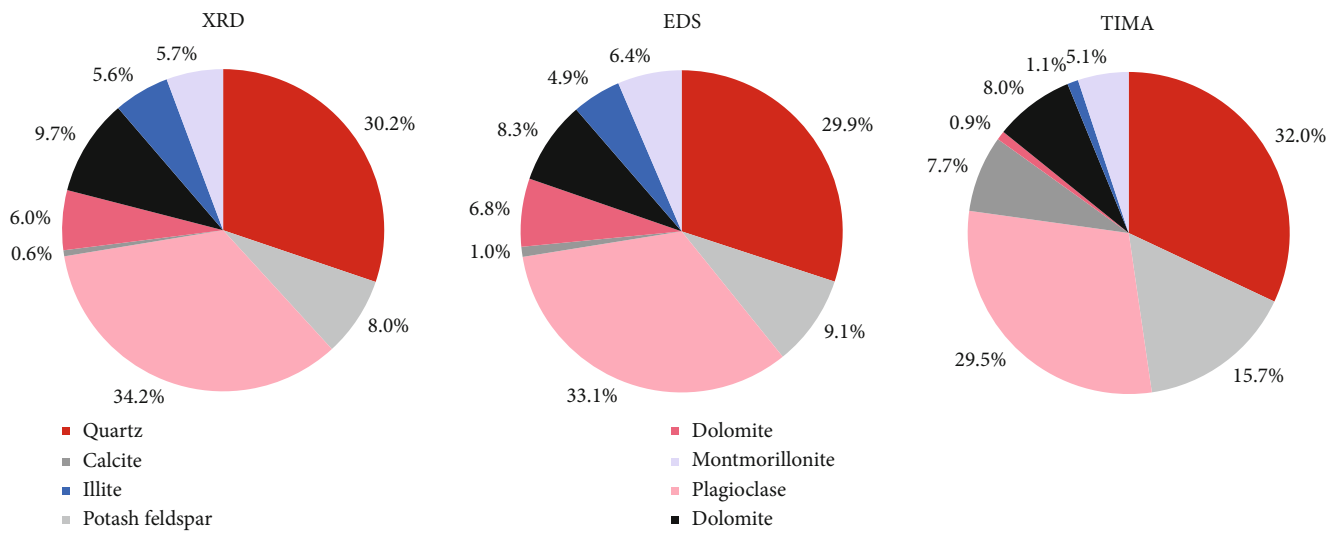

Figure 11: Results obtained via XRD, EDS method, and TIMA method, sample GJ141-7-25.

and gas industry standards. Therefore, it is also a method for coarsening mineral facies. With limited coarsening mineral facies, it focuses on the mineral component characteristics that can cause the difference of reservoir wettability and normalizes the mineral types in the reservoir, which can better serve the process of petroleum exploration and development and perhaps has stronger practical application value.

5. Conclusions

With the continuous development of hydrocarbon exploration, how to efficiently, economically, accurately, and comprehensively obtain mineral species, composition, structure, and diagenesis information has become one of the hot topics in both the academia and industry. By scanning electron microscopy (SEM) and energy dispersive spectroscopy (EDS), a new method of qualitative mineral identification and quantitative measurement is established. Typical tight sandstone reservoir rock samples in the Ordos Basin are selected; through the element surface scanning image of "mineral element composition" and "pixel element combination," mineral types are distinguished, and mineral parameters such as types, characteristics, and content are rapidly and accurately determined. Meanwhile, such results achieved via the new method are compared with those of conventional XRD and TIMA methods. The results show that the new method exhibits several advantages: cost advantages compared to XRD experiment analysis technology and TIMA system and ability to analyze low-content minerals which XRD techniques are hard to identify; it allows quantitative characterization on the phenomenon of mineral miscibility, which is of great significance to explore the mineral diagenetic evolution.

This paper proposes a new method for quantitative mineral deification, namely, the "EDS method." The main conclusions are as follows:

(1) A new method of qualitative mineral identification and quantitative measurement is established. This method employs the element surface scanning image of "mineral element composition" and "pixel element combination" to distinguish mineral types and determine mineral parameters such as types, characteristics, and content

(2) This method is applied to analyze the samples from the 6th layer of Triassic Yanchang Formation, Ordos Basin. The results show that skeleton minerals (quartz, albite, and potassium feldspar) dominate the study area, accounting for 66.01%. It also contains a lot of carbonate minerals (calcite and dolomite), accounting for 19.5%. The proportion of clay minerals is 10.59%, with chlorite and montmorillonite as the main minerals and kaolinite and illite as the second. The porosity is 3.78%, which is significantly lower than the results of physical property test, indicating that the development of clay minerals in this area played an important role in the formation of reservoir stratified pores

(3) The comparison of the "EDS method" with other methods shows that the results of the new EDS method are consistent with XRD, but there is a certain degree of deviation from the identification results of TIMA. This mainly resulted from the difference between the laboratory standard energy spectrum database established by TIMA and the actual sample. The "EDS method" is a mineral analysis method specially designed for reservoir rocks in the field of petroleum geology. Compared with XRD experimental analysis and TIMA system, the EDS method has obvious cost advantages and can better serve the process of petroleum exploration and development, suggesting potential stronger practical application value

Data Availability

The data is privileged information, not to be shared with the general public.

Conflicts of Interest

The authors declare that they have no conflicts of interest.

References

[1] C. R. Clarkson, M. Freeman, L. He et al., "Characterization of tight gas reservoir pore structure using USANS/SANS and gas adsorption analysis," *Fuel*, vol. 95, no. 1, pp. 371–385, 2012.

[2] X. Cui, A. M. M. Bustin, and R. M. Bustin, "Measurements of gas permeability and diffusivity of tight reservoir rocks: different approaches and their applications," *Geofluids*, vol. 9, no. 3, 223 pages, 2009.

[3] X. H. Yu, S. L. Li, and Z. H. Yang, "Discussion on depositon-diagenesis genetic mechanism andbot issues of tight sandstone gas reservoir," *Lithologic Reservoirs*, vol. 27, no. 1, pp. 1–13, 2015.

[4] R. K. Zhu, B. Bai, J. Cui et al., "Research advances of microstructure in unconventional tight oil and gas reserviors," *Journal of Palaeogeography*, vol. 15, no. 5, pp. 615–623, 2013.

[5] B. Li, D. Y. Liang, and L. L. Zhang, "Process mineralogy of an apatite-rich complex rare earth ore," *Journal of the chinese society of rare earths*, vol. 30, no. 6, pp. 761–765, 2012.

[6] R. D. Pascoe, M. R. Power, and B. Simpson, "QEMSCAN analysis as a tool for improved understanding of gravity separator performance," *Minerals Engineering*, vol. 20, no. 5, pp. 487–495, 2007.

[7] T. Saif, Q. Lin, A. R. Butcher, B. Bijeljic, and M. J. Blunt, "Multi-scale multi-dimensional microstructure imaging of oil shale pyrolysis using X-ray micro-tomography, automated ultra-high resolution SEM, MAPS Mineralogy and FIB-SEM," *Applied Energy*, vol. 202, pp. 628–647, 2017.

[8] B. Allard and C. Sotin, "Determination of mineral phase percentages in granular rocks by image analysis on a microcomputer," *Computers & Geosciences*, vol. 14, no. 2, pp. 261–269, 1988.

[9] G. Du, K. Y. Wang, J. Ran, F. Y. Wang, and Z. X. Pan, "Application of IR/SEM and other modern instruments for mineral identification," *Rock and mineral analysis*, vol. 33, no. 5, pp. 625–633, 2014.

[10] L. Ji, J. Qiu, Y. Q. Xia, and T. Zhang, "Micro-pore characteristics and menthane adsorption properties of common clay minerals by electron microscope scanning," *Acta Petrolei Sinica*, vol. 33, no. 2, pp. 249–256, 2012.

[11] S. J. Jiao, H. Han, Q. P. Weng, F. Yang, D. Q. Jiang, and L. S. Cui, "Scanning electron microscope analysis of porosity in shale," *Journal of Chinese Electron Microscopy Society*, vol. 31, no. 5, pp. 432–436, 2012.

[12] T. Du, Z. X. Zhou, L. M. Li, and Z. J. Zhang, "Mass effect of particle energy dispersive spectrometer quantitative analysis in scanning electron microscope," *Physical and Chemical Inspection (Physics Section)*, vol. 48, no. 6, pp. 365–369, 2012.

[13] Z. Q. Fu, J. C. Guo, C. C. He, J. Y. Zhao, and X. B. Liu, "Studies on standardization of nanometer scale measurement by SEM," *Standard Science*, vol. 3, pp. 34–37, 2012.

[14] J. Workman and J. L. Weyer, "Practical guide to interpretive near infrared spectroscopy," Chemical Industry Press, Beijing, 2009.

[15] Y. Li, Y. P. Wang, C. Y. Zhao, and L. U. JL, "The FTIR study on structure changes of coal kerogen in the maturation process," *Bulletin of Mineralogy, Petrology and Geochemistry*, vol. 32, no. 1, pp. 97–101, 2013.

[16] S. Cheng, J. Cao, Y. Li, G. Hu, and Z. Yi, "TEM observations of particles in groundwater and their prospecting significance in the Bofang copper deposit, Hunan, China," *Ore Geology Reviews*, vol. 95, pp. 382–400, 2018.

[17] G. Hu, J. Cao, and T. Jiang, "Discovery and prospecting significance of metal-bearing nanoparticles within natural invertebrate tissues," *Ore Geology Reviews*, vol. 99, pp. 151–165, 2018.

[18] Y. L. Zou, Q. L. Huo, and X. Yu, "The analytical technique of the micro infrared spectra of the hydrocarbon inclusions and its application," *Bulletin of Mineralogy, Petrology and Geochemistry*, vol. 25, no. 1, pp. 105–108, 2006.

[19] M. C. He and Z. J. Zhang, "The application of laser Raman microspectroscopy to study of mineral deposits," *Rock and mineral analysis*, vol. 20, no. 1, pp. 43–46, 2001.

[20] Y. H. Huang, *Quantitative Reserch of Fluid Inclusions by Laser Raman and Infrared Spectroscopy*, China University of Geosciences, 2018.

[21] T. P. Mernagh and A. R. Wilde, "The use of the laser Raman microprobe for the determination of salinity in fluid inclusions," *Geochimica et Cosmochimica Acta*, vol. 53, no. 4, pp. 765–771, 1989.

[22] J. D. Pasteris, C. A. Kuehn, and R. J. Bodnar, "Applications of the laser Raman microprobe RAMANOR UH000 to hydrothermal ore. deposits; Carlin as an example," *Economic Geology*, vol. 81, no. 4, pp. 915–930, 1986.

[23] G. J. Rosasco, E. Roedder, and J. H. Simmons, "Laser- excited Raman spectroscopy for nondestructive partial analysis of individual phases in fluid inclusions in minerals," *Science*, vol. 190, no. 4214, pp. 557–560, 1975.

[24] M. Futamata, P. Borthen, J. Thomassen, D. Schumacher, and A. Otto, "Application of an ATR method in Raman spectroscopy," *Applied Spectroscopy.*, vol. 48, no. 2, pp. 252–260, 1994.

[25] F. Ni, L. Thomas, and T. M. Cotton, "Surface-enhanced resonance Raman spectroscopy as an ancillary high-performance liquid chromatography detector for nitrophenol compounds," *Analytical Chemistry*, vol. 61, no. 8, pp. 888–894, 1989.

[26] E. Roth and W. Kiefer, "Surface-enhanced Raman spectroscopy as a detection method in gas chromatography," *Applied Spectroscopy*, vol. 48, no. 10, pp. 1193–1195, 1994.

[27] D. A. Stuart, C. R. Yonzon, X. Zhang et al., "Glucose sensing using near-infrared surface-enhanced Raman spectroscopy: gold surfaces, 10-day stability, and improved accuracy," *Analytical Chemistry*, vol. 77, no. 13, pp. 4013–4019, 2005.

[28] H. P. Klug and L. E. Alexander, "X-ray diffraction procedures: for polycrystalline and amorphous materials," John Wiley & Sons, New York, 2nd edition, 1974.

[29] Y. F. Hao and A. L. Zhao, "A simple method of quantitative analysis for calcite and dolomite in rock by X-ray diffraction," *Non-ferrous mining and metallurgy*, vol. 21, no. 5, pp. 61–63, 2005.

[30] Q. Q. Zhong, S. J. Huang, M. L. Zou, H. P. Tong, K. K. Huang, and X. H. Zhang, "Controlling factors of order degree of dolomite in carbonate rocks: a case study from Lower Paleozoic in Tahe Oilfield and Triassic in northeastern Sichuan Basin," *Lithologic reservoirs*, vol. 21, no. 3, pp. 50–55, 2009.

[31] G. C. Chi, L. H. Song, N. Wang, D. S. Cui, and G. X. Zhou, "Identification of alteration mineral composition of kimberlite from Shandong Mengy by X-ray powder diffractometer," *Rock and mineral analysis*, vol. 29, no. 4, pp. 475–477, 2010.

[32] G. C. Chi, G. Xiao, Y. L. Chen et al., "Application of X-ray powder diffractometer in the identification and classification of phyllite," *Geology and resources*, vol. 22, no. 5, pp. 409–414, 2013.

[33] X. L. Pang, X. C. Liu, and Y. Xue, "Application of powder X-ray diffraction in petrology and mineralogy," *Rock and mineral analysis*, vol. 28, no. 5, pp. 452–456, 2009.

[34] M. Redwan, D. Rammlmair, and J. A. Meima, "Application of mineral liberation analysis in studying micro-sedimentological structures within sulfide mine tailings and their effect on hardpan formation," *Science of the Total Environment*, vol. 414, pp. 480–493, 2012.

[35] Y. Liu, R. Gupta, A. Sharma et al., "Mineral matter-organic matter association characterisation by QEMSCAN and applications in coal utilisation," *Fuel*, vol. 84, no. 10, pp. 1259–1267, 2005.

[36] T. S. Song, X. Li, Y. Zhang et al., "QEMSCAN mineral quantitative analysis of tight sandstone diagenesis in Fuyu oil layer, Daqing Placanticline," *Geological Science and Technology Information*, vol. 35, no. 3, pp. 193–198, 2016.

[37] L. G. Wen, P. S. Zeng, and X. C. Zhan, "Application of the automated mineral identification and characterization system (AMICS) in the identification of rare earth and rare minerals," *Rock and Mineral Analysis*, vol. 37, no. 2, pp. 121–129, 2018.

[38] R. A. Creelman and C. R. Ward, "A scanning electron microscope method for automated, quantitative analysis of mineral matter in coal," *International Journal of Coal Geology*, vol. 30, no. 3, pp. 249–269, 1996.

[39] P. Ying and H. D. Yu, "Application of synthetic energy dispersive spectra(Eds) to identification and search of uncommon mineral," *Mining and Metallurgy*, vol. 14, no. 3, pp. 83–86, 2005.

[40] K. Guanira, T. M. Valente, C. A. Ríos et al., "Methodological approach for mineralogical characterization of tailings from a Cu(Au,Ag) skarn type deposit using QEMSCAN (quantitative evaluation of minerals by scanning electron microscopy)," *Journal of Geochemical Exploration*, vol. 209, p. 106439, 2020.

[41] X. Li, Y. Li, J. Li et al., "Characteristics of pore structures from the Lower Paleozoic shale gas reservoirs in northern Guizhou, South China," *Journal of Natural Gas Geoscience*, vol. 5, no. 5, pp. 241–253, 2020.

[42] Z. Liu, D. Liu, Y. Cai, and Y. Qiu, "Permeability, mineral and pore characteristics of coals response to acid treatment by NMR and QEMSCAN: insights into acid sensitivity mechanism," *Journal of Petroleum Science and Engineering*, vol. 198, p. 108205, 2021.

[43] A. M. Nazari, A. Ghahreman, and S. Bell, "A comparative study of gold refractoriness by the application of QEMSCAN and diagnostic leach process," *International Journal of Mineral Processing*, vol. 169, pp. 35–46, 2017.

[44] L. Santoro, M. Boni, G. K. Rollinson, N. Mondillo, G. Balassone, and A. M. Clegg, "Mineralogical characterization of the Hakkari nonsulfide Zn(Pb) deposit (Turkey): the benefits of QEMSCAN®," *Minerals Engineering*, vol. 69, pp. 29–39, 2014.

[45] M. U. Shafiq, H. K. Ben Mahmud, and M. Arif, "Mineralogy and pore topology analysis during matrix acidizing of tight sandstone and dolomite formations using chelating agents," *Journal of Petroleum Science and Engineering*, vol. 167, pp. 869–876, 2018.

[46] F. L. da Silva, G. F. Moreira, K. S. Pires, F. L. von Kruger, and F. G. da Silva Araujo, "Quantitative phases characterization of clayey ceramics containing manganese ore tailings," *Journal of Materials Research and Technology*, vol. 9, no. 5, pp. 11884–11894, 2020.

[47] X. Tang, Z. Jiang, S. Jiang, and Z. Li, "Heterogeneous nanoporosity of the Silurian Longmaxi Formation shale gas reservoir in the Sichuan Basin using the QEMSCAN, FIB-SEM, and nano-CT methods," *Marine and Petroleum Geology*, vol. 78, pp. 99–109, 2016.

[48] A. D. Van Rythoven, K. Pfaff, and J. G. Clark, "Use of QEMSCAN® to characterize oxidized REE ore from the Bear Lodge carbonatite, Wyoming, USA," *Ore and Energy Resource Geology*, 2020, article 100005.

[49] A. Beinlich, T. John, J. C. Vrijmoed, M. Tominaga, T. Magna, and Y. Y. Podladchikov, "Instantaneous rock transformations in the deep crust driven by reactive fluid flow," *Nature Geoscience*, vol. 13, no. 4, pp. 307–311, 2020.

[50] Q. Chen, W. L. Song, J. K. Yang et al., "Principle of automated mineral quantitative analysis system and its application in petrology and mineralogy: an example from TESCAN TIMA," *Mineral Deposits*, vol. 40, no. 2, pp. 345–368, 2021.

[51] T. Hrstka, P. Gottlieb, R. Skála, K. Breiter, and D. Motl, "Automated mineralogy and petrology - applications of TESCAN Integrated Mineral Analyzer (TIMA)," *Journal of Geosciences*, vol. 63, pp. 47–63, 2018.

Hindawi
Geofluids
Volume 2021, Article ID 5972497, 13 pages
https://doi.org/10.1155/2021/5972497

Research Article

Hydrogeochemical Characteristics and Water–Rock Interactions of Coalbed-Produced Water Derived from the Dafosi Biogenic Gas Field in the Southern Margin of Ordos Basin, China

Yuan Bao,[1,2] **Chao An**,[1] **Chaoyong Wang**,[2] **Chen Guo**,[1] **and Wenbo Wang**[1]

[1]*Geological Research Institute for Coal Green Mining, College of Geology and Environment, Xi'an University of Science and Technology, Xi'an 710054, China*
[2]*Key Laboratory of CBM Resource and Reservoir Formation Process, Ministry of Education, School of Resources and Geosciences, China University of Mining and Technology, Xuzhou 221008, China*

Correspondence should be addressed to Yuan Bao; baoyuan8384@163.com and Chaoyong Wang; wangcy@cumt.edu.cn

Received 12 April 2021; Accepted 21 May 2021; Published 8 June 2021

Academic Editor: Yanjun Meng

The hydrogeochemical characteristics of coalbed-produced water can provide insights into the sources of ions and water, the groundwater environments, hydrodynamic conditions, and water-rock interactions of depositional basins. To study the water-rock reaction process and reveal whether there is a microbial activity in the groundwater, a case of the Dafosi biogenic gas field was chosen by testing the ionic concentrations and hydrogen and oxygen isotopic compositions of coalbed-produced water and employing R-type cluster and principal component analyses. The results showed that Na^+, Cl^-, and HCO_3^- are the principal ions in the coalbed-produced water, while the water type is mainly a Na–Cl. Due to the hydrolysis of HCO_3^-, the pH in this region was controlled primarily by HCO_3^-. As the main cation in water, Na^+ contributed substantially to the total dissolved solids. Na^+ is also related to the exchange between rock-bound Na^+ and Ca^{2+} and Mg^{2+} in water or surrounding rocks. The coalbed-produced water's oxygen isotopes displayed a characteristic ^{18}O drift and enrichment, indicating that the ^{16}O isotope in the water was preferentially exchanged with the coal organic matter. Early evaporation is also contributed to the enrichment of TDS (total dissolved solids) and ^{18}O in the water. The central part of the study area, including the Qijia anticline, was affected by the Yanshanian uplift and denudation and subsequently developed a water-conducting fissure zone and was recharged atmospheric precipitation; these conditions were conducive to the formation of secondary biogenic gas.

1. Introduction

Coalbed methane (CBM), as a cleaner unconventional natural gas resource [1–3], has been widely prioritized development in major coal-producing countries (e.g., China, the United States, Canada, and Australia) [4–6]. The United States was the first to begin commercially developing CBM; China, Canada, and Australia are also entering the initial industrial CBM development stages [7]. In the mining of CBM, it is necessary to desorb the gas from the coal pores via drainage and reductions in pressure, which results in the discharge of coalbed-produced water. Important in this is that coalbed-produced water contains abundant geological information, which can positively impact CBM development. Understanding the storage, migration, and development of CBM by identifying trends across strata and analyzing the water sources is of great value. Thus, in recent years, the geochemical characteristics of water produced from coalbed have attracted extensive attention worldwide [8–11].

Since Craig [12] first proposed the linear relationship between the hydrogen and oxygen isotopes in global precipitation ($\delta D = 8\delta^{18}O + 10$) as the global meteoric water line (GMWL), hydrogen and oxygen isotopic compositions have been widely used in hydrogeochemical research [13], primarily to determine the sources of water and the types of and mechanisms underlying water-rock interactions [14, 15]. The main types of water-rock interactions include ion exchange, calcite and dolomite precipitation, and the

dissolution of silicates, gypsum, CO_2, and evaporites [16–18]. Guo et al. [8] found that coalbed-produced waters in the Bide-Santang basin of western Guizhou exhibit a *D* drift indicative of hydrogen content in the coalbed that is higher than that of oxygen and established a template for identifying water sources. Wu et al. [19] analyzed the hydrogen and oxygen isotopes of the water produced by CBM wells. They showed that it was mainly derived from atmospheric precipitation (i.e., meteoric water) and was subject to water-rock interactions and evaporation.

Various statistical methods (e.g., cluster analysis [20], canonical analysis [21], discriminant analysis [22], and principal component analysis [9, 23]) have been adopted to study the relationships among groundwater ion concentrations, total dissolved solids (TDS), and pH. Chemical changes that control coalbed-produced water have also been widely used for inference in different basins [24–26]. For example, Zhang et al. [9] studied the relationship between ions and suggested that the Na^+ and HCO_3^- concentrations in the Qinshui basin might be related to ion exchange and silicate weathering. Li et al. [21] analyzed the relationship between anions and cations in the Guohua phosphate mine of Guizhou province using cluster analysis. They asserted that natural effects, such as carbonate dissolution and rock weathering, were the main mechanisms affecting the mine's water chemistry. Redwan et al. [26] also studied the influence of the chemical characteristics of the water and water-rock interactions on the chemical elements of coal-bearing rocks and combined statistical methods to identify and evaluate water-rock reaction process. Thus, it has been demonstrated that analyses of the relationships between different ions in water can reveal the types of water-rock interactions occurring in a basin and the ion exchange processes. It is essential for exploring the primary ion sources of groundwater and CBM storage and migration.

The Dafosi gas field is located in the Binchang mining area of the Huanglong coal field along the Ordos basin's southern margin. The development potential of CBM resources is enormous, and its gas origin is biogenic gas [27]. Much research has been conducted on the occurrence and exploitation of CBM in this area. For example, favorable areas of CBM prospecting were identified by analyzing the thickness of coalbeds, hydrogeological conditions, CBM content, apex, and floor characteristics [28]. Ma et al. [2] stated that CO_2-enhanced coalbed methane technologies are feasible and improve the recovery of CBM, while Lin et al. [29] studied the pores of Dafosi coal samples and established a gas drainage model to enhance the efficiency of CBM drainage. Bao et al. [27] analyzed the genetic types and distributions of gas in this area based on gas and stable isotope data, recognizing that the gas is mainly biogenic CBM. However, there are few studies focused on the water-rock interaction mechanism of the study area.

The ionic characteristics of coalbed-produced water and the water sources have an important influence on predicting areas enriched in CBM. Therefore, in this study, we collected nine water samples from different CBM drainage wells in the Binchang mining area of the Dafosi biogenic gas field and tested their main ionic and hydrogen and oxygen isotope compositions to analyze the compositional characteristics of ions, water type, and water source. The correlations among the main influencing factors of various hydrochemical parameters were examined through Pearson correlation analysis, cluster analysis, and principal component analysis. The ion source and groundwater environment of coalbed groundwater were also explored. These analyses enabled us to determine the mechanisms underlying the water-rock reaction process and reveal whether there is a microbial activity in the groundwater if the water comes from meteoric precipitation.

2. Geological Setting

The stratigraphic sequence in the study area is as follows: Upper Triassic Hujiacun Formation (T_3h), Lower Jurassic Fuxian Fm. (J_1f), Middle Jurassic Yan'an Fm. (J_2y), Zhiluo Fm. (J_2z), Anding Fm. (J_2a), Lower Cretaceous Yijun Fm. (K_1y), Luohe Fm. (K_1l), Huachi Fm. (K_1h), Neogene (N), and Quaternary (Q). The principal aquifer of the K_1l is recharged by Quaternary phreatic water and surface water infiltration. Although the mudstone layer of the K_1h causes vertical recharge to be very weak, the K_1h is missing in some areas, which provides the conditions necessary for the infiltration of water into the Luohe Fm. The site is rich in coal resources, the surface is covered by loess spanning a large area, and the strata are relatively flat. The deep Jurassic has a monoclinic structure with an N60°–70° E strick and an NW–NNW tendency inherited from the Triassic basement.

The Ordos basin, in which the study area is located, is vast and complex. It may be divided into five water-bearing systems according to their hydrogeological structures and water-bearing media types [30]. These systems are the Cambrian-Ordovician, Cretaceous, Carboniferous-Jurassic, Cainozoic, and bedrock water systems (Figure 1(a)). The Dafosi gas field is located in the southern Binchang mining area of the Ordos basin (Figure 1(b)) and belongs to a Cretaceous clastic fissure-pore aquifer system.

The only coal-bearing strata in the Dafosi biogenic gas field is the Jurassic Yan'an Fm. The thickness of the strata ranges ~40.05–168.57 m (average: 75.57 m). There are unstable, thickly bedded sandstones at the bottom, limestone intercalated thick coalbeds in the lower layers, and medium-fine-grained sandstones in the middle. Sandstones and mudstones are interbedded with thin coalbeds, and the upper sandstones and mudstones interbedded with coal contain many plant fossils. The main coalbeds are nos. 4 and 4^{upper} coals, with the 4^{upper} coal being a bifurcated coalbed of the no. 4 coal, of which the average coal thickness is 17 m, meaning that it is the most mineable. The average thickness of the no. 4 coal is 11.6 m, and it is a mineable coalbed throughout the area. The Dafosi gas field is a specific biogenic gas mining area based on the gas component and its stable isotopes analysis [27].

CBM resources are rich in the Dafosi biogenic gas field. The coalbed permeability is 0.11-6.84 mD, and the coal structure is primary-cataclastic. Figure 1(c) shows the favorable area for CBM exploration and development. The fold

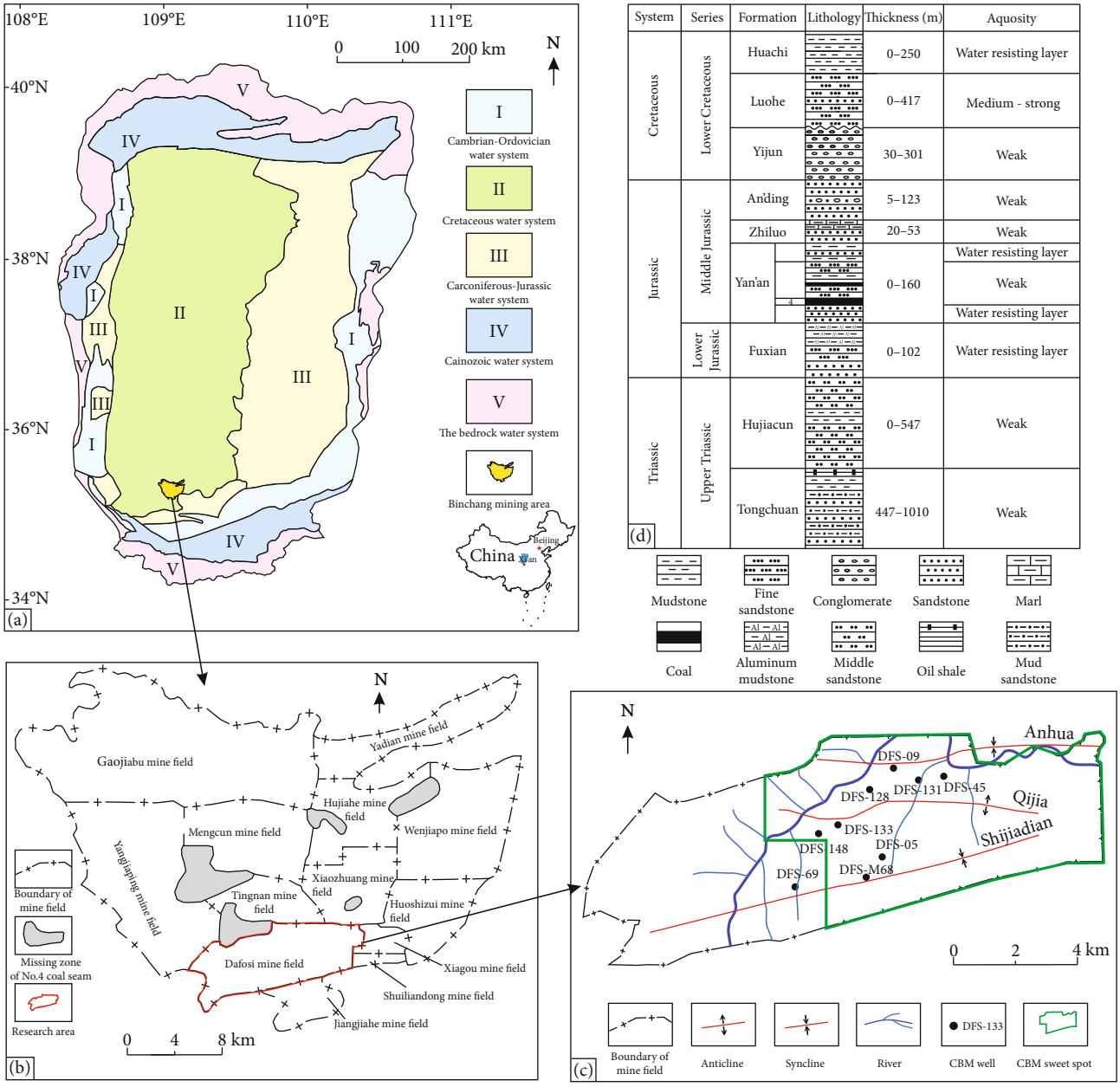

Figure 1: Regional structure, groundwater systems, and distribution of sampling locations: (a) groundwater systems; (b) distribution of mines in the Binchang mining area; (c) structure of the surface water system and sampling locations in the Dafosi biogenic gas field; (d) comprehensive stratigraphic column of the mining area.

structure developed in the Dafosi biogenic gas field is relatively broad and generally displays an undulating monoclinic system that includes the two synclines and one anticline (Figure 1(c)). The stratigraphic dip is relatively gentle, there are no igneous rocks, and the overall structure is simple. The Lower Jurassic Yan'an Fm is the primary coal-bearing unit in the study area (Figure 1(d)). The strata underlying this formation are the Lower Jurassic Fuxian Fm's mudstones, while the overlying strata include a fractured aquifer in the Middle Jurassic Zhiluo Fm. The study area's stratum integrity is good, and the roof and floor of the coalbed are mainly composed of mudstone and sandstone waterproof layers. There is no direct hydraulic connection between each layer. Therefore, the hydrogeological conditions in the mine area are of simple to moderate complexity.

3. Materials and Methods

The CBM wells in the study area have been producing gas continuously for more than 48 months [31]. Therefore, the collected coalbed-produced water can be regarded as the original formation of water. To characterize the water chemistry's distribution characteristics throughout the area, we designed three sampling lines along the fold direction. As the east side of the study area is a future CBM exploitation planning area, and the west side is an underground coal

Table 1: Geochemical parameters and water types of coalbed-produced water.

Parameters	Sample ID								
	DFS-05	DFS-09	DFS-45	DFS-69	DFS-128	DFS-131	DFS-133	DFS-148	DFS-M68
pH	8.2	7.9	8.1	9.0	7.7	8.0	8.3	8.3	7.2
TDS	9828.0	14199.0	12545.7	14886.1	13819.2	13318.7	15076.0	16505.6	7601.9
Na^+	3824.2	5395.5	4826.4	6052.0	5275.4	5045.2	5933	6367.6	2968.0
K^+	13.0	18.8	18.4	8.1	19.3	59.1	14.5	30.8	9.4
Mg^{2+}	15.0	59.5	40.2	5.2	50.1	47.9	8.7	10.8	11.5
Ca^{2+}	52.0	109.8	60.5	7.7	81.3	79.9	7.6	12.8	30.3
NH_4^+	11.3	16.9	23.2	0.0	21.8	15.4	9.2	0.0	9.7
Cl^-	5457.7	8441.8	7238	6229.8	8118.7	7840.3	6462.1	6347.4	4096.6
SO_4^{2-}	4.3	2.2	22.6	126.9	3.3	7.5	1142.4	2385.7	1.2
HCO_3^-	885.6	285.5	613.7	4092.2	477.0	427.1	2747.0	2426.1	936.5
CO_3^{2-}	0.0	0.0	0.0	371.0	0.0	0.0	114.9	123.0	0.0
Water type	Na–Cl	Na–Cl	Na–Cl	Na–Cl–HCO_3	Na–Cl	Na–Cl	Na–Cl	Na–Cl	Na–Cl

Note: the unit of ions and TDS are mg/L.

mining area without CBM wells, our coalbed-produced water samples were mainly concentrated in the central study area. After sampling, the 10 L buckets were sealed and sent to the laboratory for testing immediately. The sampling locations are shown in Figure 1(c).

Ions of K^+, Na^+, Mg^{2+}, Ca^{2+}, Cl^-, and SO_4^{2-} in coalbed-produced water were detected by dual system ion chromatography (ICS-2000, Thermo Fisher Scientific, USA); Fe^{2+} was detected according to the coal industry-standard (MT/T) by colorimetry; HCO_3^-, CO_3^{2-}, and pH values were detected by corresponding titration and electrode methods according to the same standard. The pH was measured using a PP-50-p11 meter (Sartorius, Germany), and a DDSJ-308A conductivity meter (Yantain Stark Instrument, Co., Ltd., China) was employed to measure TDS. The water's hydrogen and oxygen isotopic compositions were tested by LGR 912-0032 liquid water isotope analyzer (Los Gatos Research, USA) at the key laboratory of water disaster prevention and control in Shaanxi province. The Vienna standard mean ocean water (V-SMOW) standard was employed for stable isotopic analysis, and the analytical accuracies were $\delta D < \pm 0.5‰$ and $\delta^{18}O < \pm 0.2‰$, respectively.

4. Results and Discussion

4.1. Ionic Compositions and pH Values. Table 1 shows the main ion contents, pH values, TDS, and other basic geochemical data of the coalbed-produced water in the Dafosi biogenic gas field. The study area's pH ranges from 7.7 to 9.0 (average: 8.1), showing weak alkalinity. The concentration of TDS ranges from 7601.9 to 16505.6 mg/L. The mining area is relatively enriched in Na^+, Cl^-, and HCO_3^- and poor in Ca^{2+}, Mg^{2+}, and SO_4^{2-}. The trends are similar to those observed in previous studies, such as the Zhijin block and Dingji coal mine [32, 33]. The order of cation content is as follows: $Na^+ > Ca^{2+} > Mg^{2+} > K^+ > NH_4^+$. Sodium contents range from 2968 to 6367.6 mg/L and account for >96% of all cations. The order of anion content is $Cl^- > HCO_3^- > SO_4^{2-} > NO_3^-$, in which the Cl^- content ranges from 4096.6 to 8441.8 mg/L and accounts for 60–97% of all anions.

The lowest HCO_3^- concentration was 285.5 mg/L, and the highest was 4092.2 mg/L, accounting for 3–40% of all anions. The difference in the HCO_3^- concentrations reflected the different well locations and may be related to the dissolution of CO_2 in CBM. The water type of the coalbed-produced was mainly Na–Cl in the study area, containing a small Na–Cl–HCO_3-type (Table 1 and Figure 2). The TDS of the research area was high, with the lowest being 7601.9 mg/L and the highest being 16505.6 mg/L. Because the average concentration of Na^+ in the coalbed-produced water was 5076 mg/L, while that of Ca^{2+} was only 49 mg/L, the ratio of $Na^+/(Na^+ + Ca^{2+})$ ranged between 0.98 and 1, with an average of 0.99. Although no extremes in $Na^+/(Na^+ + Ca^{2+})$ were observed, the ratio of $Cl^-/(Cl^- + HCO_3^-)$ exceeded 0.6, with an average of 0.83. By projecting Dafosi coalbed-produced water data into a Gibbs diagram (Figure 3), it was found that the $Na^+/(Na^+ + Ca^{2+})$ and $Cl^-/(Cl^- + HCO_3^-)$ values all plotted in the upper right corner, indicating that the ions in this water were affected by evaporation.

4.2. Isotopic Compositions of Hydrogen and Oxygen and Identification of Water Source. When a water sample receives atmospheric precipitation, it will plot on the China meteoric water line (CMWL) [35]. In contrast, water samples subject to evaporation or water-rock interaction will generally deviate plot below the line [36]. Table 2 shows that the hydrogen and oxygen isotopic compositions of water produced by CBM wells were relatively close, with δD values ranging from -85.8‰ to -79.5‰ (average: -82.3‰) and $\delta^{18}O$ values ranging from -12.2‰ to -9.3‰ (average: -11‰). Projection of these composition data in Figure 4 revealed that most well data in the study area were distributed below the CMWL and displayed an ^{18}O drift, reflecting a strong evaporation existence in this region (line slope is 1.87). Only the data for well DFS-133 plotted along the CMWL, while those of

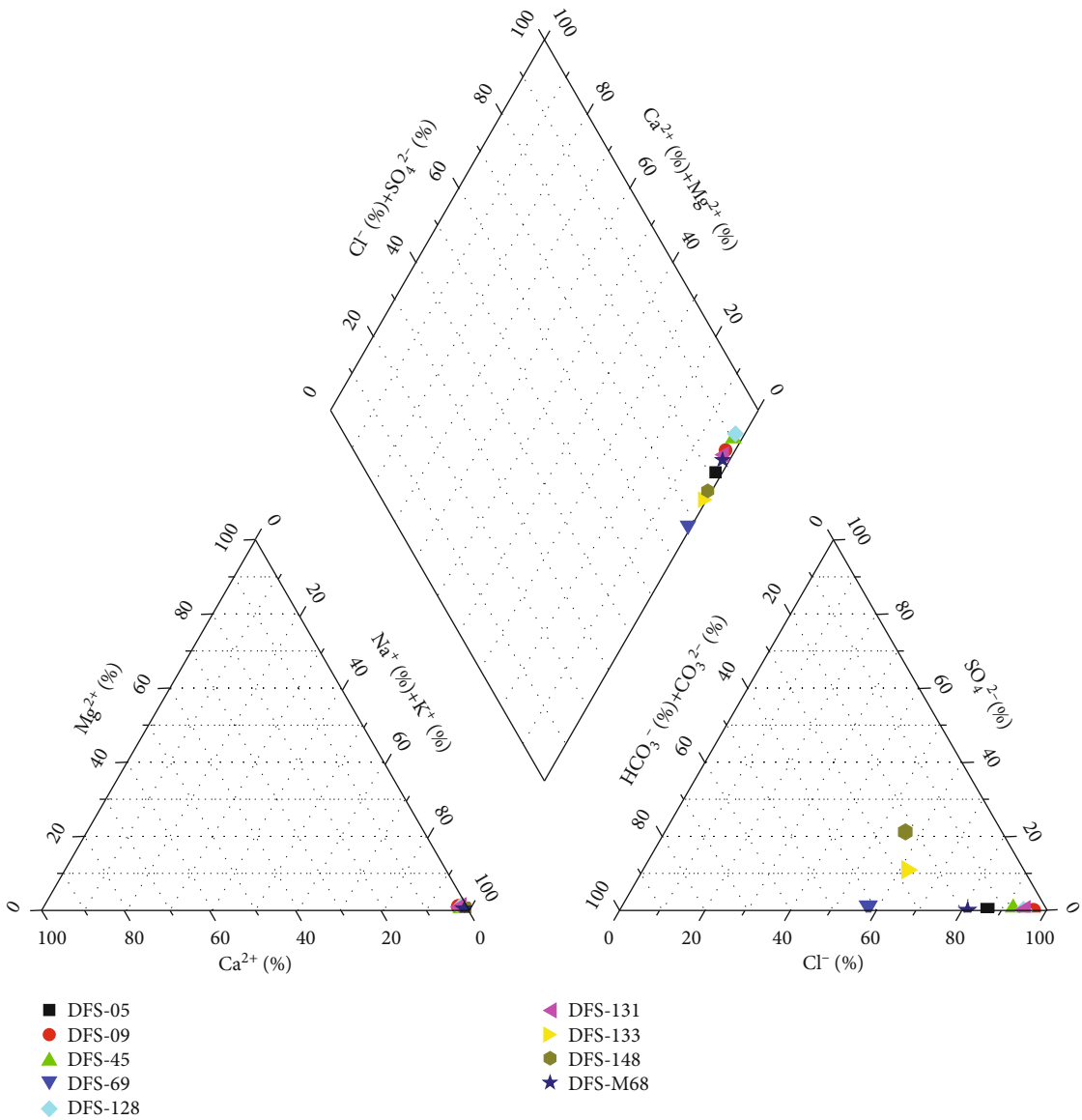

Figure 2: Piper diagram of coalbed-produced water in the Dafosi biogenic gas field indicating the water type.

three wells, DFS-148, DFS-131, and DFS-M68, plotted close to this line. The information for the remaining five wells deviated markedly from the CMWL.

4.3. Multivariate Statistical Analyses of Different Geochemical Indicators. Analyzing the correlations between different ion contents is a simple and effective method by which the geochemical characteristics of coalbed-produced waters may be studied [37, 38]. We analyzed the correlations between major ions in coalbed-produced water using Pearson's correlation analyses performed in SPSS v. 21 (IBM Corp., USA). As shown in Table 3, the correlation between TDS and Na^+ reached $R^2 = 0.994$ at a significance level of $p = 0.01$, which indicates that Na^+ in this area contributed greatly to TDS. The pH value was significantly correlated with CO_3^{2-}, Na^+, HCO_3^-, and HCO_3^-, among which HCO_3^-, CO_3^{2-}, and pH displayed the most apparent positive relationships, reaching $R^2 = 0.758$ and $R^2 = 0.808$, respectively.

Factor analysis is a process of reducing the dimensionality of data. Several original variables with specific correlations are collated into a new variable, and the newly constructed variable represents the overall difference in the data caused by such variables. This approach can reduce the number of variables needed to explain the variance in the data while maintaining much of the original integrity of the data [39] and enabling us to analyze the relationship between ions in coalbeds rapidly. As the two ends of the rotated factor loading matrix are concentrated, which can better explain the main factors, we used the rotated factor loads and extracted the four main elements, principal components 1–4 (i.e., PC1, PC2, PC3, and PC4). According to the component matrix (Table 4) and total variance (Table 5) obtained via factor rotation of the maximum variance in SPSS, the variance described by the four factors was obtained. The most important four factors accounted for 32.61%, 32.36%, 21.74%, and 10.76% of

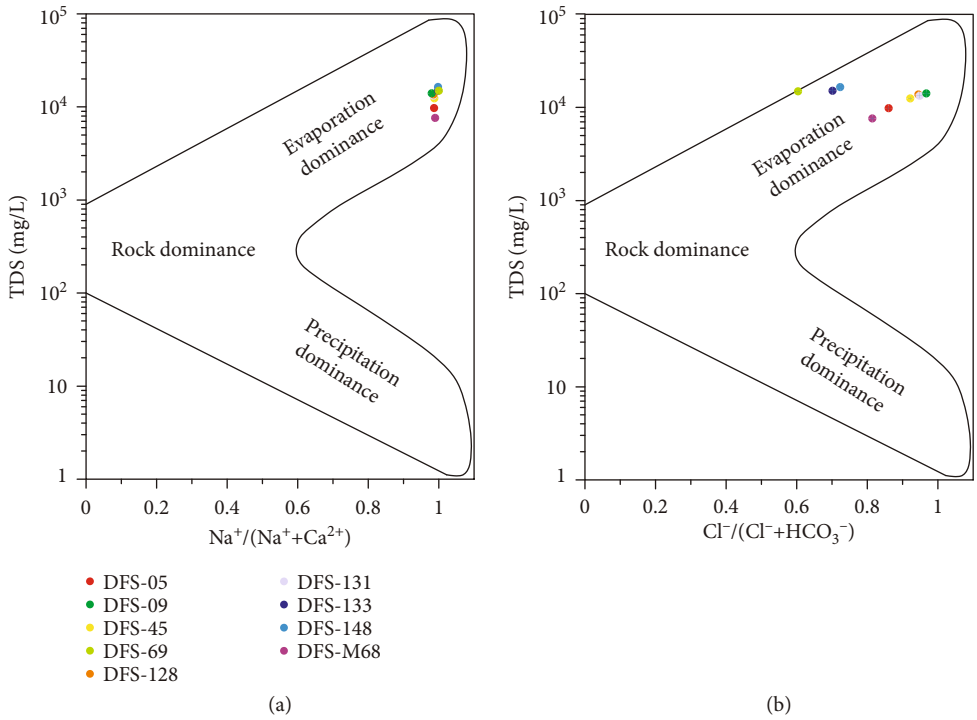

Figure 3: Gibbs distribution model of coalbed-produced water indicating the ionic reactions (modified from the literature [34]).

Table 2: Hydrogen and oxygen isotopic compositions of coalbed-produced water in the Dofosi biogenic gas field.

	Sample ID								
	DFS-05	DFS-09	DFS-45	DFS-69	DFS-128	DFS-131	DFS-133	DFS-148	DFS-M68
δD (‰)	-84.2	-80.0	-81.5	-83.5	-81.4	-79.5	-84.5	-85.8	-81.7
$\delta^{18}O$ (‰)	-12.2	-9.3	-10.5	-11.0	-10.2	-10.8	-11.8	-11.7	-11.2

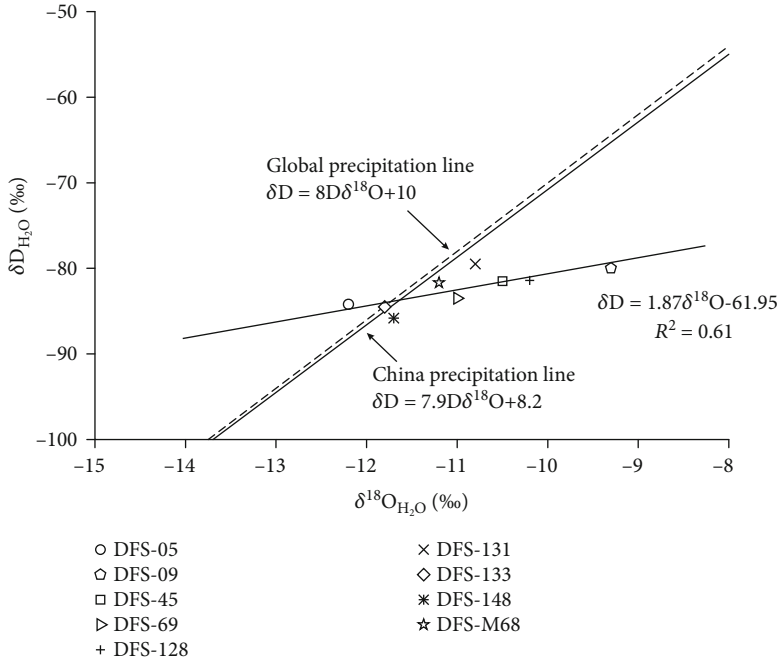

Figure 4: Relationship between $\delta D(H_2O)$ and $\delta^{18}O(H_2O)$ in coalbed-produced water of the Dafosi biogenic gas field.

Table 3: Pearson's correlation matrix between hydrogeochemical parameters of water samples.

	pH	TDS	Na^+	K^+	Mg^{2+}	Ca^{2+}	Cl^-	SO_4^{2-}	HCO_3^-	CO_3^{2-}
pH	1.000	0.623	0.687*	-0.064	-0.376	-0.441	0.119	0.277	0.758*	0.808**
TDS		1.000	0.994**	0.269	0.092	-0.116	0.609	0.577	0.457	0.475
Na^+			1.000	0.200	0.005	-0.201	0.544	0.575	0.549	0.567
K^+				1.000	0.435	0.345	0.461	0.13	-0.329	-0.287
Mg^{2+}					1.000	0.953**	0.827**	-0.453	-0.767*	-0.589
Ca^{2+}						1.000	0.684*	-0.566	-0.846**	-0.666
Cl^-							1.000	-0.122	-0.330	-0.174
SO_4^{2-}								1.000	0.472	0.268
HCO_3^-									1.000	0.945**
CO_3^{2-}										1.000

*Correlation is significant at $p = 0.05$ level (two-tailed). **Correlation is significant at $p = 0.01$ (two-tailed).

Table 4: Coefficient scores for each principal component in the factor analysis.

Parameter	Principal component			
	PC1	PC2	PC3	PC4
pH	0.923	-0.064	0.183	0.031
TDS	0.558	0.331	0.750	0.122
Na^+	0.633	0.267	0.721	0.078
K^+	-0.092	0.266	0.153	0.945
Mg^{2+}	-0.309	0.924	-0.086	0.180
Ca^{2+}	-0.392	0.854	-0.256	0.131
Cl^-	0.139	0.930	0.263	0.196
SO_4^{2-}	0.059	-0.408	0.894	0.119
HCO_3^-	0.779	-0.515	0.279	-0.180
CO_3^{2-}	0.900	-0.314	0.123	-0.159

Table 5: Total variance explained by each principal component.

PC	Rotated and squared loadings		
	Total	Variance percentage (%)	Cumulative ratio (%)
PC1	3.261	32.61	32.61
PC2	3.236	32.36	64.97
PC3	2.173	21.73	86.70
PC4	1.076	10.76	97.46

the population variance, respectively, and the accumulative total is 97.46%.

To intuitively express the relationship between individual index parameters, the R-mode cluster analyses of Pearson correlation and between-group linkage method are employed to classify the ionic composition of coalbed-produced water in the Dafosi biogenic gas field (Figure 5). After the cluster analysis, 10 parameters were divided into four categories, and the four PCs from the initial factor analysis had the same characteristics. The cluster analysis parameters, C1, C2, C3, and C4, corresponded to PC1, PC2, PC3, and PC4.

According to the coefficient scores of each PC (Table 4), and with ±0.7 set as the boundary [8], the parameters with absolute values >0.7 were highlighted (as shown in Figure 6). PC1 mainly represented the negative ions and pH represented by HCO_3^-. Since the hydrolysis of HCO_3^- (i.e., $HCO_3^- + H_2O = H_2CO_3 + OH^-$) exceeds its ionization (i.e., $HCO_3^- = H^+ + CO_3^{2-}$), causing the water was weakly alkaline [40]. Meanwhile, PC2 and PC4 were positively correlated with Cl^-, Ca^{2+}, Mg^{2+}, and K^+, which may be related to the lateral flow of groundwater or recharge of fissures when water is supplied. Most soluble ions in groundwater are diluted. PC3 was positively correlated with TDS, Na^+, and SO_4^{2-}, which indicates that Na^+ and SO_4^{2-} firmly control TDS, among which Na^+ accounts for >95% of the produced water in the coalbed contributes more to TDS. Under a low concentration of SO_4^{2-}, this is conducive to the production of secondary biogenic gas [41].

Cluster-1 (C1) corresponded to PC1, which revealed the joint controlling of pH by HCO_3^- and CO_3^{2-}. Strong correlations between pH and CO_3^{2-} and pH and HCO_3^-, $R^2 = 0.808$ and $R^2 = 0.758$, respectively (Table 3), were generally produced by the reduction of SO_4^{2-}, indicating that this process can promote water-rock interactions. Cluster-2 (C2) corresponded to PC2, in which Cl^- generally increased with increasing salinity; such a trend is often used as a marker of salt in groundwater [20]. The main cations may be related to water-rock interactions. The measured distance of Mg^{2+} and Ca^{2+} was 5 (dimensionless), indicating that the two were closely related, likely due to the recharge of water occurring close to its source. Cluster-3 (C3) corresponded to PC3 (i.e., TDS, Na^+, and SO_4^{2-}), which means that the TDS of coalbed-produced water may be related to the reduction of SO_4^{2-}. Finally, Cluster-4 (C4) corresponds to PC4. The fracturing fluid used for CBM drainage and production in the study area is clear water with 1% KCl and 0.05% bactericide. When K^+ enters a coalbed, it is diluted, consumed, and replaced by Na^+. Therefore, C4 may represent the residual K^+ in the fracturing fluid.

PC1 represents the influence factor of pH. There is more HCO_3^-, which may be further hydrolyzed to produce OH^-, and result in the produced water is weakly alkaline. PC2 describes the recharge of the water source and the resultant precipitation of Ca^{2+} and Mg^{2+}, which is affected by evaporation during the recharge process, and was mainly related to the DFS-133 sampling points being located in the core of

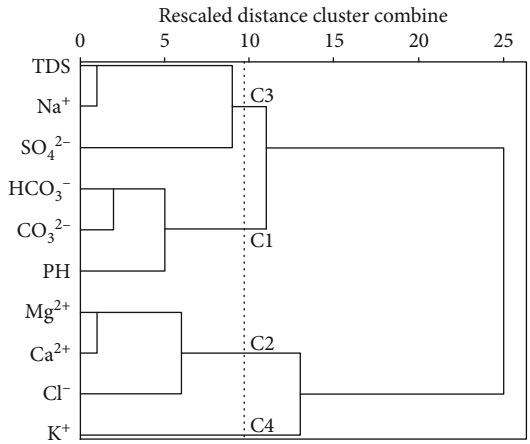

Figure 5: Classification results of the R-type cluster analysis.

Qijia anticline and its two wings. PC3 illustrates water-rock interactions and the reduction of SO_4^{2-}, which occur between groundwater and coalbeds or surrounding rocks. Low sulfate content in the samples indicates that there was a robust sulfate reduction process in the coalbed. The high sodium ion is resulted from the ion exchange and making the most outstanding contribution to TDS. These interactions will also lead to a further precipitation of Ca^{2+} and Mg^{2+}. PC4 shows the influence of fracturing fluids. After a fracturing fluid penetrates underground, large amounts of K^+ are consumed, and Na^+ ions in the surrounding rocks are dissolved into the coalbed-produced water to maintain the ionic balance, and thus, Na^+ becomes the principal cation of coalbed-produced water under the influence of water-rock interaction.

The saturation index [SI = lg (IAP/Ksp)] is the logarithm of the ion activity product (IAP) of solution and its solubility product (Ksp) ratio [42]. The SI value represents three different states of incompatible substances, the precipitate in groundwater (SI > 0), dissolve in groundwater (SI < 0), and the dissolution and sedimentation balance in groundwater. They help predict the presence of reactive minerals in the aqueous water system and estimating mineral reactivity. Due to error in mineral equilibrium constants, SI range is close to 0 (±0.5), considering that SI is in equilibrium. Table 6 shows the calculated result of anhydrite, aragonite, calcite, dolomite, gypsum, halite, and sylvite in the study area of groundwater minerals. However, partly, samples lack aragonite, calcite, and dolomite, indicating that Ca^{2+} and Mg^{2+} are mainly from the dissolution of gypsum salts and gypsum minerals. Ca^{2+} and Mg^{2+} are precipitated secondary calcite or dolomite in an alkaline environment, resulting in a few samples in supersaturation of carbonate minerals (SI > 0), such as calcite or dolomite. Na^+ is abundant, and all the halite are saturated. Therefore, halite is the main control factor to the chemical composition of groundwater ions. The K^+ in the water is low, leading to the sylvite in the unsaturated state.

4.4. Ion Source Identification. Ion sources can be determined according to the relationships between the main ion contents [43]. Most of the $(Na^+ + K^+)/Cl^-$ in the study area plotted along the line with a slope of 1 (Figure 7(a)), which indicates that the dissolution of sodium and potassium salts is the main source of most Na^+ and K^+; the concentrations of Na^+ and K^+ also exceeded that of Cl^-, which may be due to presence of other sources of Na^+ and K^+, such as cation exchange. Meanwhile, $r(HCO_3^{2-} + SO_4^{2-})$ and $r(Ca^{2+} + Mg^{2+})$ can be used to determine the main sources of Ca^{2+} and Mg^{2+} in coalbed-produced water, where r is the milligram-equivalent concentration of the ions. According to Figure 7(b), $r(SO_4^{2-} + HCO_3^{2-})$ and $r(Ca^{2+} + Mg^{2+})$ ratio do not fall on the 1 : 1 line, indicating that the Ca^{2+} and Mg^{2+} produced in the coalbed were not derived from the CO_3^{2-} dissolution. Most of the values are below the 1 : 1 line, showing that Ca^{2+} and Mg^{2+} may come from the early dissolution of silicate minerals and gypsum salts [43].

Generally, the relationship between $[(Ca^{2+} + Mg^{2+}) - (SO_4^{2-} + HCO_3^-)]$ and $(Na^+ + K^+ - Cl^-)$ can be used to determine whether or not cation exchange has occurred [44]. According to Figure 7(c), the ratio of $[(Ca^{2+} + Mg^{2+}) - (SO_4^{2-} + HCO_3^-)]$ and $(Na^+ + K^+ - Cl^-) \approx -1$, illustrating the cation exchange between Na^+ and Ca^{2+}/Mg^{2+}, is relatively common. Chloro-alkaline index (CAI) can also be regarded as the quantified cation exchange degree [44]. In the study area, CAI-I and CAI-II were almost all negative (Figure 7(d)), and their values differed substantially, indicating that differing levels of water-rock interactions occurred during groundwater migration [45]. Furthermore, Na^+ or K^+ replaced Ca^{2+} and Mg^{2+} in the water, resulting in lower Ca^{2+} and Mg^{2+} contents in coalbed-produced waters.

4.5. Mechanism of Water-Rock Interactions. Water-rock interactions occur in the situation of long-term contact of coalbed-produced water with a rock in the ground during the water flow [46]. Sandstone is located at the top of the no. 4 coalbed (Figure 1(d)), and sodium is the dominant cation accounting for the most significant ion proportion of coalbed-produced water. The forming process of sodium in the water can be interpreted as after weathering, hydrolysis, ion exchange, and other processes, Na^+ was dissolved into the coalbed-produced water. At the same time, Ca^{2+} and Mg^{2+} were precipitated into rock, leading to the enrichment of Na^+ in the produced water and a lack of Ca^{2+} and Mg^{2+} (Figure 8). Sodium also becomes an essential factor influencing TDS concentration. The ion exchange reaction mechanisms between Na^+ and Mg^{2+} and Ca^{2+} in water and rock are shown in Equations (1) and (2).

$$2Na(rock) + Ca^{2+}(water) = 2Na^+(water) + Ca(rock) \quad (1)$$

$$2Na(rock) + Mg^{2+}(water) = 2Na^+(water) + Mg(rock) \quad (2)$$

When there is a certain amount of HCO_3^- in the groundwater system, the ionic exchange between Ca^{2+} and HCO_3^- (Equations (3) and (4)) will replace Na^+ (Equation (5)) in rocks, thus reducing the content of Ca^{2+} in the water [47].

$$2HCO_3^- + Ca^{2+} \rightarrow Ca(HCO_3)_2 \quad (3)$$

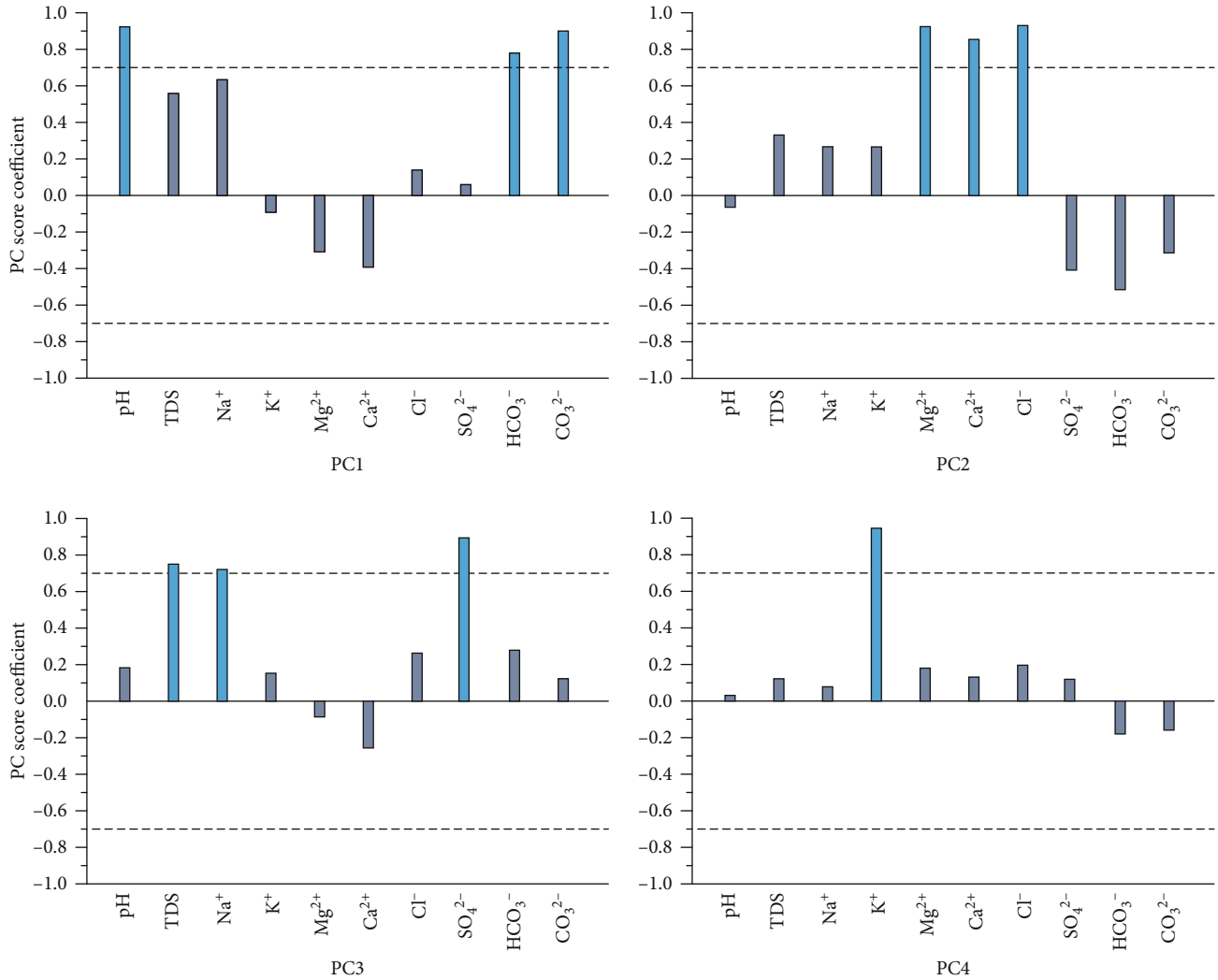

Figure 6: Coefficient scores for the PCs in the principal component analysis.

Table 6: Saturation indices (SI) of minerals in the coalbed-produced water.

Minerals	Saturation index									
	DFS-05	DFS-09	DFS-45	DFS-69	DFS-128	DFS-131	DFS-133	DFS-148	DFS-M68	Chemical formula
Anhydrite	-1.33	-1.26	-0.53	-1.29	-1.22	-0.87	-0.08	0.40	-2.11	$CaSO_4$
Aragonite	/	/	/	3.16	/	/	2.40	2.63	/	$CaCO_3$
Calcite	/	/	/	3.3	/	/	2.54	2.77	/	$CaCO_3$
Dolomite	/	/	/	6.67	/	/	5.32	5.61	/	$CaMg(CO_3)_2$
Gypsum	-1.18	-1.19	-0.43	-1.19	-1.14	-0.79	0.01	0.48	-1.92	$CaSO_4 \bullet 2H_2O$
Halite	-0.37	0.18	-0.02	-0.01	0.13	0.07	-0.02	-0.01	-0.70	NaCl
Sylvite	-2.52	-2.13	-2.22	-2.65	-2.14	1.67	-2.40	-2.10	-2.80	KCl

Note: "/" indicates that the mineral does not occur in the water.

$$Ca(HCO_3)_2 \rightarrow CaCO_3 + H_2O + CO_2 \quad (4)$$

$$Ca^{2+}(\text{water}) + 2HCO_3^- + 2Na(\text{rock}) \rightarrow 2Na^+(\text{water}) + 2HCO_3^- + Ca(\text{rock}) \quad (5)$$

Ion contents are also important indicators of the sedimentary environment [48]. The high content of Na^+ and low ranges of Ca^{2+} and Mg^{2+} of the water in the central and western parts of the study area show that the underground coalbed was in a closed groundwater environment. Because the floor of the no. 4 coalbed developed a stable, water-resistant layer, and the apex was a vulnerable aquifer. The sampling points (DFS-45, DFS-05, DFS-131, and DFS-M68) in the central and eastern parts of the Dafosi biogenic

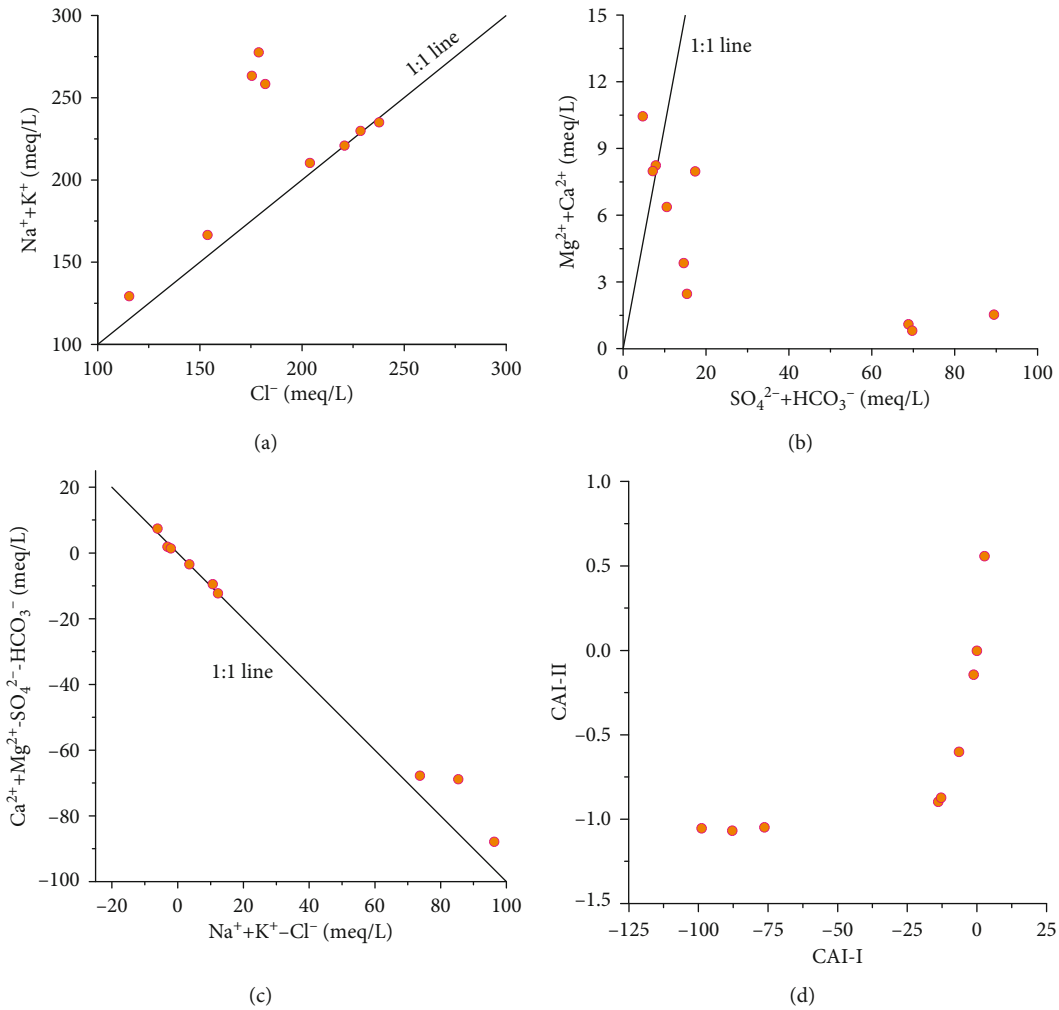

Figure 7: Relationship between hydrochemical compositions: (a) molar ratio of TDS vs. (Na^++K^+); (b) molar ratio of (SO_4^{2-}+HCO_3^-) vs. (Ca^{2+}+Mg^{2+}-SO_4^{2-}-HCO_3^-); (c) (Na^++K^+-Cl^-) vs. (Mg^{2+}+Ca^{2+}); (d) chloro-alkaline indices (CAI), CAI − I = [Cl^- − (Na^+ + K^+)]/Cl^-, CAI − II = [Cl^- − (Na^+ + K^+)]/(SO_4^{2-} + HCO_3^- + CO_3^{2-}). The ionic unit is meq/L.

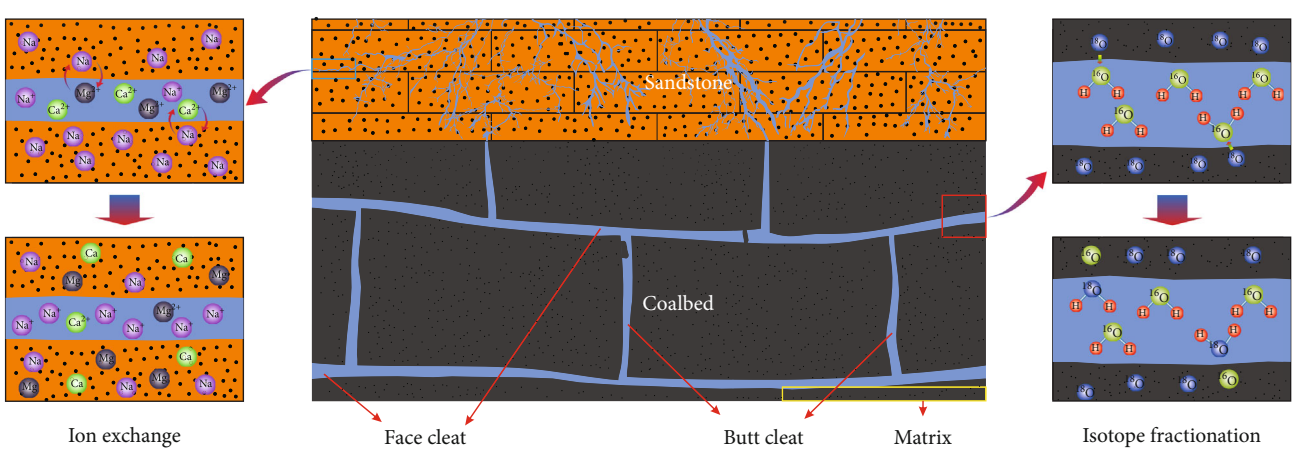

Figure 8: Schematic diagram of water-rock interaction.

gas field also had lower Na^+ concentrations which means that these areas were not entirely closed. There may be faults in the core of the Qijia anticline that allow atmospheric (meteoric) water to flow into coalbeds and migrate to both wings [27]. The TDS of the coalbed-produced water samples in the study area was generally high. Simultaneously, the

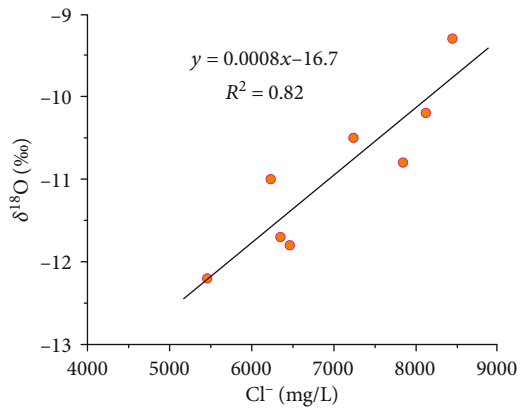

Figure 9: Chloride ion concentration and oxygen isotope composition.

coalbed depth was relatively shallow and should be affected by evaporation during early water recharge, as shown in the Gibbs diagram (Figure 3).

Hydrogen and oxygen isotopic exchange can also occur between the water and the coal organic matter when groundwater flows through the coalbed [8]. The isotopic compositions of hydrogen and oxygen of coalbed-produced water in the study area were low in ^{2}H and relatively enriched in ^{18}O in most well positions, indicating that water-rock interactions have occurred between the groundwater and coalbed. As shown in Figure 9, there was a positive correlation between chlorine ion concentration and oxygen isotope composition reflecting the mixing of meteoric water and paleoformation water in the coalbed. The lightening of the ^{16}O isotopic composition of the coal is described in Figure 8 and caused by the following reaction (Equation (6)) [8].

$$H_2{}^{16}O + {}^{18}O\,(\text{coal}) = H_2{}^{18}O + {}^{16}O\,(\text{coal}) \tag{6}$$

The ^{18}O drift characteristics of the produced water may be related because the oxygen content was higher than that of hydrogen in the coalbed [27]. The produced water sample (DFS-133) is located in the core of Qijia anticline plotted on the CMWL, showing meteoric water recharge characteristics. Therefore, evaporation also tends to enrich heavy isotopes in the residual water, with light isotopes preferring to enter the gas phase. The reason is that the crust was uplifted due to the Yanshanian orogenies, and the overlying strata were weathered and eroded, resulting in structural fissures that connected the coal-bearing strata to the surface water environment, and evaporation occurs. The recharging of source waters by atmospheric precipitation was then conducive to the generation of secondary biogenic CBM [49].

5. Conclusions

The average pH of coalbed-produced water in the Dafosi biogenic gas field is weakly alkaline, at 8.1. The Na^+ content ranges from 2968 to 6367.6 mg/L, accounting for >96% of all cations, while the Cl^- content ranges from 4096.6 to 8441.8 mg/L and accounts for 60–97% of all anions. The hydrodynamic conditions are weak, and the TDS concentration is generally high, ranging from 7601.9 to 16505.6 mg/L, indicating that groundwater is affected by evaporation during recharge. The primary ions in the produced waters of the study area are Na^+, Cl^-, and $HCO_3{}^-$.

Four main factors (PC1–4) were determined by principal component analysis. PC1 mainly represented the $HCO_3{}^-$ hydrolyzed to produce OH^-, and result in the produced water is weakly alkaline. At the same time, PC2 showed the effects of water recharge. The results of water-rock interactions are expressed as PC3, manifested as the increase in Na^+ in the produced water and the further reduction of Ca^{2+} and Mg^{2+}, and PC4 denoted the influence of fracturing fluids on the coalbed-produced water.

The Na^+ in coalbed-produced water are mainly derived from the dissolution of sodic salts and exchange with Ca^{2+} and Mg^{2+} in coalbed or surrounding rocks mainly derived from the dissolution of gypsum salts or minerals, resulting in the enrichment of Na^+ and a lack of Ca^{2+} and Mg^{2+} in the produced water. Halite is the main control factor to the chemical composition of groundwater ions. The ^{18}O drift and enrichment characteristics in the coalbed-produced water are due to oxygen isotope fractionation. Early evaporation is also contributed to the enrichment of TDS and ^{18}O in the water.

Data Availability

The (Tables 1–6) data used to support the findings of this study are included within the article.

Conflicts of Interest

The authors declare that they have no conflicts of interest.

Authors' Contributions

Yuan Bao and Chaoyong Wang contributed equally to this work.

Acknowledgments

We especially appreciate the assistance of Zheng Wang and Jiaqian Chen in collecting the samples. Liang Guo from the Xi'an University of Science and Technology is gratefully acknowledged for the discussion and constructive comments for improving the quality of the manuscript. This work was supported by the National Natural Science Foundation of China (grant numbers 41972183 and 41502156), the "Chunhui Plan" Cooperative Research for Ministry of Education and Key Laboratory of Coalbed Methane Resources, and Reservoir Formation Process of the Ministry of Education (China University of Mining and Technology) (No. 2020-001).

References

[1] Z. Zhang and Y. Qin, "A preliminary investigation on water quality of coalbed natural gas produced water for beneficial uses: a case study in the southern Qinshui Basin, North

China," *Environmental Science and Pollution Research*, vol. 25, no. 22, pp. 21589–21604, 2018.

[2] D. Ma, L. Li, X. Li et al., "Contrastive experiment of adsorption-desorption between CH_4 and CO_2 in Coal Seam 4 of Dafosi Coal Mine," *Journal of China Coal Society*, vol. 39, no. 9, pp. 1938–1944, 2014.

[3] Y. Bao, Y. Ju, Z. Yin, J. Xiong, G. Wang, and Y. Qi, "Influence of reservoir properties on the methane adsorption capacity and fractal features of coal and shale in the upper Permian coal measures of the South Sichuan coalfield, China," *Energy Exploration & Exploitation*, vol. 38, no. 1, pp. 57–78, 2020.

[4] S. Y. Park and Y. Liang, "Biogenic methane production from coal: a review on recent research and development on microbially enhanced coalbed methane (MECBM)," *Fuel*, vol. 166, no. 15, pp. 258–267, 2016.

[5] Y. Bao, Y. Ju, H. Huang, J. Yun, and C. Guo, "Potential and constraints of biogenic methane generation from coals and mudstones from Huaibei coalfield, eastern China," *Energy & Fuels*, vol. 33, no. 1, pp. 287–295, 2019.

[6] Y. Li, J. Yang, Z. Pan, S. Meng, K. Wang, and X. Niu, "Unconventional natural gas accumulations in stacked deposits: a discussion of upper Paleozoic coal-bearing strata in the east margin of the Ordos Basin, China," *Acta Geologica Sinica - English Edition*, vol. 93, no. 1, pp. 111–129, 2019.

[7] Q. Huang, S. Liu, G. Wang, B. Wu, and Y. Zhang, "Coalbed methane reservoir stimulation using guar-based fracturing fluid: a review," *Journal of Natural Gas Science and Engineering*, vol. 66, pp. 107–125, 2019.

[8] C. Guo, Y. Qin, Y. Xia et al., "Geochemical characteristics of water produced from CBM wells and implications for commingling CBM production: a case study of the Bide-Santang Basin, western Guizhou, China," *Journal of Petroleum Science and Engineering*, vol. 159, pp. 666–678, 2017.

[9] Z. Zhang, Y. Qin, J. Bai, G. Li, X. Zhuang, and X. Wang, "Hydrogeochemistry characteristics of produced waters from CBM wells in southern Qinshui basin and implications for CBM commingled development," *Journal of Natural Gas Science and Engineering*, vol. 56, pp. 428–443, 2018.

[10] C. Guo, Y. Qin, C. Wu, and L. Lu, "Hydrogeological control and productivity modes of coalbed methane commingled production in multi-seam areas: A case study of the Bide–Santang Basin, western Guizhou, South China," *Journal of Petroleum Science and Engineering*, vol. 189, p. 107039, 2020.

[11] Y. Bao, C. Wei, and B. Neupane, "Generation and accumulation characteristics of mixed coalbed methane controlled by tectonic evolution in Liulin CBM field, eastern Ordos Basin, China," *Journal of Natural Gas Science and Engineering*, vol. 28, pp. 262–270, 2016.

[12] C. Harmon, "Isotopic variations in meteoric waters," *Science*, vol. 133, pp. 1702-1703, 1961.

[13] L. Chen, H. Gui, and X. Yin, "Monitoring of flow field based on stable isotope geochemical characteristics in deep groundwater," *Environmental Monitoring and Assessment*, vol. 179, no. 1-4, pp. 487–498, 2011.

[14] C. Hao, Y. Huang, P. He, and W. Sun, "Isotope drift characteristics in Ordovician limestone karst water caused by coal mining in northern China," *Mine Water and the Environment*, vol. 38, no. 3, pp. 507–516, 2019.

[15] E. Bozau, T. Licha, and W. LieBmann, "Hydrogeochemical characteristics of mine water in the Harz Mountains, Germany," *Chemie der Erde-Geochemistry*, vol. 77, no. 4, pp. 614–624, 2017.

[16] X. Li, X. Fu, Y. Ge, and X. Chang, "Research on sequence stratigraphy, hydrogeological units and commingled drainage associated with coalbed methane production: a case study in Zhuzang syncline of Guizhou province, China," *Hydrogeology Journal*, vol. 24, no. 8, pp. 2171–2187, 2016.

[17] X. Huang, G. Wang, X. Liang, L. Cui, L. Ma, and Q. Xu, "Hydrochemical and stable isotope (δD and δ^{18}O) characteristics of groundwater and hydrogeochemical processes in the Ningtiaota coalfield, Northwest China," *Mine Water and the Environment*, vol. 37, no. 1, pp. 119–136, 2018.

[18] Q. Li, Y. Ju, W. Lu, G. Wang, B. Neupane, and Y. Sun, "Water-rock interaction and methanogenesis in formation water in the southeast Huaibei coalfield, China," *Marine and Petroleum Geology*, vol. 77, pp. 435–447, 2016.

[19] C. Wu, Z. Yang, Y. Qin, J. Chen, Z. Zhang, and Y. Li, "Characteristics of hydrogen and oxygen isotopes in produced water and productivity response of CBM wells in western Guizhou," *Energy & Fuels*, vol. 32, no. 11, pp. 11203–11211, 2018.

[20] C. Guo, Y. Qin, D. Ma et al., "Ionic composition, geological signature and environmental impacts of coalbed methane produced water in China," *Energy Sources, Part A: Recovery, Utilization, and Environmental Effects*, vol. 11, pp. 1259–1273, 2021.

[21] P. Li, R. Tian, and R. Liu, "Solute geochemistry and multivariate analysis of water quality in the Guohua phosphorite mine, Guizhou province, China," *Exposure and Health*, vol. 11, no. 2, pp. 81–94, 2019.

[22] W. Chen, B. Pradhan, S. Li et al., "Novel hybrid integration approach of bagging-based fisher's linear discriminant function for groundwater potential analysis," *Natural Resources Research*, vol. 28, no. 4, pp. 1239–1258, 2019.

[23] Z. Zhang, D. Yan, X. Zhuang et al., "Hydrogeochemistry signatures of produced waters associated with coalbed methane production in the Southern Junggar Basin," *Environmental Science and Pollution Research*, vol. 26, no. 31, pp. 31956–31980, 2019.

[24] B. Neogi, A. K. Singh, D. D. Pathak, and A. Chaturvedi, "Hydrogeochemistry of coal mine water of north Karanpura coalfields, India: implication for solute acquisition processes, dissolved fluxes and water quality assessment," *Environment and Earth Science*, vol. 76, no. 14, pp. 489–506, 2017.

[25] Y. Chen, S. Zhu, and S. Xiao, "Discussion on controlling factors of hydrogeochemistry and hydraulic connections of groundwater in different mining districts," *Natural Hazards*, vol. 99, no. 2, pp. 689–704, 2019.

[26] M. Redwan, A. A. Abdel Moneim, and M. A. Amra, "Effect of water–rock interaction processes on the hydrogeochemistry of groundwater west of Sohag area, Egypt," *Arabian Journal of Geosciences*, vol. 9, no. 2, pp. 111–125, 2016.

[27] Y. Bao, W. Wang, D. Ma et al., "Gas origin and constraint of δ^{13}C (CH_4) distribution in the Dafosi mine field in the southern margin of the Ordos Basin, China," *Energy & Fuels*, vol. 34, no. 11, pp. 14065–14073, 2020.

[28] H. Xu, D. Z. Tang, D. M. Liu et al., "Study on coalbed methane accumulation characteristics and favorable areas in the Binchang area, southwestern Ordos Basin, China," *International Journal of Coal Geology*, vol. 95, pp. 1–11, 2012.

[29] B. Lin, H. Li, D. Yuan, and Z. Li, "Development and application of an efficient gas extraction model for low-rank high-

gas coal beds," *International Journal of Coal Science & Technology*, vol. 2, no. 1, pp. 76–83, 2015.

[30] G. Hou, M. Zhang, and F. Liu, *Groundwater Exploration in Ordos Basin*, Geo. Publ. House, 2008.

[31] Z. Li, S. Tang, X. Wang et al., "Relationship between water chemical composition and production of coalbed methane wells, Qinshui basin," *Zhongguo Kuangye Daxue Xuebao(Journal of China University of Mining & Technology)*, vol. 40, no. 3, pp. 424–429, 2011.

[32] J. Qian, L. Wang, L. Ma, Y. H. Lu, W. Zhao, and Y. Zhang, "Multivariate statistical analysis of water chemistry in evaluating groundwater geochemical evolution and aquifer connectivity near a large coal mine, Anhui, China," *Environmental Earth Sciences*, vol. 75, no. 9, pp. 747–757, 2016.

[33] B. Zhou, Y. Qin, and Z. Yang, "Ion composition of produced water from coalbed methane wells in western Guizhou, China, and associated productivity response," *Fuel*, vol. 265, p. 116939, 2020.

[34] R. J. Gibbs, "Mechanisms controlling world water chemistry," *Science*, vol. 170, no. 3962, pp. 1088–1090, 1970.

[35] S. Zheng, G. Hou, and B. Ni, "Study on hydrogen and oxygen stable isotopes of meteoric water in China," *Chinese Science Bulletin*, vol. 13, pp. 801–806, 1983.

[36] S. D. Golding, C. J. Boreham, and J. S. Esterle, "Stable isotope geochemistry of coal bed and shale gas and related production waters: a review," *International Journal of Coal Geology*, vol. 120, pp. 24–40, 2013.

[37] R. K. Steinhorst and R. E. Williams, "Discrimination of groundwater sources using cluster analysis, MANOVA, canonical analysis and discriminant analysis," *Water Resources Research*, vol. 21, no. 8, pp. 1149–1156, 1985.

[38] T. Helstrup, N. O. Jørgensen, and B. Banoeng-Yakubo, "Investigation of hydrochemical characteristics of groundwater from the Cretaceous-Eocene limestone aquifer in southern Ghana and southern Togo using hierarchical cluster analysis," *Hydrogeology Journal*, vol. 15, no. 5, pp. 977–989, 2007.

[39] J. E. Cortes, L. F. Muñoz, C. A. Gonzalez et al., "Hydrogeochemistry of the formation waters in the San Francisco field, UMV basin, Colombia - a multivariate statistical approach," *Journal of Hydrology*, vol. 539, pp. 113–124, 2016.

[40] H. Huang, S. Sang, Y. Miao, Z. Dong, and H. Zhang, "Trends of ionic concentration variations in water coproduced with coalbed methane in the Tiefa Basin," *International Journal of Coal Geology*, vol. 182, pp. 32–41, 2017.

[41] V. Voast and A. Wayne, "Geochemical signature of formation waters associated with coalbed methane," *AAPG Bulletin*, vol. 87, no. 4, pp. 667–676, 2003.

[42] Y. Guo, J. Wei, H. Gui, Z. Zhang, and M. Hu, "Evaluation of changes in groundwater quality caused by a water inrush event in Taoyuan coal mine, China," *Environmental Earth Sciences*, vol. 79, no. 24, p. 528, 2020.

[43] E. Lakshmanan, R. Kannan, and M. S. Kumar, "Major ion chemistry and identification of hydrogeochemical processes of ground water in a part of Kancheepuram district, Tamil Nadu, India," *Environmental Geosciences*, vol. 10, no. 4, pp. 157–166, 2003.

[44] Y. Li, S. Tang, S. Zhang, Z. Xi, and P. Wang, "Biogeochemistry and water–rock interactions of coalbed methane co-produced water in the Shizhuangnan block of the southern Qinshui basin, China," *Water*, vol. 12, no. 1, pp. 130–148, 2020.

[45] P. Li, H. Qian, J. Wu, Y. Zhang, and H. Zhang, "Major ion chemistry of shallow groundwater in the Dongsheng coalfield, Ordos basin, China," *Mine Water and the Environment*, vol. 32, no. 3, pp. 195–206, 2013.

[46] P. Liu, N. Hoth, C. Drebenstedt, Y. Sun, and Z. Xu, "Hydrogeochemical paths of multi-layer groundwater system in coal mining regions – using multivariate statistics and geochemical modeling approaches," *Science of The Total Environment*, vol. 601-602, pp. 1–14, 2017.

[47] K. Zhang, J. Gao, B. Jiang, J. Han, and M. Chen, "Experimental study on the mechanism of water-rock interaction in the coal mine underground reservoir," *Journal of China Coal Society*, vol. 44, no. 12, pp. 3760–3772, 2019.

[48] C. Song, Y. Zeng, M. Yan et al., "Sedimentary conditions of evaporites in the late Jurassic Xiali formation, Qiangtang Basin: evidence from geochemistry records," *Acta Geologica Sinica - English Edition*, vol. 91, no. 1, pp. 156–174, 2017.

[49] Q. Li, Y. Ju, Y. Bao, Z. Yan, X. Li, and Y. Sun, "Composition, origin, and distribution of coalbed methane in the Huaibei Coalfield, China," *Energy & Fuels*, vol. 29, no. 2, pp. 546–555, 2015.

Hindawi
Geofluids
Volume 2021, Article ID 9940375, 12 pages
https://doi.org/10.1155/2021/9940375

Research Article

In Situ Stress Distribution and Its Control on the Coalbed Methane Reservoir Permeability in Liulin Area, Eastern Ordos Basin, China

Peng Feng,[1,2] **Song Li**,[1,2] **Dazhen Tang**,[1,2] **Liangjun Wu**,[3] **Yan Zhang**,[1,2] **and Guanghao Zhong**[1,2]

[1]*School of Energy Resources, China University of Geosciences (Beijing), Beijing 100083, China*
[2]*Coal Reservoir Laboratory of National Engineering Research Center of CBM Development & Utilization, China University of Geosciences (Beijing), Beijing 100083, China*
[3]*Changqing Oilfield Company Oil Production Plant No. 8, China*

Correspondence should be addressed to Song Li; lisong@cugb.edu.cn

Received 9 March 2021; Accepted 7 May 2021; Published 25 May 2021

Academic Editor: Andrew Manning

Permeability is one of the important factors that affect the production efficiency of coalbed methane, and it is mainly controlled by in situ stress. Therefore, it is very essential to study the in situ stress and permeability for the extraction of coalbed methane. Based on the injection/falloff well test and in situ stress measurement of 35 coalbed methane wells in the Liulin area in the east of the Ordos basin, the correlations between initial reservoir pressure, in situ stress, lateral stress coefficient, permeability, and burial depth were determined. Finally, the distribution characteristics of in situ stress and its influence on permeability were analyzed systematically. The results show that with the increase of burial depth, the initial reservoir pressure and in situ stress both increase, while the lateral stress coefficient decreases. The permeability variation is related to the type of stress field in different burial depths, and its essence is the deformation and destruction of coal pore structures caused by stress. The distribution characteristics of in situ stress at different depths and its effect on permeability are as follows: at depths < 800 m, the horizontal principal stress is dominant ($\sigma_H \geq \sigma_v > \sigma_h$) and the permeability is a simple decreasing process with the increase of the depth; at depths > 800 m, the vertical stress is dominant ($\sigma_v \geq \sigma_H > \sigma_h$). The permeability of most coal is very small due to the large in situ stresses in this depth zone. However, because of the stress release at the syncline axis, coal with high permeability is still possible at this depth zone. Due to the existence of high permeability data points at burial depth (>800 m) and the fitting relationship between permeability and vertical stress, the maximum and minimum horizontal principal stress is poor. However, the coal permeability and lateral stress coefficient show a good negative exponential relationship. This indicates that the lateral stress coefficient can be used to predict permeability better.

1. Introduction

In situ stress is a type of internal stress in the Earth's crust, which is mainly controlled by gravity and tectonic activity [1–5]. Permeability is one of the important factors affecting the efficiency of coalbed methane (CBM) production. Because the porosity and permeability of coal seams are very low, the commercial production capacity of coal seams can only be improved through large-scale fracturing, and in situ stress is the key factor affecting the effect of fracturing [6–8]. In situ stress can also help predict permeability and fluid flow in coalbed methane reservoirs [9–12]. The vertical stress is relatively simple and is mainly affected by the overlying rock mass. The horizontal principal stress is

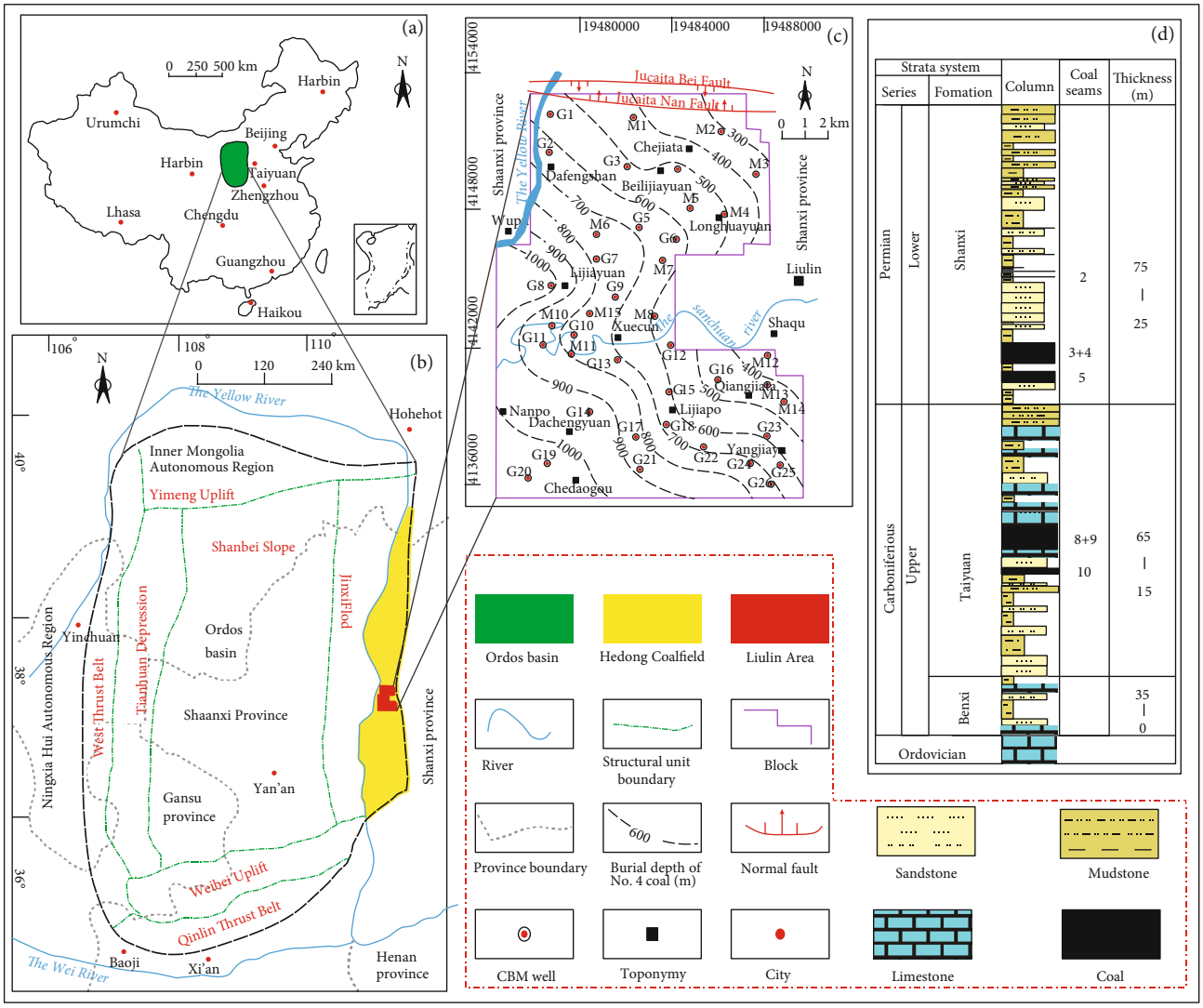

Figure 1: Location of the Liulin area: (a) locations of the Ordos basin in the China map; (b) general location of the eastern margin of the Ordos basin in the tectonic division map; (c) specific locations of the CBM blocks and wells in the eastern margin of the Liulin area; (d) composite stratigraphic column showing coal-bearing formations in the Liulin area.

mainly influenced by tectonic activity and rock geological activity, and it is much more complex because it is constantly changing over time [13]. Clearly, it is an indispensable link for the extraction of coalbed methane to study the in situ stress and permeability of coal seams [14–19].

The Ordos basin is located in the middle of the North China Plate and has become the second largest coalbed methane development base after the Qinshui Basin since the 1980s [20–23]. Liulin area is located in the east of the Ordos basin. Due to the advantages of many layers of coal, large thickness, high gas content, simple geological structure, and moderate burial depth, this area has attracted extensive attention of coalbed methane geologists. In the 1990s, Liulin area was even called "China's San Juan" by geologists. Enron, Phillips, ARCO, BP, Texaco, Lowell, PetroChina, and Sinopec have successively conducted coalbed methane exploration in this area. Liulin area has become a new highlight of typical medium-size coalbed methane exploration and development in China [24–26].

Up to now, little research has been carried out on the geology of the coalbed methane field in the Liulin area. For example, some of the specific studies include the following: the porous characteristics of coal developed in different coal facies have been studied [27]; the causes of abnormally high pressure in the Carboniferous No. 8 coal reservoir were considered to be closely related to local hydrodynamic traps [24]; the characteristics of water production during coalbed methane extraction were studied by analyzing stable isotopes in groundwater [28]; the coalbed methane preservation mechanism was researched by analyzing coalbed methane geology, hydrogeology, and experimental data [29]; and the migration mechanism of coalbed methane was studied by analyzing the evolution stage of coalbed methane [30]. However, in terms of in situ stress and permeability, most scholars take the

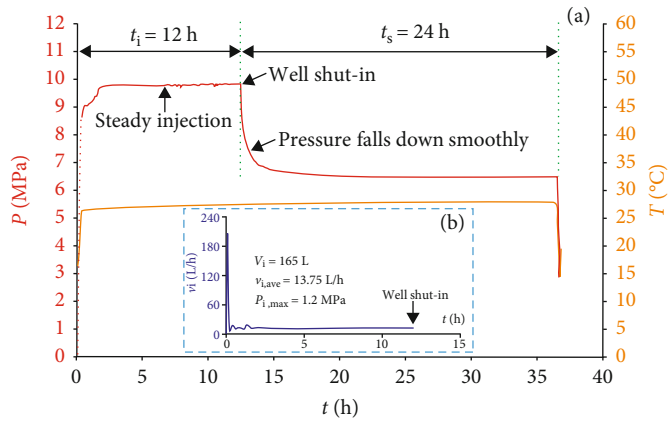

Figure 2: Injection/falloff curves of an actual CBM well: (a) relationship between pressure/temperature and time; (b) the relationship between the injection rate at the surface and time: V_i represents the total injection volume, $v_{i,ave}$ represents the average injection rate at the surface, P represents the pressure, P_i represents the maximum injection pressure at the surface, t represents the time, t_i represents the injection time, t_s represents the well shut-in time, and T represents the coal reservoir temperature.

eastern part of the Ordos basin as the study area, and few scholars have systematically studied the Liulin area [31–35]. Therefore, the distribution characteristics of in situ stress and its influence on permeability in the Liulin area still need more systematic study.

In this study, the correlations among parameters such as in situ stress, permeability, and burial depth were determined by statistical analysis and regression analysis using data from 35 coalbed methane wells in the Liulin area. Finally, the influence of in situ stress on the permeability of the coal reservoir in the Liulin area is revealed, which provides a basis for the reasonable exploration and development of coalbed methane in this area.

2. Geological Setting

Liulin area is located in the west of Shanxi Province (Figure 1(a)). The geographical coordinates are 110°44′00″ ~110°53′00″ east longitude and 37°21′00″~37°31′00″ north latitude. The east-west width of this area is approximately 10.5 km and the north-south length is approximately 18.5 km, covering an area of 194.4156 km^2 (Figure 1(b)).

The structural position of the Liulin area is located in the north-south tectonic belt from the east bank of the Yellow River to the west slope of Lüliang Mountain. It is a monoclinic structure inclined to the west, and some secondary folds are developed on the monoclinic structure. There are few faults in this area and its structure is stable. Only in the north of the area are two large normal faults in the south and north of Jucaita and some small faults derived from them (Figure 1(c)). The topography of this area is high in the east and south and low in the west and north. The surface erosion is serious, and the surface water system develops with the topography. There are 14 coal seams in this area (Figure 1(d)), and the main coal-bearing strata are the Shanxi Formation and Taiyuan Formation, including 9 in the Taiyuan Formation and 5 in the Shanxi Formation [24, 36]. The main coal seams for coalbed methane extraction are

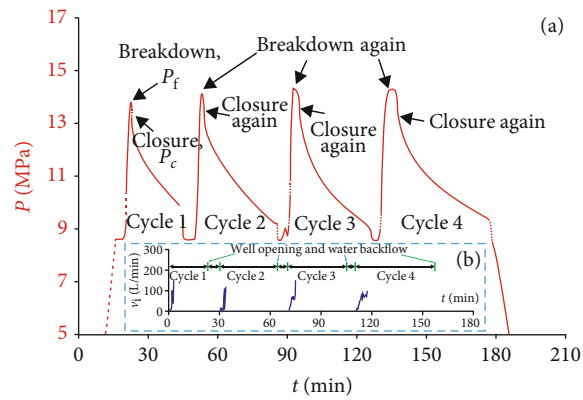

Figure 3: In situ stress measurement curve of an actual CBM well: (a) relationship between pressure and time; (b) relationship between the injection rate and time at the surface: P_f represents the fracturing pressure and P_c represents the closing pressure.

the No. 3 + 4 and No. 5 coal seams in the Shanxi Formation and No. 8 + 9 coal seam in the Taiyuan Formation [26]. The Taiyuan Formation was affected by an epicontinental sea and the coal seams were formed in a tidal flat environment after marine regression [37]. However, when the Shanxi Formation was deposited, the environment evolved to a prograded delta, and coal seams were formed on the floodplain of the delta interdistributary area [6].

3. Methodology

3.1. Test Method. The calculation of in situ stress often requires some parameters. To obtain these parameters, the coalbed methane well test method is generally adopted [31, 33]. The basic principle of this test is that by changing the pressure of the well, the equilibrium state of the fluid flow in the reservoir will be broken. And a pressure disturbance will be caused at the bottom of the well, which will continue

Table 1: Injection/falloff and in situ stress test parameters in the Liulin area.

Sample	H (m)	K (mD)	T (°C)	P_o (MPa)	P_c (MPa)	P_f (MPa)	σ_h (MPa)	σ_H (MP)	σ_v (MPa)	λ
Well 1	479.32	0.83	23.61	4.39	8.82	9.42	8.82	13.45	12.94	0.86
Well 2	486.91	1.43	25.35	2.94	6.98	8.17	6.98	10.63	13.15	0.67
Well 3	488.00	0.03	24.57	3.62	11.04	12.12	11.04	18.17	13.18	1.11
Well 4	495.25	0.06	24.72	4.21	9.31	10.42	9.31	14.10	13.37	0.88
Well 5	539.50	1.92	26.55	4.82	6.50	7.75	6.50	7.73	14.57	0.49
Well 6	540.05	0.09	28.35	2.23	12.66	14.16	12.66	22.39	14.58	1.20
Well 7	553.66	0.16	28.60	5.07	13.24	13.67	13.24	21.78	14.95	1.17
Well 8	562.59	0.06	28.40	5.10	13.31	13.60	13.31	22.03	15.19	1.16
Well 9	564.80	0.64	N	2.58	8.19	9.19	8.19	13.60	15.25	0.71
Well 10	577.45	0.28	28.00	2.95	12.15	13.36	12.15	20.94	15.59	1.06
Well 11	584.35	0.08	26.80	4.94	15.00	15.11	15.00	25.75	15.78	1.29
Well 12	585.75	0.04	28.20	3.03	10.40	11.48	10.40	17.49	15.82	0.88
Well 13	611.26	0.12	29.30	5.43	16.01	17.56	16.01	25.84	16.50	1.27
Well 14	617.30	0.10	31.10	5.42	14.82	15.22	14.82	24.62	16.67	1.18
Well 15	620.74	N	N	N	17.73	18.99	17.73	29.54	16.76	1.41
Well 16	624.23	N	N	N	12.61	12.87	12.61	21.23	16.85	1.00
Well 17	671.55	0.26	28.75	5.41	13.00	13.60	13.00	20.79	18.13	0.93
Well 18	678.55	0.13	29.00	5.59	13.42	13.96	13.42	21.51	18.32	0.95
Well 19	698.76	0.06	30.10	6.29	14.38	15.22	14.38	22.43	18.87	0.98
Well 20	710.10	0.11	30.06	7.49	15.71	17.04	15.71	23.40	19.17	1.02
Well 21	719.54	0.06	30.71	6.82	16.47	17.16	16.47	26.23	19.43	1.10
Well 22	746.19	0.11	30.20	8.33	16.10	16.88	16.10	23.89	20.15	0.99
Well 23	759.33	0.26	28.70	6.58	13.43	11.33	13.43	23.18	20.50	0.89
Well 24	760.97	0.02	28.20	6.55	13.63	14.47	13.63	20.67	20.55	0.83
Well 25	760.97	0.18	30.50	8.41	15.67	16.81	15.67	22.59	20.55	0.93
Well 26	769.48	0.62	33.15	8.25	14.48	16.03	14.48	19.96	20.78	0.83
Well 27	817.16	N	N	N	14.73	18.42	14.73	18.09	22.06	0.74
Well 28	862.83	N	N	N	12.11	12.55	12.11	18.22	23.30	0.65
Well 29	871.96	1.70	27.76	6.43	13.65	14.22	13.65	21.10	23.54	0.74
Well 30	913.68	N	N	N	11.39	12.76	11.39	15.43	24.67	0.54
Well 31	965.15	0.07	35.90	8.90	17.72	18.05	17.72	27.01	26.06	0.86
Well 32	973.90	0.21	36.80	9.05	16.85	17.59	16.85	24.71	26.30	0.79
Well 33	1013.59	1.39	32.67	7.85	14.87	15.47	14.87	22.09	27.37	0.68
Well 34	1016.00	0.18	38.50	9.34	16.89	18.29	16.89	23.84	27.43	0.74
Well 35	1019.85	2.26	32.52	7.08	16.42	20.91	16.42	22.07	27.54	0.70

to expand around the well over time until a new equilibrium state is formed. Therefore, we use the test instrument to record the change of bottom hole pressure with time; the parameters we need can be obtained. This test mainly includes two parts: the injection/falloff test and the multicycle hydraulic fracturing method.

The process of the injection/falloff test is first to inject water into the well with a constant rate and low injection pressure (lower than the fracture pressure of coal). After a period of time, a high pressure (higher than the original reservoir pressure) distribution area will be generated around the well, and then, the well is closed, allowing the pressure to gradually balance with the original reservoir pressure. During both the injection and shut-in periods, the change of bottom hole pressure with time is recorded (Figure 2). Finally, the data are analyzed by using the semilog (Horner) and double-log linear analysis methods; the reservoir pressure (P_o), permeability (K), and other parameters of the coal seam can be obtained [6, 38].

In situ stress is usually measured by the multicycle hydraulic fracturing method [33, 39, 40]. The process of hydraulic fracturing is briefly described as follows: in the initial stage of water injection, the fractures of target seams are closed due to the small pressure in the fractures (less than the fracture closure pressure), while the fractures are opened when the pressure in them increases to greater than the

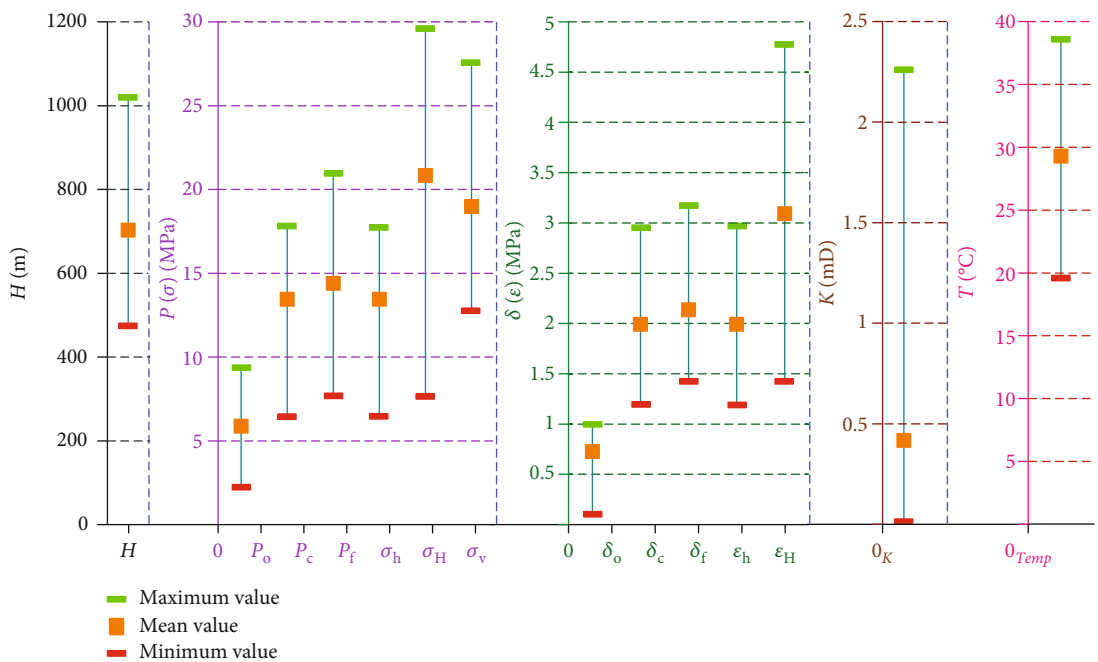

Figure 4: Stock chart of injection/falloff well test and in situ stress measurement parameters in Liulin area. H: represents the burial depth; P_o: represents the initial reservoir pressure; P_c: represents closure pressure; P_f: represents fracture pressure; σ_h: represents the minimum horizontal principal stress; σ_H: represents the maximum horizontal principal stress; σ_v: represents vertical stress; δ_o: represents the initial reservoir pressure gradient; δ_c: represents closure pressure gradient; δ_f: represents fracture pressure gradient; ε_h: represents the minimum horizontal principal stress gradient; ε_H: represents the maximum horizontal principal stress gradient; K: represents the permeability; Temp: represents the reservoir temperature.

closing pressure. At this point, the water injection will be stopped, and the pressure in the fracture will gradually decrease over time. By using the time square root method to analyze the curve of the pressure changing with time, the fracture pressure (P_f) and closure pressure (P_c) can be further obtained. To reduce the error, the above process is generally carried out in four cycles, and two or three cycles with clear fracturing and closing effects were chosen for analysis (Figure 3).

3.2. Calculation Method. The horizontal principal stress can be calculated by using the parameters obtained from the above tests, including reservoir pressure, closure pressure, and fracture pressure. It is generally considered that the minimum horizontal principal stress is equivalent to the closure pressure [41].

$$\sigma_h = P_c, \tag{1}$$

where σ_h is the minimum horizontal principal stress (MPa).

The maximum horizontal principal stress can be calculated as follows [42]:

$$\sigma_H = 3P_c - P_o - P_f + T, \tag{2}$$

where σ_H is the maximum horizontal principal stress (MPa), P_c is the closure pressure (MPa), P_f is the fracture pressure (MPa), P_o is the rock pore pressure (initial reservoir pressure), and T is the tensile strength of the rock around the borehole (MPa), and the value of T in this study is 0.8.

The vertical stress is equivalent to the gravity of the overlying rock and is proportional to the depth. Brown and Hock collected 116 original in situ stress test data from all over the world and analyzed the relationship between vertical stress and depth as follows [1]:

$$\sigma_v = 0.027H, \tag{3}$$

where σ_v is the vertical stress (MPa) and H is the burial depth (m).

4. Results

4.1. Results of In Situ Stress and Injection/Falloff Well Tests. A total of 35 injection/falloff and in situ stress test data were collected, and the data is plotted in Table 1. It can be seen that at coal seam burial depths (H) 479.32-1019.85 m (average 704.59 m), the initial reservoir pressure (P_o) is 2.23-9.34 MPa (average 5.84 MPa) and the pressure gradient (δ_o) is 0.10-0.98 MPa/100 m (average 0.73 MPa/100 m), which represent an underpressured reservoir. The closure pressure (P_c) is 6.50-17.73 MPa (average 13.42 MPa), and the pressure gradient (δ_c) is 1.21-2.98 MPa/100 m (average 1.98 MPa/100 m). The coal seam fracture pressure (P_f) is 7.75-20.91 MPa (average 14.40 MPa), and the pressure

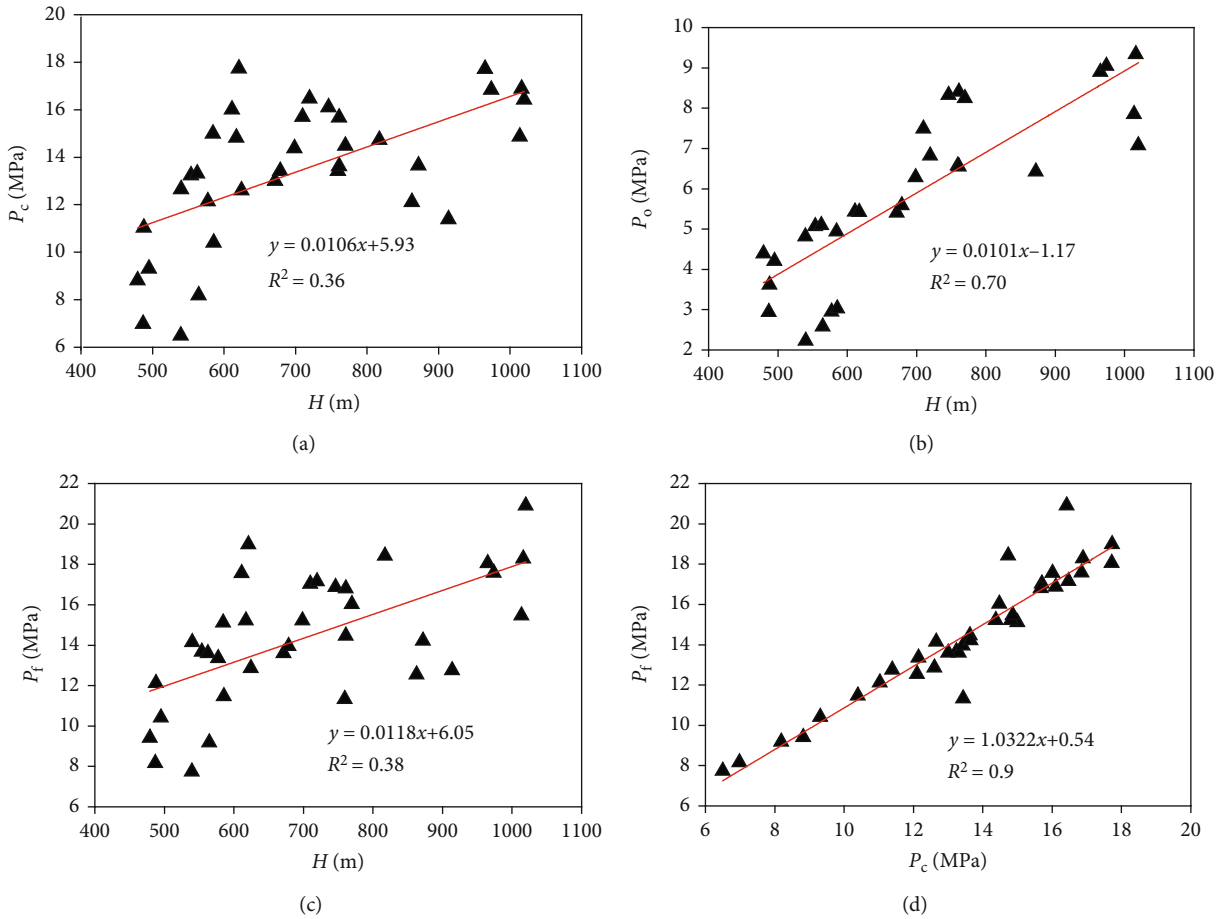

Figure 5: Scatter diagrams of reservoir pressure, fracture pressure, closure pressure, and burial depth.

gradient (δ_f) is 1.40-3.38 MPa/100 m (average 2.12 MPa/100 m). The coal reservoir temperature (T) is 23.61-38.50°C with an average of 29.55°C (Figure 4). The permeability (K) of coal reservoirs is 0.02-2.26 mD (average 0.45 mD), most of which are less than 1 mD. This indicates that the study area is dominated by coal reservoirs with low permeability.

According to the above test results, the horizontal principal stress and vertical stress can be calculated by formulas (1), (2), and (3), respectively. The minimum horizontal principal stress (σ_h) is 6.50-17.73 MPa with an average of 13.42 MPa, for which the stress gradient (ε_h) is 1.21-2.95 MPa/100 m with a mean value of 2.0 MPa/100 m. The maximum horizontal principal stress (σ_H) is 7.73-29.54 MPa with an average of 20.76 MPa, and the stress gradient (ε_H) is 1.43-4.76 MPa/100 m and averaged at 3.1 MPa/100 m. And the vertical stress (σ_v) is 12.94-27.54 MPa with an average of 19.02 MPa (Figure 4). In general, the maximum horizontal principal stress in the study area is dominant compared to other stresses.

The results of in situ stress and injection/falloff well tests were analyzed, and it was found that there was a significant linear relationship between the initial reservoir pressure and burial depth (Figure 5(b)). The closure pressure and fracture pressure have a linear relation with burial depth, but the squares of the two correlation coefficients are small (0.36 and 0.38, respectively) (Figures 5(a) and 5(c)). Besides, there is a very obvious linear relationship between closure pressure and fracture pressure (Figure 5(d)).

4.2. Principal Stress Variation with Depth. According to the relationship between horizontal principal stress and vertical stress, the stress field is usually divided into a static stress field, dynamic field, and quasistatic stress field [6]. It is found that in different depth zones, the variation trend of the three in situ stresses is different, and the stress field also shows different results accordingly (Figure 6).

At depths < 800 m, the three in situ stresses all increase with the increase of burial depth, and compared with the vertical stress, the maximum and minimum horizontal principal stresses increase faster. The relationship of these three in situ stresses in the coal reservoir is $\sigma_H \geq \sigma_v > \sigma_h$, that is, the type of stress field is a dynamic field, and the coal reservoir is under a state of extrusion from horizontal direction at this time.

At depths > 800 m, as the burial depth increases, the maximum and minimum horizontal principal stress growth rates decrease and gradually tend to be stable, while the vertical stress still increases at the previous growth rate and

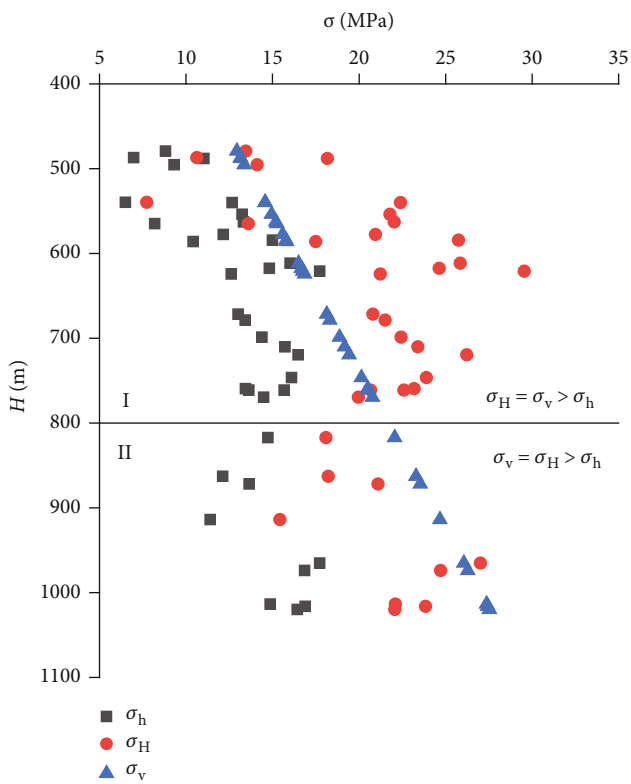

Figure 6: Scatter diagrams of maximum horizontal principle stress, minimum horizontal principle stress, vertical stress, and burial depth (I represents dynamic field; II represents static stress field).

becomes the dominant stress. The relationship of these three in situ stresses in the coal reservoir is $\sigma_v \geq \sigma_H > \sigma_h$, the type of stress field has been transformed into a static stress field, and the coal reservoir is no longer in a horizontal extrusion state in this depth zone.

4.3. The Lateral Stress Coefficient with Depth. To quantitatively reveal the stress state at the specific burial depth, the parameter of the lateral stress coefficient is introduced. Generally, the lateral stress coefficient is defined as the ratio of the average horizontal principal stress to the vertical stress and is expressed as

$$\lambda = \frac{\sigma_H + \sigma_h}{2\sigma_v}, \tag{4}$$

where λ is the lateral stress coefficient.

Through calculation, it can be seen that the lateral stress coefficient of the Liulin area ranges from 0.49 to 1.41, with an average of 0.93. These values are between the Hoek–Brown inner and outer in situ stress envelopes representing the relationship between the ratio and the burial depth worldwide and are close to the Chinese in situ stress envelope (Figure 7). On the whole, the lateral stress coefficient in the study area decreases with the increase of burial depth. However, the coefficient shows different characteristics in different depth zones. At depths < 800 m, this parameter is 0.49-1.41, with an average of 1.03. Moreover, most values are greater than 0.9, which further indicates that the horizontal principal stress is dominant in this depth zone. At depths > 800 m, this parameter is relatively stable, with a range of 0.54-0.86 and an average of 0.72. The value of this parameter is less than 0.9, which further indicates that the vertical stress is dominant in this depth zone. In general, the variation trend of the lateral stress coefficient in different depth zones also well reveals the change of stress field from a dynamic field to a static stress field with the increase of burial depth.

4.4. Permeability Variation with Depth. Reservoir permeability is one of the key factors that determine coalbed methane productivity [33, 43]. The permeability includes matrix permeability and fracture system permeability; the former is almost negligible, and the latter is the main factor to control the percolation conditions of the coal reservoir [44]. Permeability is mainly affected by geological factors such as stress field, burial depth, coal structure, and fractures [5, 45].

With the increase of burial depth, the permeability shows different characteristics in the two depth zones (Figure 8). At depths < 800 m, the permeability decreases with the increase of burial depth, which is 0.02-1.92 mD, with an average of 0.32 mD. At depths > 800 m, the average permeability of the coal reservoir is 0.97 mD, most of which are still very small, while a few increase relative to the shallow part. Compared with the variation of in situ stress with depth, the permeability inflection points at various depths are consistent with the transition points of the stress field types and states at the corresponding depths.

5. Discussions

5.1. Permeability Variation Characteristics under the Influence of Stress Field. It is well known that permeability is affected by in situ stress, so there must be a parameter related to in situ stress, which has a good correlation with permeability. To find this parameter, the minimum horizontal principal stress, maximum horizontal principal stress, vertical stress, and lateral stress coefficients were fitted to the permeability (Figure 9).

It can be seen from the results that the relationship between permeability and vertical stress is not obvious (Figure 9(c)). And the permeability has a weak negative exponential relationship with the maximum and minimum horizontal principal stress, respectively (both squared correlation coefficients are less than 0.3) (Figures 9(a) and 9(b)). It is worth mentioning that there is a good negative exponential relationship between permeability and lateral stress coefficient, and the squared correlation coefficients between them can reach 0.6 (Figure 9(d)). This is because the lateral stress coefficient combines the three in situ stresses, and the size of this parameter represents the type of stress field. The smaller the lateral stress coefficient is, the more the stress field tends to the static stress field, and the pores and fractures in coal reservoirs are more likely to expand, resulting in higher permeability. The

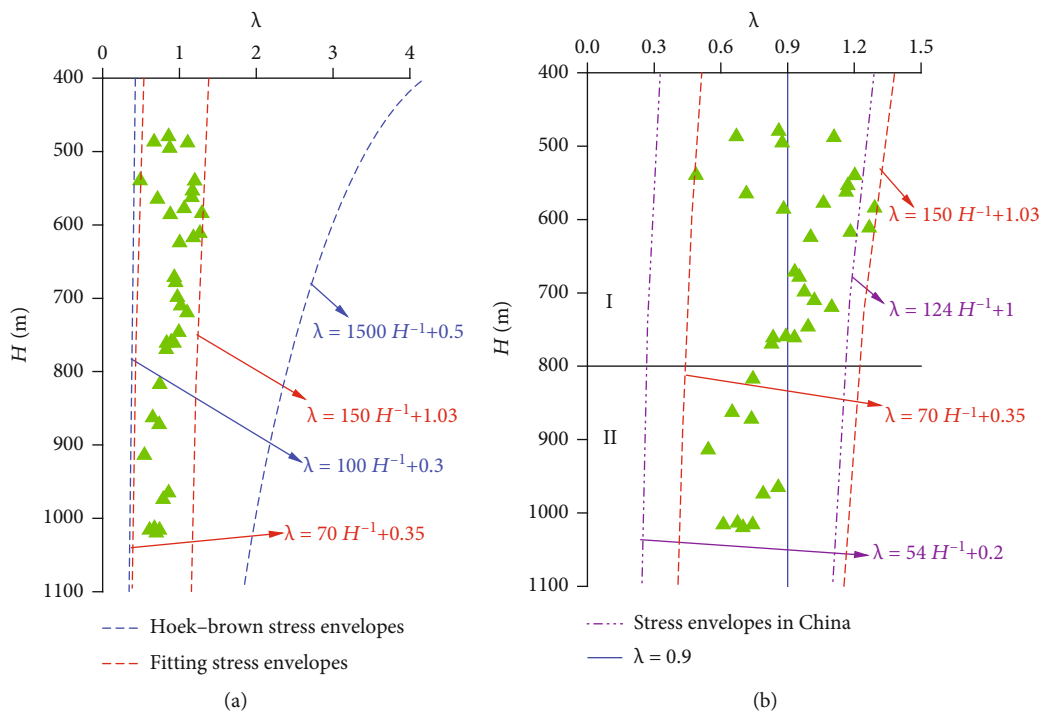

Figure 7: Scatter diagrams of coefficient of lateral stress and burial depth: (a) relationship between the lateral stress coefficient and the Hoek–Brown stress envelope; (b) the relationship between the lateral stress coefficient and the stress envelope in China.

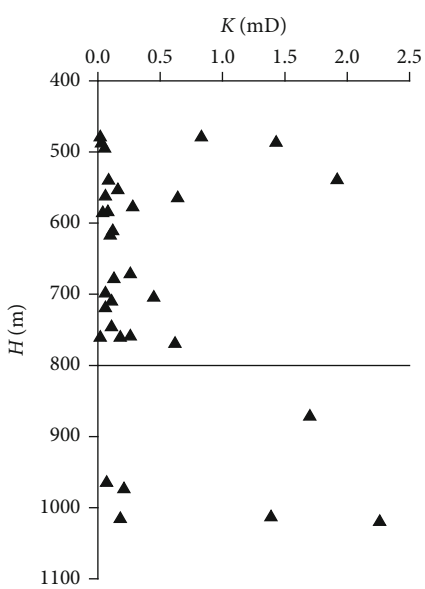

Figure 8: Scatter diagram of permeability and burial depth.

larger the lateral stress coefficient is, the more the stress field tends to the dynamic field, and the pore and fractures in the coal reservoir are seriously compressed, leading to a smaller permeability. The fitting formula of permeability and lateral stress coefficient is as follows:

$$k = 13.45e^{-\lambda/0.29} - 0.24. \quad (5)$$

However, it should be noted that the data points which cause a poor correlation between permeability and in situ stress have two common characteristics, that is, large burial depth and high permeability (Figures 9(a)–9(c)). To explore the causes of these deep high permeability data points, the structural characteristics of high permeability ($K > 0.5$ mD) coal reservoirs are analyzed (Table 2). As can be seen from Table 2, the three higher permeability points located deep (well 29, well 33, and well 35) are all located in the axial part of the syncline structure. Therefore, this article believes that it is these special structures that lead to the improvement of the permeability of deep coal reservoirs. Usually, when the horizontal strata fold, the strata tend to shorten and cause bending deformation. If there is only a single and thick rock layer, the outer arc of the rock layer will be stretched along the layer direction, while the inner arc will be compressed toward the center direction. There is always a middle plane between the two sides, which is neither stretched nor compressed. As the outer arc is stretched, some fractures perpendicular to the tensile stress tend to expand (Figure 10(a)). If the rock layer is thin and there are multiple layers superimposed, each layer will slip along the layer during the folding process, which will often produce cracks between the rock layers (Figure 10(b)). Both of the above situations may lead to an increase of permeability.

5.2. Variation Model of Coal Reservoir Parameters in Different Burial Depth Zones. Based on the above results, a comprehensive analysis is carried out by establishing the variation model of coal reservoir parameters in different depth

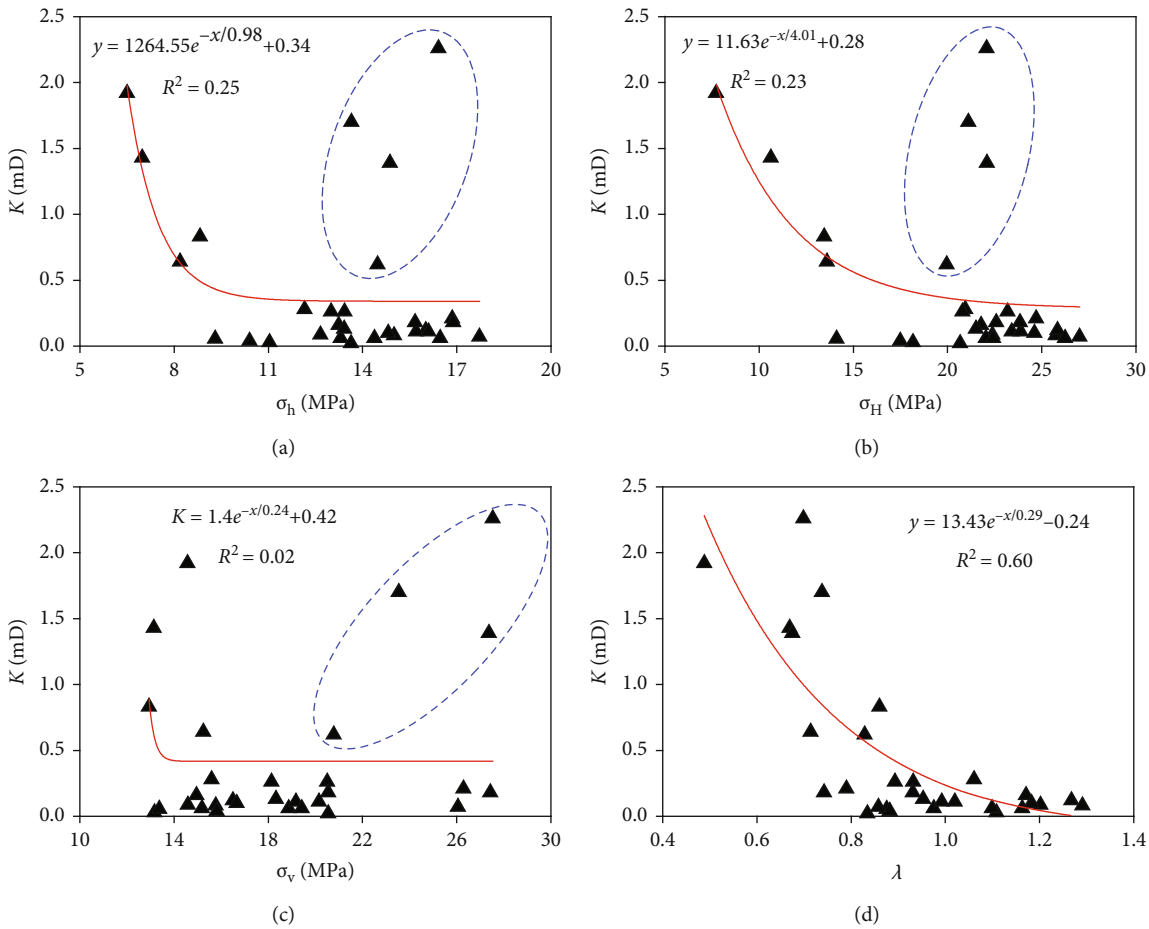

Figure 9: Scatter plot of permeability and some parameters.

Table 2: Statistical table of structural locations of data points with high permeability.

Sample	H (m)	K (mD)	Location
Well 1	479.32	0.83	No structure
Well 2	486.91	1.43	No structure
Well 5	539.50	1.92	No structure
Well 9	564.80	0.64	The wing of a syncline
Well 26	769.48	0.62	No structure
Well 29	871.96	1.70	The axis of a syncline
Well 33	1013.59	1.39	The axis of a syncline
Well 35	1019.85	2.26	The axis of a syncline

zones (Figure 11). It can be seen from this figure that the curves of permeability and lateral stress coefficient with depth have a good correlation. At the same time, the permeability is affected by in situ stress and the coal seam structure, and the influencing mechanism is different in different depth zones.

At depths < 800 m, the stress field of the coal reservoirs at most locations shows a dynamic field. The permeability is higher at the shallower locations, because the shallow coal seam bears less stress from three directions, which leads to the expansion of coal pores. On the other hand, the horizontal principal stresses of these high permeability coals are all less than the vertical stresses, indicating that they are in a state of horizontal stretch, which causes the cracks in the coal to expand more easily. The effects of these two aspects will increase the permeability of the coal seam. Subsequently, with the increase of burial depth, the in situ stress of coal reservoirs increases rapidly, and the maximum horizontal principal stress becomes dominant, which causes the coal reservoir to be severely compressed and its permeability to decrease rapidly.

At depths > 800 m, the stress field of the coal reservoirs shows a static stress field. Because the in situ stresses in the three directions are all relatively high, the porosity and fracture of the coal seam are compressed seriously, so that the coal reservoir permeability in this depth zone is generally low. However, it should be noted that at some special structural locations, such as the axis of the syncline structure, it is still possible to increase the permeability due to the influence of tectonic activity (Figure 11).

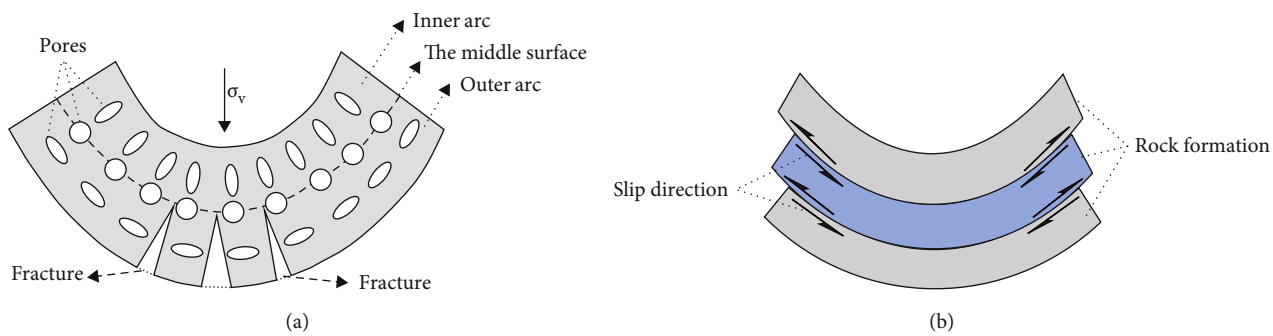

Figure 10: Diagram of the formation process of syncline structure: (a) variation characteristics of a layer of rock when it bends; (b) variation characteristics of multiple layers when they bend.

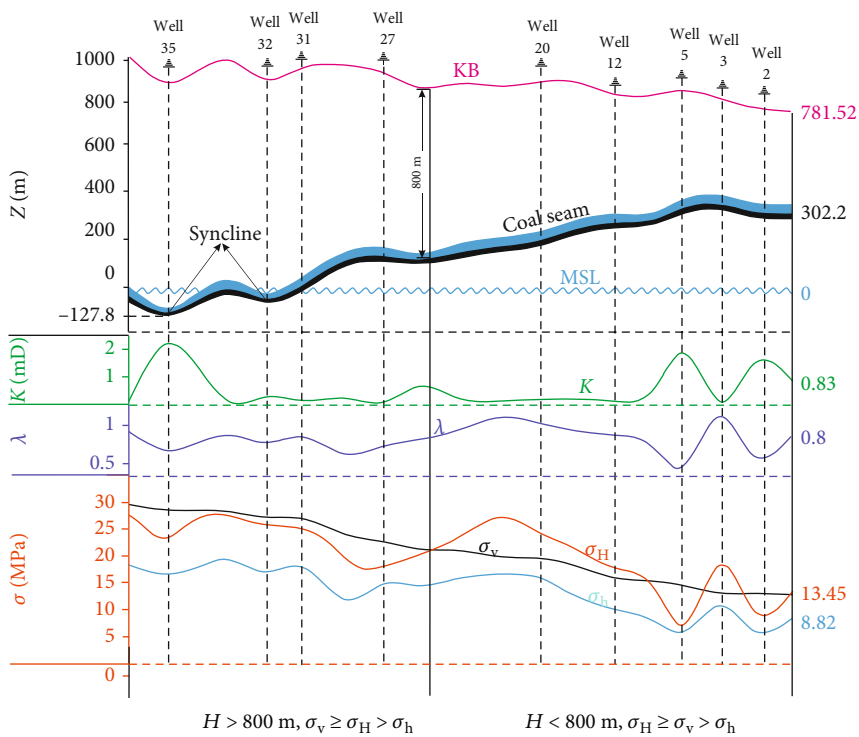

Figure 11: Variation trend of each parameter in different depth zones. Z: represents altitude, m; KB: represents the kelly bushing; MSL: represents mean sea level.

6. Conclusions

(1) With the increase of burial depth, the closure pressure, fracture pressure, and initial reservoir pressure all increase gradually; there is a very obvious linear relationship between the closure pressure and the fracture pressure. In general, there are two in situ stress states in the Liulin area. At depths < 800 m, the relationship of the three in situ stresses in the coal reservoir is $\sigma_H \geq \sigma_v > \sigma_h$. Compared with vertical stress, the horizontal principal stresses increase faster; at depths > 800 m, the relationship of the three in situ stresses is transformed into $\sigma_v \geq \sigma_H > \sigma_h$. And with the increase of burial depth, the horizontal principal stresses increase slowly and even become stable gradually

(2) The variation of coal permeability is mainly controlled by the influence of in situ stress on the pore-fracture system. At depths < 800 m, because the in situ stress increases with the increase of burial depth, the permeability is a simple decreasing process with the increase of the depth. At depths > 800 m, the porosity and fracture of coal reservoirs are compressed seriously due to the large in situ stress, resulting in the coal reservoir permeability in this depth zone being generally low. However, it is still possible to increase the permeability at some special structural locations due to the influence of tectonic activity

(3) Under the influence of data points with a large burial depth and high permeability, the fitting relationship between permeability and the three in situ stresses

is poor. There is a good negative exponential relationship between permeability and the lateral stress coefficient (the fitting formula is as follows: $k = 13.45e^{-\lambda/0.29} - 0.24$); this is because the lateral stress coefficient combines the three in situ stresses, and the size of this parameter represents the type of the stress field. This indicates that the lateral stress coefficient can be used to predict the permeability better

Data Availability

All data, models, and code generated or used during the study appear in the submitted article.

Conflicts of Interest

The authors declare that they have no conflicts of interest.

Acknowledgments

This work was supported by the National Natural Science Foundation of China (Grant nos. 41802180 and 42072198), and the Fundamental Research Funds for the Central Universities (Grant no. 2652019211).

References

[1] E. Hoek and T. Brown, *Underground Excavations in Rock*, The Institute of Mining and Metallurgy, 1980.

[2] A. Iannacchione, T. S. Bajpayee, and L. Prosser, "Methods for determining roof fall risk in underground mines," *Mining and Engineering*, vol. 59, no. 11, pp. 47–53, 2007.

[3] H. Kang, X. Zhang, and L. Si, "Study on in-situ stress distribution law in deep underground coal mining areas," in *ISRM International Symposium on Rock Mechanics*, pp. 139–143, China, May 2009.

[4] M. Cai, L. Qiao, C. Li, H. Ji, and H. Peng, "New development of in-situ stress measurement in Chinese mines," in *ISRM International Symposium on In-Situ Rock Stress*, pp. 135–142, Beijing, China, August 2010.

[5] H. Fu, D. Yan, S. Yang, X. Wang, Z. Zhang, and M. Sun, "Characteristics of in situ stress and its influence on coalbed methane development: a case study in the eastern part of the southern Junggar basin, NW China," *Energy Science & Engineering*, vol. 8, no. 2, pp. 515–529, 2020.

[6] Y. Li, D. Tang, H. Xu, and T. Yu, "In-situ stress distribution and its implication on coalbed methane development in Liulin area, eastern Ordos basin, China," *Journal of Petroleum Science and Engineering*, vol. 122, pp. 488–496, 2014.

[7] S. Chen, D.-Z. Tang, S. Tao, J. Zhao, Y. Li, and W.-Q. Liu, "Discussion about "critical depth" of deep coalbed methane in Zhengzhuang area, Qinshui basin," *Meitan Xuebao/Journal China Coal Society*, vol. 41, pp. 3069–3075, 2016.

[8] W. Ju, B. Jiang, Y. Qin et al., "The present-day in-situ stress field within coalbed methane reservoirs, Yuwang block, Laochang basin, south China," *Marine and Petroleum Geology*, vol. 102, pp. 61–73, 2019.

[9] R. Tyler, A. Scott, and W. Kaiser, *Defining coalbed methane exploration fairways: an example from the Piceance basin*, Rocky Mountain Foreland, Western United States, 1999.

[10] J. Q. Shi and S. Durucan, "A model for changes in coalbed permeability during primary and enhanced methane recovery," *SPE Reservoir Evaluation and Engineering*, vol. 8, no. 4, pp. 291–299, 2005.

[11] J. S. Bell, "In-situ stress and coal bed methane potential in Western Canada," *Bulletin of Canadian Petroleum Geology*, vol. 54, no. 3, pp. 197–220, 2006.

[12] R. Chatterjee and P. K. Pal, "Estimation of stress magnitude and physical properties for coal seam of Rangamati area, Raniganj coalfield, India," *International Journal of Coal Geology*, vol. 81, no. 1, pp. 25–36, 2010.

[13] H. Kang, X. Zhang, L. Si, Y. Wu, and F. Gao, "In-situ stress measurements and stress distribution characteristics in underground coal mines in China," *Engineering Geology*, vol. 116, no. 3-4, pp. 333–345, 2010.

[14] C. Ö. Karacan, J. P. Ulery, and G. V. R. Goodman, "A numerical evaluation on the effects of impermeable faults on degasification efficiency and methane emissions during underground coal mining," *International Journal of Coal Geology*, vol. 75, no. 4, pp. 195–203, 2008.

[15] Z. P. Meng, Y. D. Tian, and G. F. Li, "Characteristics of in-situ stress field in southern Qinshui basin and its research significance," *Meitan Xuebao/Journal China Coal Society*, vol. 35, no. 6, pp. 975–981, 2010.

[16] C. Liu, "Distribution laws of in-situ stress in deep underground coal mines," *Procedia Engineering*, vol. 26, pp. 909–917, 2011.

[17] S. Li, D. Tang, Z. Pan, H. Xu, and W. Huang, "Characterization of the stress sensitivity of pores for different rank coals by nuclear magnetic resonance," *Fuel*, vol. 111, no. 3, pp. 746–754, 2013.

[18] M. H. Talebi, S. Heidari, M. Moosavi, and M. Rahimi, "In situ stress measurements of two hydropower projects in Iran by hydraulic fracturing method," *Arabian Journal of Geosciences*, vol. 8, no. 9, pp. 7073–7085, 2015.

[19] S. Tao, S. Chen, and Z. Pan, "Current status, challenges, and policy suggestions for coalbed methane industry development in China: a review," *Energy Science & Engineering*, vol. 7, no. 4, pp. 1059–1074, 2019.

[20] C. Yang, J. Zhang, and X. Tang, "Microscopic pore types and its impact on the storage and permeability of continental shale gas, Ordos Basin," *Earth Science Frontiers*, vol. 20, pp. 240–250, 2013.

[21] J. Zhao, D. Tang, W. Lin et al., "Permeability dynamic variation under the action of stress in the medium and high rank coal reservoir," *Journal of Natural Gas Science and Engineering*, vol. 26, pp. 1030–1041, 2015.

[22] D. Feng, H. Deng, Z. Zhou, X. Gao, and L. Cui, "Paleotopographic controls on facies development in various types of braid-delta depositional systems in lacustrine basins in China," *Geoscience Frontiers*, vol. 6, no. 4, pp. 579–591, 2015.

[23] S. Li, D. Tang, Z. Pan et al., "Geological conditions of deep coalbed methane in the eastern margin of the Ordos basin, China: implications for coalbed methane development," *Journal of Natural Gas Science and Engineering*, vol. 53, pp. 394–402, 2018.

[24] X. Su, L. Zhang, and R. Zhang, "The abnormal pressure regime of the Pennsylvanian No. 8 coalbed methane reservoir in Liulin–Wupu district, eastern Ordos basin, China," *International Journal of Coal Geology*, vol. 53, no. 4, pp. 227–239, 2003.

[25] Y. Meng, D. Tang, and H. Xu, "CBM potential productivity assessment through fuzzy mathematics - a case study in Liulin

mine area, Hedong Coalfield," *Coal Geology of China*, vol. 22, pp. 17–20, 2010.

[26] Y. Meng, D. Tang, H. Xu, C. Li, L. Li, and S. Meng, "Geological controls and coalbed methane production potential evaluation: a case study in Liulin area, eastern Ordos basin, China," *Journal of Natural Gas Science and Engineering*, vol. 21, pp. 95–111, 2014.

[27] S. Zhang, S. Tang, D. Tang, Z. Pan, and F. Yang, "The characteristics of coal reservoir pores and coal facies in Liulin district, Hedong coal field of China," *International Journal of Coal Geology*, vol. 81, no. 2, pp. 117–127, 2010.

[28] H. Xu, D. Tang, S. Tang et al., "Geologic and hydrological controls on coal reservoir water production in marine coal-bearing strata: a case study of the carboniferous Taiyuan formation in the Liulin area, eastern Ordos basin, China," *Marine and Petroleum Geology*, vol. 59, pp. 517–526, 2015.

[29] Y. Li, D. Tang, H. Xu, D. Elsworth, and Y. Meng, "Geological and hydrological controls on water coproduced with coalbed methane in Liulin, eastern Ordos basin, China," *AAPG Bulletin*, vol. 99, no. 2, pp. 207–229, 2015.

[30] Y. Bao, C. Wei, and B. Neupane, "Generation and accumulation characteristics of mixed coalbed methane controlled by tectonic evolution in Liulin CBM field, eastern Ordos basin, China," *Journal of Natural Gas Science and Engineering*, vol. 28, no. 262–270, pp. 262–270, 2016.

[31] S. Chen, D. Tang, S. Tao et al., "In-situ stress measurements and stress distribution characteristics of coal reservoirs in major coalfields in China: implication for coalbed methane (CBM) development," *International Journal of Coal Geology*, vol. 182, pp. 66–84, 2017.

[32] S. P. Eng, J. Lan, C. L. Liu, Y. M. Ji, S. N. Li, and X. M. Zhang, "In-situ stress and coal reservoir pressure in southeast margin of Ordos basin and their coupling relations," *Journal of China Coal Society*, vol. 38, no. 1, pp. 122–128, 2013.

[33] J. Zhao, D. Tang, H. Xu et al., "Characteristic of in situ stress and its control on the coalbed methane reservoir permeability in the eastern margin of the Ordos basin, China," *Rock Mechanics and Rock Engineering*, vol. 49, no. 8, pp. 3307–3322, 2016.

[34] Y. Wan, H. Li, L. Yun, Z. Song, Y. Li, and P. Qi, "The field stress between late Jurassic and early Cretaceous in the eastern Ordos basin," *Earth Science*, vol. 42, no. 4, pp. 549–558, 2017.

[35] W. Ju, X. Niu, S. Feng et al., "Present-day in-situ stress field within the Yanchang formation tight oil reservoir of Ordos basin, central China," *Journal of Petroleum Science and Engineering*, vol. 187, article 106809, 2020.

[36] Z. Chen, N. Zhang, and S. Zhang, "The time and spatial evolution of sedimentary systems and coal accumulation centre in late Palaezoic coal-bearing measures on the eastern margin of Ordos basin," *Earth Science-Journal of China University of Geosciences*, vol. 14, pp. 357–366, 1989.

[37] L. I. Yong, J. Yang, Z. Pan, S. Meng, K. Wang, and X. Niu, "Unconventional natural gas accumulations in stacked deposits: a discussion of upper Paleozoic coal-bearing strata in the east margin of the Ordos basin, China," *Acta Geologica Sinica-English Edition*, vol. 93, no. 1, pp. 111–129, 2019.

[38] C. W. Hopkins, J. H. Frantz, R. W. Flumerfelt, and J. P. Spivey, "Pitfalls of injection/falloff testing in coalbed methane reservoirs," in *SPE Permian Basin Oil and Gas Recovery Conference*, Midland, TX, USA, March 1998.

[39] M. K. Hubbert and D. G. W. Willis, "Mechanics of hydraulic fracturing," *Transactions of AIME*, vol. 18, no. 1, pp. 369–390, 1972.

[40] Q. Liu, Y. Cheng, L. Yuan, B. Tong, S. Kong, and R. Zhang, "CMM capture engineering challenges and characteristics of in-situ stress distribution in deep level of Huainan coalfield," *Journal of Natural Gas Science and Engineering*, vol. 20, pp. 328–336, 2014.

[41] B. C. Haimson and F. H. Cornet, "ISRM suggested methods for rock stress estimation—part 3: hydraulic fracturing (HF) and/or hydraulic testing of pre-existing fractures (HTPF)," *International Journal of Rock Mechanics and Mining Sciences*, vol. 40, no. 7-8, pp. 1011–1020, 2003.

[42] J. D. Bredehoeft, R. G. Wolff, W. S. Keys, and E. Shuter, "Hydraulic fracturing to determine the regional in situ stress field, Piceance basin, Colorado," *Geological Society of America Bulletin*, vol. 87, no. 2, p. 250, 1976.

[43] S. Wang, D. Elsworth, and J. Liu, "Mechanical behavior of methane infiltrated coal: the roles of gas desorption, stress level and loading rate," *Rock Mechanics and Rock Engineering*, vol. 46, no. 5, pp. 945–958, 2013.

[44] J. R. Enever and A. Hennig, *The Relationship between Permeability and Effective Stress for Australian Coals and Its Implications with Respect to Coalbed Methane Exploration and Reservoir Modelling*, University of Alabama, 1997.

[45] W. F. Brace, "A note on permeability changes in geologic material due to stress," *Pure and Applied Geophysics*, vol. 116, no. 4-5, pp. 627–633, 1978.

Hindawi
Geofluids
Volume 2021, Article ID 5577740, 11 pages
https://doi.org/10.1155/2021/5577740

Research Article

Brittleness Index of High-Rank Coal Reservoir and Its Influencing Factors in Mabidong Block, Qinshui Basin, China

Yixuan Zhang,[1,2] Yanjun Meng,[1,2] Panyun Hao,[3] Yanjie Shang,[4] and Xinyu Fu[1,2]

[1]*College of Mining Engineering, Taiyuan University of Technology, Taiyuan 030024, China*
[2]*Shanxi Key Laboratory of Coal and Coal Measure Gas Geology, Taiyuan 030024, China*
[3]*No. 213 Laboratory of Shanxi Bureau of Geology and Mineral Resources, Linfen 041000, China*
[4]*PetroChina Coalbed Methane Co., Ltd., Beijing 100028, China*

Correspondence should be addressed to Yanjun Meng; mengyanjun15@126.com

Received 26 February 2021; Accepted 22 April 2021; Published 8 May 2021

Academic Editor: Qingquan Liu

Brittleness index is an important mechanical index to evaluate the fracturability of conventional oil and gas reservoirs. However, the brittleness index of an organic coal reservoir is more complex. In this study, based on array sonic logging and density logging data, coal brittleness index is calculated using an elastic parameter method in the Mabidong coalbed methane (CBM) block in southern Qinshui Basin. In combination with coal-body structure observation, the maceral analysis, and proximate data of coal cores, a comprehensive study of geological influencing factors of coal brittleness index has been carried out. According to coal fragmentation degree, the coal-body structure of coal seams can be divided into primary, cataclastic, and granulate structure. The average interval of brittleness index of primary, cataclastic, and granulate structural coals is 63.3-71.48, 73.01-74.85, and 77.41-82.77, respectively. The results indicate that generally the order of brittleness index is primary structural coal < cataclastic structural coal < granulate structural coal. Young's modulus and the brittleness index have a good positive correlation. Poisson's ratio and the brittleness index are negatively correlated in No. 3 coal seam but are positive correlated in No. 15 coal seam. The vitrinite content is positively correlated with brittleness index, and the inertinite content is negatively correlated. For the primary and cataclastic structure coal, the ash and volatile is positively correlated with the brittleness index. The correlation of brittleness index, macerals, and coal quality parameters in the primary structure coal is better than that of the cataclastic and granulate structure coal. The research results are helpful to guide the coal brittleness index and coal-body structure prediction in fracturing of CBM wells.

1. Introduction

Brittleness is a key mechanical parameter in the evaluation of hydraulic fracturing and wellbore stability of coal and shale reservoirs [1–3]. Brittleness of coal refers to the irreversible property of coal breaking, which indirectly reflects the complexity of fractures formed after fracturing in coal and is closely related to the difficulty of fracturing in coal reservoir. Brittleness can generally be quantitatively characterized by the brittleness index. The brittleness index can measure the ability of coal to resist fragmentation under pressure, it significantly affects the cutability and coal production rate during coal mining [2, 4] and affects the drilling efficiency during the well drilling process [5]. The brittleness index is also the key index to evaluate the fracturability of coal reservoirs [1, 6].

Various researchers have devoted to the studies on the evaluation method of rock brittleness [7–14]. There were divergences between researchers on how to determine the brittleness index of rock. The evaluation of rock brittleness was put forward through uniaxial tensile and compressive experiments in 1974 by Hucka and Das [7]. The relationship between rock brittleness and hardness coefficient and fracture toughness, the functional relationship between rock brittleness and rock tensile and compressive strength, were established through mechanical property experiments and tests in succession [8, 9]. Since the beginning of this century, with the rise of the unconventional oil and gas industry, the

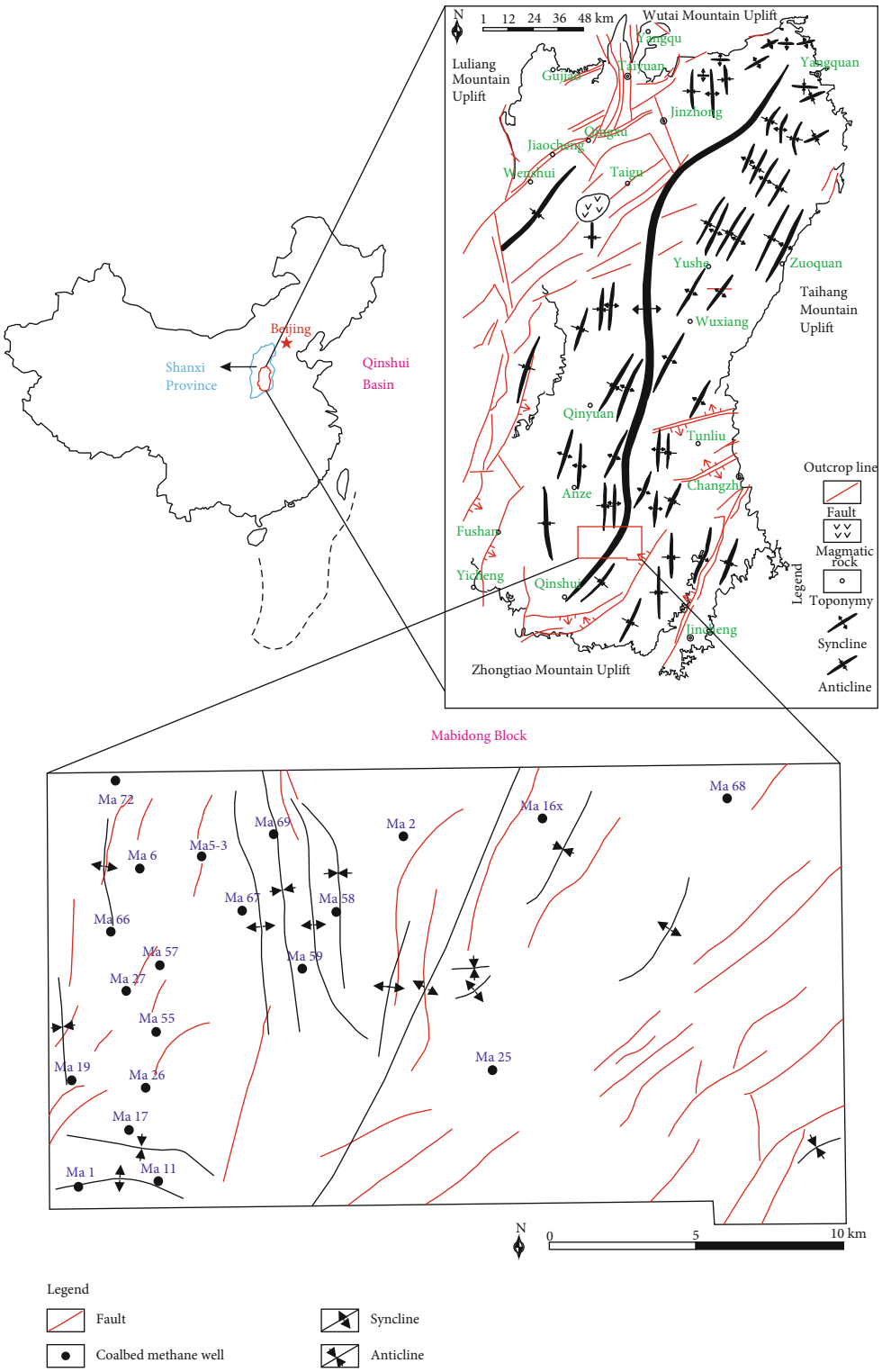

Figure 1: Map of the Mabidong block showing major structures and locations (modified from [20]).

research of brittleness index in coal reservoirs has been widely concerned by scholars. Different researchers summed up the definition of brittleness index and put forward different quantitative calculation methods of the brittleness index. A brittleness index evaluation method based on the rock brittle mineral content was proposed based on the correlation between mineral composition and brittleness in shales [10]. Another method to quantitatively calculate the brittleness index was proposed based on Young's modulus and Poisson's ratio in the rock mechanics parameters [11]. Then, a new method was proposed to evaluate the brittleness of shale by using X-fluorescence element logging data [12]. Some

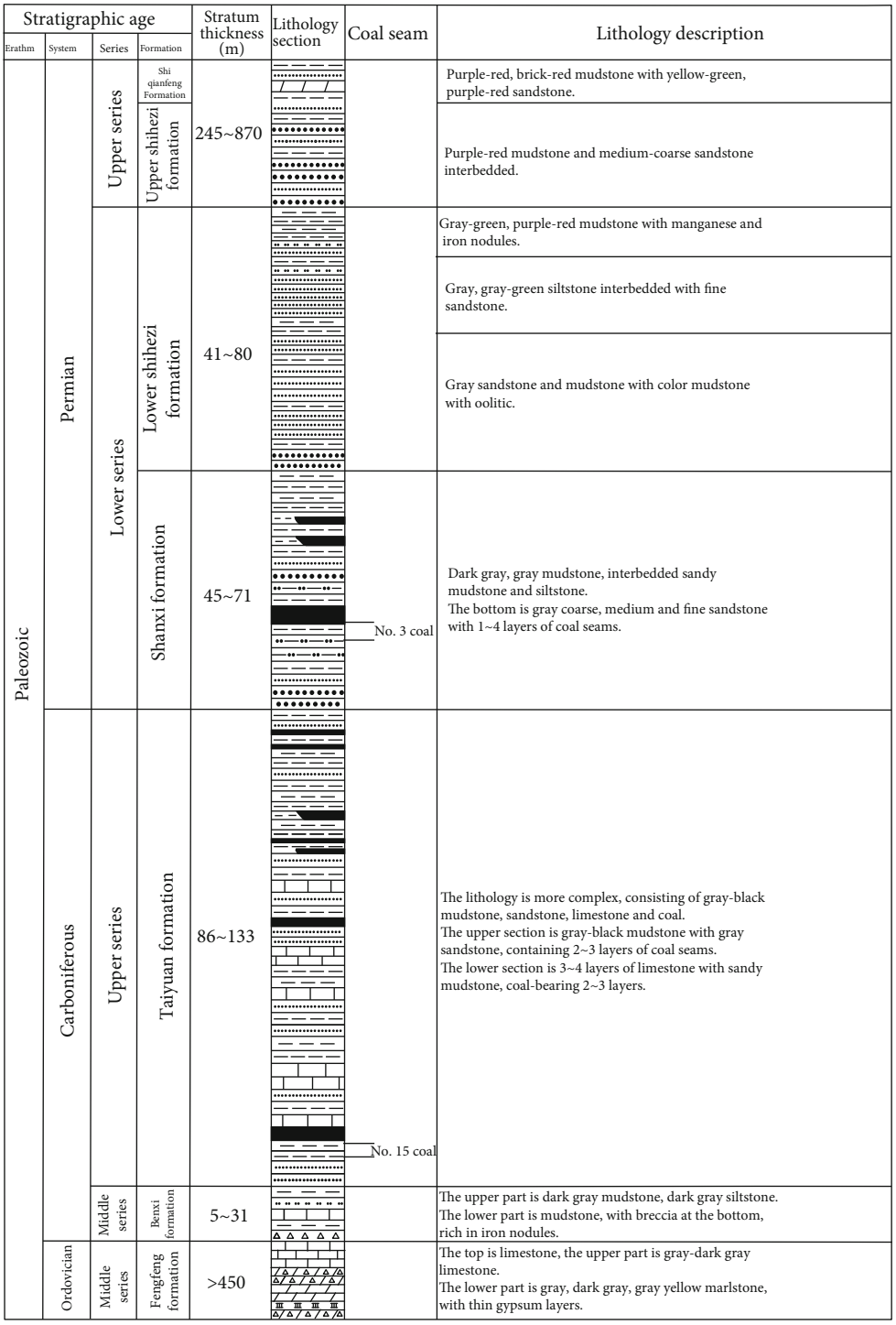

Figure 2: Stratigraphic column of coal-bearing sequences in the Mabidong block.

scholars thought that the brittleness index could be quantified from the perspective of influencing factors and coal brittleness evaluation method could be revised from that of shale [13, 14]. A review of the previous literatures makes it clear that different researchers have different definitions for the concept of rock brittleness.

So far, brittleness index studies have been widely used in shale gas and tight sandstone gas [1, 10–13]. However, limited by logging technology and the traditional low-cost exploration concept of CBM, there were few researches on the evaluation of brittleness index in coal reservoirs [15–18], especially the influence factors of coal brittleness index. Previous studies have shown that the coal brittleness was mainly affected by coal rank, composition, and coal-body structure [15–17, 19]. However, current scholars are still unclear on the quantitative relationship between coal

Table 1: Coal-body structure division of a coal seam in the Mabidong block (refer to reference [21]).

Coal-body structure	Coal core shape	Coal core photograph	Description of coal core characteristics
Primary structure	Column, block		The band of coal lithotype and primary structure are clear, block structure, and hard.
Cataclastic structure	Column, block, coal broken		The band is visible, but the coal is intersected by exogenous fractures without clear displacement and is also block.
Granulated structure	Crushed, coal broken seriously		The primary band and block structure are damaged, and particle structure, small cracks in different directions developed, test by hand, it has a certain hardness and can be crushed into small fragments.

Table 2: Coal brittleness index seams with different coal-body structures in the Mabidong block.

Well number/coal seam	Primary structure	Well number/coal seam	Cataclastic structure	Well number/coal seam	Granulated structure
Ma 1/No. 3	58.18-68.06	Ma 69/No. 3	71-75.1	Ma 11/No. 3	79.7-83.4
Ma 17/No. 3	56.6-73.2	Ma 1/No. 15	76.24-77.13	Ma 27/No. 3	75.4-84.2
Ma 58/No. 3	61.4-70.9	Ma 59/No. 15	71.8-72.33	Ma 66/No. 3	76.5-89
Ma 67/No. 3	62.9-67.9			Ma 68/No. 3	77.09-77.44
Ma 6/No. 15	68.25-75.02			Ma 58/No. 15	75.92-82.4
Ma 25/No. 15	72.58-73.77			Ma 66/No. 15	79.87-80.15
Average	63.3-71.48	Average	73.01-74.85	Average	77.41-82.77

brittleness and inherent influencing factors of coal reservoir. Therefore, the establishment of the coal brittleness index calculation method based on the coal-body structure and composition has important practical significance for brittleness evaluation of coal reservoirs in CBM exploration and development.

In this research, the brittleness index of a high-rank coal reservoir and its influencing factors were studied in Mabidong CBM block, Qinshui Basin, China. Based on the observation and description of coal cores of 15 CBM exploration wells, array sonic logging, density logging, and coal quality test data, the elastic parameter method was used to calculate

the coal brittleness index reservoirs in this block, and the geological factors on coal brittleness index were analyzed and discussed.

2. Research Method, Process and Data Source

2.1. Evaluation Method of Coal Brittleness Index Reservoirs. Coal reservoirs are typical organic reservoirs, so the mineral component method commonly used in shale brittleness index evaluation is unable to be used in evaluation of the coal brittleness index. Therefore, the elastic parameter method was adopted in this study to calculate the brittleness index of high-rank coal reservoir. The calculation of rock brittleness by the elastic parameter method can provide a convenient and practical means for evaluating rock reservoir brittleness by using logging and seismic data [17, 18]. Rickman et al. first used normalized Young's modulus and Poisson's ratio to characterize rock brittleness [11]. The calculation formula and definitions of brittleness used in this study are formulated as follows:

$$E = \frac{\rho\left(3\Delta ts^2 - 4\Delta tc^2\right)}{\Delta ts^2\left(\Delta ts^2 - \Delta tc^2\right)}, \tag{1}$$

$$\mu = \frac{0.5\Delta ts^2 - \Delta tc^2}{\Delta ts^2 - \Delta tc^2}, \tag{2}$$

$$\mathrm{BI} = \left(0.5 \times \frac{E - E\min}{E\max - E\min} + 0.5 \times \frac{\mu - \mu\max}{\mu\min - \mu\max}\right) \times 100, \tag{3}$$

where E is Young's modulus, GPa; μ is Poisson's ratio, dimensionless; ρ is the density, g/cm^3; Δts is the transverse wave time difference, μm/s; Δtc is the longitudinal wave time difference, μm/s; BI is the coal brittleness index, dimensionless; $E_{\max}$ and $E_{\min}$ are the maximum and minimum values of Young's modulus in a certain coal seam section in a certain block, GPa; and $\mu_{\max}$ and $\mu_{\min}$ are the maximum and minimum values of Poisson's ratio in a certain coal seam section in a certain block, dimensionless.

According to the statistics of elastic parameters of coal reservoirs in Mabidong block, the $\mu_{\max}$ and $\mu_{\min}$ of coal used in the normalization of brittleness index calculation are 0.3 GPa and 0.2 GPa, and the $E_{\max}$ and $E_{\min}$ are 0.9 GPa and 0.3 GPa in this study.

2.2. Research Processes and Data Source. The overall research approach of this study is to use the elastic parameter method to calculate the coal brittleness index and combine the coal core analysis data to find out the influencing factors of the coal brittleness index reservoirs. The specific research process is detailed as follows: (1) Based on the core test data of CBM exploration wells in the Mabidong block, the vitrinite reflectance, macerals, and industrial analysis data of the tested coal samples were obtained. (2) Based on core photograph features corresponding to the depth of coal samples, the coal-body structure types of the corresponding coal seam were qualitatively determined. (3) Through the process of core true depth determination, the density logging parameters (density logging value) and array acoustic logging parameters (transverse wave time difference and longitudinal wave time difference) corresponding to the sampling depth of core were obtained, and then, the coal brittleness index was obtained by elastic parameter method. (4) The influence of the coal-body structure and mechanical parameters on the coal brittleness index was analyzed. (5) The influence of coal quality parameters on the brittleness index is analyzed.

Table 3: Mechanical parameters of No. 3 and No. 15 coal seams in the Mabidong block.

Coal-body structure	Coal seam	Modulus of elasticity	Poisson's ratio
Primary structure	No. 3	0.593	0.2269
	No. 15	0.660	0.2312
Cataclastic structure	No. 3	0.635	0.2335
	No. 15	0.610	0.2300
Granulate structure	No. 3	0.715	0.2279
	No. 15	0.741	0.2305

In this study, all the data of array acoustic logging, density logging, coal maceral composition, and coal quality parameters were approved and obtained from the field and laboratory test report of Huabei Oilfield Company of PetroChina. There are 9 wells with data from No. 3 coal seam and 6 wells with data from No. 15 coal seam.

3. Geological Setting

The Mabidong block is located in the southwest of Qinshui Basin, Shanxi Province, North China. The main structures in this block include the Qinshui synclinorium with NNE-trending and a series of associated NNE-trending normal faults [20]. According to the direction perpendicular to the synclinorium structural line strike, Mabidong block can be roughly divided into three tectonic units, and they are the western slope zone, the central trough zone and the eastern slope zone (Figure 1). The structure of the west wing is simple, and it is a monocline dipping toward southeast. The faults in this area are mostly small ones with short extension distance and the NNE strike. Compared with the west wing, the overall structure of the east wing is more complex, with more developed faults, generally smaller fault spacing, steeper occurrence, and shorter extension length. The results of structural interpretation show that the central and northern part of the block is relatively simple in structure, with large buried depth and good preservation conditions, and is a sweet spot for further CBM exploration.

The main coal-bearing strata in the block are Taiyuan Formation and Shanxi Formation in the Carboniferous-Permian. The No. 3 coal seam in Shanxi Formation and No. 15 coal seam in Taiyuan Formation are the target strata of CBM development (Figure 2). The burial depth of No. 3 coal seam in the block is 860~1420 m. The burial depth is shallow in the west and deep in the east, and the thickness is 4.6~8.0m with an average of 6.2 m. The maximum reflectance of vitrinite of No. 3 coal ranges from 2.61% to 3.36%, with an average of 2.96%. The No. 3 coal belongs to

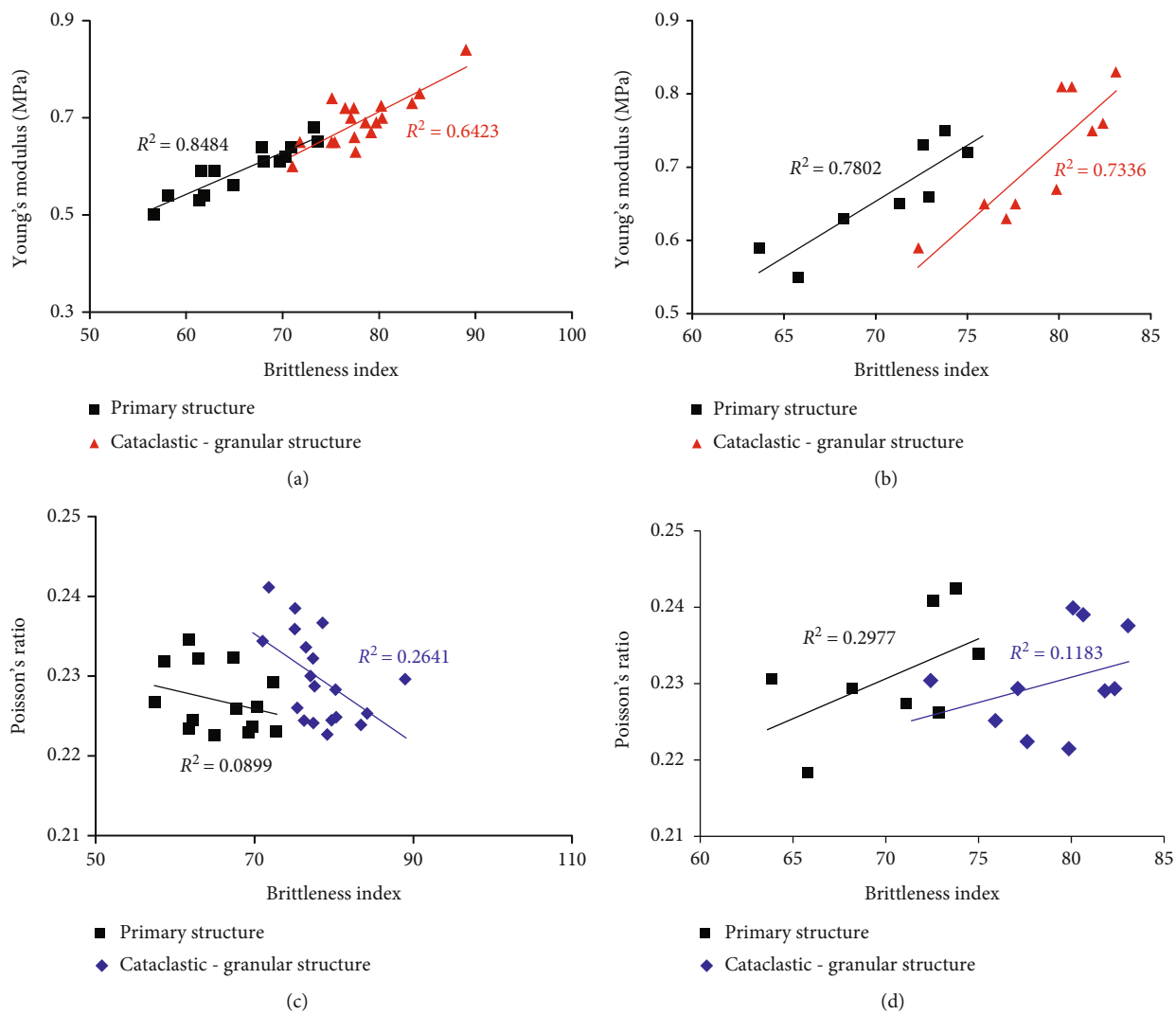

Figure 3: Relationship between mechanical parameters and the brittleness index of No. 3 and No. 15 coal: (a, c) No. 3 coal and (b, d) No. 15 coal.

anthracite. The burial depth of No. 15 coal seam is 980~1520 m, about 100 m deeper than No. 3 coal seam. The burial depth trend is the same as No. 3 coal seam, shallow in the west and deep in the east. The thickness is mostly between 3.5 and 5.5 m, with an average of 5.1 m. The maximum reflectance of vitrinite of No. 15 coal ranges from 2.65% to 2.71%, with an average of 2.68%. The No. 15 coal also belongs to anthracite.

4. Influencing Factors of Coal Reservoir Brittleness Index in Mabidong Block

4.1. Relationship between Coal-Body Structure and Brittleness Index. The coal-body structure has great influence on the physical properties of coal reservoir properties [21, 22]. Due to the complex structural conditions (Figure 1), the tectonic coal is relatively developed in the Mabidong block. According to the characteristics of core shape, photograph, and the description of core characteristics (macrostructure and fracture), the coal core samples are divided into primary structure coal, cataclastic structure coal, and granular structure coal (Table 1). The primary structure coal retains the original sedimentary structure characteristics, while the cataclastic structure coal and granulate structure coal were affected by the Indosinian Movement, Yanshan Movement, and Himalayan Movement and were strongly compressed, uplifted, and eroded. The degree of fragmentation of the cataclastic structure coal is larger than that of the primary structure coal, and the degree of fragmentation of granulate structure coal is the largest.

According to the density logging and array sonic logging data of CBM wells in the Mabidong block, the mechanical parameters are obtained, and the brittleness indexes are calculated according to the mechanical parameters. The brittleness indexes are compared with the coal-body structure types of drilling core samples. The relationship between the coal-body structure and brittleness index is studied and classified statistic (Table 2). The calculation results show that the average interval of the coal brittleness index of the primary structural coal, cataclastic structural coal, and granulate structural

coal is 63.3-71.48, 73.01-74.85, and 77.41-82.77, respectively. It reveals that, according to the coal-body structure, the order of the coal brittleness index is primary structural coal < cataclastic structural coal < granulate structural coal (Table 2). The results are consistent with previous studies [15, 16]. It reveals that as the brittleness index generally is increasing, the degree of coal fragmentation increases. The reason may lie in the influence of Young's modulus. Previous studies have shown that Young's modulus of coal is closely related to density, porosity, and effective stress of the coal [23, 24]. The Mabidong block is located in the core of syncline of Qinshui Basin, and the regional tectonic stress field is dominated by compression stress. Therefore, in the process of tectonic coal formation, the pores and fractures in coal seams were compressed and closed, the porosity decreases, and Young's modulus increases. There are a certain crossover and overlap between the brittleness indexes of different coal-body structures, which are affected by the characteristics of coal seam structure, heterogeneity, resolution of logging tools, continuity of logging response values, well bore, well section, and roof and floor lithology [15].

4.2. Influence of Mechanical Parameters on Coal Brittleness Index. The main mechanical parameters that affect the coal brittleness index are Young's modulus and Poisson's ratio. The relevant parameters based on statistics are shown in Table 3. In the study area, Young's modulus of granulate structure coal is relatively high, and Poisson's ratio of cataclastic structure coal is relatively high. Young's modulus and Poisson's ratio of No. 15 primary structure coal are both greater than that of No. 3 primary structure. The possible reason is that in the deeper coal-forming and water-covered environment of No. 15 coal, the gelation of peat is more thorough, and there are more homogeneous vitrinite and matrix vitrinite content [25].

The correlation among the brittleness index, Young's modulus, and Poisson's ratio of No. 3 coal seam and No. 15 coal seam is shown in Figure 3. Young's modulus has a good positive correlation with the brittleness index. Young's modulus and the brittleness index of primary structure coal of No. 3 coal seam have the best correlation, followed by the primary structure coal of No. 15 coal seam (Figures 3(a) and 3(b)). This is because the coal body of the primary structural coal is complete and its mechanical properties are more stable. Poisson's ratio and brittleness index are negatively correlated in No. 3 coal seam (Figure 3(c)) but are positive correlated in No. 15 coal seam (Figure 3(d)). The correlation coefficient between Poisson's ratio and the coal brittleness index is small. The difference in the correlation between the same mechanical parameter and the brittleness index is comprehensively affected by the coal-body structure, coal macerals, and coal quality parameters.

4.3. Influence of Macerals on Coal Brittleness Index. The brittleness index is a complex function of lithology, composition, temperature, and porosity [26]. Due to the different mechanical properties of different coal macerals, the composition of coal macerals has an important influence on the coal brittleness index. According to some of the measurement results of coal macerals of 13 wells (15-layer coal seams) in the Mabidong block, the macerals and the brittleness index data of coal with different coal-body structures are obtained.

Table 4: Statistics of macerals of coal with different coal-body structures in the Mabidong block.

Coal-body structure	Coal seam	Vitrinite (%)	Inertinite (%)	Minerals (%)
Primary structure	No. 3	82.65	17.3	4.80
	No. 15	91.66	9.00	4.37
	Average	84.49	14.81	4.50
Cataclastic structure	No. 3	81.01	18.99	3.67
	No. 15	83.94	16.06	6.40
	Average	81.98	18.02	4.58
Granulate structure	No. 3	78.21	21.79	4.32
	No. 15	91.95	8.05	6.96
	Average	83.94	16.06	5.86

As shown in Table 4, the macerals of high metamorphic anthracite is mainly vitrinite. The vitrinite content and the mineral content of No. 15 coal seam is generally higher than that of No. 3 coal seam, and the inertite content is lower than that of No. 3 coal seam, which is caused by the deep water covering of the coal formation environment of No. 15 coal seam [25]. The average vitrinite content of primary structure, cataclastic structure, and granulate structure coals is 84.49%, 81.98%, and 83.94%. The average inertinite content of primary structure, cataclastic structure, and granulate structure coals is 14.81%, 18.02%, and 16.06%. The average mineral content of primary structure, cataclastic structure, and granulate structure coals is 4.50%, 4.58%, and 5.86%. There is no exinite in coal of this block, because aliphatic components in the exinite will be converted into gaseous hydrocarbons in the middle to high coalification stage.

The brittleness index varies with changes in the maceral and microlithotype composition of coal. In the Mabidong block, the vitrinite content is positively correlated with the coal brittleness index (Figure 4(a)), while the inertite content is negatively correlated with the coal brittleness index (Figure 4(b)). The correlation between the brittleness index and macerals in the primary structure coal is better than that of the cataclastic and granulate structure coal (Figures 4(a) and 4(b)). Previous studies have shown that different components of coal have different effects on brittleness, grindability, and breakability of coal, and the brittleness of the coal structure rather than its hardness dominates coal grindability [19, 27, 28]. The vitrinite is the brittleness component in coal, and the inertinite is the hardness component in coal. As a result, for the primary structure coal, the coal brittleness index is positively correlated with the vitrinite content, but negatively correlated with the inertinite content obviously. The correlations between the mineral and brittleness index of different coal-body structures are poor (Figure 4(c)). The main reason is that the content of minerals in coal is relatively low, and it is easily affected by the deformation of coal structure. Nevertheless, it can be seen that there is a certain positive correlation between the brittleness index and mineral content in primary structural coal (Figure 4(c)). Because Young's

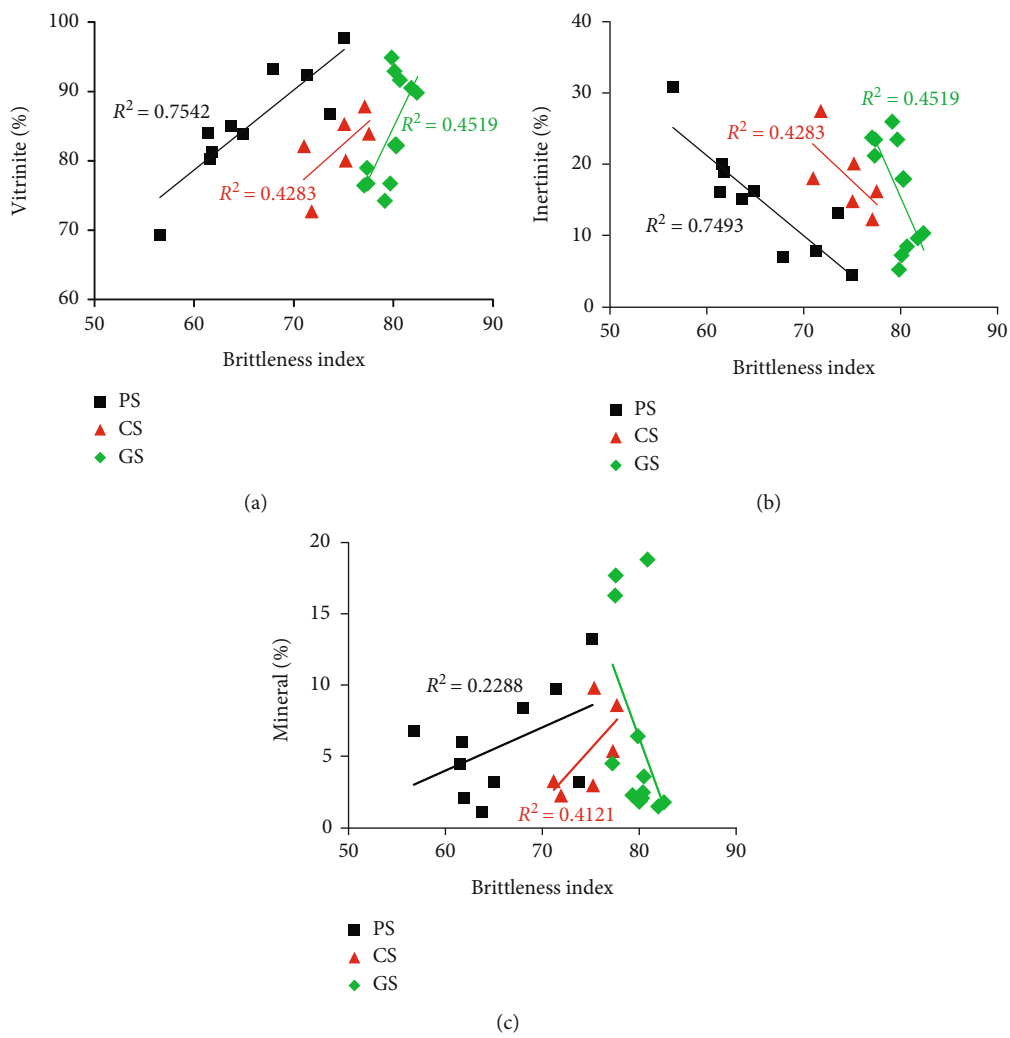

Figure 4: Relationship between microscopic composition, brittleness index, and Young's modulus. PS is primary structure, CS is cataclastic structure, and GS is granulate structure.

modulus of inorganic minerals is generally higher than that of organic coal, the presence of inorganic minerals can increase Young's modulus of the coal.

4.4. Influence of Coal Quality Parameters on Coal Brittleness Index. The proximate analysis of coal is the most common experimental analysis method in coal quality analysis. The proximate analysis indexes of coal include ash, moisture, volatile, and fixed carbon. Based on the proximate analysis of coal samples from CBM wells, coal quality parameters of No. 3 and No. 15 coal seams in the Mabidong block are obtained. As shown in Table 5, the coal quality parameters of No. 3 and No. 15 coal seams have little differences. The moisture content of No. 15 coal seam is less than that of No. 3 coal seam, the volatile of primary structural coal and cataclastic structural coal of No. 15 coal seam is both larger than that of No. 3 coal seam, and the volatile of granulate structural coal are smaller than that of No. 3 coal seam. The ash content of granular structure coal is the highest, which is consistent with the highest mineral content of granular structure coal.

The correlation between coal quality parameters and brittleness index data of different coal-body structure in Mabidong block of Qinshui Basin is obtained by statistical analysis (Figure 5). It is obvious that the correlation between the brittleness index and coal quality parameters is obviously affected by the coal-body structure, showing different correlation rules. For the primary structure coal and cataclastic structure coal, the content of ash and volatile is positively correlated with the brittleness index, while the content of fixed carbon is negatively correlated with the brittleness index. However, for the granulate structure coal, these correlation rules are just opposite (Figures 5(a), 5(b), and 5(d)). The positive correlation between ash content and coal brittleness is consistent with the results in Figure 4(a), because the presence of inorganic minerals increases Young's modulus of the coal [24]. The correlation between the brittleness index and coal quality parameters in the primary structure coal is significantly better than that of the cataclastic and granulate structure coals. This phenomenon reveals that the influence of the coal-body structure on the brittleness index is higher than that of coal quality parameters. The higher the failure

Table 5: Coal quality parameters of No. 3 and No. 15 coal seams in the Mabidong block (air-dried basis).

Coal-body structure	Coal seam	Moisture (%)	Ash (%)	Volatile (%)	Fixed carbon (%)
Primary structure	No. 3	0.82	10.026	8.26	69.75
	No. 15	0.807	19.52	9.9	80.91
	Average	0.811	12.875	8.75	77.56
Cataclastic structure	No. 3	0.98	10.505	8.39	79.545
	No. 15	0.125	11.835	8.495	80.125
	Average	0.695	10.948	8.425	79.932
Granulate structure	No. 3	0.978	17.57	9.96	71.486
	No. 15	0.954	12.552	8.89	84.183
	Average	0.968	15.48	9.52	76.103

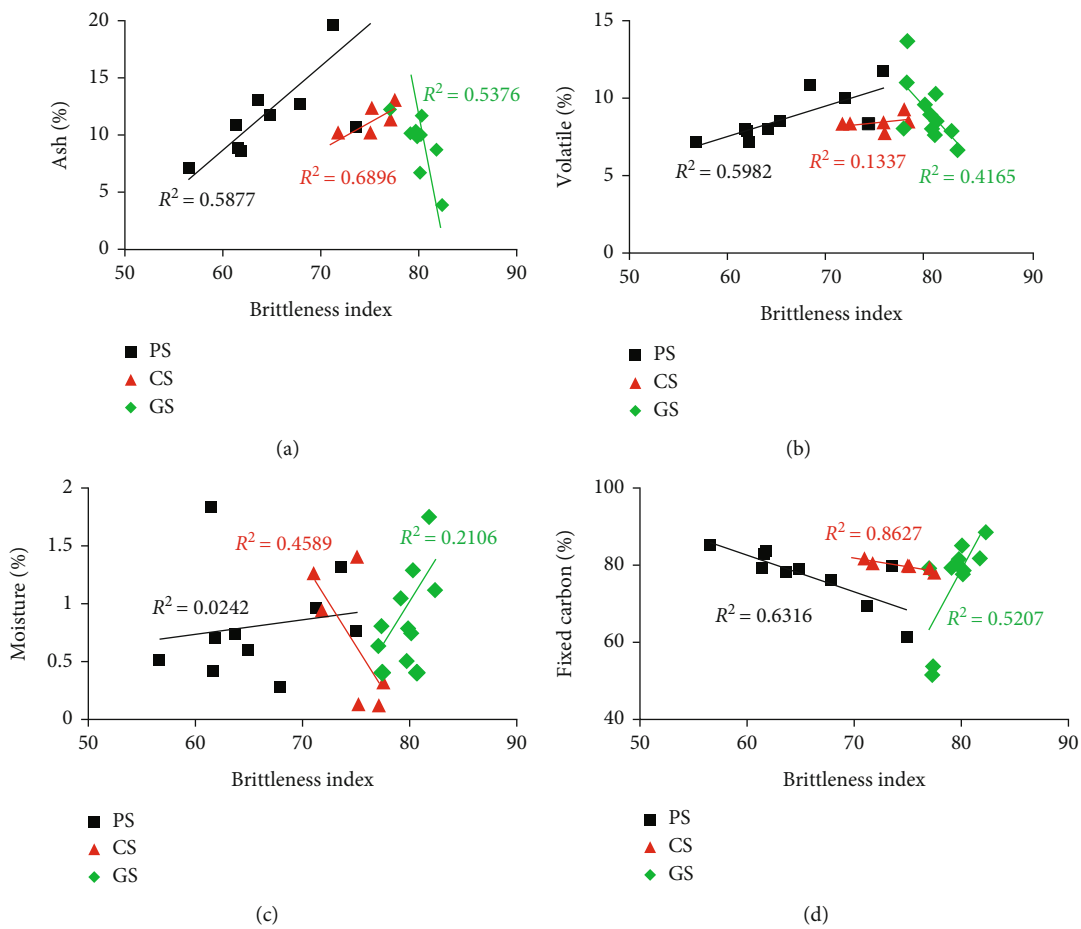

Figure 5: Relationship between the coal quality index and brittleness index. PS is primary structure, CS is cataclastic structure, and GS is granulate structure.

degree of coal-body structure, the more complex the factors affecting the coal brittleness index. The correlations between moisture and the brittleness index of different coal-body structures are poor (Figure 5(c)). The reason is that the differences of moisture (intrinsic water) in the coal seam within the same block are very tiny, and the brittleness index calculated by logging may be more affected by external water in coal fissures.

5. Conclusion

(1) The calculation results of coal brittleness by elastic parameter method show that, according to the coal-body structure, the order of the coal brittleness index is primary structural coal < cataclastic structural coal < granulate structural coal. This may be because under the background of compressive stress field,

pores and fractures in coal seam are compressed and closed, porosity decreases, and Young's modulus increases. There is a good correlation between mechanical parameters and the coal brittleness index, and the brittleness index is more affected by Young's modulus than Poisson's ratio

(2) Coal macerals are closely related to Young's modulus and Poisson's ratio, which can influence the brittleness of coal. The vitrinite content is positively correlated with the brittleness index, while the content of inertinite is negatively correlated in different types of coal-body structures. The vitrinite and inertinite content in primary structure coal has the best correlation with brittleness index. In addition, the mineral content of coal also affects the brittleness of coal in different degrees

(3) For the primary and cataclastic structure coals, the ash and volatile is positively correlated with the brittleness index. However, for the granulate structure coal, these correlation rules are just opposite. The correlation of the brittleness index and coal quality parameters in the primary structure coal is significantly better than that of cataclastic and granulate structure coals. It reveals that the influence of the coal-body structure on the brittleness index is higher than that of coal quality parameters

(4) The mechanical parameters, macerals, and coal quality index of coal are closely related to each other, and together affect the coal brittleness index. This study can provide a useful reference for brittleness characteristics and the relationship between brittleness index and composition of high-rank coal with different coal-body structures. The results are helpful to guide the application of the coal brittleness index and coal-body structure prediction in fracturing of CBM wells. More research on the influencing mechanism of microstructure on the coal brittleness index needs to be carried out in the future

Data Availability

All data are derived from field logging and sampling test data from CBM Wells of Huabei Oilfield Company of PetroChina, which are given in the article and described in Acknowledgements.

Conflicts of Interest

The authors declare that they have no conflicts of interest.

Acknowledgments

We are grateful to Huabei Oilfield Company of PetroChina and Dr. Qianhua Xiao from Chongqing University of Science & Technology for providing some useful data and suggestion for this study. This work was funded by the National Natural Science Foundation of China (NSFC) Project (41702175, U1910204), National Science and Technology Major Project (Oil & Gas) (2017ZX05064, 2016ZX05065), and Research project of China United Coalbed Methane Co., Ltd (ZZGSSAYJPYTH2020-300).

References

[1] J. Lai, G. W. Wang, Z. Y. Fan et al., "Research progress on brittleness index logging evaluation methods for unconventional oil and gas reservoirs," *Petroleum Science Bulletin*, vol. 1, no. 3, pp. 2096–1693, 2016.

[2] B. Liu, S. Wang, X. Ke et al., "Mechanical characteristics and factors controlling brittleness of organic-rich continental shales," *Journal of Petroleum Science and Engineering*, vol. 194, article 107464, 2020.

[3] Y. Li, J. H. Yang, Z. J. Pan, and W. S. Tong, "Nanoscale pore structure and mechanical property analysis of coal: an insight combining AFM and SEM images," *Fuel*, vol. 260, article 116352, 2020.

[4] S. P. Singh, "Brittleness and the mechanical winning of coal," *Mining Science and Technology*, vol. 3, no. 3, pp. 173–180, 1986.

[5] R. Altindag, "Assessment of some brittleness indexes in rock-drilling efficiency," *Rock Mechanics and Rock Engineering*, vol. 43, no. 3, pp. 361–370, 2010.

[6] R. Feng, Y. Zhang, A. Rezagholilou, H. Roshan, and M. Sarmadivaleh, "Brittleness Index: from conventional to hydraulic fracturing energy model," *Rock Mechanics and Rock Engineering*, vol. 53, no. 2, pp. 739–753, 2020.

[7] V. Hucka and B. Das, "Brittleness determination of rocks by different methods," *International Journal of Rock Mechanics and Mining Sciences and Geomechanics Abstracts*, vol. 11, no. 10, pp. 389–392, 1974.

[8] B. R. Law and D. B. Marshal, "Residual stress effects in failure from flaws," *Journal of the American Ceramic Society*, vol. 62, no. 1-2, pp. 106–108, 1979.

[9] R. Altindag, "Correlation of specific energy with rock brittleness concepts on rock cutting," *Journal of the South African Institute of Mining and Metallurgy*, vol. 103, no. 3, pp. 163–171, 2003.

[10] D. M. Jarvie, R. J. Hill, T. E. Ruble, and R. M. Pollastro, "Unconventional shale-gas systems: the Mississippian Barnett Shale of North-Central Texas as one model for thermogenic shale-gas assessment," *AAPG Bulletin*, vol. 91, no. 4, pp. 475–499, 2007.

[11] R. Rickman, M. J. Mullen, J. E. Petre, B. Grieser, and D. Kundert, "A practical use of shale petrophysics for stimulation design optimization: all shale plays are not clones of the Barnett Shale," in *SPE Annual Technical Conference & Exhibition*, pp. 21–24, Denver, Colorado, USA, September, 2008.

[12] X. H. Zhang, X. C. Zou, H. Y. Zhao, F. Li, and L. M. Qin, "A new method for evaluating shale brittleness using X-fluorescence element logging data," *Petroleum Drilling Technology*, vol. 40, no. 5, pp. 96–99, 2012.

[13] H. Wang and J. Tang, "Research on influencing factors and evaluation methods of shale gas reservoir brittleness," in *China Earth Sciences Joint Academic Annual Conference*, vol. 27, pp. 56-57, Beijing, China, 2016.

[14] Y. J. Lu, Z. Z. Yang, V. V. Shelepov, J. X. Han, X. G. Li, and W. Han, "Evaluation and research of brittleness on simulated

reservoir volume in coal," *Oil and Gas Reservoir Evaluation and Development*, vol. 8, no. 1, pp. 64–70, 2018.

[15] L. Ai, M. S. Zhou, J. Zhang, X. Liang, B. W. Qian, and D. R. Liu, "Logging quantitative identification of coal-body structure based on coal brittleness index," *Lithologic Reservoirs*, vol. 29, no. 2, pp. 139–144, 2017.

[16] J. Zhang, L. H. Fan, J. Mei, N. N. Feng, and J. Liu, "Application of logging technology in the identification of coal and rock structure in Fanzhuang area," *China Coalbed Methane*, vol. 14, no. 3, pp. 12–16, 2017.

[17] H. B. Wu, P. S. Zhang, S. H. Dong, Y. P. Huang, and M. Zhang, "Brittleness index analysis of coal samples," *Acta Geophysica*, vol. 67, no. 3, pp. 789–797, 2019.

[18] J. Zhang, C. Ai, Y. W. Li, M. G. Che, R. Gao, and J. Zeng, "Energy-based brittleness index and acoustic emission characteristics of anisotropic coal under triaxial stress condition," *Rock Mechanics and Rock Engineering*, vol. 51, no. 11, pp. 3343–3360, 2018.

[19] T. OKI, J. TANAKA, and T. HARADA, "Cause of coal grindability correlation of coal rank, maceral composition, hardness, and brittleness," *Shigen to Sozai*, vol. 112, no. 1, pp. 37–42, 1996.

[20] Y. H. Yang, Y. T. Wang, L. W. Chen et al., "Optimization technology of efficient CBM productivity areas in Qinnanxi-Mabidong Block, Qinshui Basin, Shanxi, China," *Journal of China Coal Society*, vol. 43, no. 6, pp. 1620–1626, 2018.

[21] X. D. Zhang, Z. G. Du, and P. P. Li, "Physical characteristics of high-rank coal reservoirs in different coal-body structures and the mechanism of coalbed methane production," *Science China Earth Sciences*, vol. 60, no. 2, pp. 246–255, 2017.

[22] Y. Cheng and Z. Pan, "Reservoir properties of Chinese tectonic coal: a review," *Fuel*, vol. 260, article 116350, 2020.

[23] J. Q. Li, D. M. Liu, S. F. Lu, H. T. Xue, and W. H. Li, "Experimental study on Young's modulus of medium and high rank coals and its influencing factors," *Coal Science and Technology*, vol. 44, no. 1, pp. 102–108, 2016.

[24] Q. Li, J. Chen, and J. J. He, "Physical properties, vitrinite reflectance, and microstructure of coal, Taiyuan Formation, Qinshui Basin, China," *Applied Geophysics*, vol. 14, no. 4, pp. 480–491, 2017.

[25] H. Liu, W. H. Huang, X. X. Lu, S. P. Liu, and J. L. Luo, "Research on the control of coal micro-coal composition on micro-cracks of Qinnan no.3 coal seam and no.15 coal seam," *Resources and Industry*, vol. 14, no. 4, pp. 81–87, 2012.

[26] M. Heidari, G. R. Khanlari, M. Torabi-Kaveh, S. Kargarian, and S. Saneie, "Effect of porosity on rock brittleness," *Rock Mechanics and Rock Engineering*, vol. 47, no. 2, pp. 785–790, 2014.

[27] A. E. Hansen and J. C. Hower, "Notes on the relationship between microlithotype composition and hardgrove grindability index for rank suites of eastern Kentucky (central Appalachian) coals," *International Journal of Coal Geology*, vol. 131, pp. 109–112, 2014.

[28] C. L. Hou, B. Jiang, H. W. Liu, Y. Song, and S. C. Xu, "The differences of nanoscale mechanical properties among coal maceral groups," *Journal of Natural Gas Science and Engineering*, vol. 80, article 103394, 2020.

Hindawi
Geofluids
Volume 2021, Article ID 5522282, 13 pages
https://doi.org/10.1155/2021/5522282

Research Article

Numerical Investigation of Multistage Fractured Horizontal Wells considering Multiphase Flow and Geomechanical Effects

Jun Li,[1] Yuetian Liu,[1] and Kecong Ma[2]

[1]*China University of Petroleum-Beijing, Changping District, Beijing 102249, China*
[2]*Changqing Oilfield, CNPC, Xi'an 710000, China*

Correspondence should be addressed to Yuetian Liu; lyt51@163.com

Received 25 January 2021; Revised 6 April 2021; Accepted 12 April 2021; Published 4 May 2021

Academic Editor: Yong Li

Hydraulic fracturing is a key technology in unconventional reservoir production, yet many simulators only consider the single-phase flow of shale gas, ignoring the two-phase flow process caused by the retained fracturing fluid in the early stage of production. In this study, a three-dimensional fluid–gas–solid coupling reservoir model is proposed, and the governing equations which involve the early injection water phenomenon and stress-sensitive characteristics of shale gas reservoirs are established. The finite element–finite difference method was used for discretisation of stress and strain equations and the equations of flow balances. Further, a sensitivity analysis was conducted to analyse fracture deformation changes in the production. Fracture characteristics under different rock mechanics coefficients were simulated, and the influence of rock mechanics parameters on productivity was further characterised. The stimulated reservoir volume zone permeability could determine the retrofitting effect, the permeability increased from 0.02 to 0.1 mD, and cumulative gas production increased from 18.08 to 26.42 million m^3, thus showing an increase of 8.34 million m^3, or 46%. The effect of Young's modulus on the yield was smaller than Poisson's ratio and the width and length of the fractures. Production was most sensitive to the length of the fractures. The length of the fracture increased from 200 to 400 m, and the cumulative gas production increased from 26.44 to 38.34 million m^3, showing an increase of 11.9 million m^3, or 45%. This study deepens the understanding of the production process of shale gas reservoirs and has significance for the fluid–gas–solid coupling of shale gas reservoirs.

1. Introduction

Shale gas reservoirs have vast reserves globally and have received considerable attention for decades [1, 2]. Hydraulic fracturing is a key technology which creates a wide range of fracture networks around the well of a shale gas reservoir. The permeability of fracture networks is higher than that of the shale matrix and makes shale gas flow available; therefore, the development of the fracture networks influences the gas flow rate and total recovery. It is essential to study the characteristics of complex fracture networks after hydraulic fracturing to facilitate more accurate predictions of production.

The formation of fracture networks is complex, and many factors influence their properties [3, 4]. Laboratory experiments show that the permeability of shale is highly stress-sensitive. Hideaki et al. [5]. investigated rock permeability and found that permeability was determined by the chemomechanical effects. Liu et al. [6] introduced a two-dimensional matrix-fracture flow experiment to study the stress-sensitive phenomenon and found that the decrease in flow pressure led to the compression of the rock volume and the deformation of the fracture geometry, and the porosity and permeability of the fracture decreased directly, which resulted in a decrease in flow capacity recovery [7–9]. In a field test, Karal et al. [10] used well log data to analyse the permeability of natural fractures. However, both laboratory tests and field tests have limitations. The monitoring of the in situ stress field generally only operates in a relatively small area around the test well and is expensive, making massive

implementation difficult. While in the laboratory, the test environment is typically inconsistent with the actual geologic conditions; thus, certain physical processes cannot be successfully implemented. Therefore, for convenience and to facilitate higher accuracy, numerical simulation is a suitable method to study fracture permeability with fluid–solid coupling in the entire reservoir [11, 12].

During the hydraulic fracturing process, the fracturing fluid, which is retained in the fracture network, can be produced with shale gas in the early stage of production, which decreases the fracture permeability. Many cases have been reported in field development [13]. Several researchers have established a numerical simulator to solve problems related to fluid–solid coupling from different aspects; the procedure for numerical simulation includes mathematical model establishment, model discretisation methods, and the solution of model equations. Gan and Elsworth [14] introduced a continuum model which considers the permeability of fracture rock masses in discrete fracture networks considering the coupled stress and fluid flow. Further, commercial numerical reservoir simulators use the rock compression coefficient to simulate the rock block deformation. However, the rock compression coefficient is measured under laboratory conditions; thus, it fails to represent the true variations in stress changes, especially for a complex fracture network reservoir. The unique geological characteristics of shale gas reservoirs make it difficult for the compression coefficient to meet the conditions of laboratory measurements. Julio et al. [15] noticed the geomechanical effects of the fracture rock masses incorporated in the model for fluid flow in deformable fractured media and represented the evolution of the fracture rock mass permeability. Sanaee et al. [16] analysed the core flood laboratory experimental data using two different numerical methods, and both methods involved the overburden stress effects on the fracture-matrix core permeability. It is considered more effective to solve the problem by combining a numerical reservoir simulator and an in situ stress simulator to compute the effective stress distribution in the formation.

Therefore, it is essential to build a special fluid structure coupling simulator, especially for shale gas reservoirs with complex fracture networks [17]. In the numerical simulation, there are many discrete methods to cope with the complex fracture network problem, including the finite difference, finite volume, and finite element methods. Among them, the finite element method is widely used in geomechanics. Shin and Santamarina [18] applied the finite element framework to an implicit joint-continuum model to simulate the hydromechanical process in fractured rock masses. Similarly, Li et al. [4] introduced the extended finite element method to simulate the interaction in complex fracture networks and found that different working conditions, such as fracture azimuth and fluid pressure, showed different fracture morphologies. Sutopo and Sato [19] conducted a mixed finite volume element method on a flux continuous model to simulate flow in fractured reservoirs. The finite volume method is based on irregular grid simulation. Using this, Xu et al. [20] introduced an element-based finite volume method to a three-dimensional embedded discrete fracture model and improved the flexibility of fracture patterns. Special discrete methods such as the discontinuous finite element method can solve many difficult problems, such as highly permeable anisotropic reservoirs. Vu et al. [21] introduced the boundary element method to solve the two-dimensional flow problem with an anisotropic porous medium including several intersecting curved fractures. To date, the finite difference method is the first preference for commercial simulators because of its stability and convenience. However, there are few reports on the combined finite element–finite difference (FE-FD) method to deal with the coupling problem. This is likely because the realisation of FE–FD in commercial software is often based on an explicit solution, while its numerical cost is high and stability is doubtful.

This study begins by addressing this issue. Section 2 describes the establishment of the equilibrium equation, boundary conditions, and discrete method. Sections 3 and 4 consider the influence of different fracture characteristic parameters on the reservoir properties and field performance and present conclusions.

2. Mathematical Model Equations

This chapter presents a fluid–solid coupling model. The reservoir is divided into a series of regular units on a three-dimensional scale. The physics process assumes that oil and water are immiscible and that the fluid follows Darcy's law. The capillary force and gravity were not considered, and consideration of the matrix diffusion was excluded temporarily. For the gas component, an equation for mass conservation is established in the local element:

$$-\nabla\left(\rho_g v_g\right) + \frac{\partial\left(\rho_{\mathrm{g}}\phi S_{\mathrm{g}}\right)}{\partial t} + \rho_{\mathrm{g}} q_{\mathrm{g}} = 0, \tag{1}$$

where the physical meaning of q_{g} is the well production volume per unit grid volume. The physical meaning of Equation (1) is that in the local element, the sum of the mass change caused by the diffusion term (left one) and the accumulation term (left two) is zero. In the uncoupled process, the diffusion term only considers the flow of the fluid. For the fluid–solid coupling process, the diffusion term of the fluid in the porosity media needs to consider the rock volume strain caused by solid deformation, where ρ_{l} is the fluid density, ϕ is the porosity, S_{l} is the fluid saturation, and q_{l} is the fluid l source.

$$v_{\mathrm{g}} = v_{\mathrm{g}s} + v_{\mathrm{gl}}. \tag{2}$$

The rate of change of the bulk modulus is the total normal displacement of solid deformation per unit time, assuming u_x, u_y, and u_z are the rock displacements along the x, y, and z axes, respectively, and the equation is as follows:

$$\nabla v_{\mathrm{g}s} = \phi S_{\mathrm{g}} \frac{\partial \varepsilon_v}{\partial t} = \phi S_g \frac{\partial}{\partial t}\left(\frac{\partial u_x}{\partial x} + \frac{\partial u_y}{\partial y} + \frac{\partial u_z}{\partial z}\right). \tag{3}$$

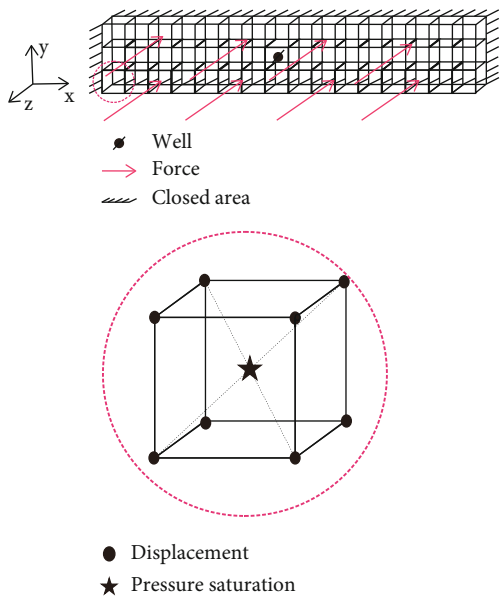

Figure 1: The locations of pressure, saturation, and displacement in the cell.

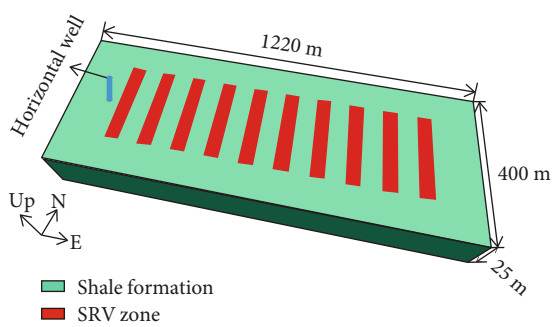

Figure 2: Numerical simulation model of multistage fracturing of horizontal well in the shale gas reservoir.

The flow velocity of the fluid in the porous media is expressed by Darcy's law, as described above:

$$\nabla v_{gl} = -\nabla \frac{K_{rg} K}{\mu_g} P_g, \tag{4}$$

where K_{rg} is the relative permeability of the gas, K is a function of the gas saturation, μ_g is the gas viscosity, and P_g is the gas pressure. Because the capillary force and gravity are not considered, the gas pressure P_g is equal to the fluid pressure P.

The second term is the derivative of the cumulative term, over time. The derivative of the cumulative term over time is divided into three parts: density, porosity, and saturation, as follows:

$$\frac{\partial\left(\rho_g \phi S_g\right)}{\partial t} = \rho_g \phi \frac{\partial S_g}{\partial t} + \phi S_g \frac{\partial \rho_g}{\partial t} + \rho_g S_g \frac{\partial \phi}{\partial t}. \tag{5}$$

Table 1: Basic parameters of numerical simulation model.

Parameter	Value
Length of horizontal section (m)	1000
Fracture number	10
Fracture half length (m)	100
Height of fracture (m)	25
Fracture conductivity factor	1000
Width of SRV zone (m)	50
SRV regional permeability (mD)	0.1
Original permeability of shale gas reservoir (mD)	0.005
The porosity of the SRV zone	0.09
Original pressure (MPa)	32
Langmuir pressure (MPa)	25
Langmuir volume (cubic meter/ton)	28
Critical desorption pressure (MPa)	10
Gas content (cubic meter/ton)	8

Table 2: Fracture extension scales under different Young's moduli.

Num.	Poisson's ratio	Young's modulus (GPa)	Fracture width (m)	Fracture length (m)	Fracture height (m)
1		2	20.5	111.9	25
2		4	22.1	104.9	25
3	0.3	6	25.1	92.7	25
4		8	26.3	87.9	25
5		10	27	85	25

Table 3: Fracture extension scales under different Poisson's ratios.

Num.	Young's modulus (GPa)	Poisson's ratio	Fracture width (m)	Fracture length (m)	Fracture height (m)
1		0.2	24.8	93.9	25
2		0.23	24.8	93.7	25
3	6	0.26	24.9	93.3	25
4		0.29	25	92.9	25
5		0.32	25.1	92.5	25

For the unknown terms in the equation, the volume strain, pressure, and saturation are the first unknown terms, which can be solved directly. The remaining unknown terms, including permeability, phase permeability, density, and porosity, are the second unknown terms. These are functions of time and the first unknown terms. They must be transformed into a function of the first unknown terms. Next, we discuss how to represent the second unknown terms.

For the gas component, the change in density with pressure cannot be directly expressed by the compression

Table 4: Gas production condition with different Young's moduli.

Young's modulus (GPa)	Peak gas production (10^4 m^3/d)	Cumulative production (10^4 m^3)	Compared to the minimum permeability increase (10^4 m^3)	Compared to the minimum permeability growth rate
2	3.4	2599	0	0%
4	3.4	2467	-132	-5%
6	3.47	2477	-122	-5%
8	3.46	2329	-270	-10%
10	3.45	2327	-272	-10%

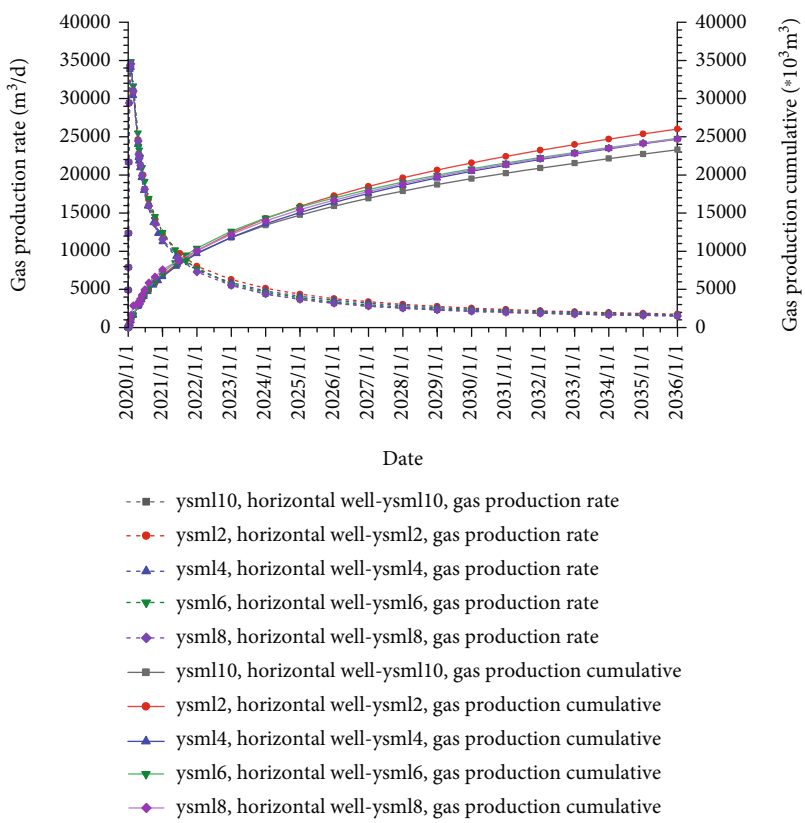

Figure 3: Gas production curves under different Young's moduli.

coefficient. The compression coefficient is not constant or linear with pressure, showing nonlinear characteristics. It is assumed that shale gas is an ideal gas and that the density can be expressed by the equation of state of the ideal gas:

$$PM = \rho_g RT. \tag{6}$$

By deriving the above formula from time, we can obtain the reciprocal of density with respect to time, which is proportional to the derivative of pressure:

$$\frac{\partial \rho_g}{\partial t} = \frac{M}{RT}\frac{\partial P}{\partial t}. \tag{7}$$

Permeability is important for accurately describing the fluid flow. At present, many empirical formulas have been used to simulate the change in permeability with effective stress. However, for shale gas reservoirs with complex fracture networks, the change in the stress field is more complex because of the characteristics of the fracture networks. Thus, laboratory measurement conditions cannot accurately match the underground conditions; therefore, it is difficult to directly apply the permeability formula related to the effective stress. However, another definition of permeability may also be used, in which permeability is a function of porosity. Under the condition of low permeability, the permeability is expressed as

$$k = k_0\left(\frac{\phi}{\phi_0}\right)^3. \tag{8}$$

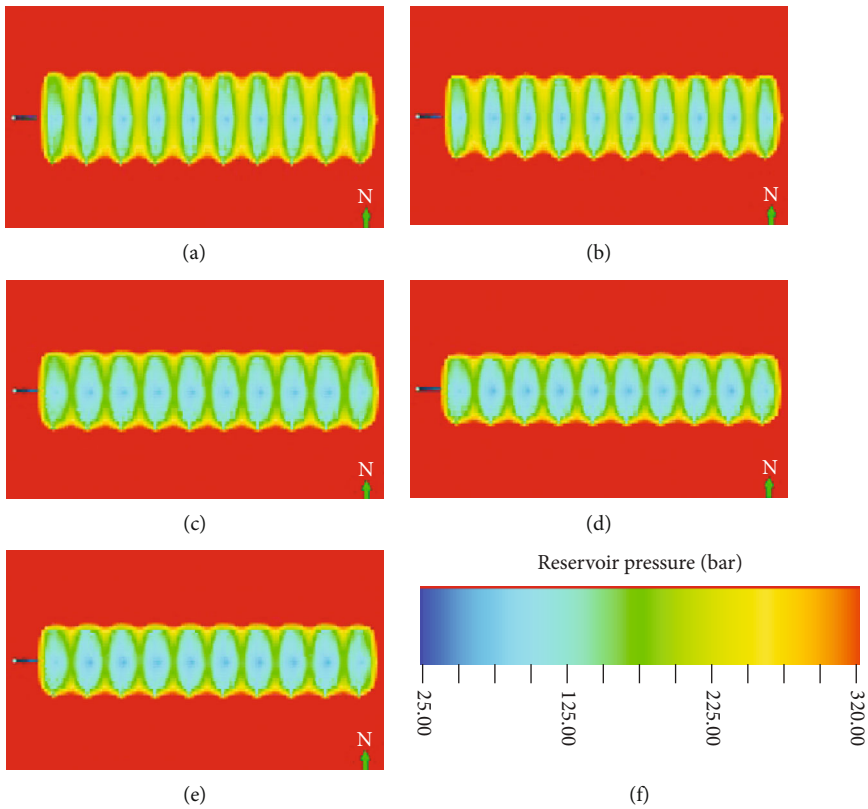

Figure 4: Pressure drop at the end of production with different Young's moduli: (a) Young's modulus is 2 GPa, (b) Young's modulus is 4 GPa, (c) Young's modulus is 6 GPa, (d) when Young's modulus is 8 GPa, (e) Young's modulus is 10 GPa, and (f) the legend of reservoir pressure.

Porosity is expressed as the fluid pressure P, block modulus of elasticity K_s, initial porosity ϕ_0, the Biot coefficient α, and volume strain ε_v (Erdinc, 2017):

$$\frac{d\phi}{dt} = \frac{\alpha - \phi}{K_s}\frac{dP_1}{dt} + (\alpha - \phi)\frac{d\varepsilon_v}{dt}. \tag{9}$$

By integrating these formulas, the control equations for the displacement, pressure, and saturation are established:

$$-\nabla\left(\nabla\frac{K_{rg}K}{\mu_g}P\right) + S_g\alpha\frac{\partial\varepsilon_v}{\partial t} + S_g\frac{\alpha-\phi}{K_s}\frac{\partial P}{\partial t} + \phi S_g\frac{M}{RT}\frac{\partial P}{\partial t} + \phi\frac{\partial S_g}{\partial t} + q_g = 0. \tag{10}$$

For the control equation of the water component, the derivation method is the same as the gas component with one difference, i.e., the compressibility of water is much smaller than that of gas, so the compressibility of water capacity can be expressed by a constant compression coefficient, and the water density is directly proportional to the compression coefficient:

$$\frac{\partial\rho_1}{\partial t} = \rho_1 C_1\frac{\partial P}{\partial t}, \tag{11}$$

where ρ_1 is the density of the liquid, and C_1 is the compressibility of the liquid.

To obtain the solution of the model, the aforementioned governing equation requires auxiliary conditions. In addition to the assumption that the capillary force and gravity are ignored, it is also assumed that the pressure of the gas and that of water can be uniformly expressed as fluid pressure:

$$P_w = P_o = P. \tag{12}$$

According to the principle of phase equilibrium, the sum of the liquid phase saturation and gas phase saturation is equal to 1, that is,

$$S_w + S_g = 1. \tag{13}$$

The governing equation of water can be expressed as follows:

$$-\nabla\left(\nabla\frac{K_{rw}K}{\mu_w}P\right) + S_w\alpha\frac{\partial\varepsilon_v}{\partial t} + S_w\frac{\alpha-\phi}{K_s}\frac{\partial P}{\partial t} + \phi S_w C_w\frac{\partial P}{\partial t} + \phi\frac{\partial S_w}{\partial t} + q_w = 0. \tag{14}$$

Next, the in situ stress governing equation for a local element is described. For this, the reservoir is assumed to be an elastic medium; therefore, in a given element of the reservoir, the sum of the derivations of the stress in

all directions is zero:

$$\nabla\sigma = 0, \tag{15}$$

where σ is the total stress tensor, and its physical meaning is the sum of the effective stress and fluid pressure in the element. Generally, the Biot coefficient is added to describe the degree of fluid pressure on rock deformation. The effective stress of the element can be expressed as

$$\sigma = \sigma_{\text{eff}} - \alpha \mathbf{I} P, \tag{16}$$

where the plus/minus sign indicates the direction of stress.

In the numerical model of the reservoir, the absolute displacement of the element has no practical application significance. Generally, the relative displacement is considered to estimate the degree of deformation of an element. It is assumed that under the initial conditions of the reservoir, a force balance is obtained between the initial in situ stress and fluid pressure in the shale gas reservoir, and the effective stress is zero. Thus, the displacement of each point in the initial state of the formation should also be zero. When the fluid pressure changes, the calculated value corresponds to the relative displacement of the element. By substituting these conditions into the above formula, the following relationships can be obtained:

$$\begin{aligned} \sigma_0 &= 0 - \alpha \mathbf{I} P_0, \\ \sigma - \sigma_0 &= \sigma_{\text{eff}} - \alpha \mathbf{I}(P - P_0). \end{aligned} \tag{17}$$

Because the unknown term to be solved is displacement, these equations of stress need to be transformed into a displacement equation. After special conservation, the following equilibrium equations of displacement and fluid pressure are obtained, where D denotes the elastic tensor, and u is the displacement tensor:

$$\nabla\left(\sigma_0 + L^T D L u - \alpha \mathbf{I}(P - P_0)\right) = 0. \tag{18}$$

Finally, Equations (10), (14), and (18) are combined to form a complete fluid–solid coupling equation for the shale gas reservoir. The above mathematical equations need to be discretised into numerical models, in which the standard finite element method is used to discretise the geomechanical equations and the finite difference method to discretise the fluid equations. In the finite difference method, the upstream weight method was used to determine the relative permeability to ensure the stability of the numerical simulation. The displacement variable is at the corner of the element, and the pressure and saturation are at the centre of the element. The locations of the pressure, saturation, and displacement in the cell are shown in Figure 1.

The discretisation results are as follows, where n is the trial function of the finite element, V is the unit volume, and Ω is the reservoir area:

$$\begin{aligned}
&\int_\Omega N\nabla\left(\sigma_0 + L^T D L u + \alpha \mathbf{I}(P - P_0)\right) d\Omega = 0, \\
&\left(\frac{A_x K_x K r_{gx}}{\mu_g \Delta x}\right)_{i+(1/2),j,k} \left(p_{i+1,j,k} - p_{i,j,k}\right) \\
&\quad - \left(\frac{A_x K_x K r_{gx}}{\mu_g \Delta x}\right)_{i-(1/2),j,k} \left(p_{i,j,k} - p_{i-1,j,k}\right) \\
&\quad + \left(\frac{A_y K_y K r_{gy}}{\mu_g \Delta y}\right)_{i,j+(1/2),k} \left(p_{i,j+1,k} - p_{i,j,k}\right) \\
&\quad - \left(\frac{A_y K_y K r_{gy}}{\mu_g \Delta y}\right)_{i,j-(1/2),k} \left(p_{i,j,k} - p_{i,j-1,k}\right) \\
&\quad + \left(\frac{A_z K_z K r_{gz}}{\mu_g \Delta z}\right)_{i,j,k+(1/2)} \left(p_{i,j,k+1} - p_{i,j,k}\right) \\
&\quad - \left(\frac{A_z K_z K r_{gz}}{\mu_g \Delta z}\right)_{i,j,k-(1/2)} \left(p_{i,j,k} - p_{i,j,k-1}\right) + q_g V \\
&= V S_{g,i,j,k} \alpha \frac{\partial \varepsilon_{v,i,j.k}}{\partial t} + V S_{g,i,j,k} \frac{\alpha - \phi}{K_s} \frac{\partial P_{i,j.k}}{\partial t} \\
&\quad + \phi V S_{g,i,j,k} \frac{M}{RT} \frac{\partial P_{i,j.k}}{\partial t}, \phi V \frac{\partial S_{g,i,j,k}}{\partial t} \left(\frac{A_x K_x K r_{wx}}{\mu_w \Delta x}\right)_{i+(1/2),j,k} \\
&\quad \cdot \left(p_{i+1,j,k} - p_{i,j,k}\right) - \left(\frac{A_x K_x K r_{wx}}{\mu_w \Delta x}\right)_{i-(1/2),j,k} \left(p_{i,j,k} - p_{i-1,j,k}\right) \\
&\quad + \left(\frac{A_y K_y K r_{wy}}{\mu_w \Delta y}\right)_{i,j+(1/2),k} \left(p_{i,j+1,k} - p_{i,j,k}\right) \\
&\quad - \left(\frac{A_y K_y K r_{wy}}{\mu_w \Delta y}\right)_{i,j-(1/2),k} \left(p_{i,j,k} - p_{i,j-1,k}\right) \\
&\quad + \left(\frac{A_z K_z K r_{wz}}{\mu_w \Delta z}\right)_{i,j,k+(1/2)} \left(p_{i,j,k+1} - p_{i,j,k}\right) \\
&\quad - \left(\frac{A_z K_z K r_{wz}}{\mu_w \Delta z}\right)_{i,j,k-(1/2)} \left(p_{i,j,k} - p_{i,j,k-1}\right) + q_w V \\
&= V S_{g,i,j,k} \alpha \frac{\partial \varepsilon_{v,i,j.k}}{\partial t} + V S_{g,i,j,k} \frac{\alpha - \phi}{K_s} \frac{\partial P_{i,j.k}}{\partial t} \\
&\quad + \phi S_w C_w V \frac{\partial P_{i,j.k}}{\partial t} + \phi V \frac{\partial S_{g,i,j,k}}{\partial t}.
\end{aligned} \tag{19}$$

In the production of shale gas reservoirs, the conditions of production are usually well-maintained under constant wellbore pressure conditions. The Peaceman well model was used to simulate the production well in this study.

The initial condition of the reservoir was set as follows. Under the assumption of setting the fluid pressure, the initial in situ stress in the model is obtained by the following formula:

$$P = P_0 \text{ at } t = t_0. \tag{20}$$

The boundary conditions for the stress and flow are listed. The boundary of the flow conforms to Neumann

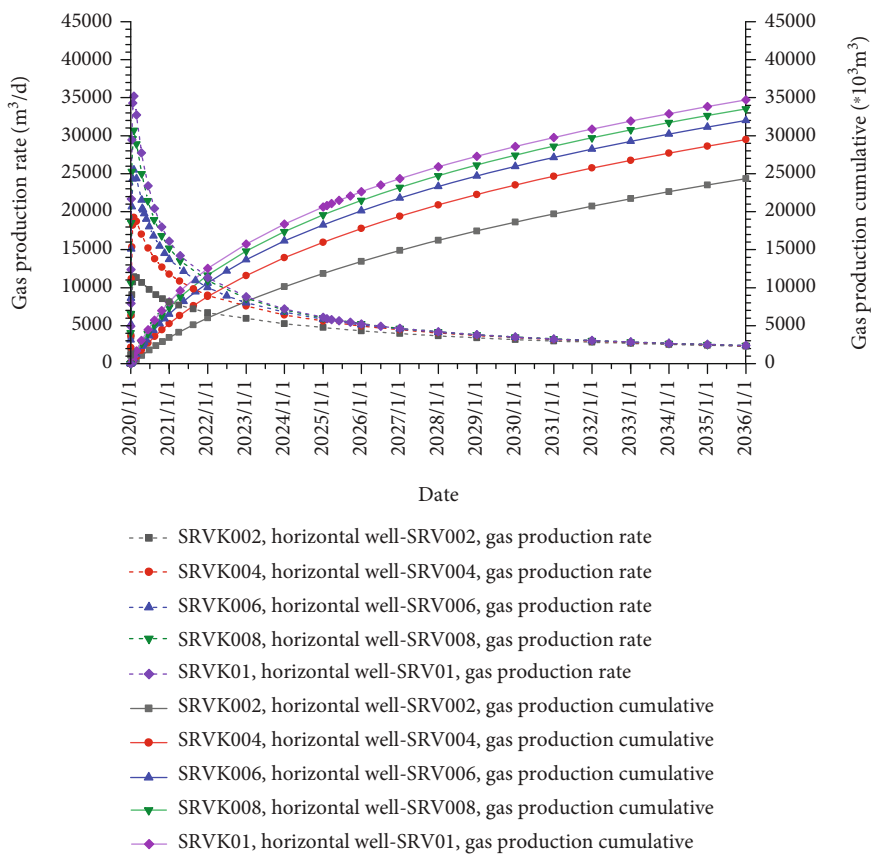

Figure 5: Production curves showing that horizontal well gas production under different SRV permeability is greater than that of cumulative gas production.

boundary conditions, and the shale gas reservoir is in a closed state:

$$\left.\frac{\partial P}{\partial n}\bullet n\right|_{\Gamma} = \mathbf{0}. \tag{21}$$

For the boundary condition of the in situ stress, the normal direction of the upper boundary is influenced by the constant overburden stress. The displacement from other surfaces in the direction of the normal direction was 0. The mathematical expressions are as follows:

$$\begin{aligned} \mathbf{u}\bullet\mathbf{n}|_{\Gamma 1} &= 0, \\ \sigma\bullet\mathbf{n}|_{\Gamma 2} &= \mathbf{0}. \end{aligned} \tag{22}$$

The complex fracture network consists of a hydraulic fracture and a natural fracture group around it. To describe the fluid flow between the fracture and rock around smoothly, the local grid refinement (LGR) scheme was used to indicate a high-permeability fracture network. The distribution of the cells around the hydraulic fractures obeys a logarithmic distribution, and the natural fractures caused by hydraulic fracturing around the hydraulic fracture were represented in the REV region. The coupled set of equations was then solved using the Newton–Raphson method.

3. Results

A numerical simulation model for the horizontal well staged fracturing development of a shale gas reservoir was established (Figure 2). The basic geological parameters of the base case are listed in Table 1. The model was 1220 m long, 400 m wide, and 25 m high, with an area of 0.488 km^2. The grid cells of length direction, width direction, and height direction were $300 \times 200 \times 7$, respectively, and the total number of grids was 420,000.

The model considers the fluid–structure coupling effect, and the permeability and porosity change with the change in pressure in the production process. The Durcan model was used to describe the stress-sensitive effect of the shale reservoir. The model considered the adsorption of shale gas. Curtis, a well-known scholar in the field of shale gas research in the United States, proposed in 2002 that shale gas is essentially continuously generates biochemically derived gas and thermally derived gas. He states that shale gas has a hidden accumulation mechanism with multiple types of lithological closure, a relatively short migration distance, and a general formation saturation gas content, which can exist in both a free state in natural cracks and pores and in an adsorbed state on the surface of kerogen and clay particles, and can also even dissolve into kerogen and asphaltene states [22]. In the study of adsorption phenomena, the adsorption isotherm curve is the most common way to express the adsorption

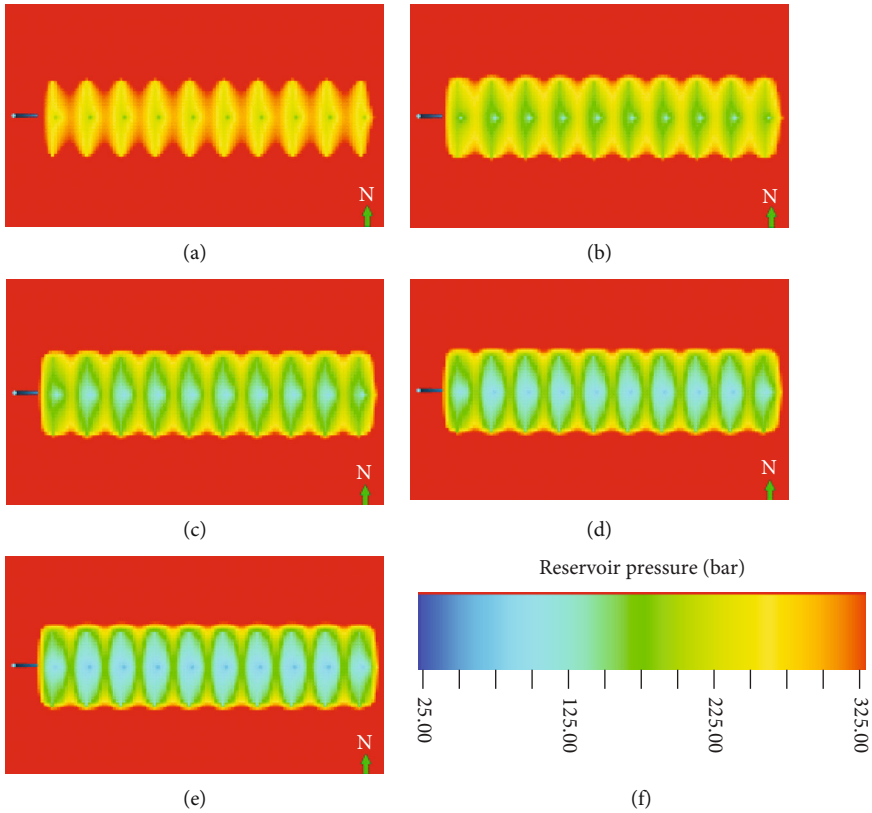

Figure 6: End-production pressure distribution under different permeability conditions in SRV zones: (a) SRV permeability is 0.02 mD, (b) SRV permeability is 0.04 mD, (c) SRV permeability is 0.06 mD, (d) SRV permeability is 0.08 mD, (e) SRV permeability is 0.1 mD, and (f) the legend of reservoir pressure.

performance, and its shape can well reflect the physical and chemical interactions between the adsorbent and the adsorbed substance. Therefore, in this study, the Langmuir isothermal adsorption equation was used to describe the change process of adsorbed gas with pressure in the shale gas production process. The numerical simulation was conducted using the simulation software of Schlumberger.

3.1. Degree of Rock Deformation. The degree of formation degeneration is controlled by Young's modulus E and Poisson's ratio V. In an elastomer, the higher the value of Young's modulus, the less obvious the deformation effect is under the premise of the same stress [23, 24]. Poisson's ratio determines the ratio of the longitudinal to transverse deformation of the elastomer. In the fluid–structure coupling process of this study, Young's modulus determines the volume modulus of the rock and controls the volume strain of the reservoir in the formation [25, 26].

Young's modulus and Poisson's ratio mainly affect the fracture elongation effect, which then affects the gas well productivity. Therefore, before studying the influence of Young's modulus and Poisson's ratio on productivity, it is necessary to simulate the fracture generation process. The fracturing simulation software FRCPT was used to simulate the fracturing process, and the effect of fracture extension under different Young's moduli and Poisson's ratios under the same fracturing scale and pumping program were studied. The research conclusions are presented in Tables 2 and 3.

It is evident from the tables that the influence of Young's modulus on the fracture elongation effect is greater than that of the Poisson's ratio, mainly because in general, Poisson's ratio has a smaller variation range, while Young's modulus has a larger variation range. Under different Poisson's ratios, the difference in fracture width variation was no more than 0.3 m, and the difference in fracture length was no more than 1.4 m. Under such width and fracture length variations, there was almost no influence on productivity. Therefore, this sensitivity analysis does not discuss the influence of Poisson's ratio on production and instead focuses on the influence of Young's modulus on productivity.

Based on the fracturing simulation with different Young's moduli, a reservoir numerical simulation model was established to predict the productivity of horizontal wells with different Young's moduli (Table 4).

The final results (Figures 3 and 4) show that with the increase in Young's modulus, the range of SRV zones becomes smaller under the same fracturing system, and accordingly, the reservoir transformation effect becomes worse. The difference in peak gas production was not large, increasing from 34,000 to 34,500 m^3/d. The cumulative gas production decreased from 25.99 to 23.27 million m^3, a production decrease of 10%.

Table 5: Peak and cumulative gas production at different permeability levels.

Permeability (mD)	Peak gas production (10^4 m^3/d)	Cumulative production (10^4 m^3)	Compared to the minimum permeability increase (10^4 m^3)	Compared to the minimum permeability growth rate
0.02	1.1	1808	0	0%
0.04	3.6	2204	396	22%
0.06	3.1	2411	603	33%
0.08	2.5	2545	737	41%
0.1	2	2642	834	46%

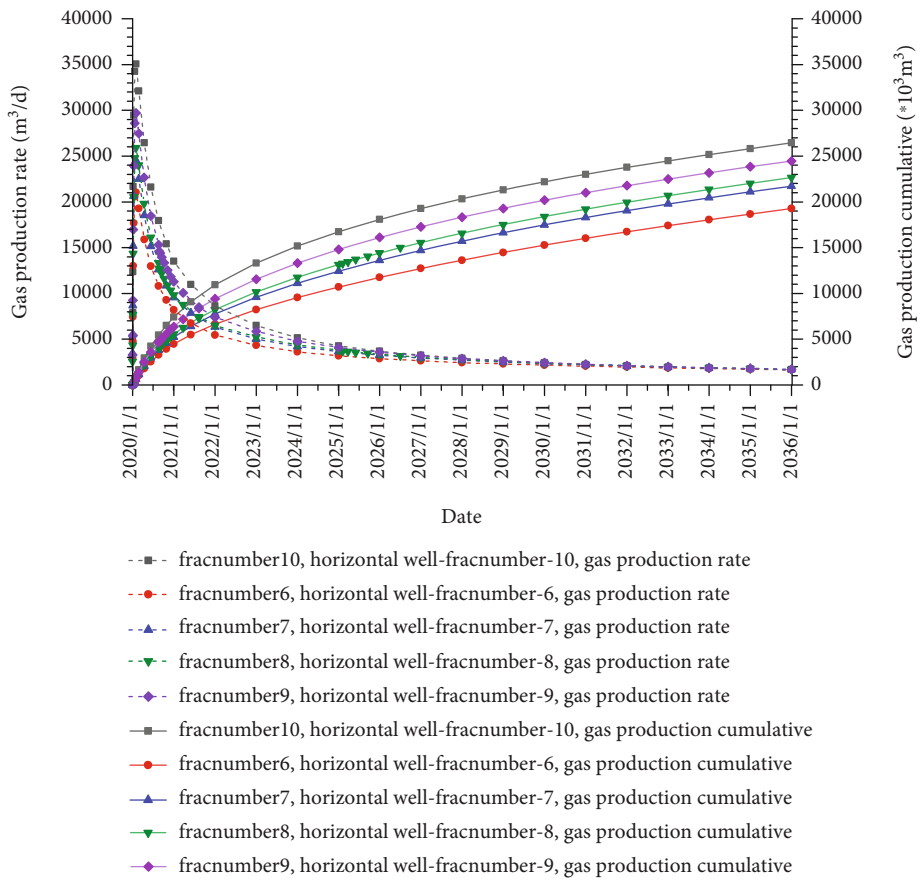

Figure 7: Horizontal well gas production under different fracture spacing.

Compared with the other three parameters, Young's modulus has less effect on the production, mainly in the process of 2 GPa to 10 GPa, the fracturing parameters, fracturing scale, and fracturing system under the same fracture of the SRV area changed little, and the extent and effect of the SRV area were the key factors influencing the shale gas reservoir; therefore, in comparison, the influence of the output of Young's modulus on the other three parameters.

3.2. SRV Regional Permeability. Owing to the influence of hydraulic fracturing technology, a large number of natural microfractures are produced around the pressure fractures. These natural fractures improve the reservoir permeability in these areas and are the main seepage channels of shale gas reservoirs, which are important factors for improving productivity. We call these artificially fractured high-permeability SRV zones. Permeability in SRV zones is usually obtained through subsurface core sampling and logging experiments.

Under the original conditions, the permeability of the shale gas reservoir is relatively small, and commercial airflow cannot be obtained without reservoir modification. The permeability of the reformed shale gas reservoir can reach 0.1–0.01 mD in the modified area. Combined with the high-pressure characteristics of shale gas reservoirs, commercial airflow can be obtained under the conditions of permeability.

On the one hand, the permeability of the SRV zone determines the productivity of the shale gas well. On the other hand, the SRV zone itself is small; thus, the productivity will inevitably reach an inflexion point after the permeability reaches a certain height. Therefore, based on the permeability of the revamp zone, five groups of parameters of the revamp

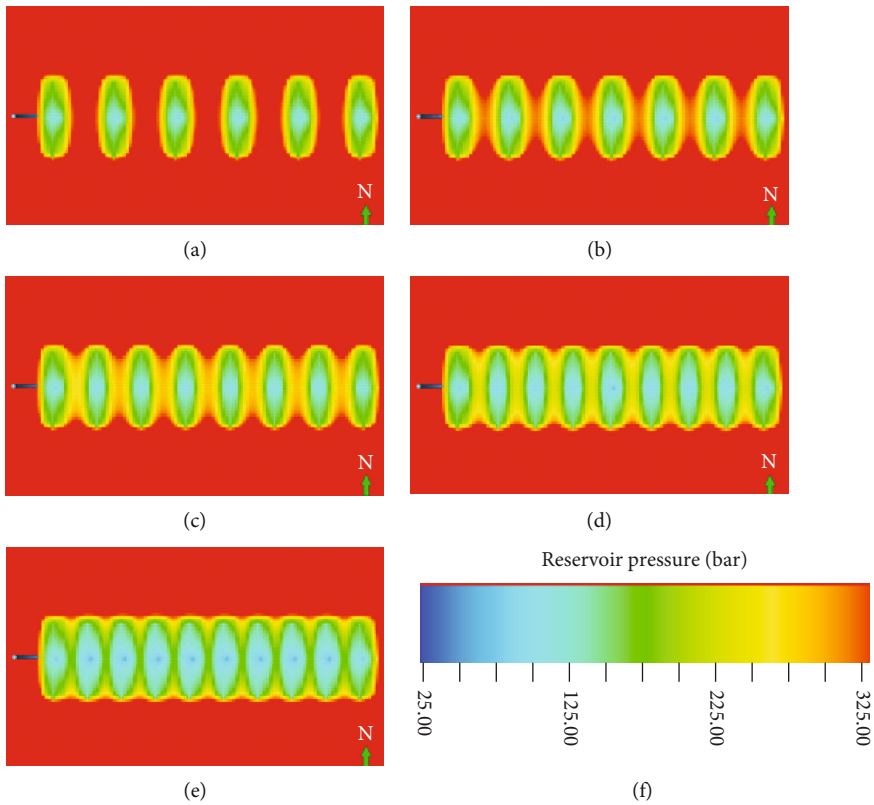

Figure 8: End-production pressure distribution under different fracture numbers: (a) 6 fractures, (b) 7 fractures, (c) 8 fractures, (d) 9 fractures, (e) 10 fractures, and (f) the legend of reservoir pressure.

Table 6: Peak and cumulative gas production at fracture number.

Fracture number	Peak gas production (10^4 m^3/d)	Cumulative production (10^4 m^3)	Compared to the minimum permeability increase (10^4 m^3)	Compared to the minimum permeability growth rate
6	2.1	1926	0	0%
7	2.4	2172	246	13%
8	2.6	2264	338	18%
9	3	2445	519	27%
10	3.5	2644	718	37%

zone (0.02, 0.04, 0.06, 0.08, and 0.1 mD) were selected to study the influence of the permeability of the SRV zone on the productivity of a single well.

The results (Figures 5 and 6 and Table 5) show that the SRV zone permeability had a significant impact on the final cumulative gas production per well. When the permeability increased from 0.02 to 0.1 mD, the cumulative gas production increased from 18.08 to 26.42 million m^3, a 46% increase in production. However, when the SRV permeability reached 0.06 mD, the increase in cumulative gas production decreased. This is owing to two factors: (1) the SRV area permeability could meet the corresponding area of the gas extraction; thus, permeability was no longer the bottleneck of production and (2) from the point of production at the end of pressure distribution, the gas was output from most but not all of the SRV area of low permeability, and the pressure nearly did not decrease the SRV area, which reached a considerable recovery. At that time, the increasing permeability had not increased the gas well production and only by expanding the SRV area could the single-well production capacity be increased; therefore, in the SRV transformation, the transformed effect of permeability did not affect the SRV area, but the SRV area itself expanded in width, as demonstrated in the fracture length sensitivity analysis.

3.3. Fracture Spacing. Fracture spacing is an important factor that determines the effect of reservoir development [27, 28]. Moreover, fracture spacing can change the control area of fractures and the variation law of stress field between fractures.

In certain cases, the horizontal well length determines the spacing between the fractures' own control areas, in that, the greater the gap spacing and the fracture control area, the less the recovery efficiency of the horizontal control area, cost reduction, the 1000 m horizontal wells, based on base case, respectively, set up seam article 6, article 7, article 8 seam sewing seam, article 9, 10, the corresponding joint spacing for, in order to study the effect of joint spacing on horizontal well productivity.

The results (Figures 7 and 8 and Table 6) showed that with the decrease in fracture spacing, the number of fractures increased and the SRV zone expanded and the cumulative

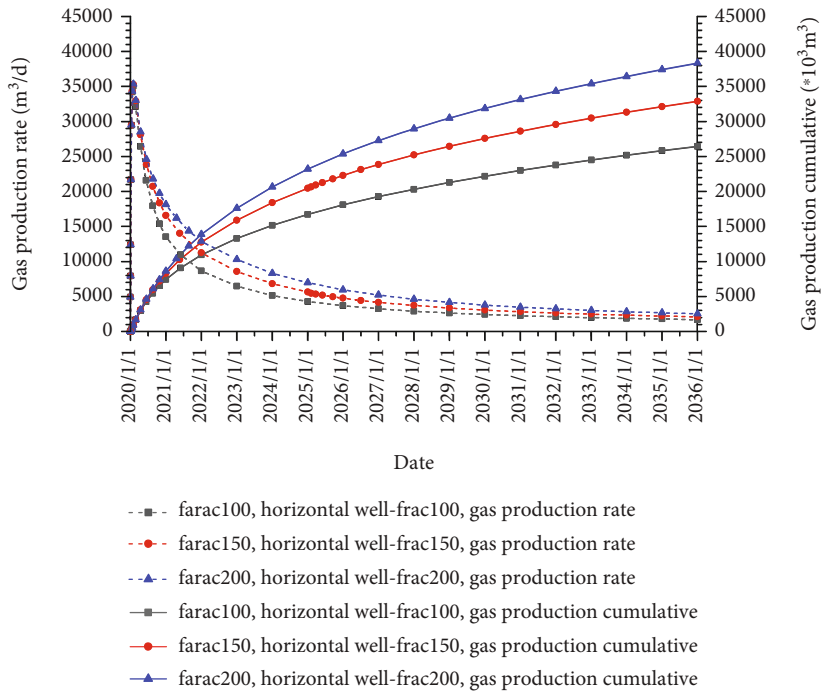

Figure 9: Cumulative gas production per well at different fracture lengths.

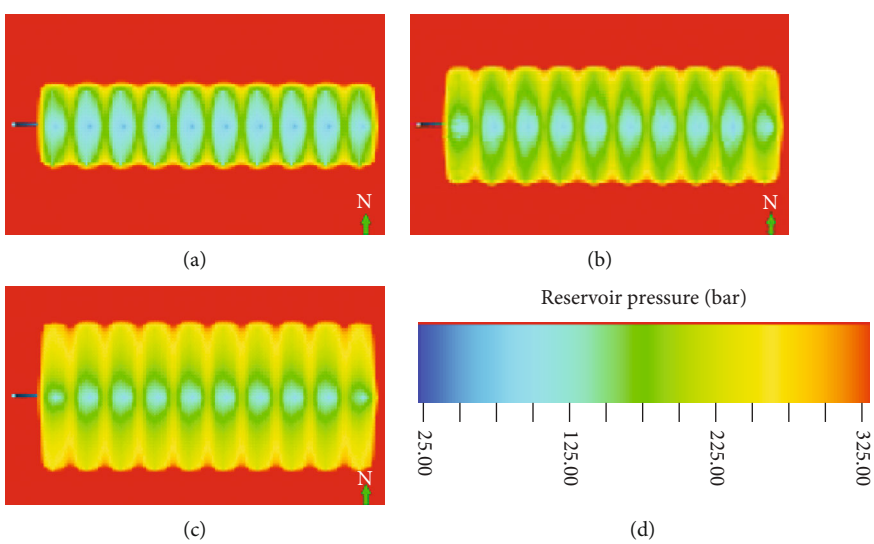

Figure 10: Pressure drop at the end of production with different fracture lengths: (a) the fracture length is 200 m, (b) the fracture length is 300 m, (c) the fracture length is 400 m, and (d) the legend of reservoir pressure.

gas production per well increased accordingly. Fractures in the bar or the increase in the number did not quickly improve the recovery of a single well. From the point of this model, when the fracture number increased to 7, the pressure between the fractures began to decline, compared with 8 fractures, article 9 and article 10 of fractures of the pressure did not expand much or affect the scope. The inflection point on this performance in the accumulative gas production appeared between 6 to 7 fractures; unlike the increase in fracture length, the increase in fracture number was less sensitive to enhanced recovery. The cumulative gas production of 6 to 7 fractures increased from 1926×10^4 m^3 to 2172×10^4 m^3, and one fracture increased production by 13 to 2.46 million m^3. However, with 8 fractures, 1 fracture increased production by 9% to 1.69 million m^3, and the production capacity of a single fracture decreased.

Moreover, in the process of fracturing, the increase in fracture stages is associated with an increase in the economic cost. Therefore, in the optimisation process of fracture stages, the influence of economic factors should be fully considered, and the optimisation of fracture stages should be conducted with economic indicators as the object.

Table 7: Peak and cumulative gas production at different fracture lengths.

Fracture length (m)	Peak gas production (10^4 m^3/d)	Cumulative production (10^4 m^3)	Compared to the minimum permeability increase (10^4 m^3)	Compared to the minimum permeability growth rate
200	34500	2644	0	0%
300	34800	3287	643	24%
400	35000	3834	1190	45%

3.4. Fracture Length. The following will consider the impact of fracture length on development results. The fracture length will directly determine the width of the SRV zone, which has a significant impact on seepage flow [29, 30].

Based on base case, three groups of fracture lengths were set: 200 m (fracture half-length is 100 m), 300 m (half-length, 150 m), and 400 m (half-length, 200 m). In all three cases, the length of the SRV zone increased with the increase in fracture length, whereas the fracture width remained unchanged.

The numerical simulation results (Figures 9 and 10 and Table 7) show that the fracture length has a direct effect on the cumulative gas production of a single well. The longer the fracture, the greater the cumulative gas production of a single well, and there was no inflexion point. Therefore, the size of the SRV region is a key factor in determining the success of an SRV. When the fracture length increased from 200 to 400 m, cumulative gas production per well increased from 2644×10^4 m^3 to 3834×10^4 m^3, an increase of 45%.

4. Conclusions

(1) The effect of Young's modulus on yield is smaller than that of the other three parameters, and under different Poisson's ratios, the width and length of fractures vary by a relatively small range. Poisson's ratio itself changed slightly from 0.2 to 0.32, the fracture width and length changed by 0.3 and 1.4 m, respectively, and the variation in the width and length had almost no effect on productivity

(2) The fracture length has a direct effect on cumulative gas production per well, in that, the longer the fracture, the greater the cumulative gas production per well, and there was no inflexion point. The length of the fracture increased from 200 to 400 m, and the cumulative gas production increased from 26.44 to 38.34 million m^3, an increase of 11.9 million m^3, or 45%. Therefore, in SRV retrofitting, it is not the SRV zone permeability that determines the retrofitting effect, but the SRV zone expansion width

(3) As the number of fractures increased from 6 to 10, the cumulative gas production increased from 19.26 to 26.44 million m^3, an increase of 7.18 million m^3, or 37%. However, in the process of fracturing, such an increase in fracture stages would mean an increase in the economic cost. Therefore, in the optimisation process of fracture stages and the influence of economic factors should be fully considered, and the optimisation of fracture stages should be conducted with economic indicators as the object

Data Availability

The research results of this paper are based on the application of formula derivation, and all the formulas and related data are included in the paper.

Conflicts of Interest

The authors declare that they have no conflicts of interest.

References

[1] F. S. Zhang, B. Damjanac, and S. Maxwell, "Investigating hydraulic fracturing complexity in naturally fractured rock masses using fully coupled multiscale numerical modeling," *Rock Mechanics and Rock Engineering*, vol. 52, no. 12, pp. 5137–5160, 2019.

[2] Y. Li, J. Yang, Z. Pan, S. Meng, K. Wang, and X. Niu, "Unconventional natural gas accumulations in stacked deposits: a discussion of Upper Paleozoic coal-bearing strata in the east margin of the Ordos Basin, China," *Acta Geologica Sinica (English Edition)*, vol. 93, no. 1, pp. 111–129, 2019.

[3] Y. Li, Y. Wang, J. Wang, and Z. J. Pan, "Variation in permeability during CO_2-CH_4 displacement in coal seams: Part 1 - Experimental insights," *Fuel*, vol. 263, p. 116666, 2020.

[4] P. L. Li, Y. Dong, S. Wang, and P. C. Li, "Numerical modelling of interaction between hydraulic fractures and natural fractures by using the extended finite element method," *Advances in Civil Engineering*, vol. 2020, Article ID 8848900, 9 pages, 2020.

[5] H. Yasuhara, M. Takahashi, N. Kinoshita, S. Nakashima, and K. Kishida, "Spontaneous alteration of rock permeability under constant confining pressure and temperature condition," *Journal of Nursing Science*, vol. 59, no. 2, pp. 156–165, 2012.

[6] K. Liu, D. Y. Yin, Y. H. Sun, and L. Xia, "Analytical and experimental study of stress sensitivity effect on matrix / fracture transfer in fractured tight reservoir," *Journal of Petroleum Science and Engineering*, vol. 195, p. 107958, 2020.

[7] D. Youn and M. Gutierrez, "Effect of fracture distribution on permeability of fractured rock masses," in *Paper presented at the 45th U.S. Rock Mechanics/Geomechanics Symposium*, San Francisco, California, June 2011.

[8] K. Farahmand, A. Baghbanan, K. Shahriar, and M. S. Diederichs, "Effect of fracture dilation angle on stress-dependent permeability tensor of fractured rock," in *Paper presented at the 49th U.S. Rock Mechanics/Geomechanics Symposium*, San Francisco, California, June 2015.

[9] Y. D. Chen, H. J. Lian, W. G. Liang, J. Yang, V. P. Nguyen, and S. P. A. Bordas, "The influence of fracture geometry variation on non-Darcy flow in fractures under confining stresses," *International Journal of Rock Mechanics and Mining Sciences*, vol. 113, pp. 59–71, 2019.

[10] K. O. Kraal, B. F. Ayling, K. Blake, L. Hackett, T. S. P. Perdana, and R. Stacey, "Linkages between hydrothermal alteration, natural fractures, and permeability: Integration of borehole data for reservoir characterization at the Fallon FORGE EGS site, Nevada, USA," *Geothermics*, vol. 89, p. 101946, 2021.

[11] G. L. Sheng, Y. L. Su, and W. D. A. Wang, "A new fractal approach for describing induced-fracture porosity/permeability/ compressibility in stimulated unconventional reservoirs," *Journal of Petroleum Science and Engineering*, vol. 179, pp. 855–866, 2019.

[12] Q. F. Tao, A. Ghassemi, and C. A. Ehlig-Economides, "A fully coupled method to model fracture permeability change in naturally fractured reservoirs," *International Journal of Rock Mechanics and Mining Sciences*, vol. 48, no. 2, pp. 259–268, 2011.

[13] J. D. Williams-Kovacs, C. R. Clarkson, and B. Zanganeh, "Case studies in quantitative flowback analysis," in *SPE/CSUR Unconventional Resources Conference*, Calgary, Alberta, Canada, October 2015.

[14] Q. Gan and D. Elsworth, "A continuum model for coupled stress and fluid flow in discrete fracture networks," *Geomechanics and Geophysics for Geo-Energy and Geo-Resources*, vol. 2, no. 1, pp. 43–61, 2016.

[15] J. A. Rueda Cordero, E. C. Mejia Sanchez, and D. Roehl, "Integrated discrete fracture and dual porosity - dual permeability models for fluid flow in deformable fractured media," *Journal of Petroleum Science and Engineering*, vol. 175, pp. 644–653, 2019.

[16] R. Sanaee, G. F. Oluyemi, M. Hossain, and M. B. Oyeneyin, "Stress effects on flow partitioning in fractured reservoirs: equivalent porous media versus poro-elasticity coupled modeling," in *Paper presented at the 47th U.S. Rock Mechanics/Geomechanics Symposium*, San Francisco, California, June 2013.

[17] Q. H. Lei, J. P. Latham, and C. F. Tsang, "The use of discrete fracture networks for modelling coupled geomechanical and hydrological behaviour of fractured rocks," *Computers and Geotechnics*, vol. 85, pp. 151–176, 2017.

[18] H. S. Shin and J. C. Santamarina, "An implicit joint-continuum model for the hydro-mechanical analysis of fractured rock masses," *International Journal of Rock Mechanics and Mining Sciences*, vol. 119, pp. 140–148, 2019.

[19] A. N. Sutopo and K. Sato, "Simulation of naturally fractured reservoirs with effective permeability," in *Paper presented at the SPE Asia Pacific Oil and Gas Conference and Exhibition*, Jakarta, Indonesia, April 2001.

[20] Y. Xu, I. C. M. Lima, F. Marcondes, and K. Sepehrnoori, "Development of an embedded discrete fracture model for 2D and 3D unstructured grids using an element-based finite volume method," *Journal of Petroleum Science and Engineering*, vol. 195, article 107725, 2020.

[21] M. N. Vu, A. Pouya, and D. M. Seyedi, "Theoretical and numerical study of the steady-state flow through finite fractured porous media," *International Journal for Numerical & Analytical Methods in Geomechanics*, vol. 38, no. 3, pp. 221–235, 2014.

[22] J. B. Curtis, "Fractured shale-gas systems," *AAPG Bulletin*, vol. 86, no. 11, pp. 1921–1938, 2002.

[23] X. Liang, X. Liu, H. L. Shu et al., "Characterization of complex multiscale natural fracture systems of the Silurian LongMaXi gas shale in the Sichuan Basin, China," in *Paper presented at the SPE Asia Pacific Unconventional Resources Conference and Exhibition*, Brisbane, Australia, November 2015.

[24] S. Zamiran, S. Rafieepour, and M. Ostadhassan, "A geomechanical study of Bakken Formation considering the anisotropic behavior of shale layers," *Journal of Petroleum Science and Engineering*, vol. 165, pp. 567–574, 2018.

[25] L. Maerten, P. Gillespie, and J. M. Daniel, "Three-dimensional geomechanical modeling for constraint of subseismic fault simulation," *AAPG Bulletin*, vol. 90, no. 9, pp. 1337–1358, 2006.

[26] X. Weng, O. Kresse, C. E. Cohen, R. Wu, and H. Gu, "Modeling of hydraulic fracture network propagation in a naturally fractured formation," in *Paper presented at the SPE Hydraulic Fracturing Technology Conference*, The Woodlands, Texas, USA, 2011.

[27] T. L. Blanton, "Propagation of hydraulically and dynamically induced fractures in naturally fractured reservoirs," in *Paper presented at the SPE Unconventional Gas Technology Symposium*, Louisville, Kentucky, 1986.

[28] H. Wu, A. Chudnovsky, J. W. Dudley, and G. K. Wong, "A map of fracture behavior in the vicinity of an interface," in *Paper presented at the Gulf Rocks 2004, the 6th North America Rock Mechanics Symposium (NARMS)*, Houston, Texas, 2004.

[29] A. S. Athavale and J. L. Miskimins, "Laboratory hydraulic fracturing tests on small homogeneous and laminated blocks," in *Paper presented at the 42nd U.S. Rock Mechanics Symposium (USRMS)*, San Francisco, California, 2008.

[30] J. Kear, J. White, A. P. Bunger, R. Jeffrey, and M. A. Hessami, "Three dimensional forms of closely-spaced hydraulic fractures," in *Paper presented at the ISRM International Conference for Effective and Sustainable Hydraulic Fracturing*, Brisbane, Australia, 2013.

Hindawi
Geofluids
Volume 2021, Article ID 5560634, 17 pages
https://doi.org/10.1155/2021/5560634

Research Article

Characteristics of the Coal Fines Produced from Low-Rank Coal Reservoirs and Their Wettability and Settleability in the Binchang Area, South Ordos Basin, China

Yue Chen,[1,2] **Zhuoyuan Ma**,[1] **Dongmin Ma**,[1,2] **Zhicang Zhang**,[3] **Weibo Li**,[4] **Fu Yang**,[2] **Yusong Ji**,[1] **and Tao Peng**[1]

[1]*College of Geology and Environment, Xi'an University of Science and Technology, Xi'an 710054, China*
[2]*Key Laboratory of Coal Resources Exploration and Comprehensive Utilization, Ministry of Natural Resources, Xi'an 710021, China*
[3]*Shaanxi Coalbed Methane Development Co., Ltd, Xi'an 710119, China*
[4]*Shaanxi Geological Science and Technology Center, Xi'an 710054, China*

Correspondence should be addressed to Yue Chen; cyxust@126.com

Received 25 February 2021; Revised 18 March 2021; Accepted 25 March 2021; Published 5 April 2021

Academic Editor: Yanjun Meng

By using proximate analysis, X-ray diffraction mineral analysis, scanning electron microscope, contact angle measurement, and settlement simulation experiment, the coal fines produced from the coalbed methane wells of Binchang area were used to study the characteristics including particle size distribution, composition, morphology, wettability, and settleability. The results show that the particle size of coal fines produced from coalbed methane wells are mainly >20 mesh, ranging of 1-400 μm, and the particle size distribution curve is mainly dominated by the main-secondary bimodal type, with the main peak of 30-300 μm. The particle size from large to small is drill cutting coal fines, flowback coal fines, bailing coal fines, and pipeline filter coal fines. In terms of ash content, coal fines are higher than coal seam, and drilling cuttings are higher than bailing coal fines, while the fixed carbon content of the former is lower than that of the latter. The minerals of coal fines are mainly kaolinite, illite, quartz, and other 6 minerals, and the mineral types of drilling coal fines are the most abundant, while the bailing coal fines only contain illite and quartz. The roundness of coal fine particles ranges from excellent to poor in the order of bailing coal fines, pipeline filter coal fines, flowback coal fines, and drilling cuttings. However, the sorting of drilling cuttings is excellent, and the particle edges are straight, neat, and smooth, while the sorting of bailing coal fines is poor, and the particle edges are curved, uneven, and rough. The contact angles of coal fines are 40.25°-69.5°, indicating hydrophilous. The wettability of bailing coal fines is better than that of drilling cuttings. The particle size has a negative correlation with the wettability effect. The more obvious the modification effect of positive wetting agent is, the worse the modification effect of negative wetting agent is. The modification of surfactant has nothing to do with the particle size of the coal fines, but is closely related to organic components and minerals. The larger the coal particle size, the higher the settling rate, and the higher the ash content and the lower the fixed carbon content, the faster the settling rate. With the dividing point 150 mesh, the settling rate of large particles is mainly affected by particle size, while that of small particles is affected by the composition.

1. Introduction

Coal has the characteristics of low compressive strength, small Young's modulus, small Poisson's ratio, fragile, poor cementation, and easy to collapse. Therefore, coal fines are generally produced in the process of coalbed methane drainage, which blocks pore channels and damages the permeability of the coal seam, which in turn affects the pressure reduction effect of the coal seam [1–6]. According to the generation mechanism of coal fines, coal fines are divided into primary and secondary coal fines. Primary coal fines refer to the coal fines that have always existed in the coal reservoir before the development of coalbed methane during the evolution of the reservoir and are produced under the effects of

coalification and structural deformation. This part of coal fines mainly exists in fault planes, interlayer sliding planes, and pores in coal [7–9]. Secondary coal fines refer to coal fines produced during the development of coalbed methane, which are divided into two types. One type of coal fines is formed during the compression, deformation, and crushing of coal and rock and is mostly produced during drilling, completion, and fracturing. The other type is caused by factors such as hydrodynamic denudation, coal destruction, and mechanical differences in different microscopic coal and rock components. This type of coal fines has a small particle size and is mostly produced in the drainage and gas recovery process of coalbed methane (CBM) wells [10–12]. The produced coal fines move into the wellbore along with the flow of gas and water, blocking the wellbore and hindering drainage. At the same time, the plunger and the pump are worn out, and the pump stuck or buried in the serious case, which seriously threatens the long-term and stable drainage process of the CBM well [2, 13–16].

At present, the researches on coal fines in CBM development mainly focus on three aspects, i.e., characteristics and causes of coal fines, gas and water transport and the rule of coal fine production in drainage and production process, and coal fine prevention and control technology [17–21]. According to the mechanism of coal fine production, it can be divided into three genetic types: inherent, produced by mechanical failure, and produced by stress failure. The nature of coal seam itself is the material basis of coal powder production, including coal rock, coal quality, and coal body structure; also, engineering is the inducing factor of coal fine production, such as drilling, fracturing, and drainage [22–25]. The rule of coal fine production in the process of discharge and production mainly focuses on the rule of coal fine production in each production stage of the gas well, the migration of multiphase flow of coal fines, the rule of settlement and its restricting factors, and the simulation of the rule of coal production driven by gas and water in coal sample [26–32]. The coal fine prevention and control technology mainly include regulation and control of discharge and production system, coal fine control equipment, and additive injection [33–37]. To avoid coalbed methane production problems caused by coal fine production, researchers have used transmission light microscopy, reflection polarization optical microscopy, laser particle size analysis, X-ray diffraction, scanning electron microscopy, and other experimental methods to study the morphological characteristics of coal at different discharge stages, particle size distribution, and material composition [38]. Guo et al. [39] conducted a laboratory investigation on the production of coal fines and believed that the main component of the coal fines produced was clay minerals. Wei et al. [40] believed that the migration law of coal fines is affected by the particle size of coal fines and the content of inorganic minerals. Liu et al. [41] explored change of fuel microstructure during high-temperature coke combustion was analyzed, and the reaction process and particle change behavior were revealed. Kuang et al. [42] analyzed the flow and chemical reaction characteristics at different oxygen concentrations and inlet velocities, and the temperateness was determined. However, there are relatively few studies on the wettability of coal fines. After the activator used in the production process penetrates into the coalbed methane reservoir, it may cause changes in the wettability of the coal rock surface and then changing the wettability and sedimentation of the coal fines. This changes the movement and migration of coal fines in gas and water in the pores and affects the productivity of coalbed methane [43–46].

However, previous studies mainly focused on the Qinshui Basin and the eastern margin of Ordos Basin in China and other middle-high coal-rank areas, while less involved low-rank coal reservoirs. Based on the actual development of low-rank coalbed methane in the Binchang area of the southern Ordos Basin, the author conducts a comprehensive study on the particle size distribution, material composition, morphological characteristics, wettability, and subsidence of coal fines produced from coalbed methane wells. It is hoped to provide a reference for formulating reasonable coal fine control measures to avoid the adverse effects of coal fines on production.

2. Geological Settings

Huanglong Jurassic coalfield is located in Shaanxi Province in the southwest of Ordos Basin, extending to Shaanxi-Gansu boundary in the north, Longxian county in Baoji in the west, and Huangling to the east. Yan'an formation coal seam outcrops in the south, with a total area of 9300 km^2 [47]. It is divided into Yonglong mining area, Binchang mining area, Xunyao mining area, Jiaoping mining area, and Huangling mining area. The tectonic straddles the Weibei fault uplift area and the western margin fold-thrust belt on the southern margin of the Ordos Basin. The NE-trending and EW-trending fold tectonics are mainly developed, and the fault tectonics are less developed and are mainly located in the southeast and southwest margin of the coalfield (Figure 1). The area is rich in coal resources, with coal resources up to 6.7×10^9 t, and the recoverable coal seam is mainly Jurassic Yan'an formation coal seam, mainly low-rank weakly caking coal and long flame coal and gas coal [48, 49]. The Dafosi minefield is located in the Binchang mining area in the middle of the coalfield. The internal structure is relatively simple, fault is undeveloped, strata are gentle, and the dip angle is generally less than 5°. The main mining coal seam is Yan'an formation, and the coal seam has a high gas content, ranging from 1.44 to 2.56 m^3. The prospect of coalbed methane development is good. The exploration and development of coalbed methane in Dafosi minefield began in 2009. By the end of 2019, more than 40 coalbed methane drills have been carried out, mainly horizontal wells, and the maximum gas production per well is more than 3×10^4 m^3/d, which has achieved good gas production results [50].

3. Samples and Methods

3.1. Samples. The experimental samples are collected from the coalbed methane well and the coal fines produced by

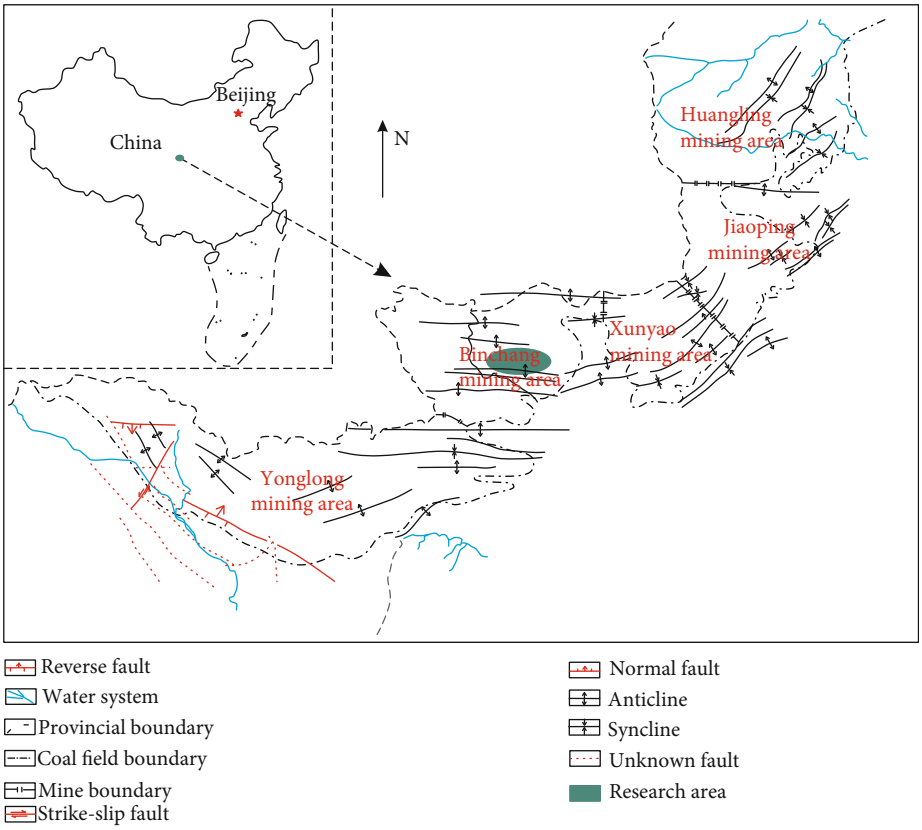

Figure 1: Tectonic outline of the Huanglong coalfield.

Table 1: Basic information of coal fine sample collection.

Serial number	Sample number	Collection location	Coal fine type
1	ZX	DFS-143 well	Drill cutting coal fines
2	LS	DFS-68 well	Bailing coal fines
3	FP	DFS-143 well	Flowback coal fines
4	LS-1	Upper section of DFS-69 well	Bailing coal fines
5	LS-2	Middle section of DFS-69 well	Bailing coal fines
6	LS-3	DFS-69 downhole section	Bailing coal fines
7	LX	Gathering pipeline filter element	/

the gathering pipeline in the Dafosi minefield of Binchang mining area, and the source coal seam is the Yan'an formation coal seam of Jurassic. The specific information is shown in Table 1. The types of coal fines include drilling cuttings in the drilling process of coalbed methane wells (ZX), coal fines discharge in the initial stage of production (FP), bailing coal fines in the process of workover (LS), and coal fines on the filter element of coalbed methane gathering and transportation pipeline (LX). After collecting the coal fine samples on the spot, the drilling cutting coal fines, the flowback coal fines, and the pipeline filter coal fines are directly dried, screened, and processed according to the test requirements, and the bailing coal fine samples are precipitated, filtered, stirred, screened, and dried. Prepare the required experimental samples according to the test requirements. The particle size of coal fines is screened with three kinds of sieves: 20 mesh, 80 mesh, and 150 mesh. According to the particle size, the coal fines are divided into four particle size ranges: <20 mesh (>830 μm), 20-80 mesh (180-830 μm), 80-150 mesh (106-180 μm), and more than 150 mesh (<106 μm).

3.2. Experimental Methods. The coal quality analysis was conducted according to the coal industry standard of the People's Republic of China (GB/T212-2008), and the average value of each sample was taken after 2 samples were tested. Particle size analysis uses sieving weighing method and laser particle size analysis method, in which the advantage of laser particle size analysis is efficient, accurate, and can obtain continuous particle size distribution, but the test particle size range is relatively limited (0.001-1000 μm), and particle size >1 mm needs to be supplemented by screening weighing method.

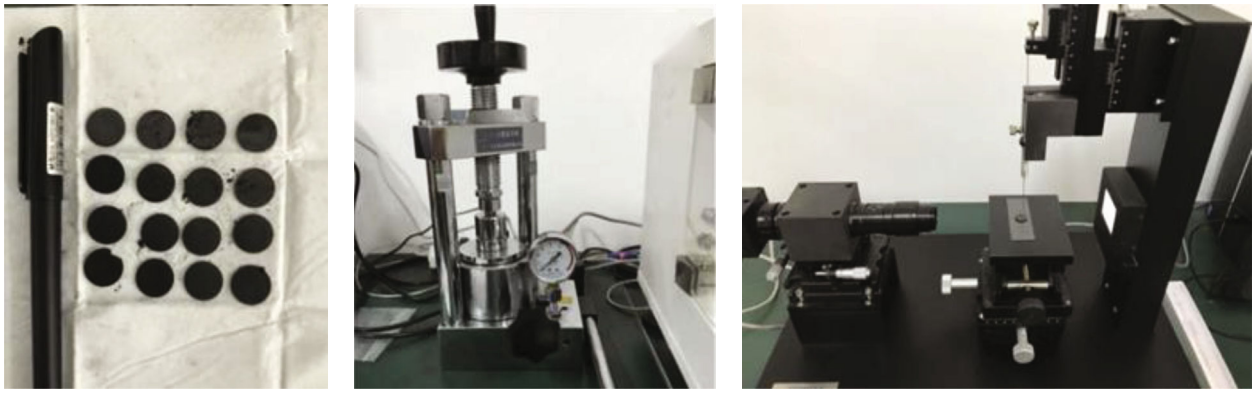

(a) (b) (c)

Figure 2: Sample preparation and measurement of contact angle ((a) pressed coal sheet sample, (b) YP-15 tablet machine, and (c) JC2000 video contact angle measuring instrument).

The contact angle characterization method is used to analyze the wettability of coal fines. Firstly, the coal fine sample is pressed into a round sheet with a diameter of about 2 cm (Figure 2(a)) with a YP-15 pressing machine (Figure 2(b)). Then, the contact angle is measured by the JC2000 video contact angle measuring instrument (Figure 2(c)). The liquid is distilled water, and each sample is tested in different parts for 3 times, and the average value is taken. Besides, to analyze the effect of different surfactants on the wettability of coal fines, three kinds of surfactant solutions with 2% volume concentration of 6501 (coconut oil fatty acid diethanolamide) solution, ethylene glycol solution, and clay curing agent solution were tested.

In the coal fine settling experiment, the final settling rate of coal fine particles is studied by tracking the movement process of coal fine particles in a "vertical wellbore" filled with water. Before the start of the experiment, the coal fine sample was fully wetted with water, and the whole process of coal fine particle settling in the field of view (rate measurement section) was recorded with a high-definition digital camera. In the later stage, the length of the scale inside the video tube was measured, combined with the time interval recorded by the stopwatch, and the average settling rate of coal fine settlement was calculated (Figure 3). In the experiment of each sample, 10 representative settling rates of coal fine particles are calculated and the average value is taken.

4. Results and Discussions

4.1. Particle Size Distribution

4.1.1. Sieve Particle Size. The screening results of drilling cutting coal fines (ZX) and bailing coal fines (LS) show (Figure 4) that the particle size distribution of coal fines is wide, and it is distributed from millimeter to micron. The weight ratios of <20 mesh, 20-80 mesh, 8-150 mesh, and >150 mesh of drilling cutting coal fines are 3.7%, 22.22%, 66.67%, and 7.41%, and the bailing coal fines are 10.67%, 12.67%, 66.67%, and 23.33%. The particle size of coal fines is more than 20 mesh microns in general, more than 89 percent. However, the content of coal fines with a particle size above a millimeter is less than 11%. There is a significant difference in particle size between drill cutting coal fines and bailing coal fines. The millimeter grade (<20 mesh) coal fines in bailing coal fines are nearly 3 times higher than that of drilling cutting coal fines. The micron particles in the drill cutting coal fines are mainly 20-80 mesh and 80-150 mesh, and the particle size is relatively coarse, especially the 80-150 mesh particles account for 66.67%, while the small size particles >150 mesh account for less than 10%. But the bailing coal fines are different, the micron particles are mainly 80-150 mesh and >150 mesh, and the particle size is relatively fine. The particle size of 20-80 mesh is only 12.67%, which is lower than that of drilling cutting coal fines. Therefore, from the point of view of mass proportion, the particle size of drilling cutting coal fines is thicker than that of sand bailing coal fines, and both of them are mainly micron particles of >20 mesh.

4.1.2. Laser Particle Size Distribution. To further analyze the characteristics of the detailed particle size distribution of coal fines below millimeter level, which is dominant in coal fines, seven coal fines samples are tested by laser particle size analyzer, and the particle size distribution curves of each sample are shown in Figures 5 and 6. The particle size distribution curve of coal fines is mainly bimodal, one primary and one secondary (Figures 5(a)–5(c)).

The dividing line between the secondary peak and the main peak of pipeline filter coal fines (LX) element is not obvious (Figure 5(d)), which may be related to the difference of particle size of organics and inorganics in coal fines. Because the bailing coal fines are screened by groundwater flow, its mineral content is higher and the bimodal characteristics are more obvious, while the main components of core pipeline filter coal fines are organic, and the secondary peaks are undeveloped. The particle sizes of all kinds of coal fines are between 1 μm and 1 000 μm, mainly between 10 μm and 500 μm, which are consistent with the screening results, and there are few coal fine particles with particle sizes less than 10 μm and more than 400 μm. The former accounts for about 10%, while the latter generally accounts for less than 10%. The D10 value of the particle size cumulative

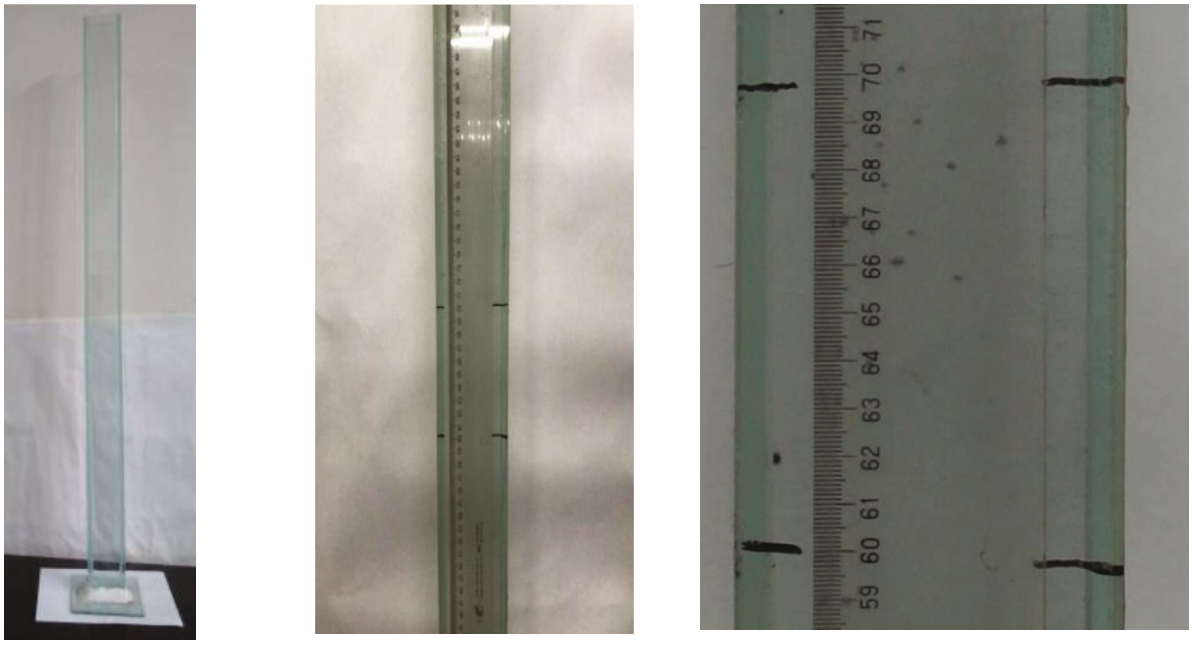

(a) Cylindrical transparent utensils (b) Calibration distance of camera plastic ruler (c) Coal fine particles pass through the field of view

Figure 3: Settling experiment of coal fines.

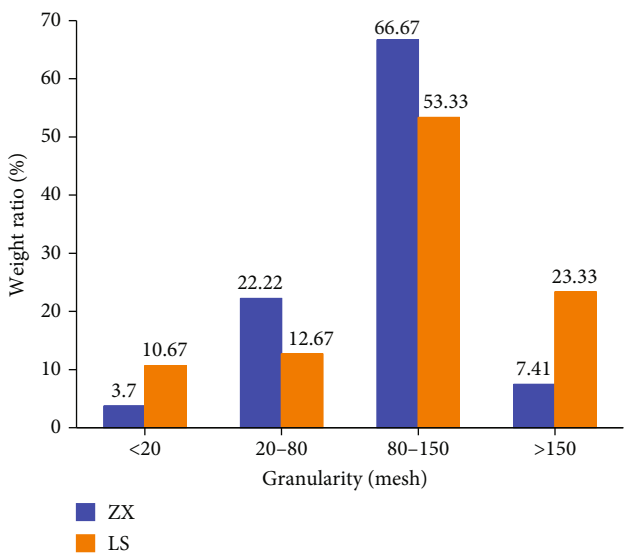

Figure 4: Particle size distribution of coal fines through sieving.

distribution curve is between 3.85 μm and 12.32 μm, while the D90 value is between 75.05 μm and 412.50 μm. Based on the comparative analysis of the particle size distribution of all kinds of coal fines, it is found that the particle size of drilling cutting coal fines is the thickest, and the D50 and D90 values of particle size distribution are 162.30 μm and 412.50 μm, respectively. The particle size of the main peak is about 300 μm. The second is the flowback coal fines at the initial stage of gas well production. The main peak particle size of the particle size distribution curve is about 100 μm, and the D50 and D90 values are 82.25 μm and 218.80 μm, respectively, which are smaller than those of drilling cutting coal fines, and the overall particle size is generally less than 200 μm. The particle size of bailing coal fines is finer, and the particle size of the main peak is about 100 μm, which is close to that of coal fines, but the values of D50 and D90 are obviously lower, which are 44.71 μm and 194.00 μm, respectively, because the second peak is more developed. The coal fine particle size of the pipeline filter is the finest; the peak particle size curve is about 30 μm, and there is only one main peak, and the secondary peak is not developed. The values of D50 and D90 are 22.72 μm and 75.06 μm, respectively, and the particle size is the smallest among the four coal fine samples. Therefore, in terms of the overall particle size of pulverized fines, from large to small is drill cutting coal fines, flowback coal fines, bailing coal fines, and pipeline filter coal fines. At the same time, it shows that there may be differences in the genesis of different types of coal fines. It is speculated that drill cutting coal fines and flowback coal fines are mainly formed by mechanical crushing in engineering, and flowback coal fines are mainly caused by the transport and production of coal fines left in the wellbore during drilling. The bailing coal fines and the pipeline filter coal fines are the coal fines formed by the primary coal fines in the coal reservoir and the particles on the pore fracture surface with the flow of gas and water and then transported to the wellbore by gas and water, and the larger coal fine particles subside, and the small particles are carried to the ground by gas and water to produce. Besides, due to differences in particle size, material composition, and wettability, the subsidence speed of each particle size of coal fines in the wellbore is different, which is confirmed by the subsidence experimental results later.

By comparing and analyzing the particle size distribution of bailing coal fines at different positions in the same

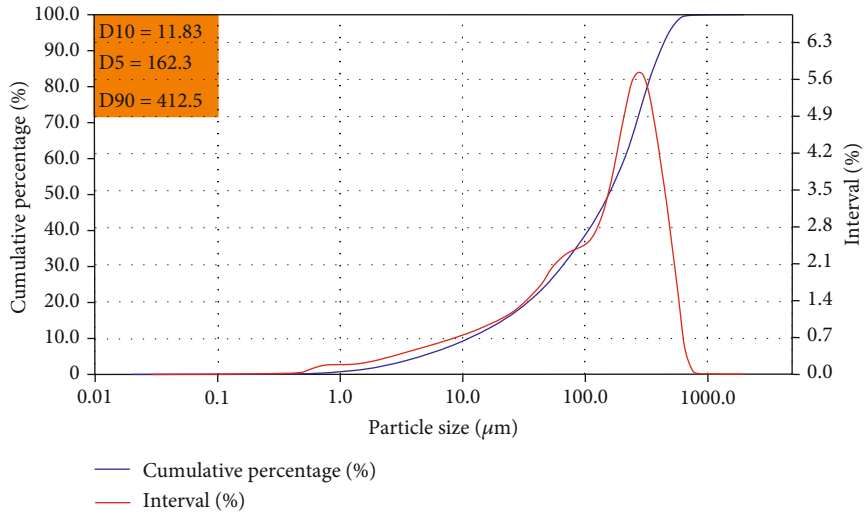

(a)

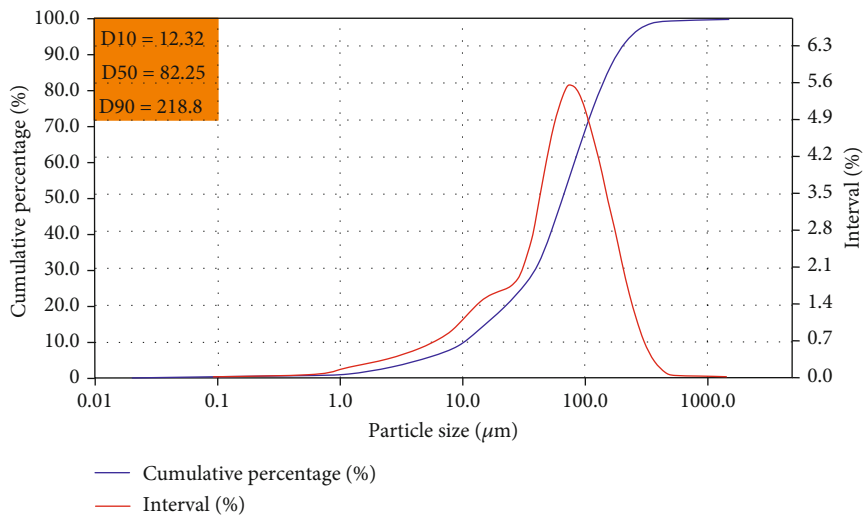

(b)

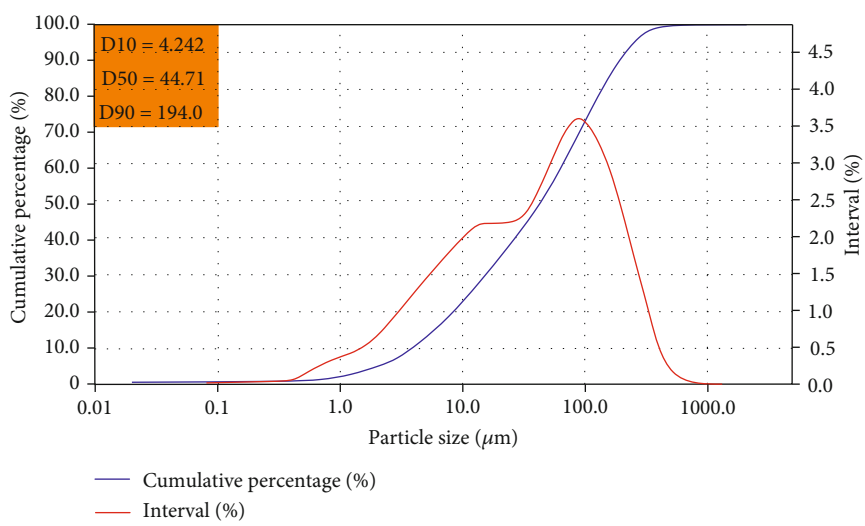

(c)

Figure 5: Continued.

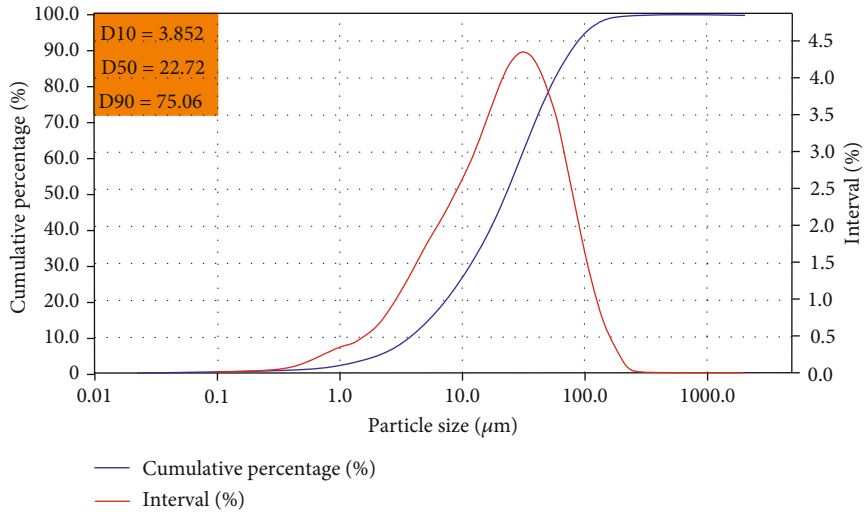

(d)

Figure 5: Particle size distribution curves of different coal fine types ((a) ZX, (b) FP, (c) LS, and (d) LX).

wellbore, it is found that the particle size distribution of bailing coal fines (LS-3) is conspicuous different (Figure 6). The particle size of bailing coal fines (D50) at the bottom is the thickest, and the D50 and D90 values of the main peak and peak diameter are 21.88 μm and 175.30 μm, respectively (Figure 6(c)). The bailing coal fines (LS-1) located in the uppermost part have the finest particle size, and the D50 and D90 values of the main peak are about 30 μm, 14.77 μm, and 63.10 μm, respectively (Figure 6(a)). On the other hand, the particle size of the bailing coal fines located in the middle is between the two, and the main peak particle size is about 90 μm, and D50 and D90 are 77.72 μm and 252.40 μm, respectively (Figure 6(b)).

Therefore, in terms of particle size, the order of bailing coal fines from coarse to fine is LS-3, LS-2, LS-1, that is, lower section > middle section > upper section. Moreover, if the secondary peak of the segmented bailing coal fine particle size curve at 1 μm is ignored, it is in good agreement with the particle size curve of LS, the secondary peak of LS is the same as the main peak of LS-1, and the particle size of LS is between the main peak of LS-2 and LS-3, which shows that the subsidence rate of coal fines in the wellbore is closely related to the particle size, and the sedimentation process plays a certain role in sorting.

4.2. Material Composition

4.2.1. Proximate Analysis. To compare the material composition characteristics of different size particles of different types of coal fines, the drilling cutting coal fines and bailing coal fines of four-particle sizes were analyzed in industry, and the results are shown in Figure 7. First of all, the average values of moisture, ash, volatile, and fixed carbon of drill cutting coal fines are 3.34%, 26.22%, 25.90%, and 42.65%, respectively, and those of bailing coal fines are 4.54%, 15.86%, 25.39%, and 57.99%, respectively. There are some differences between them, especially ash and fixed carbon. The ash content of drilling cutting coal fines is higher, while the fixed carbon content of bailing coal fines is higher. This is because the particles of coal seam gangue and surrounding rock of roof and floor are easy to mix into drilling cutting coal fines during drilling, so that the ash content is much higher than the average ash content of this coal seam. On the other hand, the bailing coal fines are mainly formed by the coal reservoir, and its composition is closer to the coal seam itself, but its ash content is still slightly higher than that of the coal seam, because the properties of organic components and inorganic minerals in coal are different, which leads to different particle migration and output capacity. Besides, the transport and separation as well as differential sedimentation of gas flow make the minerals in the bailing coal fines relatively enriched. There is little difference in moisture and volatile content between the two kinds of coal fines, which is close to the average value of coal seam. Comparatively speaking, the moisture content of drilling cutting coal fines is slightly lower than that of bailing coal fines, and the volatile content is slightly higher.

Secondly, there are great differences in the material composition of coal fine particles of different sizes. In terms of ash content, the ash content of particles with drill cutting coal fines <20 mesh and >150 mesh is particularly high, which is 28.36% and 29.09%, respectively, while the ash content of particles with 20-80 mesh and 80-150 mesh is slightly lower, which is only 24.91% and 22.51%. The ash content of bailing coal fines is relatively low, which is 11.05% and 25.47%, and is closely related to the particle size. The particle size is inversely proportional to the ash content. In terms of moisture, the moisture of 20-80 mesh particles of drill cutting coal fines is the highest, and the overall change is little, and the moisture of each particle diameter of bailing coal fines is the same, about 4.5%. In terms of volatile matter, the volatile content of the particles with drilling cutting coal fines <20 mesh is the lowest, and that of 20-80 mesh particles is the highest, while the volatile content of bailing coal fines decreases with the decrease of particle size.

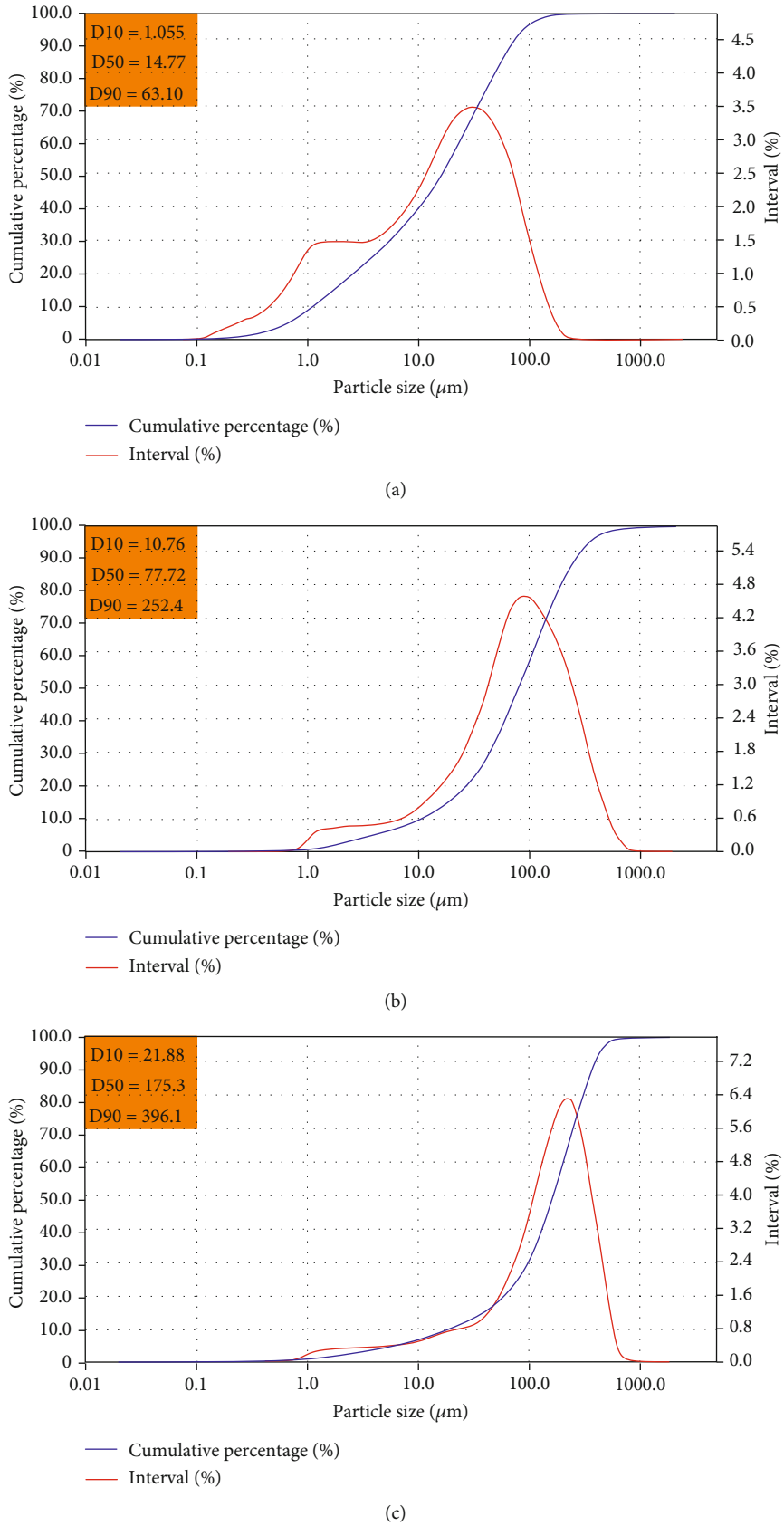

Figure 6: Particle size distribution curves of the upper, middle, and lower parts of bailing coal fines ((a) LS-1, (b) LS-2, and (c) LS-3).

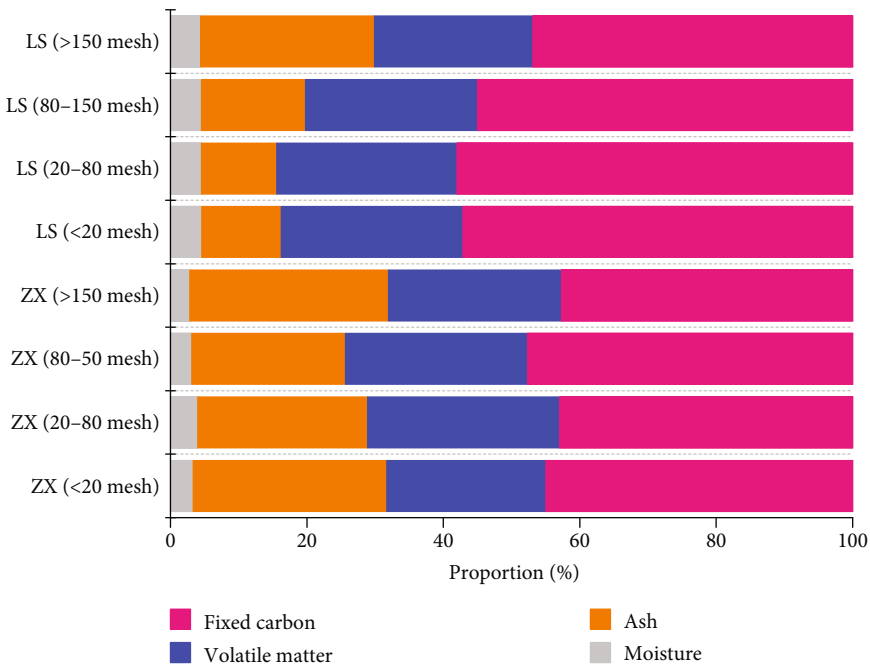

Figure 7: Proximate analysis results of drilling cuttings and bailing coal fines.

4.2.2. Mineral. X-ray diffraction mineral analysis is often used to determine the types of minerals in rocks. The X-ray diffraction pattern of coal fines can be interpreted concerning the atlas of mineral thermal analysis, power-crystal analysis, and phase transition [51], as shown in Figure 8. The results show that different types of coal fines contain different kinds of minerals, and the most kinds of minerals are drill cutting coal fines, including kaolinite, illite, anhydrite, quartz, calcite, and magnetite (Figure 8(a)). The high ash content of drill cutting coal fines can confirm each other. The second is flowback coal fines, which mainly contain kaolinite, illite, quartz, calcite, and magnetite (Figure 8(b)), which is similar to drilling cutting coal fines, while magnetite may be formed by wear and tear of metal equipment in drilling engineering. It can be seen that the flowback of coal fines in the initial stage of production of CBM wells mainly comes from the coal fines remaining in the wellbore and the pores of the reservoir, which is formed by drilling, reservoir modification, and other projects that cause the coal to be fractured, which is consistent with the previous understanding. However, the mineral characteristics of bailing coal fines are quite different from the above two, and there are few kinds of minerals, only illite and quartz (Figures 8(c)–8(e)). The reason may be that after the formation of coal fines, through the transportation, sorting, and dissolution of groundwater, the soluble minerals such as calcite and anhydrite are dissolved and transported out, resulting in fewer kinds of minerals and relative accumulation of minerals which are difficult to transport or easy to subside. Based on the further analysis of the bailing coal fines at different positions, it is found that there is only one kind of quartz in the upper part of the sample, while illite and quartz are found in the middle and lower sections, which may be related to the subsidence rate and wettability of different minerals in the water.

4.3. Topographic Characteristics

4.3.1. Micromorphology. By observing the morphology of fine coal particles under microscope, it is found that the shapes of fine coal particles are various, and the roundness, surface roughness, and edge morphology of coal fine particles are different. The roundness of coal fine particles is divided into four levels: angular, subangular, subcircular, and circular (Figure 9). It is generally believed that the roundness of coal fines is affected by genesis, and that round and subcircular coal fines are mainly caused by erosion in the process of transportation, while angular and subangular coal fines are the result of a brittle failure caused by force. Such as the drilling process, fracturing process and mechanical damage and stress changes caused in the process of drainage and production. Drilling cutting coal fines are mainly subangular, and the flowback coal fines and drilling cutting coal fines have a similar genesis and also have the characteristics of erosion in the process of transportation, so they are mainly subangular and subcircular. On the other hand, the bailing coal fines have experienced long-distance transportation, which is mainly round and subcircular. Because of the small particles, the pipeline filter coal fines suffer a slightly lower degree of erosion in the process of transportation, mainly subcircular. However, the three-dimensional shape of coal fines is mainly short columnar and granular, and flake coal fines are rarely developed, because the coal structure of Dafosi minefield is relatively complete, mainly primary structure and cataclastic structure, and structural coal is not developed. Therefore, the main causes of coal fines are mechanical damage and gas-

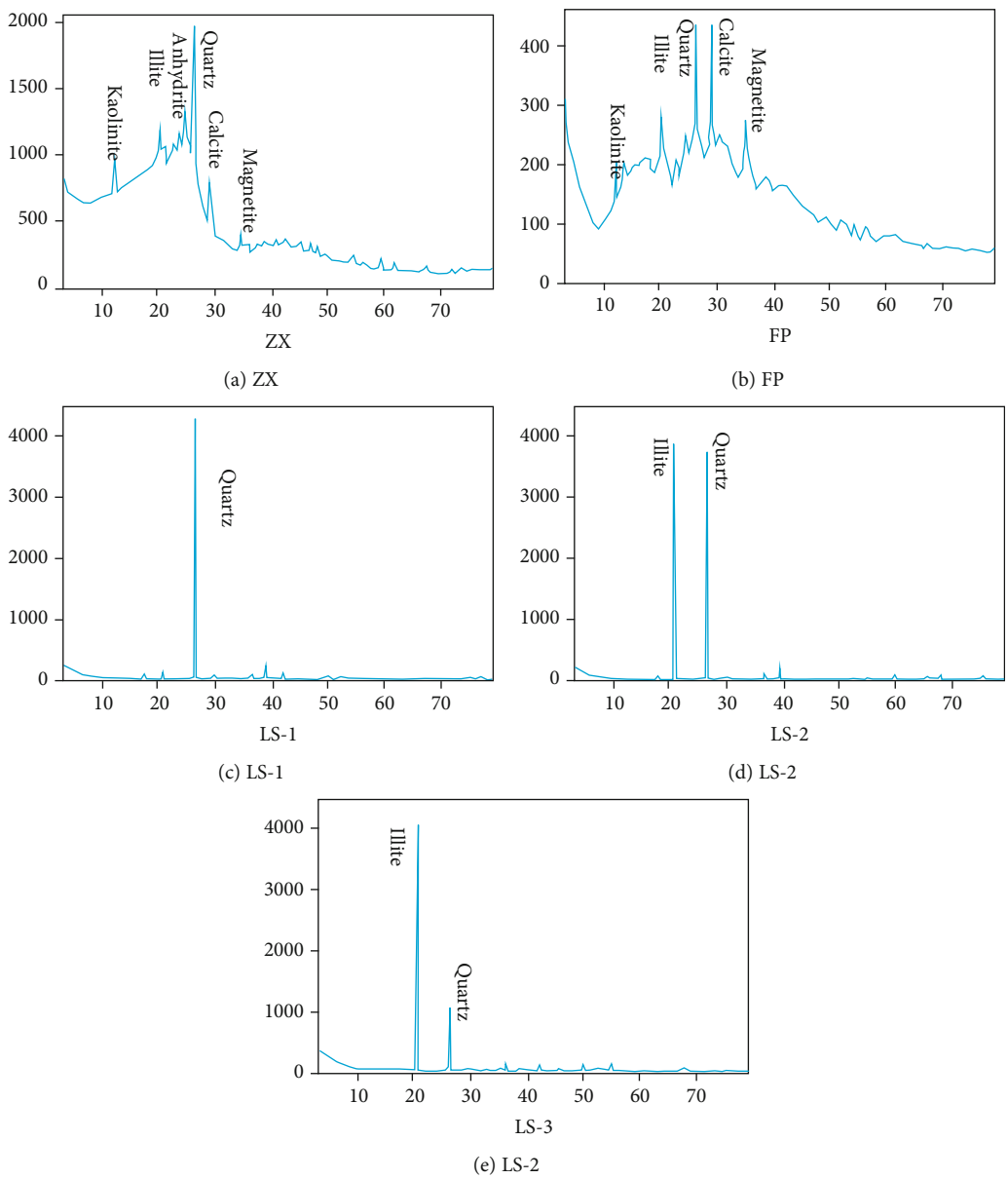

Figure 8: X-ray diffraction mineral analysis of different coal fines.

water scouring, and generally, there is no flake exfoliation genesis (mainly for scaly structural coal, mylonite coal, and other structural coal).

4.3.2. SEM Feature. At the same time, drilling cutting coal fines and bailing coal fines also have different morphological characteristics under the scanning electron microscope (SEM). First of all, at the same magnification, the drill cutting coal fine particles are larger and the bailing coal fine particles are smaller (Figure 10), which is consistent with the results of the previous particle size analysis. Secondly, the edge of drilling cutting coal fine particles is relatively straight, neat, and smooth, which accords with the genetic characteristics of rapid mechanical failure, while the edge of bailing coal fines is curved, staggered, and rough, which is mainly controlled by the original particle characteristics and certain transportation and erosion. Thirdly, the size distribution of drilling cutting coal fines is more uniform, the separability is good, and the size distribution of bailing coal fine particles is uneven, especially for coal fine particles less than 10 μm, which has a great difference in size and poor separability, because it changes with the rate of gas and water products. The particles of different sizes on the pore surface of the coal reservoir are washed off into coal fines and then mixed through transportation and settlement, resulting in uneven particle size and poor sorting.

4.4. Wettability

4.4.1. Contact Angles. The contact angles of solid-liquid interface are commonly used to characterize the wettability of solid surface. The smaller the contact angle is, the better the

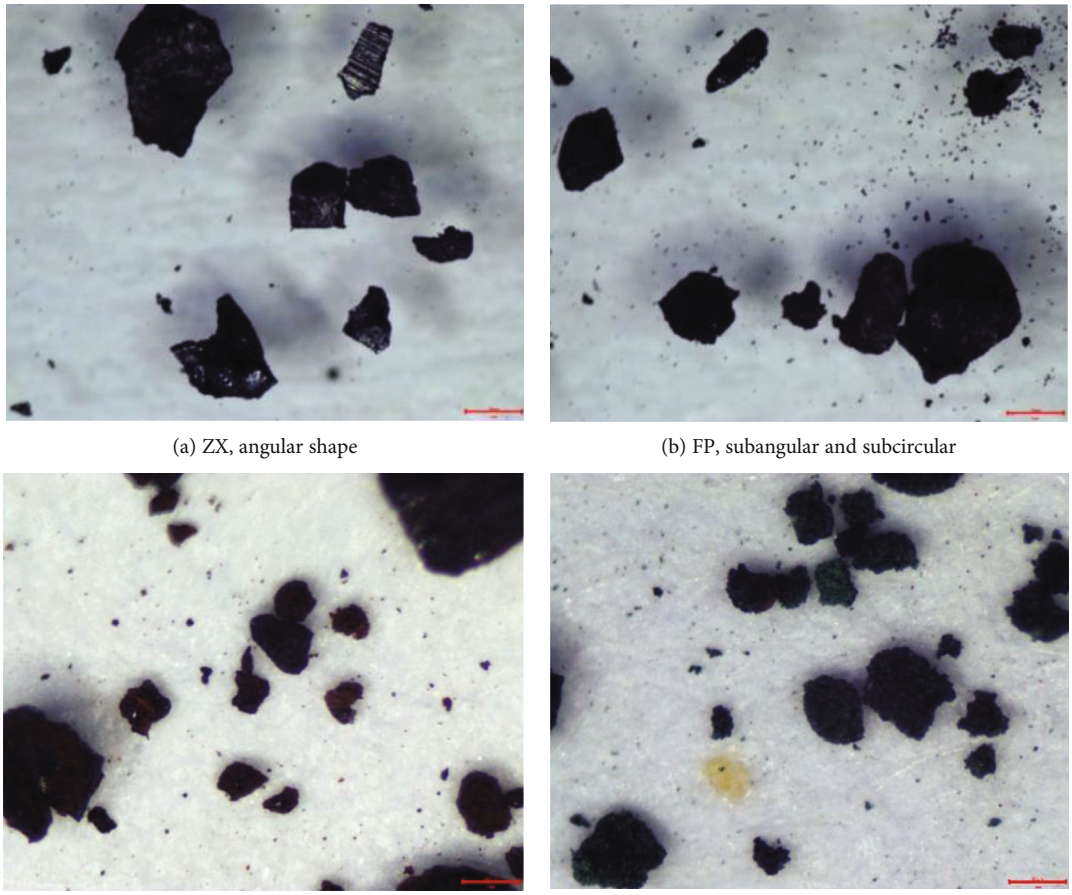

(a) ZX, angular shape

(b) FP, subangular and subcircular

(c) LS, subcircular and circular

(d) LX, subcircular

Figure 9: Photomicrograph of different types of coal fines.

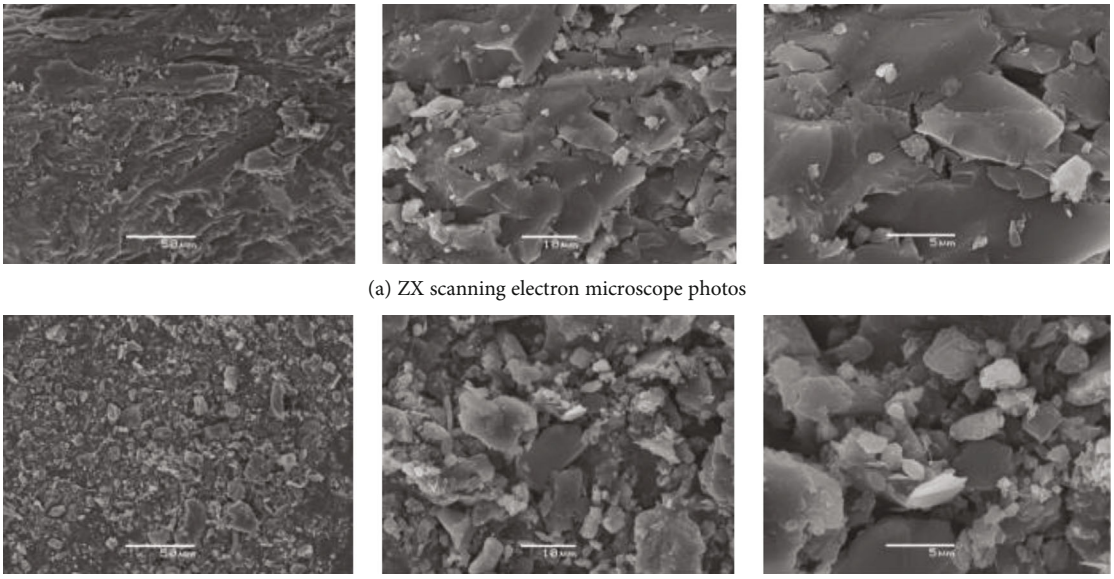

(a) ZX scanning electron microscope photos

(b) LS scanning electron microscope photos

Figure 10: SEM of different types of coal fines.

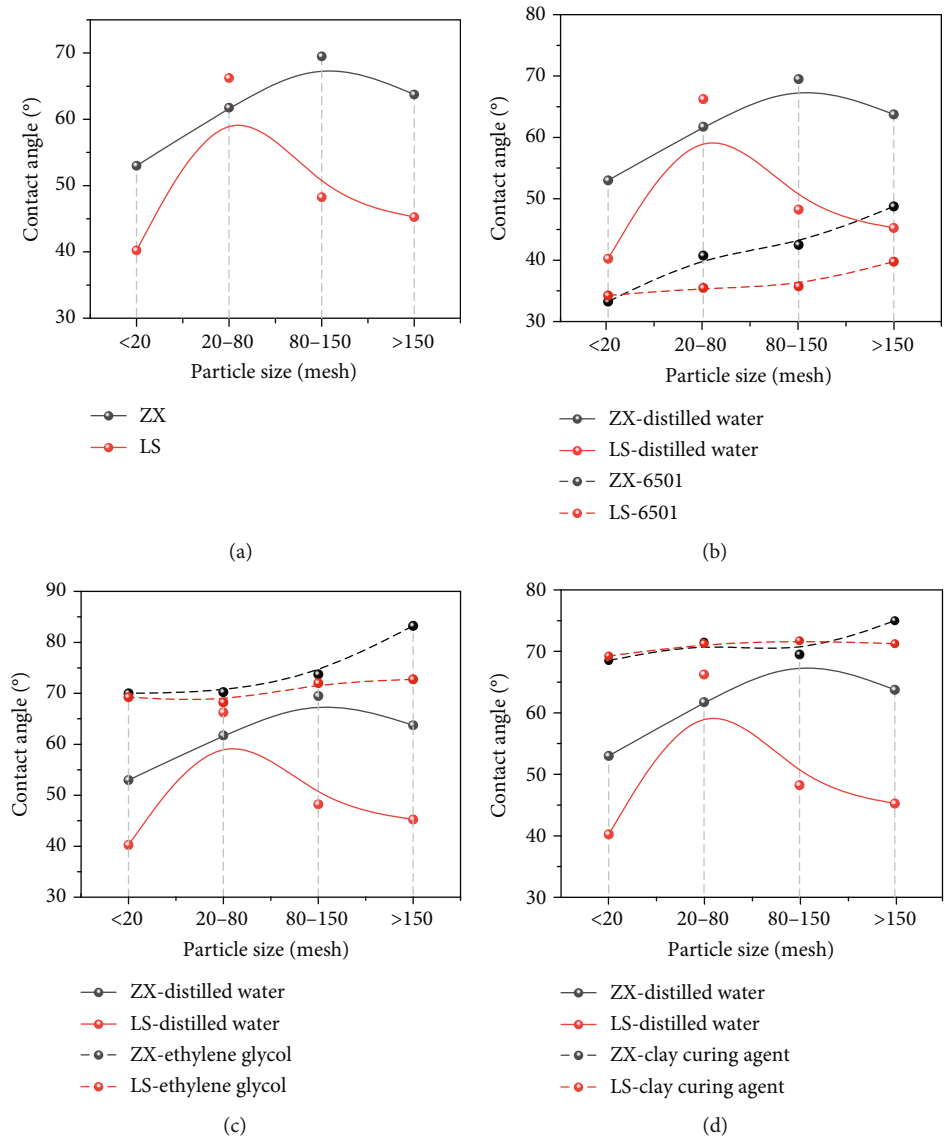

Figure 11: Contact angles of coal fines measured with different liquids ((a) distilled water, (b) 6501 solution, (c) glycol, and (d) clay curing agent).

wettability is. The contact angles of coal fines measured by distilled water are 40.25°-69.5°, all less than 90° (Figure 11(a)). The results show that the samples of each particle size of drilling cutting coal fines and bailing coal fines are hydrophilic, which is related to the fact that low-rank coal contains more polar oxygen-containing functional groups on the one hand, and more hydrophilic inorganic minerals in coal fines on the other hand. The contact angles of samples with different particle sizes of drilling cutting coal fines and bailing coal fines are 53°-69.5° and 40.25°-60.25°, respectively. The contact angle of the latter is relatively small, and the wettability is better. Besides, the wettability is closely related to the particle size of coal fines. Generally speaking, the larger the particle size of coal fine particles, the better its wettability performance. At the same time, it is also affected by the material composition. The higher the mineral content, the better the wettability. For example, the contact angle of the particles with particle size >150 mesh should be the largest, but in fact this is not the case, because the coal fines with particle size >150 mesh have high ash content and many minerals, and the enhancement effect on wettability completely counteracts the negative effect of small particle size, but the contact angle is lower. Because of low ash content, high volatile content, and fixed carbon, the contact angle of 20-80 mesh coal fine particles is abnormally high under the double negative action of material composition and particle size, while the coal fine particles of 80-150 mesh and >150 mesh have higher wettability because of high ash content.

4.4.2. Wettability Modification. As a positive wetting agent of coal, 6501 can effectively reduce the contact angle of coal-water interface, and the change of contact angle before and after the action of 6501 is 5.50°-30.75°. The wettability

modification effect of drilling cutting coal fines is better than that of bailing coal fines. The change rate of contact angle of ZX sample is 23.53% and 33.85%, and that of LS sample is 12.15% and 46.42%. Except for 20-80 mesh samples, the change rate of other ZX samples is higher than that of LS samples. The degree of modification is related to the mineral content and composition of coal fines. The worse the original wettability is, the greater the modification space is.

However, the wettability after the action of 6501 has a certain inheritance with the original wettability of the sample, that is, the original wettability is good, and the wettability after modification is also relatively good. The modification did not cause qualitative changes in the wettability of drill cutting coal fines and bailing coal fines (Figures 11(b) and 12). Secondly, the relationship between the modification strength of 6501 and the particle size of coal fines is not obvious, indicating that the particle size is not sensitive to the reaction of wetting agent. Ethylene glycol and clay curing agent are both negative wetting agents, both of which make the wettability of coal fines worse and the contact angle larger (Figures 11(c) and 11(d)). After the action of ethylene glycol, the contact angle of coal fines varies from 2° to 29°, the change rate of contact angle of ZX sample is from 6.12% to 32.08%, and that of LS sample is from 3.02% to 72.05%. The wetting modification effect of ethylene glycol on coal fines is stronger (Figure 12). Because the original wettability of bailing coal fines is better, the contact angle is smaller, the space for hydrophobic transformation is larger, and it is more sensitive to the action of ethylene glycol, while the original wettability of drilling cutting coal fines is worse, the contact angle is relatively large, and the space for further hydrophobic transformation is limited. Therefore, the degree of sensitivity to the action of ethylene glycol is low. Moreover, the relationship between the modification effect of ethylene glycol and the particle size of coal fines is not obvious; but affected by its modification limit, the wettability of the modified samples tends to be the same, and the difference between them becomes smaller. The effect of clay curing agent is similar to that of ethylene glycol, and the contact angle of coal fines is increased by 0°-29°. The change rate of ZX sample and LS sample is 0%-29.25% and 7.55%-72.05%, respectively. The wettability of bailing coal fines is stronger than that of drilling cutting coal fines, and it is also affected by the hydrophobic transformation space of the sample (Figure 12). At the same time, the effect of particle size on the modification of clay curing agent is not obvious, and the wettability of the modified coal fine samples is similar to that of ethylene glycol. Compared with ethylene glycol, the modification effect of clay curing agent is slightly worse.

To sum up, the modification effect of surfactant on coal fines is mainly affected by the wettability and material composition of coal fines, the original wettability is poor, the modification effect of positive wetting agent is strong, the modification effect is good, and the wettability before and after modification has a certain inheritance, and the type and content of minerals may promote the modification of positive wetting agent to a certain extent. The better the original wettability is, the more significant the modification effect of negative wetting agent is, the modification effect is limited

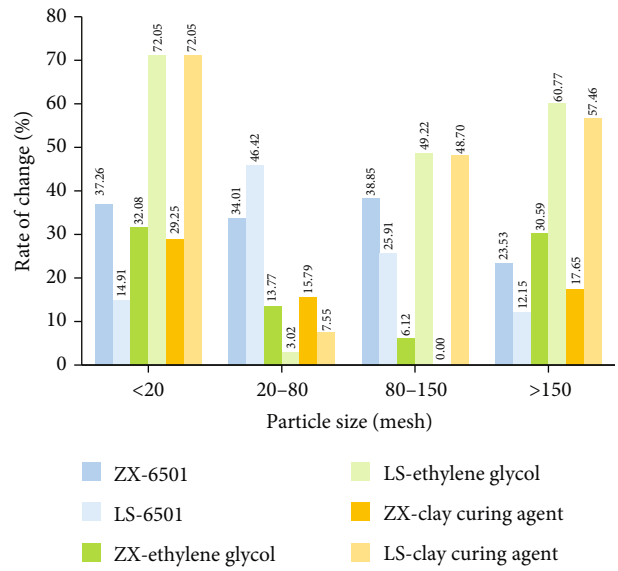

Figure 12: Modification effects of different active agents on coal fines.

by the reformable space, and the modification effect is limited, and the wettability of each coal fine sample tends to be the same after modification. Because the active agent acts mainly by adsorbing on the solid surface to form a hydrophilic layer or hydrophobic layer, the effect of coal fine particle size on the effect of surfactant is not obvious.

4.5. Settleability

4.5.1. Settling Rate. The settling rate of each sample is calculated through the static settling simulation experiment of coal fines. The results show that the settling rate of coal fines is between 6.97 and 47.60 cm/s. The largest settling rate is <20 mesh coal fines, and the smallest is 80-150 mesh bailing coal fines (Figure 13(a)). Affected by the particle size, the settling rate of drilling cutting coal fines and bailing coal fines is an interval. When the size is less than 80 mesh, the settling rate of bailing coal fines is higher, and the sedimentation in water is faster. When it is more than 80 mesh, on the contrary, the settlement of drilling cutting coal fines is faster. Generally speaking, the settling rate of coal fines is closely related to particle size. The larger the particle size is, the greater the settling rate is, which is consistent with the traditional understanding of the settlement of solid particles in water. However, it is worth noting that when the particle size reaches more than 150 mesh, the settling rate does not continue to decrease, but increases against the trend, indicating that the main factors controlling the settling rate of extremely small coal fine particles have changed.

4.5.2. Influencing Factors. Due to the complexity of the material components of coal fines, including a variety of organic matter and inorganic minerals, there are differences in the density, wettability, and morphology of various components, which comprehensively affect the settleability of coal fine particles. The ash content of the samples with the particle size range of more than 150 mesh of drilling cutting coal fines and

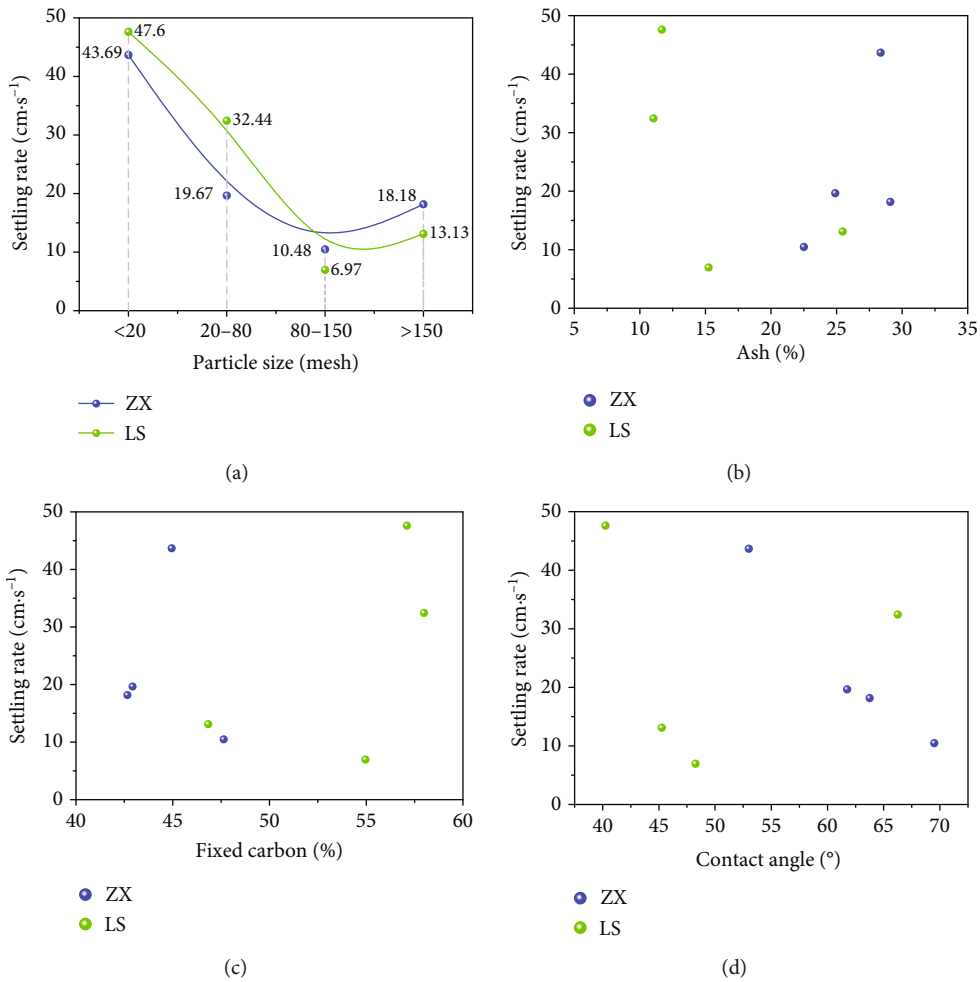

Figure 13: Settling rates of different coal fines and analysis of its influence factors ((a) different settling rates of coal fines, (b) relationship between settling rate of coal fines and ash content, (c) relationship between settling rate of coal fines and fixed carbon content, and (d) relationship between settling rate of coal fines and contact angle).

bailing coal fines is higher than that of other particle sizes, so it is inferred that the ash content is the main factor to control the settling rate of coal fines in this section. Compared with organic matter, the density of ash in coal is higher and the higher the ash content is, the greater the overall density of coal fine particles is and the faster the settling rate is. The analysis of the relationship between coal fine ash and settling rate shows that there is a better positive correlation between them (Figure 13(b)). Especially for drilling cutting coal fines and small particle size bailing coal fines, the relationship between ash content and settling rate is more obvious. On the contrary, the higher the fixed carbon content is, the more organic matter is contained in the coal fines, the overall specific gravity becomes smaller, and the settlement is slower, so there is a negative correlation between the settling rate of coal fines and the fixed carbon content (Figure 13(c)). Besides, the wettability of coal fines will also affect its settling rate. It is generally believed that the wettability of coal fines is good, which is conducive to the dispersion and suspension of coal fine particles in water and is not easy to settle [46]. However, the experimental results show that there is a negative correlation between the contact angle of coal fines and the settling rate (Figure 13(d)). That is to say, good wettability is conducive to the sedimentation of coal fines, which is inconsistent with previous research understanding, and it may be caused by the difference in particle size.

5. Conclusions

(1) The particle size of coal fines produced by coalbed methane wells in Binchang mining area is mainly micron, the particle size of drilling cuttings is mainly distributed in 20-150 mesh, and the bailing coal fines is mainly >80 mesh. The main type of laser particle size distribution curve of all kinds of coal fines is main-secondary bimodal type, the main peak particle size is between 30 μm and 300 μm, and the main particle size is 1-400 μm. The particle size is as follows: drill cutting coal fines > flowback coal fines > bailing coal fines > pipeline filter coal fines; bailing coal lower section > middle section > upper section

(2) The ash content of coal fines is higher than that of raw coal, drilling cutting coal fines is higher than

bailing coal fines, and the fixed carbon of the former is lower than that of the latter, and the coarser the particle size of coal fines is, the lower the ash content is. Coal fines mainly contain kaolinite, illite, quartz, and other six kinds of minerals, drilling cutting coal fines are the most abundant, and bailing coal fines only contain illite and quartz

(3) The roundness of coal fine particles from good to bad is bailing coal fines, pipeline filter coal fines, flowback coal fines, and drilling cutting coal fines, drilling cutting coal fines are well sorted, the edge of particles is straight, neat, and smooth, and the sorting of bailing coal fines is poor. The edge of the particles is curved, staggered, and rough, and the morphological characteristics are closely related to the origin of coal fines

(4) The contact angle of coal fines is from 40.25° to 69.5°, which is hydrophilic. The wettability of bailing coal fines is better than that of drilling cutting coal fines. The larger the particle size of coal fines is, the worse the wettability is. The worse the wettability is, the more obvious the modification effect of positive wetting agent is, the better the wettability is, and the better the modification effect of negative wetting agent is. The modification of surfactant has nothing to do with the particle size of coal fines but is closely related to organic components and minerals

(5) The static settling rate of coal fines is 6.97-47.60 cm/s. The larger the particle size of coal fines is, the greater the settling rate is. The higher the ash content of coal fines is, the lower the fixed carbon content is, and the faster the settling rate is. Taking 150 mesh as the demarcation point, the settling rate of large particle coal fines is mainly affected by particle size, and the settling rate of small particle coal fines is mainly affected by material composition

Data Availability

All data, models, and code generated or used during the study appear in the article.

Conflicts of Interest

The authors declared no potential conflicts of interest with respect to the research, authorship, and publication of this article.

Acknowledgments

This work is supported by the National Natural Science Foundation of China (Grant No. 41902175 and Grant No. 41972183), the Shanxi Province Science and Technology Major Special Funding Project (Grant No. 20201101002), the Shaanxi Province Natural Science Basic Research Program Funding Project (Grant No. 2019JQ-245), the Shaanxi Provincial Department of Education 2018 Special Scientific Research Project (18JK0518), the Open Project Funding Project of the Key Laboratory of Coal Resources Exploration and Comprehensive Utilization of the Ministry of Natural Resources (Grant No. KF2019-2), and the Projects Funded by China Postdoctoral Science Foundation (Grant No. 2019M653873XB). The authors also thank Editor and anonymous reviewers very much for valuable comments and suggestions that have greatly improved the manuscript.

References

[1] I. D. Palmer, Z. A. Moschovidis, and J. R. Cameron, "Coal failure and consequences for coalbed methane wells," in *SPE Annual Technical Conference and Exhibition*, Dallas, Texas, October 2005.

[2] Y. Wei, D. Cao, Y. Yuan et al., "Characteristics of pulverized coal during coalbed methane drainage in Hancheng block, Shaanxi Province, China," *Energy Exploration & Exploitation*, vol. 31, no. 5, pp. 745–757, 2013.

[3] T. Bai, Z. Chen, S. M. Aminossadati, T. E. Rufford, and L. Li, "Experimental investigation on the impact of coal fines generation and migration on coal permeability," *Journal of Petroleum Science and Engineering*, vol. 159, pp. 257–266, 2017.

[4] Z. Guo, P. N. H. Vu, and F. Hussain, "A laboratory study of the effect of creep and fines migration on coal permeability during single-phase flow," *International Journal of Coal Geology*, vol. 200, pp. 61–76, 2018.

[5] S. Tao, D. Tang, H. Xu, and S. Li, "The influence of flow velocity on coal fines output and coal permeability in the Fukang Block, southern Junggar Basin, China," *Scientific Reports*, vol. 7, no. 1, article 14124, 2017.

[6] Z. Jian-xun and W. Youzhi, "Influence of tectonic action on coal petrography pore structure and CBM diffusion mode," *Unconventional Oil & Gas*, vol. 2, no. 4, pp. 40–47+12, 2017.

[7] H. Zhang, Y. X. Mo, M. Sun, and X. Y. Wei, "Determination of the mineral distribution in pulverized coal using densitometry and laser particle sizing," *Energy & Fuels*, vol. 19, no. 6, pp. 2261–2267, 2005.

[8] Y. Jintao, S. Jianbo, L. Gang, and X. Jie, "Literature review of permeability dynamic change law in CBM reservoir," *Unconventional Oil & Gas*, vol. 2, no. 4, pp. 114–118, 2017.

[9] D. Cao, A. Wang, S. Ning et al., "Coalfield structure and structural controls on coal in China," *International Journal of Coal Science & Technology*, vol. 7, no. 2, pp. 220–239, 2020.

[10] Z. Meng, J. Zhang, and R. Wang, "In-situ stress, pore pressure and stress-dependent permeability in the Southern Qinshui Basin," *International Journal of Rock Mechanics and Mining Sciences*, vol. 48, no. 1, pp. 122–131, 2011.

[11] I. Shovkun and D. N. Espinoza, "Coupled fluid flow-geomechanics simulation in stress-sensitive coal and shale reservoirs: impact of desorption-induced stresses, shear failure, and fines migration," *Fuel*, vol. 195, pp. 260–272, 2017.

[12] P. Bedrikovetsky, F. D. Siqueira, C. A. Furtado, and A. L. S. Souza, "Modified particle detachment model for colloidal transport in porous media," *Transport in Porous Media*, vol. 86, no. 2, pp. 353–383, 2011.

[13] S. Jinxing, Y. Shiyao, and S. Xianbo, "Study on velocity sensitivity damage mechanism and its proof test of coal reservoir," *Coal Science and Technology*, vol. 46, no. 6, pp. 173–177, 2018.

[14] W. Yingchun, L. Chao, C. Daiyong, Z. Aoxiang, Y. Zheng, and X. Xianyue, "The output mechanism and control measures of

the pulverized coal in coalbed methane development," *Coal Geology & Exploration*, vol. 46, no. 2, pp. 68–73, 2018.

[15] Y. S. Zou, S. C. Zhang, and J. Zhang, "Experimental method to simulate coal fines migration and coal fines aggregation prevention in the hydraulic fracture," *Transport in Porous Media*, vol. 101, no. 1, pp. 17–34, 2014.

[16] X. Liu, C. Liu, and G. Liu, "Dynamic behavior of coalbed methane flow along the annulus of single-phase production," *International Journal of Coal Science & Technology*, vol. 6, no. 4, pp. 547–555, 2019.

[17] C. Daiyong, Y. Yuan, W. Yingchun, L. Shenggui, L. Xiaoming, and W. Qingwei, "Comprehensive classification study of coal fines genetic mechanism and origin site," *Coal Geology of China*, vol. 24, no. 1, pp. 10–12, 2012.

[18] W. Haoqiang, P. Xiaolong, Z. Suyang, and F. Ning, "Research progress of coal fine formation, migration and control in CBM well," *Reservoir Evaluation and Development*, vol. 10, no. 4, pp. 70–80, 2020.

[19] Z. Junfang, W. Shengwei, Q. Yi et al., "Characteristics and origin of coal powder in coalbed methane well," *Natural Gas Geoscience*, vol. 24, no. 6, pp. 1316–1320, 2013.

[20] L. Shenggui, H. Aimei, S. Bo, and L. Huifang, "Coal powder concentration warning and control measure during CBM well drainage," *Journal of China Coal Society*, vol. 37, no. 1, pp. 86–90, 2012.

[21] Q. Yaoguang, Z. Fenna, L. Bing et al., "Calculation on discharge flow of pulverized coal in gas production channel for coalbed methane well," *Journal of China Coal Society*, vol. 38, no. 9, pp. 1627–1633, 2013.

[22] H. Fansheng, K. Yili, L. Xiangchen, Y. Lijun, and X. Chengyuan, "Incipient motion mechanisms and control measures of coal fines during single-phase water flow in coalbed fractures," *Acta Petrolei Sinica*, vol. 38, no. 8, pp. 947–954, 2017.

[23] W. Hanxiang and L. Wenjian, "Discussion on formation mechanism of coal powder in coalbed methane well," *China Coal*, vol. 38, no. 2, pp. 95–97+105, 2012.

[24] X. Zhao, S. Liu, S. Sang et al., "Characteristics and generation mechanisms of coal fines in coalbed methane wells in the southern Qinshui Basin, China," *Journal of Natural Gas Science & Engineering*, vol. 34, pp. 849–863, 2016.

[25] C. Zhenhong, W. Yibing, and S. Ping, "Destructive influences and effectively treatments of coal powder to high rank coalbed methane production," *Journal of China Coal Society*, vol. 34, no. 2, pp. 229–232, 2009.

[26] C. Daiyong, Y. Zheng, L. Xiaoming, W. Yingchun, H. Aimei, and S. Bo, "Rules of coal powder output under physical simulation experiments of single-phase water flow displacement," *Journal of China Coal Society*, vol. 38, no. 4, pp. 624–628, 2013.

[27] C. Jinbang, L. Pei, M. Dongmin, L. Zhi, Z. Ke, and M. Fanyuan, "Experiment study on migration law of pulverized coal in borehole of coalbed methane horizontal well," *Coal Science and Technology*, vol. 44, no. 5, pp. 74–78+176, 2016.

[28] L. Shenggui, H. Xiaohei, and L. Fanghui, "Production mechanism and control measures of coal powder in coalbed methane horizontal well," *Journal of Liaoning University of Technology (Natural Science edition)*, vol. 30, no. 4, pp. 508–512, 2011.

[29] M. Tian, M. Dongmin, C. Yue et al., "Start-migration law of coal powder with different particle sizes under multi-phase flow conditions in coalbed methane wells," *Coal Science and Technology*, vol. 48, no. 5, pp. 188–196, 2020.

[30] C. Wenwen, W. Shengwei, Q. Yi et al., "Migration and control of coal powder in CBM well," *Journal of China Coal Society*, vol. 39, no. S2, pp. 416–421, 2014.

[31] Y. Yanhui, T. Dazhen, Y. Yanlei, C. Longwei, and T. Shu, "Influence on velocity sensitivity effect of coal reservoir to production law of pulverized coal and gas productivity," *Coal Science and Technology*, vol. 43, no. 2, pp. 96–99+103, 2015.

[32] W. Yingchun, C. Maolin, Z. Jin, M. Tao, and Y. Zheng, "Aggregation and sedimentation experiments of coal fines with different particle sizes during CBM development," *Coal Geology & Exploration*, vol. 48, no. 5, pp. 40–47, 2020.

[33] C. Lihu, Z. Suian, S. Huining, B. Jianmei, W. Huan, and Z. Wei, "Coal dust migration and treatment for coalbed methane horizontal wells in Qinshui Basin," *Oil Drilling and Production Technology*, vol. 34, no. 4, pp. 93–95, 2012.

[34] Y. Wei, C. Li, D. Cao, A. Zhang, A. Wang, and X. Xiang, "New progress on the coal fines affecting the development of coalbed methane," *Acta Geologica Sinica-English Edition*, vol. 92, no. 5, pp. 2060–2062, 2018.

[35] X. Yaobo, "Research on the production rule and prevention method of pulverized coal in horizontal CBM well," *Coal Geology & Exploration*, vol. 44, no. 1, pp. 43–46, 2016.

[36] W. Yingchun, L. Chao, C. Daiyong, H. Le, and Z. Aoxiang, "Experiment on screening dispersants of pulverized coal with different sizes in CBM well-washing technology," *Journal of China Coal Society*, vol. 42, no. 11, pp. 2908–2913, 2017.

[37] Y. Zheng, C. Daiyong, W. Yingchun, Z. Xiaoyu, Z. Aoxiang, and L. Xiang, "Comprehensive analysis of prevention and control measures for coal fines in coalbed methane production," *Coal Science and Technology*, vol. 43, no. 8, pp. 124–128 +162, 2015.

[38] A. Zhang, D. Cao, Y. Wei, and T. E. Rufford, "Characterization of fines produced during drainage of coalbed methane reservoirs in the Linfen block, Ordos Basin," *Energy Exploration & Exploitation*, vol. 38, no. 5, pp. 1664–1679, 2020.

[39] Z. Guo, F. Hussain, and Y. Cinar, "Permeability variation associated with fines production from anthracite coal during water injection," *International Journal of Coal Geology*, vol. 147-148, pp. 46–57, 2015.

[40] Y. Wei, C. Li, D. Cao, A. Wang, A. Zhang, and Z. Yao, "The effects of particle size and inorganic mineral content on fines migration in fracturing proppant during coalbed methane production," *Journal of Petroleum Science and Engineering*, vol. 182, p. 106355, 2019.

[41] Y. Liu, J. Liu, Q. Lyu, J. Zhu, and F. Pan, "Microstructure analysis of fluidized preheating pulverized coal under O_2/CO_2 atmospheres," *Fuel*, vol. 292, p. 120386, 2021.

[42] Y. Kuang, B. He, W. Tong, and C. Wang, "Flow and reaction characteristics at different oxygen concentrations and inlet velocities in pulverized coal MILD combustion," *Journal of the Energy Institute*, vol. 94, pp. 63–72, 2021.

[43] C. Niu, W. Xia, and Y. Peng, "Analysis of coal wettability by inverse gas chromatography and its guidance for coal flotation," *Fuel*, vol. 228, pp. 290–296, 2018.

[44] M. Pawlik, J. S. Laskowski, and F. Melo, "Effect of coal surface wettability on aggregation of fine coal particles," *Coal Preparation*, vol. 24, no. 5-6, pp. 233–248, 2004.

[45] J. Yan, L. Chen, and Z. Li, "Removal of fine particles from coal combustion in the combined effect of acoustic agglomeration and seed droplets with wetting agent," *Fuel*, vol. 165, pp. 316–323, 2016.

[46] D. Junjun, L. Liantao, C. Jinbang et al., "Static settlement of different types of pulverized coal in CBM wells," *Journal of China Coal Society*, vol. 43, no. S1, pp. 203–209, 2018.

[47] L. Yabing, Q. Yong, W. Xing, D. Zhonghui, and M. Dongmin, "Geology and emission of mine gas in Binchang mining area with low rank coal and high mine gas," *Journal of China Coal Society*, vol. 44, no. 7, pp. 2151–2158, 2019.

[48] M. Dongmin, W. Chuantao, Y. Fu et al., "Mass transfer process of desorption of CBM in Dafosi coal reservoir," *Journal of China Coal Society*, vol. 43, no. S1, pp. 225–234, 2018.

[49] C. Yue, M. Dongmin, X. Yucheng, G. Chen, Y. Fu, and S. Kai, "Study on wettability and influencing factors of different macroscopic components in low rank coal," *Coal Science and Technology*, vol. 47, no. 9, pp. 97–104, 2019.

[50] M. Dongmin, W. Chuantao, X. Yucheng, Z. Jiarui, S. Kai, and Y. Fu, "Optimization program of fracturing parameters for coalbed methane wells in Dafosi Minefield," *Journal of Xi'an University of Science and Technology*, vol. 39, no. 2, pp. 85–91, 2019.

[51] G. Chen and Y. ZHang, *Atlas of Minerals Thermal Analysis, Power-Crystal Analysis and Phase Transition*, Sichuan Science Technology Press, Chengdu, 1989.

Hindawi
Geofluids
Volume 2021, Article ID 5538302, 15 pages
https://doi.org/10.1155/2021/5538302

Research Article

Fluidity Influencing Factors Analysis and Ratio Optimization of New Sealing Materials Based on Response Surface Method

Xin Guo,[1] **Sheng Xue**,[1] **Yaobin Li**,[1] **Chunshan Zheng**,[1] **and Gege Yang**[2]

[1]*School of Safety Science and Engineering, Anhui University of Science & Technology, Huainan 232001, China*
[2]*School of Management Studies, Shanghai University of Engineering Science, Shanghai 201620, China*

Correspondence should be addressed to Xin Guo; guoxin190510@163.com

Received 15 January 2021; Revised 6 February 2021; Accepted 22 February 2021; Published 3 March 2021

Academic Editor: Yanjun Meng

The borehole sealing material is one of the key factors affecting the gas drainage effect of a borehole. This paper takes the compressive strength, fluidity, expansion rate, and setting time of the sealing material as the main research indicators and explores the influence of each key influencing factor on the performance of the high-fluid sealing material through the single factor experiment method. Using the Design-Expert 8.0.5 Trial software designed orthogonal experiments and establishing a quadratic model between liquidity and each test factor, which showed the impact of each key factor on the fluidity. Finally, by adjusting the amount of admixtures, the optimal ratio of high-fluidity borehole sealing materials was obtained. The results showed that the key factors had the following order of significance: water – cement reducing agent > water – cement ratio > retarder > expansion agent. With the water-cement ratio and the amount of water reducing agent increase, the fluidity of the material will increase; and with the increase of the retarder and expansion agent, the fluidity will decrease. In actual use, the fluidity is the main factor, but the expansion rate, compressive strength, and setting time are also considered. The optimal percentages were found for the high-fluidity borehole sealing material: a water-cement ratio of 1, along with 0.03% retarder, 0.5% water reducer, and 8% expansion agent. These research results could provide a reference for improving the performance of gas drainage borehole sealing materials and enhancing the effect of gas drainage.

1. Introduction

China has a high frequency of gas disaster accidents. With the increasing mining depth of coal resources, China is faced with increasingly serious gas problems, which pose a serious threat to the safety and efficiency of coal mining [1–3]. In order to prevent gas accidents during coal mining, gas pre-drainage technology is usually used to extract the gas from coal seams. However, the effect of gas drainage in China is generally poor. In addition to the low air permeability of the coal seam, the performance of the borehole sealing material also affects the drilling and sealing effect to a large extent. The borehole sealing materials commonly used in China's coal mines include cement mortar and polyurethane materials. However, these materials have poor penetration in microfissures smaller than 0.1 mm, and the cracks are closed under high stress [4], resulting in poor sealing effects. This requires a borehole sealing material with good fluidity to allow it to be effectively injected into the fine cracks in the coal and rock mass [5, 6]. Ultrafine cement prepared by refining ordinary cement particles can meet the injection requirements for fine cracks. Compared with traditional borehole sealing materials, ultrafine cement materials have higher strength, better durability, and nontoxicity [7–9]. However, to ensure that the borehole sealing material can be efficiently injected into the fine cracks of the coal and rock mass, in addition to having high fluidity, it should also have relatively high stability, a certain degree of microswelling, and a suitable setting time [10].

Scholars in China and abroad have conducted numerous studies on ultrafine cement. Li et al. [11] developed an improved construction solid waste cement grouting material. The results show that when the mixing amount of modified construction solid waste cement grouting material waste red brick powder is 40-60%, the fluidity performance of grouting sealing material is the best. Zheng et al. [12] studied

Table 1: Chemical composition of raw materials/%.

Chemical composition	w (SiO_2)	w (Al_2O_3)	w (Fe_2O_3)	w (CaO)	w (MgO)	w (SO_3)	Loss	Total
HCSA expanding agent	4.96	8.52	0.99	64.18	2.67	16.97	1.19	99.48
Superfine Portland cement	20.57	9.89	3.08	57.65	2	2.7	2.6	98.49

Table 2: Single-factor experimental design scheme.

Test group	Water–cement ratio			Retarder			Water–reducing agent			Expanding agent		
Level/%	0.8	1.0	1.2	0.05	0.5	1.5	0.2	0.5	0.8	5	10	15

Table 3: Value range of each factor in orthogonal experiment.

Test group	Value range of each factor/%			
	Water–cement ratio	Retarder	Water–reducing agent	Expanding agent
ZJ1-29	0.8–1.0	0.03–0.05	0.3–0.5	8–10

Figure 1: Borehole sealing material after mixing.

Figure 2: Preparation of sample.

the effect of fly ash on the rheological properties of cement slurry. When the content of fly ash was 50%, the viscosity of cement slurry decreased by 54%, and the fluidity was improved. When the fly ash content reaches 70%, the cement slurry shows the characteristics of the Bingham fluid model. Liu et al. [13] studied the effect of nanoscale viscosity regulator on the rheological properties of cement slurry. With the incorporation of nanoscale viscosity regulator, the fluidity of cement slurry decreased significantly. Chen et al. [14] studied the fluidity of ordinary cement materials with different amounts of ultrafine cement. Wongkornchaowalit and Lertchirakarn [15] studied the influence of polycarboxylic acid superplasticizer content on the fluidity of Portland cement. The results show that when the dosage of polycarboxylate superplasticizer is 1.8%–2.4%, the fluidity of experimental cement increases greatly. Kazuki et al. [16] studied the effect of the molecular structure of superplasticizer on the fluidity of cement slurry sealing material. The results show that the smaller molecular structure is helpful to the dispersion of cement particles and improves the fluidity of slurry sealing material. Güllü et al. [17] studied the influence of geopolymer grouting material on the rheological properties of cement slurry. The rheological property of cement slurry decreases with the increase of the water/binder ratio. When the ratio of fly ash and geopolymer aggregate is 30%–40%, the rheological property of cement slurry is close to that of natural cement.

At present, the research on the modification of sealing materials is based on ordinary cement materials, which cannot be effectively filled into the fine cracks. The research on ultrafine cement materials is relatively concentrated in the repair of water conservancy, dams, foundations, and concrete engineering. Few studies have been conducted on the injected body with the characteristics of soft and broken rock, high ground pressure, and difficulty in injecting grout. Moreover, the research did not conduct comprehensive research on the composition, structure, and performance of the material, did not find a modification method that takes into account both high fluidity and super early strength, and did not develop a series of high fluidity and super early strength performance of grouting material. This research uses ultrafine silicate ultramud as the basic material and adds calcium oxide-calcium sulfate composite material as an expansion agent, and polycarboxylic acid as a water reducer and retarder, thereby developing a new type of drilling sealing material, considering the compressive strength, fluidity, and swelling rate of the material (the swelling rate of the test block after 60 days of curing). As a basis for judgment, the single factor test method and orthogonal test method are used to determine the best admixture and water quality ratio.

2. Materials and Methods

2.1. Experimental Materials. The new type of borehole sealing material was based on ultrafine Portland cement. The ultrafine cement used in the experiment was produced by Shandong Kangjing New Material Technology. The appearance

Figure 3: Cement fluidity test.

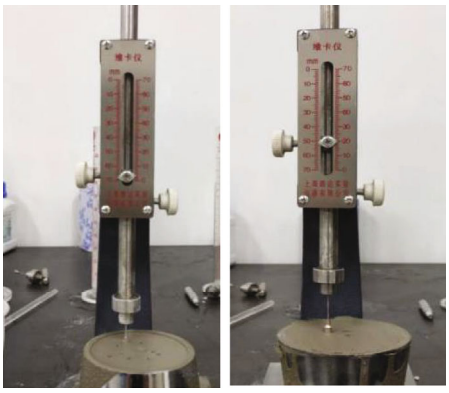

Figure 4: Determination of setting time.

Figure 5: Compressive strength test.

was a gray powder. The measured D90 value was 12.6 μm, and the measured D50 value was 5 μm. In addition, all the technical parameters and indicators met the requirements of "Superfine Portland Cement" (GB/T35161-2017). Its chemical composition is provided in Table 1. The expansion agent used in this experiment was a calcium oxide-calcium sulfate composite expansion agent (HCSA) produced by Shijiazhuang City Functional Building Materials Co., Ltd., and it had the appearance of an off-white powder. Its components are listed in Table 1. The polycarboxylic acid water-reducing agent (PCE) used in the experiment was produced by Fuyang Chengnan Building Materials Co., Ltd. It was a white powder that was easily soluble in water, and the water reduction rate was 20-35%. The retarder used in this experiment was seaweed powder produced by Jiangsu Changzhou Angu Waterproof Material Co., Ltd. The seaweed powder had the appearance of a white powder and was easily soluble in water. The solution was a colorless and transparent viscous liquid. Water was used to formulate a solution with a mass ratio of 1 : 130.

2.2. Experimental Method. Researchers have found that the addition of a retarder [18] and HCSA [19–21] will help cement hydration products to form a good spatial structure and improve the strength of cement, while the addition of PCE has a dispersing effect on cement particles and can improve the workability of cement and reduce unit water consumption [22, 23]. In a case where the interaction of various additives to the ultrafine cement and their influences on its strength and expansibility are unknown, the single factor experiment method can be used in preliminary experiments to determine the optimal dosage ranges. Then, based on an analysis of the results, the Design-Expert 8.0.5 Trial software can be used to design an orthogonal experiment in order to accurately understand the influence of each factor on the performance of a composite expansion borehole sealing material [24–26]. In this study, after the completion of the orthogonal experiment, the Design-Expert 8.0.5 Trial software was used to calculate the variance and range of the experimental data, and the influence of the compound incorporation of various additives on the performance of the borehole sealing material was studied. Finally, a response surface regression analysis was performed on the results of the orthogonal experiment, and a quantitative regression model reflecting the relationship between the compound dosing amount of the admixture and each filling performance index was obtained, which provided a basis for the optimization of the borehole sealing material formulation.

In the experiment, the standard triple test mold (70.7 mm × 70.7 mm × 70.7 mm) was first prepared. Then, the dry material and water quantities required for the production of the test piece were calculated according to the proportions in Tables 2 and 3. After mixing with water, the weighed ultrafine cement, expansion agent, and water-reducing agent were added together and mixed thoroughly (Figure 1). Finally, water was added for thorough mixing and pouring into the mold (Figure 2), which was placed in the curing box for curing (temperature 20 ± 2°C, humidity above 95%).

The fluidity test of the borehole sealing material was conducted using the specified determination method for cement mortar fluidity (GB/T2419-2005), which was expressed by the diffusion diameter (mm) of the slurry on a horizontal glass plate. The truncated cone mold had an upper mouth diameter of 36 mm, a lower mouth diameter of 60 mm, and a height of 60 mm. The evenly stirred cement slurry was placed in a round mold, the surface was flattened, and the round mold was quickly lifted off. After the cement slurry flowed, the average of the two perpendicular diameters was measured as the maximum fluidity (Figure 3).

The standard cement consistency water consumption, setting time, and stability test method (GB/T1346—2011) was used to measure the setting time. Use cement slurry standard consistency setting time tester (Vicat meter) to measure setting time. First, zero the Vicat meter. Then, water was

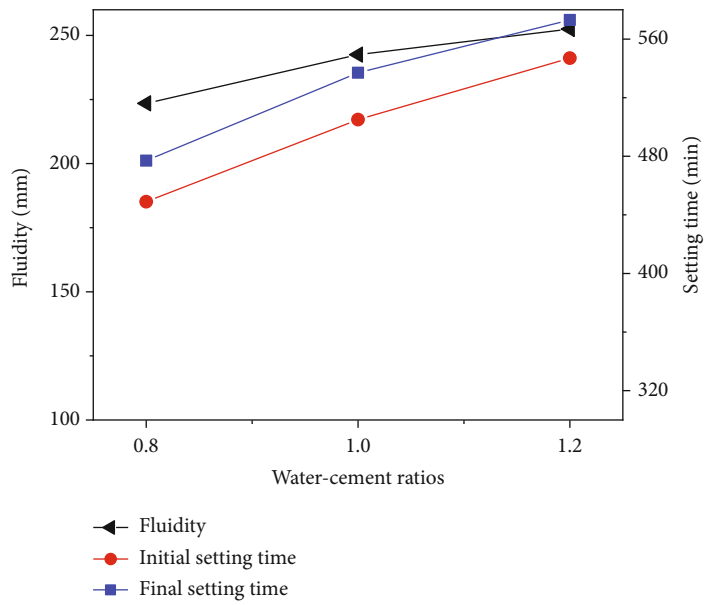

Figure 6: Effect of water–cement ratio on material setting time and fluidity.

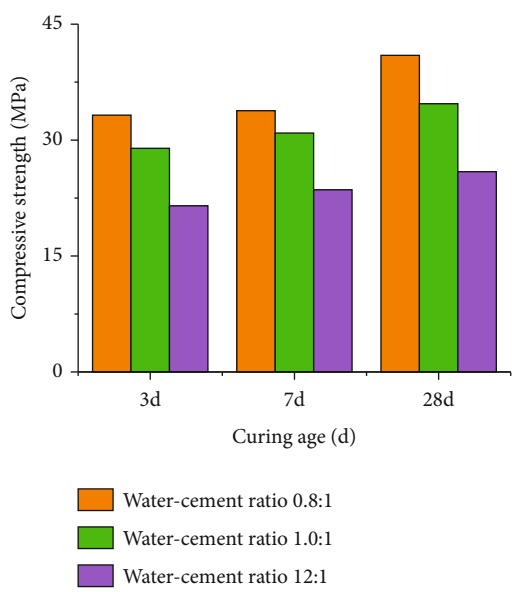

Figure 7: Effect of water–cement ratio on material strength.

separately added to the new borehole sealing material, which was evenly mixed poured into test molds, and placed in the curing box for curing after being leveled. Finally, the initial and final setting times of the material were measured according to the national standard (Figure 4).

Different materials were added to pure cement and mixed to form cement slurries. After molding, the initial volume was recorded as V1. The volume was read at corresponding time intervals, and the expansion rate was tested for two months. The volume was recorded as V_n, and the expansion rate of the test block was calculated with the following formula. The expansion rate was calculated according to the following formula:

$$\varepsilon_t = \frac{V_n - V_1}{V_1} \times 100\%. \quad (1)$$

The sample strength test utilized the standard cement mortar strength inspection method (GB/T50080-2016), with an RMT uniaxial press used to test the compressive strength of samples with different ages (Figure 5). The specific experimental steps are as follows:

(1) Wipe clean the surface of the specimen after curing

(2) Place the test piece in the testing machine. During the compressive strength test, the pressure surface of the test piece should be perpendicular to the top surface. The center of the test piece should be aligned with the center of the lower pressure plate of the testing machine

(3) During the test, the load should be applied continuously and evenly, and the loading speed should be 0.3-0.5 MPa/s

(4) When the test piece is close to failure and begins to deform rapidly, stop adjusting the switch of the testing machine until it fails. Then, record the failure load

After obtaining the optimal ratio of admixtures through the single factor and orthogonal experiments, the ultrafine cement raw materials and admixtures were prepared according to the optimal ratio, and the results were optimized and verified.

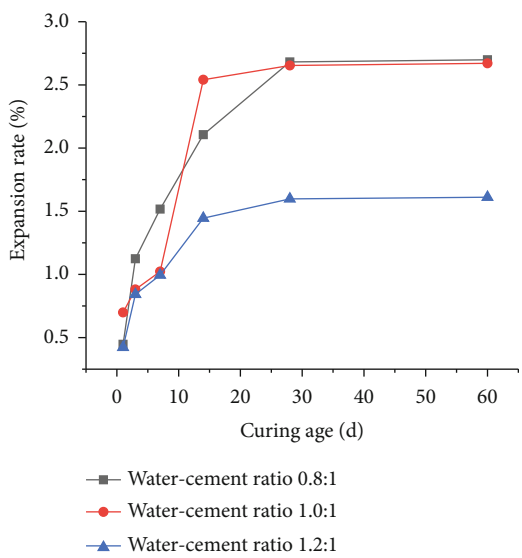

Figure 8: Effect of water–cement ratio on material expansion rate.

2.3. Single-Factor Experiment Method. Table 2 outlines the single-factor experimental design. While experimenting at the level of each control variable, the remaining influencing factors were controlled at fixed values. Among these, the retarder content was the ratio of the mass of the retarder to that of the ultrafine cement. The calculation method for the water-cement ratio, water-reducing agent, and expansion agent was the same as that for retarder, based on the flow of the material. The optimal value for the admixture content was determined based on the compressive strength and swelling property.

2.4. Orthogonal Experiment Method. Table 3 outlines the design of the orthogonal experiment. The water–cement ratio (A), retarder content (B), water-reducing agent content (C), and expansion agent content (D) were based on the optimal admixture content values found in the single factor experiments. In this experiment, three factors were given fixed values from the range of merit values, while the remaining factor was varied, with the resulting combinations representing a group of experiments. In order to ensure the accuracy of the results, the Box–Behnken experimental design function from the Design-Expert 8.0.5 Trial software was used. A total of 29 sets of experiments were carried out with the four factors and three levels, and the fluidity of the test block was taken as the response value.

3. Single-Factor Experiment Results and Analysis

3.1. Influence of Water–Cement Ratio on Performance of Borehole Sealing Material. The water–cement ratios selected in the experiment were 0.8, 1.0, and 1.2, and the effects of the water–cement ratio on the material properties are shown in Figures 6–8. It can be seen from Figure 6 that as the water–cement ratio increased, the fluidity and setting time of the material increased correspondingly because the consistency of the borehole sealing material decreased, and the solid phase of cement per unit volume of material decreased. Thus, the hydration and coagulation time was relatively prolonged. From Figure 7, it can be seen that under the same curing age, the compressive strength decreases with an increase in the water–cement ratio, and under the same water–cement ratio, as the curing time increases, the compressive strength of the test block will also increase. When the water–cement ratio is 0.8, the maximum 28-day compressive strength of the material reaches 40.97 MPa. From Figure 8, it can be seen that when the water–cement ratio increases from 0.8 to 1 and the curing age increases, the expansion rate of the material first decreases, then increases, and finally remains unchanged. When the water–cement ratio continues to increase to 1.2, the expansion rate drops from the maximum of 2.699 to 1.611, which is a decrease of 40.11%. Therefore, considering the influences of the water–cement ratio on the strength, fluidity, and expansion rate of the material, a value of 0.8–1.0 is more appropriate for the water–cement ratio.

3.2. Effect of Retarder on the Properties of Sealing Material. The amounts of retarder selected in the experiment were 0.05%, 0.5%, and 1.5%. As shown in Figure 9, as the amount of retarder increases, the fluidity of the borehole sealing material continues to decrease, and the setting time increases with the retarder. This occurs because the retarder inhibits the crystallization nucleation process of the hydration product of the cement material, and it is adsorbed on the cement particles, which has a retarding effect. From Figure 10, it can be seen that at the same age, as the content of retarder increases, the strength of the material will first decrease and then increase. The compressive strength of the material was the highest when the retarder content is 0.05%, but decreased when the retarder content increased. It can be seen from Figure 11 that with an increase in retarder content, the expansion rate of the material gradually decreases. After a curing period of 30 days, the expansion rate changed more smoothly, and it expanded when the retarder content was 0.05%. The maximum rate was 2.671%. Considering on-site application and cost control, a 0.05% retarder content would be appropriate.

3.3. Influence of Water-Reducing Agent on Performance of Borehole Sealing Material. The amounts of water-reducing agent selected in the experiment were 0.2%, 0.5%, and 0.8%. As seen in Figure 12, the fluidity and setting time of the material increase with the amount of water-reducing agent. When the amount of water-reducing agent is 0.5%, this increasing trend slows down. From Figure 13, it can be seen that the contribution of the amount of water-reducing agent to the compressive strength of the test block is not always proportional. When the amount of water-reducing agent reached 0.8%, the compressive strength decreased. This occurred because the water-reducing effect reached saturation after exceeding the saturated content of PCE (0.5%), but the PCE gradually introduced a certain amount of bubbles, with more air bubbles introduced when more water-reducing agent was added. This led to more cement stone structural defects easily forming after the slurry was hydrated and hardened, resulting in small fluctuations in the mechanical properties. When

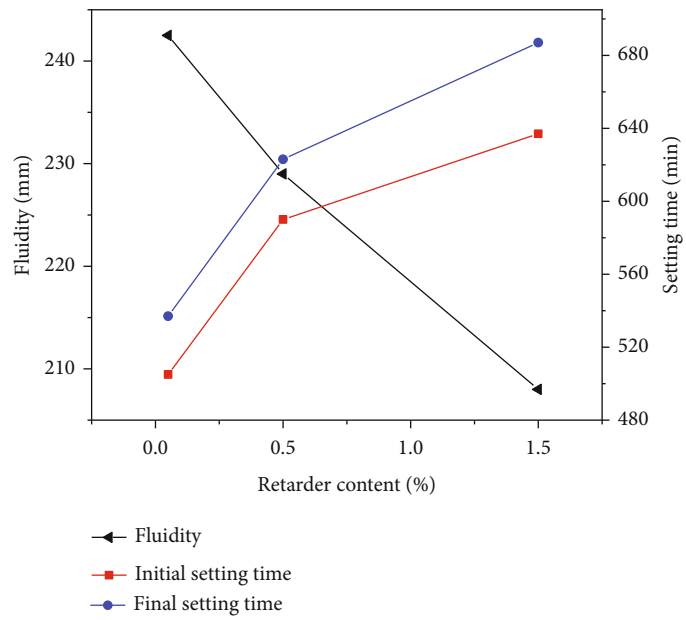

Figure 9: Effect of amount of retarder on setting time and fluidity of material.

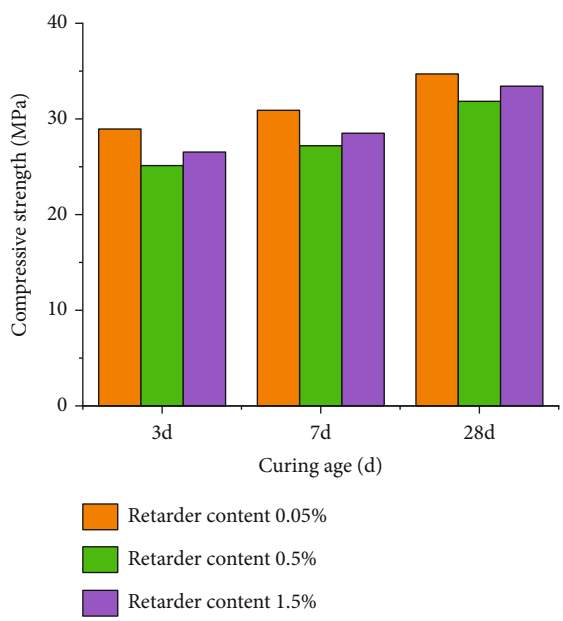

Figure 10: Effect of retarder content on material strength.

the water-reducing agent content was 0.5%, the 28-day compressive strength was 34.701 MPa. It can be seen from Figure 14 that the change law of the expansion rate is similar to that of the strength, showing a trend of increasing and decreasing. Considering the influence of the water-reducing agent on the expansion rate, strength, etc., the best dosage for the water-reducing agent was approximately 0.5%.

3.4. Influence of Expansion Agent on Performance of Borehole Sealing Material. The amounts of expansion agent selected in the experiment were 5%, 10%, and 15%. It can be seen from Figure 15 that with an increase in the amount of expansion agent, the fluidity and setting time of the test block decreased. From Figure 16, it can be seen that with an increase in the expansion agent dosage, the compressive strength of the material first slightly increases and then decreases. This is because the expansion agent HCSA promotes the growth of needle-shaped ettringite AFt crystals in the early stage, which increases the strength. However, too much expansion agent was not conducive to the formation of strength [27]. From Figure 17, it can be seen that the expansion rate of the test block increases with the increase in the expansion agent. However, after curing for 14 days, the surface of the test block with an expansion agent content of 15% has obvious cracks (as shown in Figure 18). During the actual sealing process, new air leakage channels will be produced, which is not conducive to the sealing of the drainage borehole, resulting in a decrease in the gas concentration of the drainage borehole. Therefore, the best dosage for the expansion agent is approximately 10%.

4. Orthogonal Experiment Results and Analysis

4.1. Model Establishment. The range analysis gave the best ratio for single-objective optimization, but in the actual application process, the compressive strength, fluidity, and expansion rate need to be comprehensively considered. Thus, multiobjective nonlinear formulation optimization is required to determine the optimal matching ratio. In the orthogonal experiment results listed in Table 4, the water–cement ratio, retarder content, water-reducing agent content, and expansion agent content are independent variables A, B, C, and D, respectively. This study conducted a response surface analysis of the liquidity. First, it was necessary to select a suitable model to fit the results, and the results of the orthogonal experiment (listed in Table 5) were input into the Design-Expert 8.0.5 software to fit different models. The fitting results are listed in Table 4. The Design-Expert software recommended the use of linear equation models and

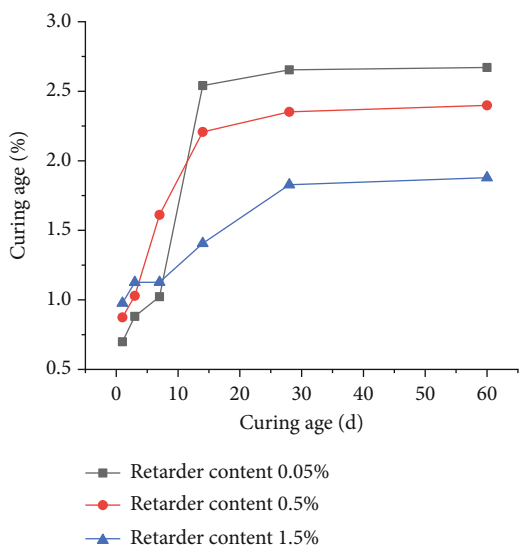

Figure 11: Effect of amount of retarder on expansion rate of material.

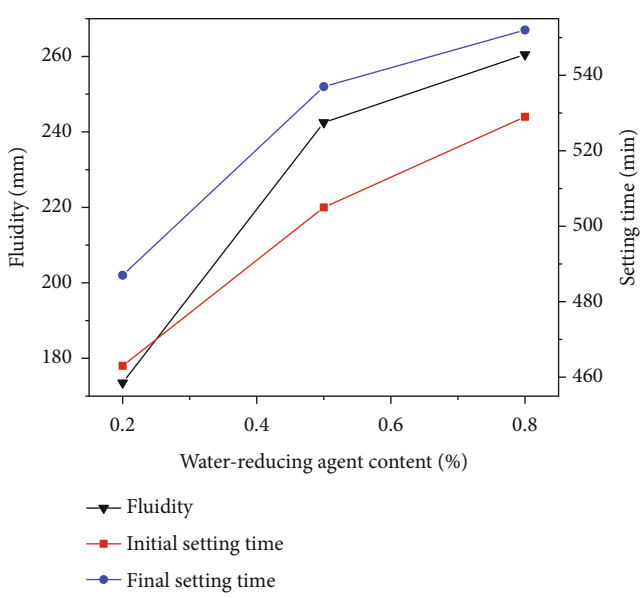

Figure 12: Effect of water-reducing agent on material setting time and fluidity.

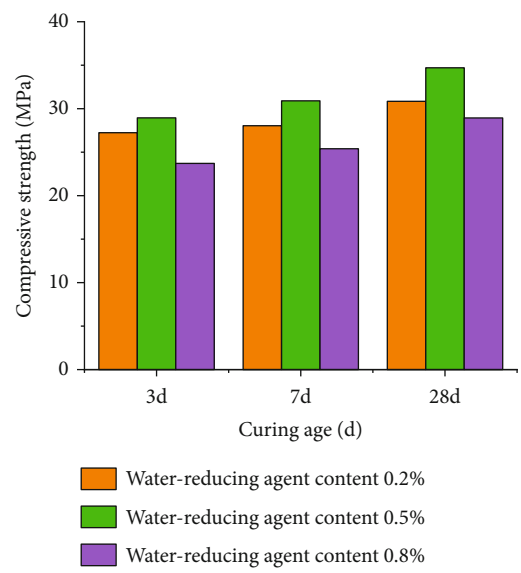

Figure 13: Effect of water-reducing agent on material strength.

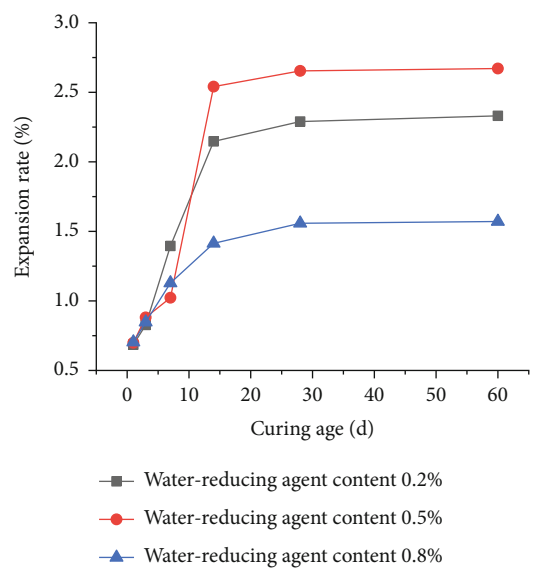

Figure 14: Effect of water-reducing agent on material expansion rate.

quadratic equation models, which had better fits than other models. It can be seen from Table 4 that the sum of the squared prediction residuals is low in several models; however, the R^2 value of the linear model is 0.685, which is smaller than the R^2 value of the quadratic equation model (0.9144), indicating that the model's correlation with the experimental results is low. Thus, the model is inaccurate. The Adj R^2 value of the linear model is small compared with that of the quadratic equation model, indicating that the model still needs further development. Based on these results, the experiment initially selected the quadratic equation model for fitting.

4.2. Variance Results and Significance Tests. From Table 6, it can be seen that the F value of the model is 10.69, the Prob $> F$ value is less than 0.0001, and the correction coefficient of determination (Adj R^2) is 0.8289, which shows that the model fits the data well and the experimental error is small. From the significance test, it can be seen that the factors had the following order of significance: C (water – reducing agent) > A (water – cement ratio) > B (retarder) > D (expansion agent). The factor combinations had the following order: AC (water – cement ratio, water – reducing agent) > CD (water – reducing agent, expansion agent) > BC (retarder, water – reducing agent) > AD (water – cement ratio, expansion agent) > AB (water – cement ratio, expansion agent) > BD (retarder, expansion agent). Among these, the

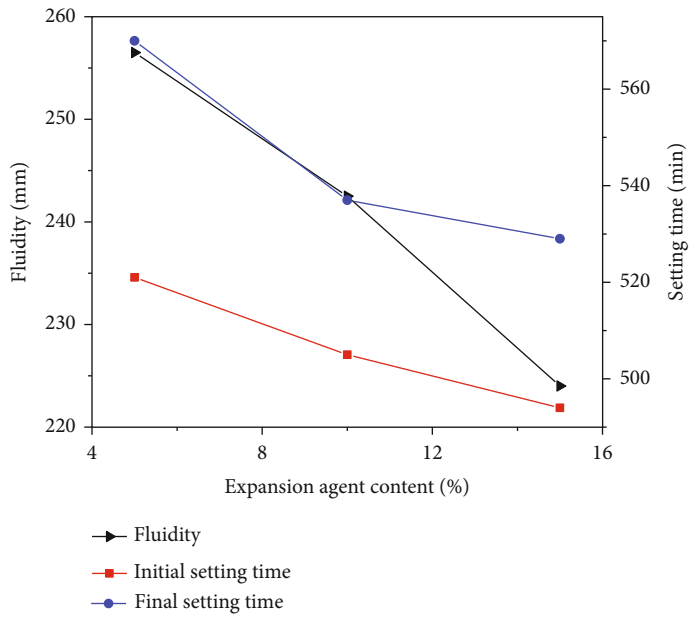

Figure 15: Effect of expansion agent on material setting time and fluidity.

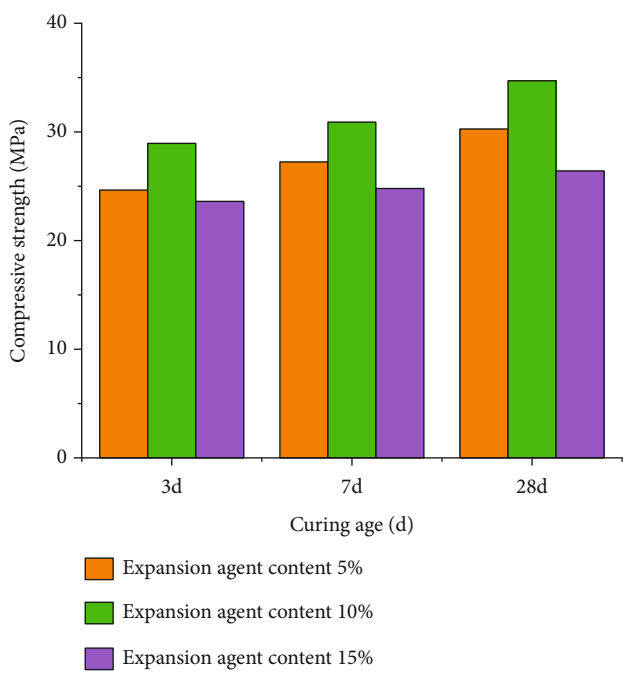

Figure 16: Effect of expansion agent on material strength.

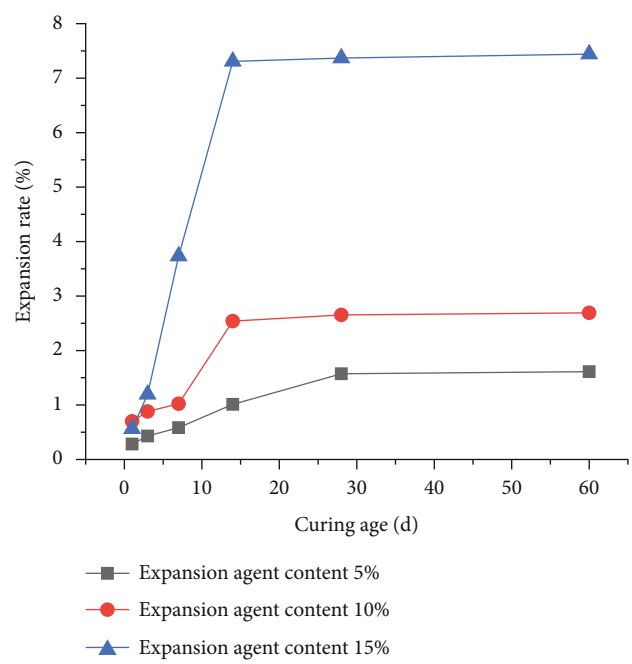

Figure 17: Effect of expansion agent on material expansion rate.

Prob > F value of the C factor was less than 0.0001, which indicated that the index was extremely significant, and the Prob > F values of factors A and B were less than 0.005, which indicated that these two indicators were significant; the interaction of AC was the most significant, and the interaction of BD was the least significant.

4.3. Response Surface Analysis. The response surface drawn according to the binomial polynomial regression equation was a three-dimensional surface obtained by the interaction of the response values of the independent variables. The response value (liquidity) could be predicted and optimized, and any two factors could also be adjusted to analyze their interaction and obtain the interaction rules. It was possible to determine when any two of the four factors (A (water–cement ratio), B (retarder content), C (water-reducing agent content), and D (expansion agent content)) remained unchanged by the interaction and laws of the other two factors.

Figure 19 shows the effect of the water–cement ratio and water-reducing agent on the fluidity results. It can be seen from Figure 19 that the fluidity varies greatly with the

Figure 18: Effect of different dilatant dosages on test block.

Table 4: Comprehensive statistical analysis of multiple models.

Source	Std. dev.	*R*-squared	Adjusted *R*-squared	Predicted *R*-squared	PRESS	
Linear	17.95	0.6850	0.6324	0.5231	11701.95	Suggested
2FI	16.86	0.7915	0.6757	0.3841	15111.63	
Quadratic	12.25	0.9144	0.8289	0.5072	12092.52	Suggested
Cubic	5.98	0.9912	0.9592	-0.2605	30927.00	

Table 5: Orthogonal test results.

No	A	B/%	C/%	D/%	R3d/MPa	R7d/MPa	R28d/MPa	Fluidity/mm	Initial setting time/min	Final setting time/min	Expansion rate/%
1	0.8	0.03	0.4	9	29.899	32.069	41.597	213.5	440	469	1.897
2	0.8	0.04	0.5	9	37.697	38.477	42.833	226	419	437	2.032
3	0.8	0.04	0.4	10	30.986	32.991	38.969	190.5	410	430	3.281
4	0.8	0.04	0.3	9	33.997	35.01	39.021	199	406	443	1.931
5	0.8	0.04	0.4	8	39.918	42.197	41.398	185.5	431	458	1.593
6	0.8	0.05	0.4	9	31.652	34.133	37.256	207.5	461	490	1.821
7	0.9	0.03	0.5	9	28.479	32.141	36.966	242	343	376	1.898
8	0.9	0.03	0.4	10	26.943	28.511	34.981	218.5	344	368	2.471
9	0.9	0.03	0.4	8	30.931	32.871	38.996	234	416	438	1.614
10	0.9	0.03	0.3	9	27.696	31.233	37.061	179	337	370	1.521
11	0.9	0.04	0.4	9	28.601	30.381	36.983	193	430	456	2.053
12	0.9	0.04	0.4	9	28.601	30.381	36.983	193	430	456	2.053
13	0.9	0.04	0.3	10	31.239	32.011	34.882	153.5	424	449	2.329
14	0.9	0.04	0.4	9	28.601	30.381	36.983	193	430	456	2.053
15	0.9	0.04	0.5	8	34.312	38.021	37.409	212	437	463	1.589
16	0.9	0.04	0.5	10	31.213	32.997	34.411	243	422	444	2.809
17	0.9	0.04	0.3	8	32.986	36.021	37.311	183.5	431	457	1.621
18	0.9	0.04	0.4	9	28.601	30.381	36.983	193	430	456	2.053
19	0.9	0.04	0.4	9	28.601	30.381	36.983	193	430	456	2.053
20	0.9	0.05	0.3	9	25.896	28.033	33.767	153.5	482	518	1.621
21	0.9	0.05	0.5	9	26.062	29.133	36.761	247	360	395	1.812
22	0.9	0.05	0.4	10	26.993	27.012	33.761	167	365	393	2.597
23	0.9	0.05	0.4	8	28.922	30.41	34.562	185	490	525	1.531
24	1	0.04	0.3	9	27.664	29.008	33.678	179	420	454	1.986
25	1	0.03	0.4	9	26.295	28.091	32.019	240	349	376	1.778
26	1	0.04	0.4	10	26.513	27.978	28.072	230	359	386	2.093
27	1	0.05	0.4	9	23.997	27.843	31.907	229.5	475	503	1.803
28	1	0.04	0.4	8	28.911	31.036	38.213	207.5	439	463	1.302
29	1	0.04	0.5	9	27.476	29.989	33.778	280	422	457	1.889

Table 6: Response surface quadratic model and analysis of variance results.

Source	Sum of squares	df	Mean square	F	Prob > F
Model	22436.79	14	1602.63	10.69	<0.0001
A	1728.00	1	1728.00	11.52	0.0044
B	1575.52	1	1575.52	10.51	0.0059
C	13500.52	1	12838.02	90.03	<0.0001
D	2.08	1	2.08	0.014	0.9078
AB	5.06	1	5.06	0.034	0.8569
AC	1369.00	1	1369.00	9.13	0.0092
AD	76.56	1	76.56	0.51	0.4866
BC	232.56	1	232.56	1.55	0.2334
BD	1.56	1	1.56	0.010	0.9201
CD	930.25	1	930.25	6.20	0.0259
A2	2200.05	1	2200.05	14.67	0.0018
B2	582.84	1	582.84	3.89	0.0688
C2	327.37	1	327.37	2.18	0.1617
D2	95.32	1	95.32	0.64	0.4386
Residual	2099.40	14	149.96		
Lack of fit	2099.40	10	209.94		
Pure error	0.000	4	0.000		
Cor total	24536.19	28			

water–cement ratio or water-reducing agent, and the response surface is steep at this time. As reflected in the contour map, the contour lines are dense. The rapid color change in the contour map also proves that the slope of the response surface is large. This indicates that the water–cement ratio and interaction of the water-reducing agent have a significant impact on the response value, which is consistent with the previous variance analysis results for each item. The two factors of the ash ratio and water-reducing agent have a more significant influence on the test results. Because with the gradual increase of the water-cement ratio, the free water content in the cement slurry gradually increases, the free water has a diluting and dispersing effect on the flocculent structure, the large-volume floccules gradually separate and become smaller, and the small-volume floccules are gradually separated disassembly and separation, so when the water-cement ratio is small, the initial apparent viscosity of the cement slurry is greater. When the water-cement ratio is 0.5 to 0.8, with the gradual increase of the water-cement ratio, on the one hand, more sufficient water molecules are provided for the physical and chemical reactions of the cement slurry, and the floc structure is produced. More effective reaction conditions, on the other hand, the increase of free water molecules causes the flocs to decompose into smaller-structured flocs, which reduces the dispersion resistance. At the same time, the free water molecules also play a better lubricating effect between the flocs. When the water-cement ratio is greater than 1.0 (the water-cement ratio is 1.0 and 2.0), because the free water content reaches a saturated state, the free water has little effect on the physical and chemical reactions of the slurry, and the free water has small. The decomposition of substances and the lubrication of flocs are the main influencing factors.

Figure 20 shows the effect of the water-reducing agent and expansion agent on the fluidity results. It can be seen from Figure 20 that when the water-reducing agent and expansion agent are taken at the upper limits of their selected level ranges, the fluidity change trend is relatively steep, indicating that the interaction between the time-reducing agent and expansion agent has a significant impact on the response value. The contour distribution trend is related to the factor level, and there is a certain distortion in the three-dimensional surface graph. The interaction of these two factors affects the particle flow, and the dense contour lines on the abscissa also indicate that the water-reducing agent has a greater impact on fluidity. Because the polycarboxylic acid water reducer can promote the hydration process of cement, the total amount of CSH gel and Ca(OH) 2 in the cement stone can be increased, and the polycarboxylic acid water reducer can greatly reduce the particles of CSH. It can increase the degree of polymerization of the gel, and the polycarboxylic acid-based water reducing agent can increase the degree of polymerization of silicon-oxygen tetrahedron in the CSH of the hydration product.

Figure 21 shows the effect of the retarder and water-reducing agent on the fluidity results. It can be seen from Figure 21 that the contour lines on the ordinate are denser, while the contour lines on the abscissa are sparse, indicating that the retarder has a greater impact on fluidity. When the upper limit of the content of the retarder is used, the response surface is relatively smooth, indicating that the retarder has a certain influence on the fluidity, but the range of this influence is small.

Figure 22 shows the effect of the water–cement ratio and expansion agent on the fluidity results. It can be seen from Figure 22 that the contour lines of the ordinate are sparse, and the contour lines of the abscissa are dense, indicating that the water–cement ratio has a greater impact on the fluidity. The expansion agent has little effect on the fluidity; the response surface is relatively smoother, indicating that the interaction of the two factors has a certain impact on the fluidity, but the range of this influence is small. When using the upper limits of the two factors, the response surface is steep, indicating that the interaction of the two factors has the greatest impact on the liquidity at this time.

Figure 23 shows the effect of the water–cement ratio and retarder on the fluidity results. The shape of the contour reflects the strength of the interaction effect. A circle indicates that the interaction of the two factors is not significant, while an ellipse shows the opposite. It can be seen from Figure 23 that the distribution of the abscissa contour lines is denser than that on the ordinate, indicating that the influence of the water–cement ratio on the response value is more significant than that of the retarder. The pattern change law is similar to the response obtained by the two-factor analysis of variance in the figure. The influence law of the value is the same, and the graph has a certain distortion. When the water–cement ratio is at the upper limit and the retarder is at

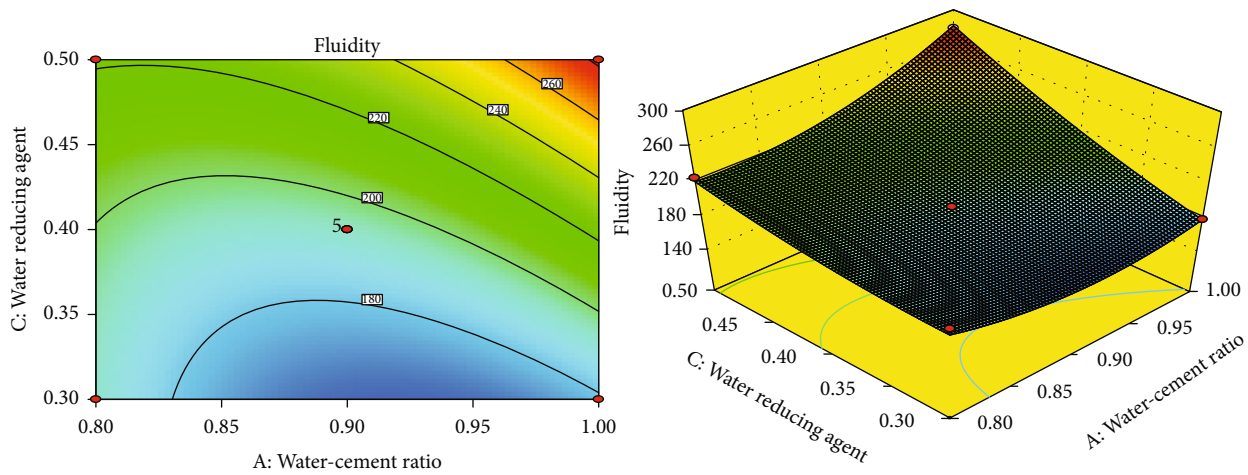

Figure 19: Effect of water–cement ratio and water reducer on fluidity.

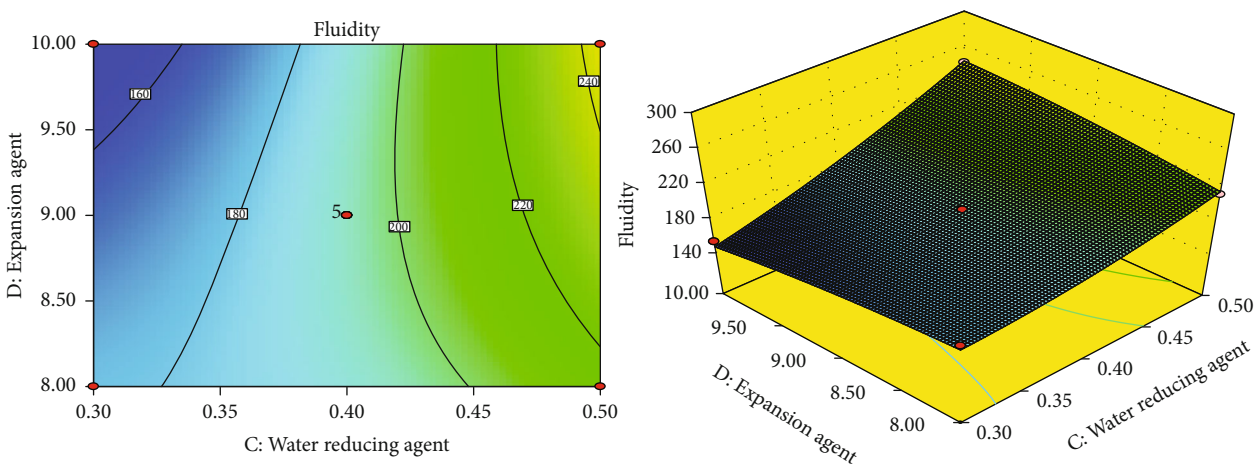

Figure 20: Effect of water-reducing agent and expansion agent on fluidity.

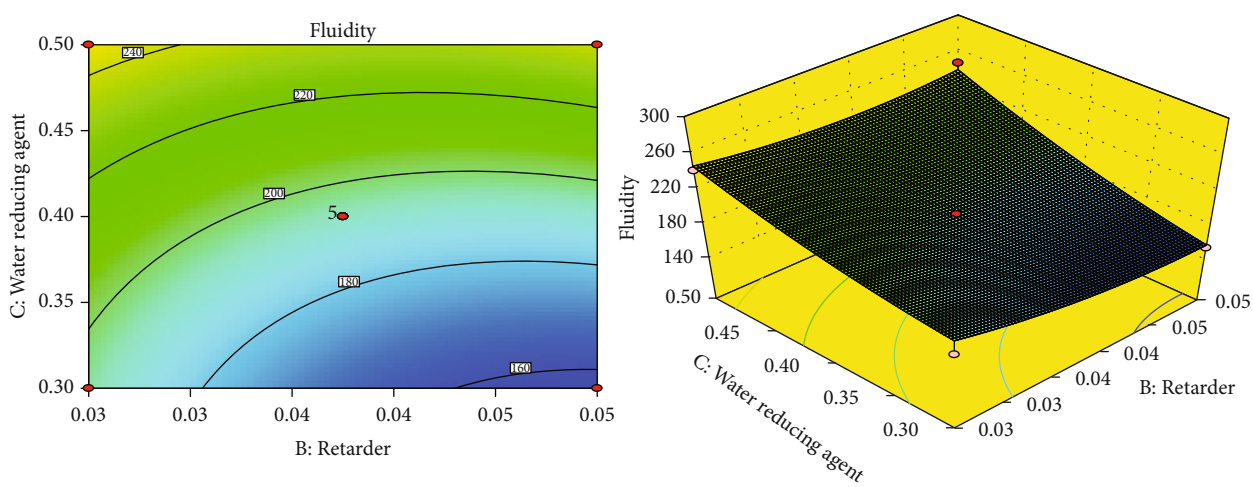

Figure 21: Effect of retarder and water-reducing agent on fluidity.

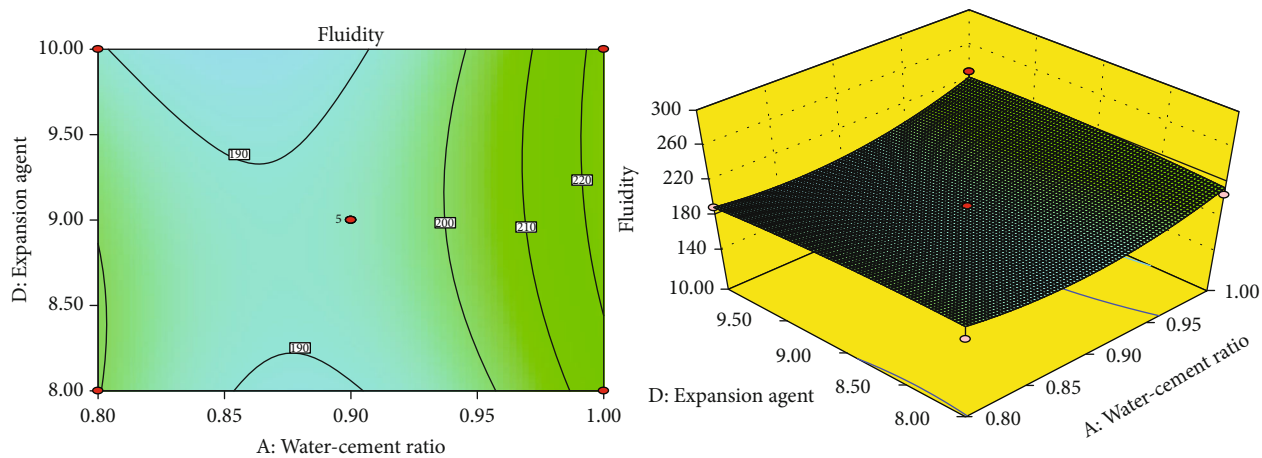

Figure 22: Effect of water–cement ratio and expansion agent on fluidity.

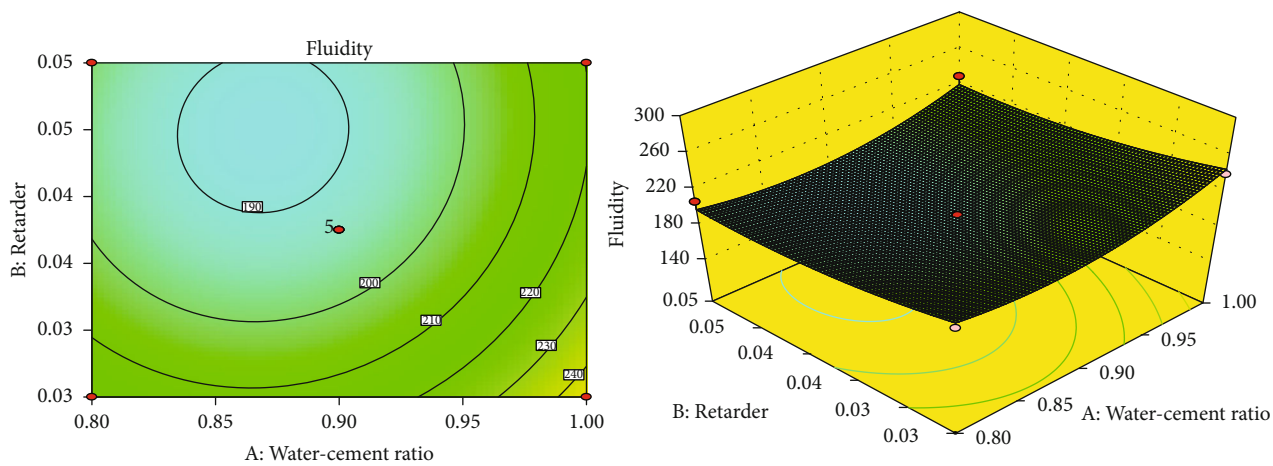

Figure 23: Effect of water–cement ratio and retarder on fluidity.

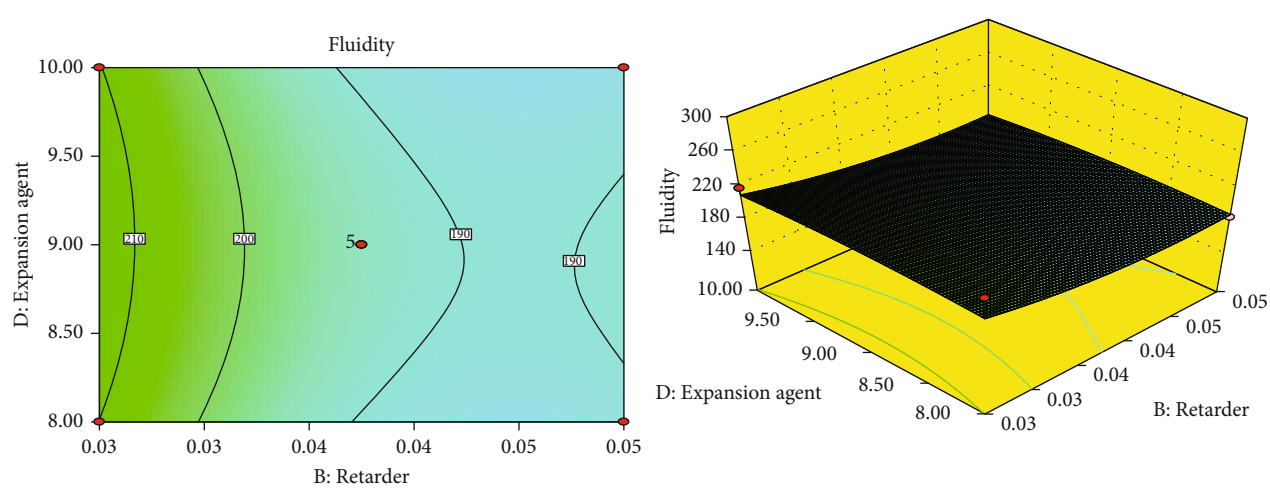

Figure 24: Effect of retarder and expansion agent on fluidity.

the lower limit, the response surface is steep, but the overall response surface is relatively flat, indicating a certain interaction between the two factors, but the effect is small.

Figure 24 shows the effect of the retarder and expansion agent on the fluidity results. As shown in Figure 24, the contour lines on the abscissa are dense, while the contour lines on the ordinate are sparse, indicating that the influence of

Table 7: Optimization scheme and results.

No	Water-cement ratio	Experimental optimization ratio		Expansion agent/%	Forecast liquidity/mm	Measured liquidity/mm	Error/%
		Retarder/%	Water reducing agent/%				
1	1	0.03	0.5	8.81	288.494	288	-0.518
2	0.99	0.03	0.49	9.11	287.832	287	-0.289
3	0.98	0.04	0.5	9.98	287.561	287.5	-0.021
4	1	0.03	0.49	9.06	288.624	286.5	-0.736
5	0.97	0.03	0.49	9.98	283.282	283.5	0.077
6	0.98	0.03	0.49	9.82	287.186	287	-0.065

the coagulant on the fluidity is greater than that of the expansion agent. This is consistent with the results of the analysis of variance, and the response surface is the smoothest when the retarder interacts with the expansion agent, indicating that the interaction between the retarder and expansion agent has the least significant effect on the fluidity. This is due to the hydration reaction of the mineral components in the expansion agent to produce more AFT, which leads to the increase of hydration products in the cement hydration system, the increase of system consistency, and the decrease of fluidity. This is due to the hydration reaction of the mineral components in the expansion agent to produce more AFT, which leads to the increase of hydration products in the cement hydration system, the increase of system consistency, and the decrease of fluidity.

4.4. Parameter Optimization and Verification. The Design-Expert software was used for a further analysis of the experimental results, using the fluidity as the optimization index to obtain the optimized experimental program by selecting the first six groups of optimized experimental programs and verifying them, as shown in Table 7.

It can be seen from Table 7 that when using the optimized ratio recommended by the Design-Expert 8.0.5 software, the maximum absolute error between the predicted value of liquidity and the actual value obtained by an actual measurement in the laboratory was only 0.736%, indicating that the model was relatively reliable. Taking into account the operability and simplicity of on-site grouting, when the water–cement ratio is relatively small, the thickness of the borehole sealing material is too large. This makes grouting more difficult, and it is prone to blockage. The retarder has a certain viscosity to increase the consistency of the material. Thus, it is appropriate to reduce the amount of retarder to increase the fluidity. The comprehensive expansion rate, fluidity, and strength were considered to select and optimize the experimental conditions as follows: water-reducing agent of 0.5%, retarder of 0.03%, water–cement ratio of 1, and expansion agent of 8%.

5. Conclusions

The results obtained in this study made it possible to draw the following conclusions.

(1) It can be seen from the experimental results that as the water-cement ratio increases, the fluidity and setting time of the material increase correspondingly. Under the same curing age, the compressive strength decreased with the water-cement ratio increased; with an increase in the retarder content, the fluidity of the borehole sealing material continued to decrease, and the setting time increased with an increase in the retarder content. At the same age, with an increase in the retarder content, the strength of the material first decreased and then increased. As the amount of water-reducing agent increased, the fluidity and setting time of the material increased. When the amount of water-reducing agent was 0.5%, this increasing trend slowed down and the contribution of the amount of water-reducing agent to the compressive strength of the test block was not always proportional. When the amount of water-reducing agent reached 0.8%, the compressive strength of the test block decreased. With the amount of expansion agent increased, the fluidity and setting time of the test block decreased. With the amount of expansion agent increased, the compressive strength of the material first increased slightly and then decreased

(2) With ultrafine cement as the base material, an expansion agent, polycarboxylic acid water-reducing agent, and retarder were added to develop a sealing material to meet the performance requirements of fluidity and expansion

(3) Orthogonal experiments were designed using the Box–Behnken module in the Design-Expert software. Fluidity was the response value, and various test factors (water–cement ratio, water-reducing agent, retarder, and expansion agent) were established and optimized. The quadratic model of time showed a high prediction accuracy

(4) The influence of each component on the fluidity of the material was obtained using a range and variance analysis and a significance test. These had the following order: C (water – reducing agent) > A (water cement ratio) > B (retarder) > D (expansion agent)

(5) According to the response surface drawn by the binomial polynomial regression equation, the interaction

of any two factors was analyzed, and the interaction laws were obtained. These effects had the following order: AC (water – cement ratio, water – reducing agent) > CD (water – reducing agent, expansion agent) > BC (retarder, water – reducing agent) > AD (water – cement ratio, expansion agent) > AB (water – cement ratio, retarder) > BD (retarder, expansion agent)

(6) The response surface analysis method combined the single factor experiment results and the actual sealing grouting situation to obtain the best experimental conditions in this experiment: a water-reducing agent content of 0.5%, a retarder content of 0.03%, a water-cement ratio of 1, and an expansion agent content of 8%

Data Availability

The data used for conducting classifications are available from the corresponding author authors upon request.

Conflicts of Interest

The authors declared no potential conflicts of interest with respect to the research, authorship, and/or publication of this article.

Acknowledgments

All authors contributed to this paper. Xin Guo prepared and edited the manuscript. Xin Guo and Sheng Xue made a substantial contribution to the data analysis and revised the article. Xin Guo, Gege Yang, and Yaobin Li reviewed the manuscript and processed the investigation during the research process. Sheng Xue and Chunshan Zheng provided fund support. We acknowledge the financial support for this work provided by the National Key Research and Development Program of China (2018YFC0808000), National Natural Science Foundation of China (51904013), Young Elite Scientists Sponsorship Program by Anhui Science and Technology Association, and Open Research Fund of State Key Laboratory of Coal Resources and Safe Mining, CUMT (SKLCRSM20KF003).

References

[1] L. Yuan, "Strategic thinking of simultaneous exploitation of coal and gas in deep mining," *Journal of China Coal Society*, vol. 41, no. 1, pp. 1–6, 2016.

[2] L. Yuan and P. S. Zhang, "Development status and prospect of geological guarantee technology for precise coal mining," *Journal of China Coal Society*, vol. 44, no. 8, pp. 2277–2284, 2019.

[3] L. Fan, H. M. Zhou, and Y. H. Zhang, "Influence of microfractures on strength parameters of engineering rock mass," *Chinese Journal of Rock Mechanics and Engineering*, vol. 30, no. 1, pp. 2703–2709, 2011.

[4] M. Wtrzykowshi, P. Trtik, and B. Munch, "Plastic shrink age of mortars with shrink age reducing admixture and lightweight aggregates studied by neutron tomography," *Cement and Concrete Research*, vol. 73, pp. 238–245, 2015.

[5] F. Pelisser, B. Aimir, and L. Henriette, "Effect of the addition of synthetic fibers to concrete thin slabs on plastic shrinkage cracking," *Construction and Building Materials*, vol. 24, no. 11, pp. 2171–2176, 2010.

[6] M. Wasil, "Effect of bentonite addition on the properties of fly ash as a material for landfill sealing layers," *Applied Sciences*, vol. 10, no. 4, article 1488, 2020.

[7] P. K. De Maeijer, B. Craeye, R. Snellings et al., "Effect of ultrafine fly ash on concrete performance and durability," *Construction and Building Materials*, vol. 263, article 120493, 2020.

[8] H. M. Sujay, N. A. Nair, H. S. Rao, and V. Sairam, "Experimental study on durability characteristics of composite fiber reinforced high-performance concrete incorporating nanosilica and ultra fine fly ash," *Construction and Building Materials*, vol. 262, article 120738, 2020.

[9] E. Boghssian and L. D. Wegne, "Use of flax fibres to reduce plastic shrinkage cracking in concrete," *Cement and Concrete Research*, vol. 30, no. 10, pp. 929–937, 2008.

[10] J. Hogancamp and Z. Grasley, "The use of microfine cement to enhance the efficacy of carbon nanofibers with respect to drying shrinkage crack resistance of Portland cement mortars," *Cement and Concrete Composites*, vol. 83, pp. 269–272, 2017.

[11] H. Y. Li, Y. C. Zhang, J. Wu, X. Y. Zhang, L. W. Zhang, and Z. F. Li, "Grouting sealing mechanism of water gushing in karst pipelines and engineering application," *Construction and Building Materials*, vol. 254, article 119250, 2020.

[12] D. P. Zheng, D. M. Wang, D. L. Li, C. F. Ren, and W. C. Tang, "Study of high volume circulating fluidized bed fly ash on rheological properties of the resulting cement paste," *Construction & Building Materials*, vol. 135, pp. 86–93, 2017.

[13] Y. Liu, J. G. Han, M. Y. Li, and P. Y. Yan, "Effect of a nanoscale viscosity modifier on rheological properties of cement pastes and mechanical properties of mortars," *Construction and Building Materials*, vol. 190, pp. 255–264, 2018.

[14] C. Chen, L. Y. Peng, and Z. H. Zhang, "Performance of superfine cement-water glass double slurry and effect analysis on sand grouting," *Bulletin of the Chinese Ceramic Society*, vol. 37, no. 12, pp. 3883–3887, 2018.

[15] N. Wongkornchaowalit and V. Lertchirakarn, "Setting time and flowability of accelerated Portland cement mixed with polycarboxylate superplasticizer," *Journal of Endodontics*, vol. 37, no. 3, pp. 387–389, 2011.

[16] M. Kazuki, S. Daiki, K. Hirokatsu, and S. Etsuo, "Effect of non-adsorbed superplasticizer molecules on fluidity of cement paste at low water-powder ratio," *Cement and Concrete Composites*, vol. 97, pp. 218–225, 2019.

[17] H. Güllü, A. Cevik, K. Al-Ezzi, and M. E. Gülsan, "On the rheology of using geopolymer for grouting: a comparative study with cement-based grout included fly ash and cold bonded fly ash," *Construction and Building Materials*, vol. 196, pp. 594–610, 2019.

[18] W. Kubissa, R. Jaskulski, and M. Grzelak, "Torrent air permeability and sorptivity of concrete made with the use of air entraining agent and citric acid as setting retardant," *Construction and Building Materials*, vol. 268, article 121703, 2021.

[19] T. Kim, K. Y. Seo, C. Kang, and T. K. Lee, "Development of eco-friendly cement using a calcium sulfoaluminate expansive agent blended with slag and silica fume," *Applied Sciences*, vol. 11, no. 1, p. 394, 2021.

[20] D. S. Vijayan and D. Parthiban, "Effect of solid waste based stabilizing material for strengthening of expansive soil- a review," *Environmental Technology & Innovation*, vol. 20, article 101108, 2020.

[21] H. Kabir and R. D. Hooton, "Evaluating soundness of concrete containing shrinkage-compensating MgO admixtures," *Construction and Building Materials*, vol. 253, article 119141, 2020.

[22] I. Cavusoglu, E. Yilmaz, and A. O. Yilmaz, "Additivity effect on properties of cemented coal fly ash backfill containing water-reducing admixtures," *Construction and Building Materials*, vol. 267, article 121021, 2021.

[23] M. Kioumarsi, F. Azarhomayun, M. Haji, and M. Shekarchi, "Effect of shrinkage reducing admixture on drying shrinkage of concrete with different w/c ratios," *Materials*, vol. 13, no. 24, article 5721, 2020.

[24] O. U. Izevbekhai, W. M. Gitari, N. T. Tavengwa, W. B. Ayinde, and R. Mudzielwana, "Response surface optimization of oil removal using synthesized polypyrrole-silica polymer composite," *Molecules*, vol. 25, no. 20, article 4628, 2020.

[25] B. S. Mohammed, V. C. Khed, and M. S. Liew, "Optimization of hybrid fibres in engineered cementitious composites," *Construction and Building Materials*, vol. 190, pp. 24–37, 2018.

[26] N. U. Kockal and T. Ozturan, "Optimization of properties of fly ash aggregates for high-strength lightweight concrete production," *Materials & Design*, vol. 32, no. 6, pp. 3586–3593, 2011.

[27] J. Carette, B. Delsaute, N. Milenkovic, J. P. Lecomte, M. P. Delplancke, and S. Staquet, "Advanced characterisation of the early age behaviour of bulk hydrophobic mortars," *Construction and Building Materials*, vol. 267, article 120904, 2021.